UTS UNIVERSITY OF TECHNOLOGY SYDNEY

ENERGY INFRASTRUCTURE SAFETY UNDER THERMAL AND MECHANICAL LOADS

by Kaiyi Chi

Thesis submitted in fulfilment of the requirements for the degree of

DOCTOR OF PHILOSOPHY

under the supervision of

Principal Supervisor:	Professor Chengqing Wu
Co-Supervisor:	Associate Professor Jun Li

University of Technology Sydney
Faculty of Engineering and Information Technology

June 2025

CERTIFICATE OF ORIGINAL AUTHORSHIP

I, Kaiyi Chi, declare that this thesis, is submitted in fulfilment of the requirements for the award of Doctor of Philosophy, in the School of Civil and Environmental Engineering at the University of Technology Sydney.

This thesis is wholly my own work unless otherwise referenced or acknowledged. In addition, I certify that all information sources and literature used are indicated in the thesis.

This document has not been submitted for qualifications at any other academic institution.

This research is supported by the Australian Government Research Training Program.

Signature: Production Note: Signature removed prior to publication.

Date: 1 June 2025

ACKNOWLEDGEMENT

First and foremost, I would like to express my deepest gratitude to my supervisors, Prof. Chengqing Wu and A/Prof. Jun Li, for their invaluable guidance, unwavering support, and constant encouragement throughout my research journey. Their expertise and constructive feedback have been fundamental in shaping my work, and I am truly fortunate to have had the opportunity to learn from them. Here, I extend my most sincere appreciation and respect to them.

I gratefully acknowledge the International Research Training Program Scholarship (IRTP) from the University of Technology Sydney (UTS), Faculty of Engineering and Information Technology, which covered my tuition fees and providing financial support for my living expenses. These scholarships have been instrumental in enabling me to fully dedicate myself to my research and achieve my academic goals.

I would also like to thank my research group members for their collaboration, friendship, and support during this journey. I am especially grateful to Ruizhe Shao, Di Chen, Jiayuan Lim, Yahao Pan, Zizheng Yu, Zhenjian Chen, Haiqian Li, Zhenhuan Xu, Jie Wei, Junjie Huang, Chaocong Wang and Shida Zhao for their camaraderie and assistance. The lively discussions, shared challenges, and teamwork have made this journey both productive and enjoyable.

To my family, thank you for your unconditional love, understanding, and patience. Your encouragement and belief in my abilities have been a constant source of motivation, even in the most difficult times. I owe much of my success to your support. I would like to express my thanks to my boyfriend, Ruizhe Li, for his unwavering support, love, and encouragement throughout this journey. Your presence has been a pillar of strength, and your understanding and care have been instrumental in helping me persevere.

This PhD journey has been one of immense growth, learning, and discovery. I am deeply grateful to everyone who has contributed to it, both directly and indirectly, and I sincerely thank you all for your support and encouragement.

LIST OF PUBLICATIONS RELATED TO THIS THESIS

JOURNAL PAPERS:

1. Chi, K., Li, J. and Wu, C., 2023. Numerical simulation of buried steel pipelines subjected to ground surface blast loading. Thin-Walled Structures, 186, p.110716.
2. Chi, K., Li, J. and Wu, C., 2024. Behaviour of reinforced ultra-high performance concrete slabs under impact loading after exposure to elevated temperatures. International Journal of Computational Methods, 21(08), p.2241001.
3. Chi, K., Li, J. and Wu, C., 2024. Behaviour of reinforced concrete panels under impact loading after cryogenic freeze-thaw cycles. Construction and Building Materials, 414, p.135058.
4. Chi, K., Li, J., Shao, R., Chen, L., Xu, S. and Wu, C., 2024. Experimental study on impact behaviour of normal strength mortar at cryogenic temperatures and after freeze-thaw cycles. Construction and Building Materials, 440, p.137497.
5. Chi, K., Li, J., Shao, R., Liu, J., Liu, Z. and Wu, C., 2024. Experimental exploration on impact characteristics of ultra-high performance concrete at low and cryogenic temperature. Journal of Building Engineering, 98, p.111478.
6. Chi, K., Li, J., Shao, R. and Wu, C., 2025. Experimental study on dynamic characterisation of ultra-high performance concrete (UHPC) after cryogenic freeze-thaw cycles. Cement and Concrete Composites, p.106011.
7. Chi, K., Li, J., Shao, R. and Wu, C., 2025. Dynamic behaviour of geopolymer-based ultra-high-performance concrete at low and cryogenic temperature. Cold Regions Science and Technology, p.104600.

8. Chi, K., Li, J. and Wu, C., 2025. Behaviour of ACLNG storage tank under blast loading considering cryogenic temperature effect. Manuscript in preparation.

CONFERENCE PAPERS:

1. Chi, K., Li, J. and Wu, C., 2022. A study on impact induced damage on ultra-high performance concrete slabs after exposure to thermal loads. The 15th International Conference on Fibre-Reinforced Concrete Structure (FRPRCS-15) &The 8th Asia-Pacific Conference on FRP in Structures (APFIS-2022), Shenzhen, China
2. Wu, C., Li, J., Chen, D., Chi, K., Shao, R. and Fang, J, 2022. Advances in Protective Structural Research at University of Technology Sydney. International Association of Protective Structures, Adelaide, Australia.
3. Chi, K., Li, J. and Wu, C., 2023. Impact induced damage on reinforced concrete beam under cryogenic freeze-thaw cycles. The 11th International Symposium on Impact Engineering (ISIE 2023), Perth, Australia.
4. Chi, K., Li, J. and Wu, C., 2024. Impact response of reinforced concrete beams exposed to cryogenic temperatures. The 1st International Conference on Engineering Structures (ICES2024), Guangzhou, China.

Table of Contents

List of Figures:

List of Tables:

LIST OF ABBREVIATIONS

ACLNG	All Concrete Liquefied Natural Gas
AE	Acoustic Emission
ALE	Arbitrary Lagrangian-Eulerian
ANZCTC	Australia-New Zealand Counter-Terrorism Committee
AS	Australian Standard
CDIF	Dynamic Increase Factor in Compression
CH_4	Methane
CO_2	Carbon Dioxide
CSCM	Continuous Surface Cap Model
C-S-H	Calcium Silicate Hydrates
CT	Computed Tomography
CUHPC	Cement-based Ultra-high Performance Concrete
DIF	Dynamic Increase Factor
EOS	Equation of State
FEM	Finite Element Method
FT	Freeze-thaw

FSI	Fluid-structure Interaction Coupling
GGBS	Ground Granulated Blast Furnace Slag
GTD	Global Terrorism Database
GUHPC	Geopolymer Ultra-high Performance Concrete
ITZ	Interfacial Transition Zone
KCC	Karagozian & Case Concrete
LNG	Liquified Natural Gas
MAOP	Maximum Allowable Operation Pressure
MC	Moisture Content
MIP	Mercury Intrusion Porosimetry
NMR	Nuclear Magnetic Resonance
NSC	Normal Strength Concrete
NSM	Normal Strength Mortar
NSW	New South Wales
OPC	Ordinary Portland Cement
PBIED	Person Borne Improvised Explosive Device
PHMSA	Pipeline and Hazardous Materials Safety Administration

PP	Polypropylene
PVA	Polyvinyl Alcohol
PVC	Polyvinyl Chloride
RC	Reinforced Concrete
SA	South Australia
SCC	Self-compacting Concrete
SCMs	Supplementary Cementitious Materials
SDOF	Single Degree of Freedom
SEA	Specific Energy Absorption
SEM	Scanning Electron Microscope
SHPB	Split Hopkinson Pressure Bar
SSI	Soil-structure interaction
TDIF	Dynamic Increase Factor in Split Tension
TNT	Trinitrotoluene
UHPC	Ultra-high Performance Concrete
VBIED	Vehicle Borne Improvised Explosive Device
δ	Wall Thickness of Pipeline

D_{bd}	Buried Depth of Pipe
d_{max}	Maximum Aggregate Size
f	Cross-sectional Flattening Ratio of Pipeline
f'_c	Unconfined Compressive Strength
$f'_{c,d}$	Dynamic Compressive Strength
f'_t	Uniaxial Tensile Strength
GFC	Fracture Energy in Uniaxial Stress
GFS	Fracture Energy in Pure Shear Stress
GFT	Fracture Energy in Uniaxial Tension
W	Magnitude of Charge Weight
w/b	Water-Binder Ratio
w/c	Water to Cement Ratio
r_0	Dimension of Explosive Charge
R_n	Close-in Range
σ	Minimum Yield Strength for Different Steel Grade
S	Stand-off Distance
ϕ	Diameter of Pipeline/SHPB Bar/Specimen

ABSTRACT

Natural gas pipelines and liquefied natural gas (LNG) storage tank are important components in energy sector. The investment and construction of gas pipelines and LNG storage tanks are developing rapidly. Understanding their response to the service and accidental loading condition is critical to the energy safety.

Pipelines convey a wide range of liquid and gas over long distances, essential for urban functionality. Shallow-buried pipelines, due to their accessibility, are vulnerable to accidental or intentional damage. In Australia, AS/NZS 2885 provides regulations to prevent damage to the pipelines by external interference, but these regulations are vague and there is a limit study in relation to the performance of pipelines against surface explosion and accidental excavator impact.

Meanwhile, the inner structure of All Concrete LNG (ACLNG) storage tanks is in direct contact with LNG (at approximately -161.5 °C). Meanwhile, during the operation, the inner tank materials may also suffer from cryogenic freeze-thaw (FT) cycle attacks. As a storing system, ACLNG tanks potentially face threats of vehicle impact and/or terrorist attacks.

This research focuses on the safety of energy infrastructure including the gas pipeline and ACLNG storage tank. The dynamic behaviour of concrete with respect to compression and splitting tension at cryogenic temperature and after FT cycles is investigated. To improve the impact/blast resistant capabilities of ACLNG storage tank, a comprehensive experimental and numerical investigation was conducted on emerging high performance concrete material, i.e., cement-based ultra-high performance concrete (CUHPC) and sustainable material geopolymer ultra-high performance concrete (GUHPC). The research covered detailed dynamic mechanical characterisation of these advanced

cementitious materials, followed by implementation in numerical models simulating structural responses of ACLNG storage tank under extreme loading conditions.

This study adopts advanced fully coupled numerical modelling approaches such as FSI (fluid-structure interaction coupling) and ALE (arbitrary Lagrangian-Eulerian) in commercial software LS-DYNA to analyse buried pipeline responses to blast loading. It examines key factors such as soil type, burial depth, pipe thickness, diameter, charge weight, explosive offset, detonation height, steel grade and internal pressure. The simulation results serve as theoretical foundation for gas pipelines safety assessment and maintenance.

Furthermore, the findings of this study provide new information for the dynamic behaviour of conventional and high performance concrete material (CUHPC and GUHPC) at cryogenic temperature and after FT cycles as well as energy infrastructure (ACLNG and gas pipeline) response under blast and impact loads, and will promote their application in civil engineering projects going forwards.

Chapter 1. INTRODUCTION

1.1 Background

The global energy landscape continues to evolve, with natural gas playing a critical role in the transition towards lower-carbon energy sources. As the world seeks to balance energy security, economic feasibility, and environmental sustainability, the critical infrastructure supporting natural gas transportation such as pipelines as well as storage systems such as liquified natural gas (LNG) storage tank or all concrete LNG (ACLNG) storage tank becomes increasingly important. However, these infrastructure components face significant challenges when exposed to extreme operational conditions, particularly cryogenic temperatures and accidental dynamic loads.

Pipelines have become widely used in the world to transport petroleum, natural gas, ammonia, alcohol fuels and water. Pipeline system plays a significant part in urban energy distribution. However, the frequent occurrence of pipeline explosion accidents in recent years emphasises the importance in protecting the pipeline system. Australia's natural gas transmission pipeline has a good safety record. More than 39,000 km of natural gas transmission pipelines are employed to transport energy to suburbs of each city in Australia. Australia's pipeline history (i.e., water transmission pipeline) can be traced back to the late 19th century. The Roma to Brisbane pipeline operated in 1969 is one of the oldest gas pipelines in Australia based on Australian Pipelines and Gas Association [1]. Appendix A lists the relevant Australian standards regarding pipelines.

Meanwhile, LNG storage tanks play a crucial role in energy infrastructure by providing secure, long-term storage of LNG at cryogenic temperatures, which minimises environmental hazards and ensures the operational stability of energy supply chains. Compared to traditional LNG storage tanks, ACLNG tanks avoid the need for expensive

materials like 9% nickel steel. This reduces costs, shortens construction time, and allows for local material sourcing. Cryogenic temperatures present unique and complex challenges for concrete materials and hence pose challenges on the structural safety. ACLNG storage systems must operate safely under temperatures as low as -162 °C [2]. At these extreme temperatures, traditional material behaviour fundamentally changes, potentially compromising structural reliability and safety.

1.1.1 Natural gas transportation and storage system

As a long-distance transportation tool, pipeline can transport a large number of liquid and gas materials to supply the normal operation of the city. As stated by pipeline and hazardous materials safety administration (PHMSA) [3], pipeline system can be divided into four parts:

- Natural gas transmission and gathering: Gathering system generally refers to the transmission of nearby original or natural gas to the treatment plant through pipeline, which is usually relatively short to reduce the transmission cost. The transmission pipeline refers to the long-distance transportation of processed or stored natural gas throughout the country. According to Australian energy regulator [4], pipeline transmission network has interconnected New South Wales (NSW), Victoria (Vic), Queensland (QLD), South Australia (SA), Tasmania (TAS) and ACT. According to AS/NZ 5601 *Gas installation [5]*, the gas installation system operating should be above 1050 kPa to connect with gas transmission network.
- Natural gas distribution: The ultimate purpose of pipeline distribution is to transport natural gas to industrial users through pipeline transmission. The distribution network is generally composed of high, medium and low-pressure

pipelines. Generally speaking, the supply and demand in densely populated areas are greater, and the pipeline operation at medium and high pressure.

- Hazardous Liquid and Carbon Dioxide: Hazardous liquid includes petroleum/refined products and crude oil, while carbon dioxide includes CO_2 or other and fuel grade ethanol.
- LNG: The main component of liquefied natural gas is methane (CH_4), and its physical properties are colourless, odourless and non-toxic. It is to compress and cool the natural gas to the freezing point to liquefy it and then transport it through the pipeline.

1.1.2 Types of pipelines

There are various materials for pipes, which are mainly divided into three categories: plastic pipelines, metallic pipelines and concrete pipelines. So far, most of the gas pipelines are made of plastic and metallic, while concrete pipelines are usually used for sewage discharge or irrigation. Further information regarding concrete pipelines can be found in AS/NZS 4058 *Precast concrete pipes (pressure and non-pressure)[6]* and AS/NZS 3725:2007 *Design for installation of buried concrete pipes [7].* There are many types of metal pipes. Aluminium alloy, copper, and steel are the most frequently used metals for pipelines. Aluminium alloy pipelines are often used to transport inert gas. According to Smith et al. [8], pure copper pipelines are not affected by hydrogen embrittlement and it can be used in hydrogen containing environment while copper alloy containing oxide is easy to be brittle.

Steels used for pipelines are classified under the Standard American Petroleum Institute (API) 5L [8]. There are two manufacture product levels for standard API 5L to produce seamless and welded steel pipe, including Product Specifications Level 1 (PSL1) and Product Specifications Levels (PSL2), where PSL1 stands for the standard quality of

pipeline and PSL2 requires tighter control over the chemical composition of the steel, ensuring improved weldability, toughness, and strength. In general, pipelines that manufacture under API 5L are used to convey oil, natural gas and water. According to the steel grade classification criteria in API [9], the alphabet before the two digital number stands for the condition of manufacturing and chemical and physical properties, while the two digital number means the minimum yield strength of that pipeline in 000's psi to this grade. For instance, X80 steel means the minimum yield strength is 80,000 psi which is approximately 551.58 MPa under "X" delivery condition.

The use of steel pipes can be traced back to the early 19th century. At first, continuously welded steel pipes were used to transport gas in London. There are many types of steel pipes, such as X42, X46, X52, X56, X60, X65, X70 etc. With the manufacturing of X70 steel in the 1970s, a significant advancement was achieved in the development of pipeline steel, transitioning from traditional heat treatment methods to thermomechanical processing techniques. [10]. With the continuous development of industry, the emergence of steel X80 gradually improves the strength by accelerating cooling after controlled rolling [11]. The development of X100, X120 and other ultra-high strength pipes also provides the pipeline with the potential ability to transport oil and natural gas at high pressure and long distance.

1.1.3 Depth of buried pipelines

In accordance with AS/NZA 2566.2: 2002 *Buried flexible pipelines Part 2: installation*, *'AS/NZS 5601.1:2013 gas installation' [5]*, AS/NZS 4645.2:2018 *Gas distribution networks Part 2: Steel Pipe systems [12]*, the minimum depth of cover shows Appendix B, where H (mm) is the vertical distance between the upper surface of pipelines and the finished surface, MAOP stands for Maximum Allowable Operation Pressure and DN (mm) is nominal pipeline diameter. In terms of the maximum depth of cover, AS/NZS

4645.2:2018 [12] states that it should not exceed 1500 mm in order to access in emergency situation. ATCO [13] reports that the depth of cover for high pressure (HP) gas pipeline should not exceed 1800 mm without special approval, where HP is from 500 kPa to 6900 kPa. In general, the depth of burial pipeline cover ranges from 300 mm to 1800 mm in Australia. More information can be seen in Appendix B.

1.1.4 ACLNG storage tank

The evolution of LNG storage tank technology has seen significant advancements over the years, particularly with the transition from traditional LNG tanks constructed with 9% nickel steel to innovative ACLNG storage tanks. Traditional LNG storage tanks are characterised by their dual-containment design, where the inner tank, made of 9% nickel steel, stores the liquefied gas at cryogenic temperatures, typically around -162 °C. The outer tank, often made of reinforced concrete, provides secondary containment and structural support.

The use of 9% nickel steel in traditional tanks has been a standard in the industry due to its excellent mechanical properties at cryogenic temperatures, including high toughness and resistance to brittle fracture. However, these tanks come with challenges, such as the high cost of nickel steel, the complexity of fabrication, and the potential for thermal expansion mismatches between the inner and outer tanks.

In contrast, ACLNG tanks employ prestressed concrete for both the inner and outer containment (see Figure 1.1). This design reduces the reliance on 9% nickel steel and concrete materials are more readily available and less expensive [14]. Additionally, the parallel construction processes for ACLNG storage tank allow for multiple tasks to be carried out simultaneously, significantly shortening the construction period and thereby

reducing costs associated with extended timelines. Utilising ACLNG storage tanks can achieve at least a 20% reduction in construction costs (see Figure 1.2).

One of the critical challenges for ACLNG tanks is the impact of cryogenic temperatures on concrete. The inner tank, in direct contact with LNG, is subjected to extreme thermal stresses and material contraction, which can lead to microcracking and increased brittleness. Moreover, the tank must endure cryogenic freeze-thaw (FT) cycles that occur during filling and emptying operations. These cycles cause repeated expansion and contraction within the concrete matrix, potentially leading to cumulative damage over time.

Despite these challenges, advancements in concrete technology, such as the development of cement based ultra-high-performance concrete (CUHPC) or geopolymer ultra-high performance concrete (GUHPC), have significantly improved resistance to cryogenic effects and FT cycles. Compared to traditional LNG tanks with 9% nickel steel, ACLNG tanks offer reduced material costs, enhanced durability, and improved environmental sustainability. This study focuses on the effects of cryogenic temperatures and FT cycles on the different types of materials subjected to impact or blast loadings.

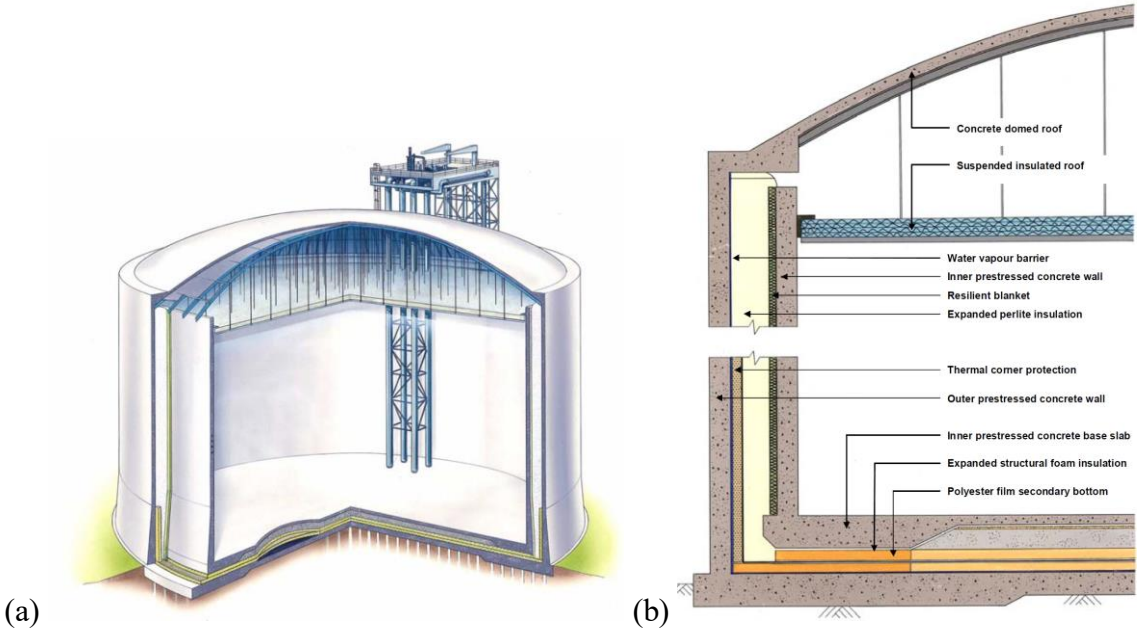

Figure 1.1 Details of ACLNG storage tank [15].

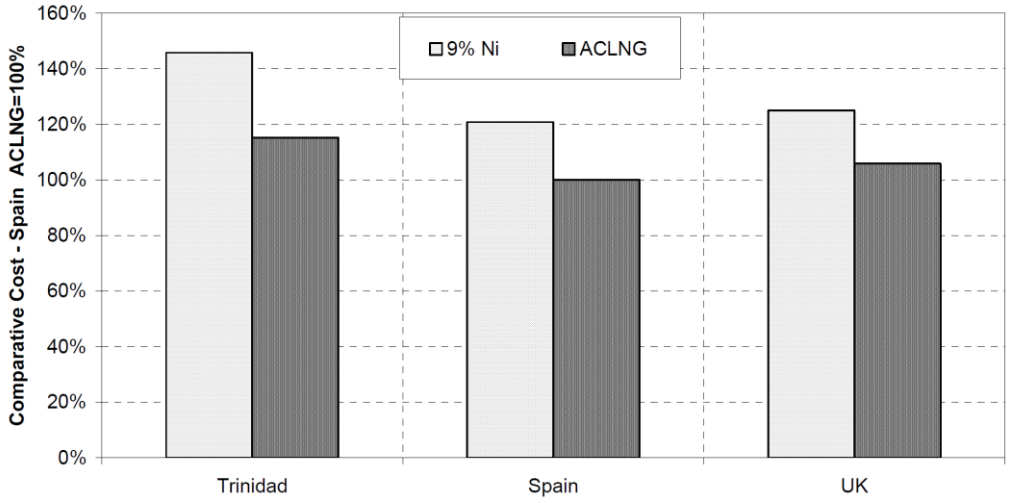

Figure 1.2 Details of ACLNG storage tank [16].

1.2 Potential threats

1.2.1 Terrorist attacks and Pipeline incidents

Pipeline explosion accidents have increased year by year. These incidents are divided into intentional acts and pipeline accidents, while intentional acts include cyber-attacks, sabotage, and terrorism as well as vandalism [17]. Global Terrorism Database (GTD) from University of Maryland [18] reports a large number of terrorist attacks with respect with pipelines around the world. According to RAND [19], Database of Worldwide

Terrorism Incidents from 1968 to 2009 shows the increasing trend of terrorist damage to pipelines all over the world, especially after 2002, and the sabotage of pipelines with large car bombs occurred in countries such as Iraq, Colombia and Pakistan. In August 2020, the explosion of a major gas pipeline crossing the Middle East, located between the towns of Ad Dumayr and Adra in the northwest of the Syrian capital Damascus, was caused by terrorist attacks. The pipeline explosion led to blackout in Syria [20].

A Vehicle Borne Improvised Explosive Device (VBIED) transported by a car or hidden in a car. It is a widely used terrorist strategy as a terrorist weapon to destroy built facilities in accordance with Australia-New Zealand Counter-Terrorism Committee (ANZCTC) [21]. However, ANZCTC [21] also points out that the amount of explosives used in small vehicles such as motorcycles may be similar to that of Person Borne Improvised Explosive Device (PBIED) which is an improvised explosive device that a person wears, carries, or deploys. The TNT mass in various vehicles is shown in Appendix C.

In recent years, natural gas pipeline transportation accidents occur frequently. It is vital to establish a safer natural gas pipeline transportation system to protect pipelines from accidents. According to Biezma et al. [11], the pipeline accident causes over 4,000 fatalities in history. The occurrence of pipeline accidents is often accompanied by the release of huge energy. For example, in the pipeline leakage accident in Ufa, Russia in 1989, the pipeline explosion caused by the spark generated by the train engine was equivalent to the explosion of 300 tons of TNT. Pipeline and hazardous materials safety administration (PHMSA) [3] summarises pipeline failure caused by corrosion (external corrosion, internal corrosion, stress corrosion cracking and selective seam corrosion), heavy equipment performing excavation damage, natural force damage such as earthquake, heavy rain, tornadoes etc., other outside force damage like sabotage or terrorism, and material/weld/equipment failure as well as incorrect operation. Figure 1.3

shows the oil and gas pipeline incident distribution from 2001 to 2020. It is evident that material/weld/equip failure, corrosion and excavation damage have become the main causes of the pipeline accidents, accounting for 30%, 20% and 17%, respectively. In accordance with European Gas pipeline Incident data Group [22], external intervention was to blame for roughly 28.4% of gas pipeline incidents in European. Zhu et al. [23] pointed out that gas pipeline may damage by terrorist attack, while some of the accidents may be caused by gas leakage, corrosions etc.

Due to the continuous growth of the world population, the consumption of oil and natural gas is increasing high. In order to improve the supply and transportation capacity, the natural gas industry increases the operating pressure or installs more pipelines, where most of the high-pressure operating is between 5 and 7 MPa [24].

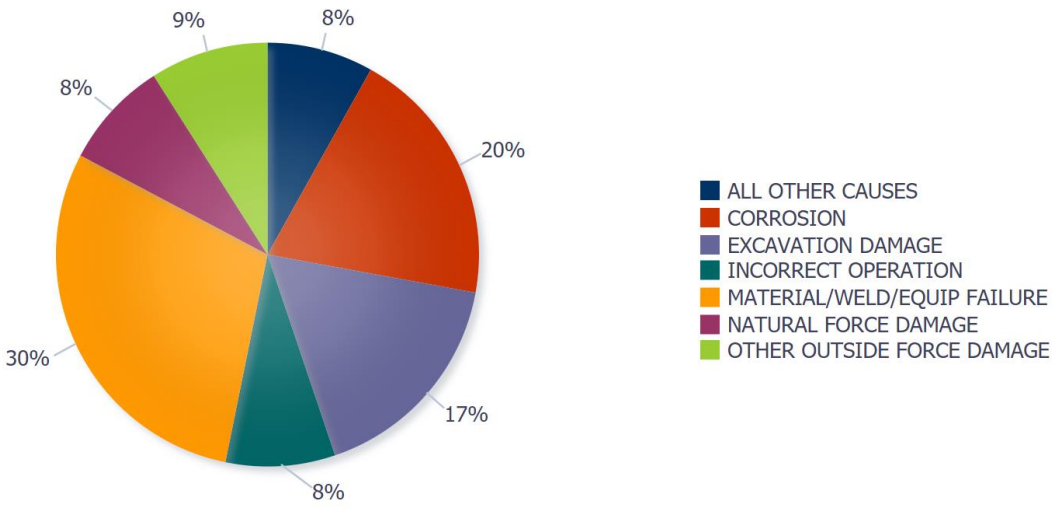

Figure 1.3 Oil and gas pipeline incident percentage from 2001 to 2020 [3].

Pipeline accidents have occurred frequently all over the world in the past two decades. Owing to the wide range of impact, pipeline incidents have brought huge casualties and economic losses to countries or regions. Here are some serious accidents that have occurred in recent years.

Australia:

Western Australia gas crisis is the most serious natural gas pipeline explosion in Australia. On the afternoon of June 3, 2008, a 12 in (30.48 cm) high-pressure pipeline burst and caused an explosion, followed by a series of explosions and fires in the adjacent pipelines (see Figure 1.4). The accident originated from an 8 m * 30 m crater with depth 2 m. The accident site was located on Varanus Island, 100 km west of Karratha. Fortunately, there is no injury or fatality. National Offshore Petroleum Safety Authority [25] investigated the pipeline accident which was attributed to the corrosion of the wall of a pipeline, from 11 mm thick to only 1.5 mm thick. This was caused by inadequate pipeline corrosion detection. The accident led to an economic loss of about AU $3 billion in Western Australia, and 30% of the natural gas supply is lost for two months (350 TJ/day) [26].

Figure 1.4 Western Australia gas crisis [27].

China:

On 4th July 2017, a severe gas pipeline explosion occurred in Songyuan City, Jilin Province, leading to 7 deaths and 85 injuries. The cause of this accident was the road reconstruction, the rotary jet grouting pile machine drilled through the burial gas pipeline in the road section (leakage diameter is about 0.06 m), resulting in the cumulative gas leakage reaching the explosion limit. The accident led to the collapse of nearby houses,

the doors and windows on the first and second floors of some houses almost blew up, and the doors and windows on the third and fourth floors burst. The polyethylene (PE) pipe had a diameter of 110 mm, a buried depth of 3.9 m and an operating pressure of 0.3 MPa.

In general, external damage of pipelines continues to increase, regardless of terrorist attacks or the damage caused by impact loads during construction. However, the pipeline is a critical factor affecting the national or regional energy transportation. Once the gas pipeline explodes, it will not only have a great impact on the surrounding areas, but also result in casualties and huge economic losses. Moreover, when the pipeline is corroded, the performance of the pipeline will be greatly reduced, and the gas pipeline will be more easily damaged under the impact load. In addition, according to the data analysis of PHMSA and EGIG, the pipeline is mostly damaged by a third party. Therefore, it is urgent to understand the vulnerability of the shallow buried pipes and develop the protection methods against external interference.

United States:

On 1st August 2019, a gas pipeline explosion took place in Lincoln country, Kentucky, causing the death of one woman and hospitalization of five others. The burned area is about 30 acre (121,406 m^2) and forming a crater of 30 foot (9.144 m) (see Figure 1.5). The damaged pipeline had 30 in (76.2 cm) diameter and 0.375 in (0.95 cm) wall thickness, and operated under 6.378 MPa pressure [28].

Nearly half-a-mile radius residents were evacuated by emergency workers. According to AP NEWS [29], during the explosion, the flame reached up to 300 feet (91 m), and the accompanying high temperature could melt the tire. Buildings within 500 yards (457 m) were damaged and at least five homes were entirely destroyed.

Figure 1.5 Burned area and explosion site in Lincoln Country, Kentucky [30].

1.2.2 Energy storage tank incidents

Throughout the history of LNG storage and transport, several notable tank explosions have occurred, with some of the most significant including the Cleveland East Ohio Gas explosion in 1944, which remains one of the deadliest incidents when multiple LNG storage tanks with 20,000 m^3 ruptured and exploded in a residential area, killing 130 people and destroying a square mile of the city. The Quebec City, Canada explosion of an LNG facility in 1972 caused significant damage to the surrounding industrial area, while the Staten Island LNG facility explosion in 1973 killed 40 workers during tank cleaning operations. More recently, the Skikda LNG facility explosion in Algeria in 2004 resulted in 27 fatalities and extensive damage to the facility, highlighting the continued importance of rigorous safety protocols in LNG storage and handling. The Buncefield disaster of December 11, 2005, was one of Britain's largest peacetime explosions, occurring when a failed gauge led to an oil tank overflow at the Hertfordshire storage terminal, creating a massive vapor cloud that ignited and caused a devastating explosion measuring 2.4 on the Richter scale, burning for days and causing £1 billion in damages but miraculously resulting in no fatalities [31]. The March 2014 explosion at the Williams Northwest Pipeline LNG storage facility in Plymouth, Washington, though resulting in

no fatalities, caused injuries and demonstrated the ongoing risks associated with LNG storage even with modern safety systems in place. In October 2015, a catastrophic incident in Rizhao, China, began with one tank explosion that triggered two more consecutive blasts and spread fire to nine storage tanks (see Figure 1.6).

Figure 1. 6 LNG storage tank explosion in Shandong, China [32].

1.3 Research significance

Terrorist attacks and accidental explosions pose severe threats to critical infrastructure, including buried gas pipelines and ACLNG storage tanks, leading to casualties and significant economic losses. Here are some of the aspects that needed to focus on:

1. Pipe safety

- Analyse pipeline response to blast loading.
- Evaluate impact of critical factors (soil type, pipe depth, thickness etc.).
- Provides insights into structural performance for buried gas pipeline under potential impact and blast loading.

2. LNG tank safety

- Characterise material performance at cryogenic temperatures and after FT cycles.
- Addresses critical knowledge gaps in ACLNG storage tank design under extreme conditions including cryogenic temperature and accidental dynamic loads.
- Understand the structural response of ACLNG storage tanks under potential impact and blast loading.
- Assess the dynamic behaviour of advanced concrete materials (CUHPC, GUHPC) under cryogenic temperature and dynamic loading scenarios, which contributes to developing more robust and sustainable construction materials for ACLNG structures.

1.4 Research questions

Given the frequent occurrence of explosion accidents and the influence of thermal loads, this research seeks to address the following key questions:

- How resistant are buried gas pipelines to impact and blast loads?
- How does concrete perform under cryogenic temperatures and after exposure to cryogenic FT cycles when subjected to extreme loading conditions?
- What are the effects of FT cycles and cryogenic temperature environments on the dynamic response of concrete structures?
- How do ACLNG storage tanks perform under blast loading, considering the effects of cryogenic temperatures? How can the findings from this study contribute to safer and more sustainable design guidelines for gas pipeline and LNG storage infrastructure?

1.5 Outline

Chapter 1 presents the research background, research significant and outline of this study.

Chapter 2 provides a literature review addressing two key areas: first, it examines potential threats to energy transmission and storage infrastructure, with particular emphasis on impact and blast loadings that can compromise system integrity. Second, it explores the mechanical properties of concrete under extreme conditions, specifically focusing on its behaviour at cryogenic temperatures and the effects of FT cycles on material performance.

In Chapter 3, the response of buried pipeline under ground surface explosion is evaluated. It details the finite element analysis framework used to simulate blast effects on pipelines. The chapter outlines the parametric study design based on Dampier to Bunbury natural gas pipeline system in Australia, covering variations in charge weight, stand-off distance, pipe diameter, wall thickness, buried depth, steel grade, and soil properties. The methodology concludes with a description of data collection procedures, strain and deformation measurement approaches, cross-sectional flattening ratio calculations, and the statistical methods used to develop the empirical formula for pipeline safety assessment.

Chapter 4 presents the experimental methodology and findings on dynamic mechanical properties of NSM under extreme temperature conditions via SHPB test at varying temperatures (20 ~ -160 °C) and after different FT cycles. Results are systematically presented, analysing the effects of cryogenic temperatures and FT cycles on key mechanical properties including dynamic compressive strength, elastic modulus, splitting strength, and strain rate sensitivity. The chapter concludes with a discussion integrating

these findings with existing literature and establishing their significance for cryogenic applications, particularly for ACLNG storage tank designs.

In Chapter 5, an experimental investigation of CUHPC under cryogenic conditions is conducted. Results are systematically organised to analyse failure patterns, dynamic strength properties, elastic modulus variations, and strain rate sensitivity through DIFs. Additionally, a comparative analysis with Chapter 4 highlights CUHPC's superior mechanical performance.

Chapter 6 investigates the dynamic compressive behaviour of CUHPC subjected to cryogenic FT cycles using the SHPB technique. The results examined the influence of FT cycles on dynamic compressive strength, SEA and CDIFs. The microstructural analysis used SEM to find out the matrix deterioration, porosity, and the fibre-matrix interface after FT cycles. A comparative analysis of CUHPC's performance across different FT cycles was presented, emphasising the rate-dependent response and degradation mechanisms. Comparing with the findings in Chapter 4, the results demonstrated exceptional dynamic mechanical properties and enhanced structural behaviour of CUHPC.

In Chapter 7, a sustainable concrete GUHPC is utilised to investigate the dynamic properties at extreme low temperatures. The use of GUHPC aligns with global sustainability goals by reducing carbon emissions associated with cement production while offering superior mechanical properties. It examined the effects of decreasing temperatures on compressive and tensile strength, strain rate sensitivity, and failure patterns at cryogenic temperatures. The development of empirical formulae for DIFs in both compression and tension provided valuable predictive tools for design applications.

X-ray CT analysis further explored microstructural transformations, identifying porosity, steel fibre distribution, and microcrack networks.

Chapter 8 presents a numerical investigation of the impact resistance of reinforced NSC panels (which design based on the dome of LNG storage tank) subjected to cryogenic FT cycles. It focused on the modification of the CSCM concrete model to incorporate FT-induced changes in concrete properties based on Chapters 2 and 4. The main results section analysed how increasing FT cycles affect impact response, examining crater dimensions, penetration depths, damage patterns, and energy absorption capabilities. Parametric studies explore the influence of various factors including impact weight and impact velocity.

Chapter 9 numerically investigates into the structural response of ACLNG storage tanks subjected to combined blast loading and cryogenic temperatures. The concrete model KCC was modified based on the experimental results from Chapter 4, 5 and 6. The study evaluated the blast resistance of UHPC compared to NSC. The effect of liquid levels inside the storage tank and impact of TNT charge weight were examined. The chapter concludes with key findings and their implications for improving the safety and durability of ACLNG storage tanks in hazardous environments.

Chapter 10 summarises the overall findings of this study and presents some issues and suggestions for future research.

Chapter 2. LITERATURE REVIEW

2.1 Blast response and failure mechanism of energy infrastructure

The increasing number in terrorist attacks and sabotages poses a serious threat to urban pipeline transportation and storage systems. As a consequence, it is of great significance to explore the wave propagation of explosion in soil and its effect for the damage on energy infrastructures.

2.1.1 Explosion and related phenomenon

Explosion is defined as a phenomenon that the accumulated energy of a substance is suddenly released under rapid oxidation or decomposition. This will cause the increasing in temperature and pressure, resulting in rapid expansion and shock wave [33]. According to the properties of explosion, it can be divided into physical explosion, chemical explosion, and nuclear explosion [34]. Common high explosives like trinitrotoluene (TNT) and nuclear explosions release energy in this form, although they produce energy in different ways [35]. Explosives can decompose rapidly in a short time and produce a large amount of heat and gas.

In recent years, there have been more and more accidental explosions and terrorist attacks around the world. Most of the incidents are owing to external interference. As for the position of explosion on pipelines, it can include contact explosion, surface explosion and far range explosion. These accidents are often close-in range explosions, which will cause severe damage to structures such as buildings, pipelines, tunnels ascribed to the unevenly distributed blast loading on the structure components [36]. A few scholars pointed out the close-in range (R_n) refers to $0<R_n<20\ r_0$ (r_0 is the dimension of explosive charge) [37], while others suggest the scale distance of close-in range explosion is less than 1.2 $\frac{m}{\sqrt[3]{kg}}$. The far range explosion defines the scale distance greater than 1.2 $\frac{m}{\sqrt[3]{kg}}$ [38, 39].

Contact explosion means that the explosive is immediately applied to the exterior surface of study object. Song et al. [40] and Stevens et al. [41] have done similar contact explosion experiments to research steel pipes' dynamic behaviour when subjected to an explosion load. The research revealed that the deformation range of steel pipes was related to the contact area of explosives. Moreover, the pipelines would undergo inelastic deformation when the charge weight was small. When the explosive equivalent was large enough, the pipeline would undergo shear failure, and the debris generated during explosion impact would form a through hole. Song et al. [40] explained that changing the pipeline wall thickness and TNT charge weight led to different failure modes of the pipeline. The main reason is the impact of the shock wave generated during the explosion on the pipeline. The pipe response can be classified into four modes: 1. Pipeline is elastically deformed under the shock wave. At this time, the pipeline wall was sunken but not damaged. 2. The pipeline has inelastic deformation and localised cracks. 3. Large fragments appear on the upper wall of the pipeline, and the high-speed fragments cause local pitting corrosion. 4. The high-speed fragment of the upper wall of the pipe forms a penetration hole under shock wave. Wu et al. [42] also pointed out that the penetration hole caused by high-speed fragment increased the damage from shock wave to the target. Furthermore, under the effect of shear stress and tensile stress, a piece of rectangular metal sheet was cut off on the pipe wall when the pipe was subjected to contact explosion [43].

Ground surface explosion is hemispherical in essence and the incident wave of explosion, and the shock wave reflected by the ground will immediately merge together. If high temperature and high-pressure gas breaks through the surface, it is called shallow underground explosion. Whether it is a surface explosion or a shallow underground explosion, part of the energy released by them will act on the ground to form a crater [33]. According to De [44], there are two principal mechanisms causing the damage in buried

pipelines, which includes direct loading by shock wave generated by explosion and large displacement in soil resulted in crater. Close-in explosion on the ground leads to crater formation with phenomenon of soil ejection, which removes the soil cover causing the exposure of buried pipelines, resulting in failure of pipelines. Moreover, far range blast loads will cause damage to buried pipelines owing to wave propagation in soil. Jiang et al. [45] stated that in the event of terrorist attacks and sabotage, the energy generated by surface explosion propagated to the distant soil layer through the rock stratum, and the induced blast wave propagation affected the safety of underground structures. In general, the whole process of shock wave propagation on buried pipelines is divided into expansion, migration and dissipation, whereas the top of the pipeline is the most vulnerable area where the earliest pressure peak occurs [46]. In summary, both cavity and wave propagation can affect the safety of buried pipelines, therefore, exploring the mechanisms of these two concepts is crucial for buried pipeline protection in terrorist attacks and sabotage events in the future.

2.1.2 Blast load propagation in the soil medium

The blast wave propagation in soil has a great impact on shallow buried structures. There are many different aspects affecting the blast wave propagation in soil, including the soil properties, saturation degree of soil, position of explosives, scale distance and so forth. Abedi et al. [47] utilised analytical solution to figure out the buried pipe displacement and peak pressure velocity in different amount of TNT under intact and weathered rock. The blast pressure wave velocity in intact rock was far greater than weathered rock, that meant, buried structure could be easier to rupture in intact rock in the same explosive charge and explosion distance. Wang & Lu [48] suggested that the blast wave propagation was highly impacted by the saturation degree of soil. Wang et al. [49] confirmed that the peak pressure and particle velocity in saturated soil was higher than in unsaturated soil

through the new three-phase soil model and the wave propagation speed in saturated soil was faster than in unsaturated soil because of the deformation mechanism and three-phase soil structure.

Explosion is often accompanied by the formation of shock waves. The high-speed shock wave will strongly compress the soil. Under the strong vibration, the bond between soil particles will be weakened, finally leading to the destruction of soil structure. Depending on the position of explosive, the energy transmission of blast load in soil will be different. Yang et al. [46] reported that the proportion of energy absorbed by air was 53% and the soil was 47% when the explosive was buried on the ground and top surface was level with the ground. Prochazka et al. [50] stated that energy could be absorbed by soil up to 30% under the contact explosion. Based on numerical simulation and technical manual TM5-855-1, Ambrosini & Luccioni [51] indicated that the attenuation of blast wave propagation in soil strongly depended on scale distance.

Due to unavailability of experimental data in open literature, the ground shock caused by explosion can be calculated by the empirical formulae from TM5-855-1[52]:

$$P_o = 160 f pc \left(\frac{R}{W^{\frac{1}{3}}}\right)^{-n} \tag{2.1}$$

where P_o is peak pressure in Pa, f is coupling factor, which is 0.14 for surface explosion, pc is acoustic impedance of soil in kg/(m²·s), R is distance of explosive in meter, W is charge weight in kg and n is attenuation coefficient of the soil.

However, this semi-analytical equation will not be applicable for the scale distance smaller than 0.4 $\mathrm{m}/kg^{1/3}$ when calculating the ground shock wave and free-field pressure [53].

Soil-structure interaction (SSI) is another crucial factor for analysing the buried structure. The interaction between soil and structure is extremely complex, and its concept can be understood as dynamic and static phenomena mediated between soil and structure. Kausel [54] summarised the development in the field of soil structure interaction from the end of the 19th century to the 20th century. Because of the emergence of computers and simulation tools, the boundary element method was widely used in engineering analysis and code formulas. He also summed up that the contents covered by SSI theory, including the response of dynamic source or static source of surrounding soil, the response of ground vibration to soil (free field problem), the influence of massless structure on ground wave in ideal state, static and dynamic stiffness, the deformation of surrounding soil due to the inertial interaction of structure, and the numerical method required to analyse SSI problems.

Nowadays, a number of researchers employ numerical techniques to analyse SSI. In the past, when studying the dynamic response under blast loading, it will be analysed by single degree of freedom (SDOF) system method as the structure is above the ground level. However, this method will ignore SSI when the structure is underground [55]. Therefore, the numerical method such as finite element method (FEM) could be adopted, which can not only build up structures and soils modelling in a more realistic way, but also consider SSI condition. Robert et al. [56] utilised the implicit and explicit finite element methods to analyse soil-pipeline interaction under quasi-static conditions, at the same time, they suggested that explicit finite element could be used to analyse buried structure under external load in dry or wet soil under quasi-static conditions. In general, considering SSI is necessary when analysing the buried structure under blast loading.

2.1.3 Crater formation

The crater is formed due to the impact of blast loading on the ground and the vaporization of soil under huge energy. The size, depth, diameter and volume of the crater are often determined by the height of the explosive or the depth buried below the ground [33]. Figure 2.1 shows the different depths and radii in relation to different height of burst (HOB) or depth of burst (DOB). R_o and D_o represent the radius and depth, respectively. Generally speaking, under the same charge weight, the diameter of crater formed by shallow burial of TNT will be larger than that formed on the surface because more energy from surface explosion will be released into the air [57]. Cooper [58] indicated that the size of the crater might also depend on the type of the soil based on the high-explosive experiments and fewer nuclear explosive tests. He also concluded the relationship between radii and depth with respect to the shape of crater (dished-shaped and bowl-shaped). The size of the final crater was larger than the initial crater due to the scouring effect of soil [59].

Many scholars have made efforts solve the relationship between blast load and crater size. Ambrosini et al. [60] did a series of experiments to simulate the relationship between crater dimension and the magnitude of TNT from 1 kg to 10 kg. Ramírez-Camacho et al. [24] summarised 90 natural gas pipeline accidents around the world via different characteristics of the pipeline such as the crater dimension, diameter and type of the pipeline, and burial depth of pipelines as well as operating pressure. Using a correlation and regression analysis, it indicated that there was a linear proportion between the depth of the crater and the depth of pipelines based on the 90 real cases. Likewise, there was a linear proportion between the length of the crater and the rupture of pipeline. Moreover, Peekema [59] reported that it needed approximately 116.12 kg TNT (256 Ibs) to form a crater similar to San Bruno, California pipeline accident, with a length was 27.9 m, width

was 7.9 m and depth was 4.3 m. Better understanding of crater formation can investigate the buried pipelines under blast load.

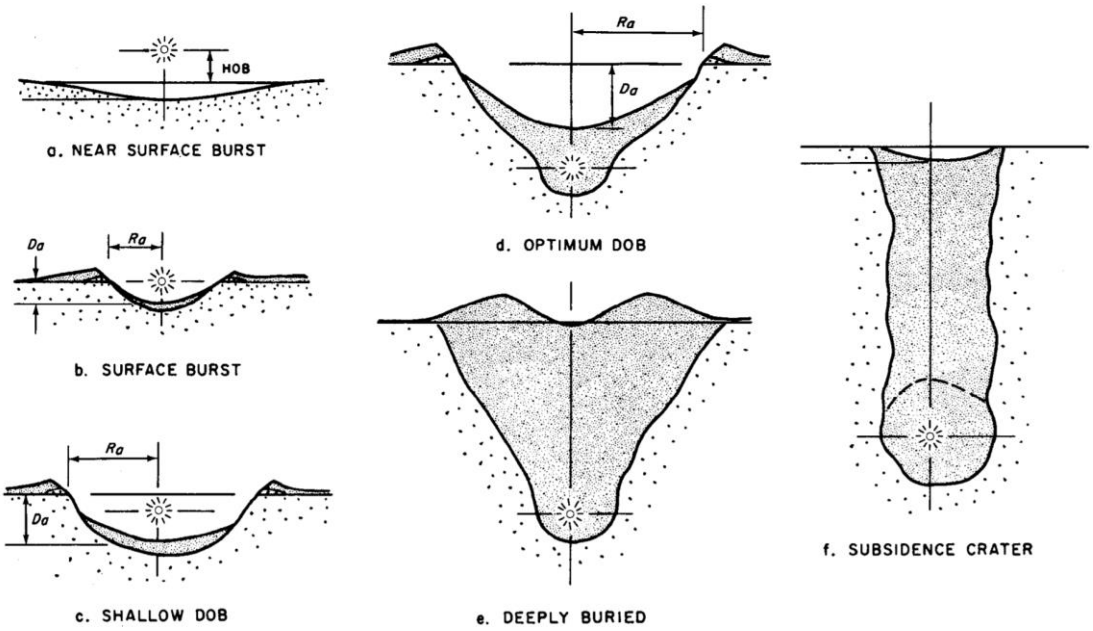

Figure 2. 1 Different sizes and shapes of crater regarding height or depth of burst [33].

2.1.4 LNG storage tank subjected to blast loadings

Lee et al. [61] evaluated the blast resistance of prestressed concrete outer walls of a 270,000 m^3. LNG storage tank under extreme loading scenarios using LS-DYNA. The research validated finite element models with test data and conducted full-scale simulations to assess structural responses to TNT charges ranging from 45.36 kg to 68.04 kg at a 1 m standoff distance. Results showed that the outer wall could safely withstand up to 68.04 kg of TNT without catastrophic failure, with minimal displacement and stress observed at 45.36 kg. The majority of damage arose from the initial impulsive pressure, and the mid-height region, having lower reinforcement density, was identified as more vulnerable. Zhang et al. [32] conducted a numerical simulation using LS-DYNA to analyse the shock response of a large LNG storage tank under blast loads, focusing on a 160,000 m^3 tank in Qingdao, China. The study found that the tank could withstand

approximately 2 t of TNT equivalent, with maximum overpressure reaching 0.3 MPa and principal tensile stress peaking at 5.79 MPa, without significant concrete cracking due to prestressed steel reinforcement. Sun et al. [62] conducted a comprehensive fluid-solid coupling numerical analysis to investigate the dynamic response and damage of a small-scaled ACLNG storage tank (outer tank diameter: 2.7 m; Height: 1 m) under penetration and explosion conditions. They used a self-programmed numerical simulation model to examine how different explosives (TNT, 8701, and Comp B) and various detonation points (external, drill penetrating, off-centre penetrating, and centre penetrating) affect shock wave propagation and tank structural damage. Their key findings revealed that shock waves rapidly attenuate after detonation, with pressure peaks varying significantly across different positions. The broken hole from projectile penetration influences pressure release, and the peak pressure correlates with the explosives' detonation characteristics. Notably, the connections between the sidewall and top/bottom plates of tank were most vulnerable to damage due to shock wave aggregation and stress concentration.

2.2 Impact load response and failure mechanism of energy infrastructure

2.2.1 Impact load response to pipelines

Pipeline accidents are often caused by the impact of external impact forces. As reported in Section 1.2.1, 17% of pipeline accidents are caused by construction excavation damage from 2001 to 2020. For example, the bucket teeth of excavators often used on construction sites have high impact, which can easily penetrate the outer wall of the buried pipeline. Figure 2.2 displays different types of bucket teeth that often used in the excavator. The depth of pipeline in Australia is normally between 300 mm to 1800 mm. Due to the shallow buried, pipeline is easy to rupture when suffering from the external pressure. Consequently, it is crucial to comprehend the impact and failure mechanisms of impact load on pipelines.

Figure 2. 2 Different types of bucket teeth [63].

Many scholars have studied pipelines subjected to different impact loads. Brooker analysed the pipeline puncture under excavator loading through experiments and numerical simulation [64-66]. It predicted the static puncture resistance of the pipeline when bucket teeth contacted perpendicular to the pipeline through numerical simulation. In addition, the centreline of the pipeline was punctured by changing different bucket tooth dimension, puncture loading angles and pipeline wall thickness, which concluded that the rotation angle of the teeth had little effect on the puncture load, while bucket tooth dimension and pipeline wall thickness had strong influence with puncture loading. Similarly, Liu et al. [67] studied buried polyethylene pipelines under excavation load via numerical simulation regarding exaction position, pipeline diameter, pipeline wall thickness and pipeline internal pressure attributed to the increasing amount of urban gas pipeline accidents caused by sharp dipper-teeth of excavator. Moreover, Xu et al. [68] analysed the static and dynamic behaviour of buried X60 gas pipes when excavators are equipped with various tooth counts (single-tooth and five-tooth) under different driving forces (boom cylinder, stick cylinder and bucket cylinder) and digging angles (0° and 45°).

Some scholars also employed dropped object to study the effect of impact load on pipelines. Jiang et al. [69] reported that impact velocity and the mass of the dropped object, shape of the dropped object, concrete coating thickness, internal pressure of pipelines, and burial depth etc. might result in the dent depth of pipelines. Furthermore,

Jiang et al. [69] also stated that the soil had a certain buffer effect on the impact load of the buried pipelines, but it could not protect the shallow buried pipelines. Generally speaking, review on the impact load acting on the pipelines is very necessary, which can provide direction for the subsequent pipeline protection measures.

2.2.2 Failure mechanism to pipeline

There are numerous reasons that contribute to pipeline failure under impact load, such as the thickness of pipeline outer wall, internal pressure of pipelines, pipeline diameter, buried depth of pipelines, excavation position/angle, soil properties, tooth shape and number of bucket teeth and so on. Conventional stress-strain of material is generally divided into four stages, which are elastic behaviour, yield, strain hardening and necking. The bearing capacity of the area subjected to impact load will be reduced, and large plastic deformation will occur as well, resulting in the pipeline stress exceeding its yield strength [67, 70]. As for thickness of pipeline outer wall, thinner wall thickness might cause larger von Mises stress, leading to low bearing capacity of higher internal pressure. Furthermore, when the pipe diameter is smaller, the pipe deformation is more obvious, because the mechanical load is borne by the whole pipe, resulting in the increase in pipe reaction force on pipeline invert [67]. According to Xu et al. [68], single-tooth might impact larger deformation than fifth-tooth on pipelines because of larger maximum equivalent strains and equivalent plastic strains acting on single-tooth. However, the shape of the excavator tooth is unlikely to provide too much additional resistance to prevent the hole formation on pipelines, therefore, when investigating the effect of tooth shape reacting on pipelines, it can be judged directly from the size of the puncture hole [66]. On summary, the damage events caused by pipeline impact load emerge one after another, therefore, in the following study, it will focus on protective methods to protect

the pipelines based on the above conditional factors that may cause failure of buried pipelines.

2.2.3 Impact load response to LNG storage tank

LNG storage tanks pose potential threats when subjected to aircraft impact loadings, as their structural integrity can be compromised under such extreme forces. Aircraft collisions, whether accidental or intentional, can result in catastrophic damage due to the kinetic energy involved and the potential ignition of LNG. The lightweight construction of modern aircraft, combined with high velocities, can penetrate tank walls or disrupt containment systems, leading to leaks or explosions.

The potential threat of aircraft impact on LNG storage tanks has been studied through finite element modelling to understand the structural responses under such extreme loadings by Zhai et al. [71]. FE models of aircraft, such as the Bombardier Challenger 850 and Boeing 757, have been developed to simulate their impact on LNG storage tanks. These models consider critical structural elements like engines, high-strength aluminium alloy materials, and strain rate effects. Simulation results demonstrated that the reticulated shell, a key structural component of LNG storage tanks, played a vital role in absorbing impact energy and mitigating damage. When aircraft impact the reticulated shell directly, localised deformations and member failures occur, but the overall structure remained intact. For LNG tanks with a concrete dome and steel-lined reticulated shell, the combined effect significantly enhances the tank's resistance to aircraft impact, dissipating kinetic energy and minimising internal damage. This highlights the importance of incorporating robust outer layers, such as concrete and reticulated shells, in LNG tank designs to address potential aircraft impact scenarios.

Peng et al. [72] conducted a comprehensive numerical analysis of the safety of large-scale LNG storage tanks against commercial aircraft impacts. They developed and validated detailed finite element models of both the Chinese Yang Shan LNG pre-stressed storage tank and an A320 aircraft, using the *Improving the Robustness of Assessment Methodologies for Structures Impacted by Missiles* (IRIS) bending behaviour test and modified Riera function respectively. Using these models, they simulated complete aircraft impact scenarios and performed parametric analyses examining different impact angles (0°, 15°, 30°, 45°), positions (half height, three-quarters height, and dome connection), and velocities (100 m/s, 125 m/s, 150 m/s). The results showed that while the outer concrete tank and steel liner experienced significant deformation and plastic strain under impact, the inner steel tank - which contains the LNG - maintained its integrity across all tested scenarios, with maximum effective plastic strains well below failure thresholds. The study found that impact angle significantly affected the damage pattern, with larger angles resulting in less severe damage, while impact position had relatively minor effects on structural response. Impact velocity proved to be a critical factor, with higher velocities causing substantially greater deformation and damage. Overall, the research demonstrated that the studied LNG storage tank design maintains its containment function under the analysed aircraft impact scenarios, providing valuable insights for the design and safety assessment of such facilities.

2.3 Resilience-based protection design

Resilience is one of an important concept in civil infrastructure system. Physical, ecology, social, economic, time, and cost to restore functions are all factors considered in resilience-based design [73]. It is more effective and efficient to protect critical infrastructure when using resilience-based design, which can sustain infrastructure performance during and after many different types of potentially disruptive events and

reduce the high consequences caused by hazards [74]. Cimellaro et al. [75] pointed out that there are four dimensions of resilience, including robustness, resourcefulness, redundancy and rapidity, which can better understand the functionality Q of the structure. Figure 2.3 shows the functionality recovery under extreme event, and the equation $R = (\frac{1}{t_r - t_0}) \int_{t_0}^{t_r} Q(HZ.TP, GM, t)dt$ can calculate the cumulative amount of reduced functionality over the recovery period $(t_0 - t_r)$. Functionality Q relative to TP (function of topology), GM (geometry), HZ (hazard) and t (time) [76, 77]. Shallow buried pipelines may degrade in function and performance due to aging and degradation during operation. Once a destructive event occurs, the functionality will be significantly reduced, and the residual functionality level after the destructive event will be used to measure robustness and determine the level of resilience. Therefore, to reduce the potential risk of shallow buried pipeline and ACLNG storage tank after destructive events, it is very necessary to protect the pipeline or ACLNG storage system to reduce the loss of function.

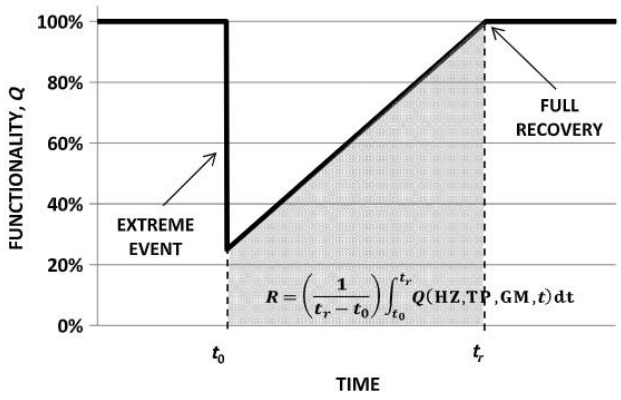

Figure 2. 3 Functional recovery under disruptive events[78].

The explosion-proof performance, maintenance cost and service life of the advanced materials can be further improved. The development of optimised protection design is particularly important for energy infrastructure protection. Two types of modern materials that can be used for energy infrastructure safety, which are CUHPC and GUHPC.

CUHPC has ultra-high durability and ultra-high mechanical properties, which are embodied in its high compressive strength and tensile strength, excellent durability and high ductility. The compressive strength of CUHPC at 28 days is greater than 150 MPa and the flexural strength is greater than 30 MPa [79]. CUHPC is a kind of cementitious material, which fills micron particles such as cement, fly ash and mineral powder into millimetre particles (aggregate). The dense microstructure and excellent durability give UHPC structural members a longer service life and lower maintenance and repair costs [80]. In spite of these points of interest, compared with normal strength concrete, CUHPC has better explosion resistance. Because CUHPC panel has a high capacity to absorb energy, the oscillation frequency of CUHPC panel is higher than that of normal strength concrete panel [81].

GUHPC is an advanced class of concrete that combines the superior mechanical properties of UHPC with the environmental benefits of geopolymer technology. Unlike conventional CUHPC, GUHPC utilises industrial by-products, such as fly ash or ground granulated blast-furnace slag (GGBS), as primary binding materials, activating them through an alkali solution [82-84]. This innovative approach reduces the reliance on ordinary Portland cement (OPC), thereby significantly lowering the carbon footprint associated with concrete production [85]. GUHPC has gained substantial popularity in modern infrastructure due to its high early strength [86] stemmed from aluminosilicate gels, primarily formed by the polycondensation of alumina and silica species in the presence of an alkaline activator [87], improved ductility [88] and fire resistance [89, 90]. The use of GUHPC aligns with global sustainability goals by minimising the carbon emissions associated with traditional concrete. Its ability to incorporate large quantities of industrial by-products promotes resource efficiency and reduces waste, making it a key material in the construction of resilient, sustainable infrastructure.

Consequently, research and industrial groups are committed to using advanced concrete materials. This can improve the potential impact or blast resistance of the ACLNG storage tank and is more environmentally friendly and economical.

2.4 Cryogenic temperature and FT cycles attack

2.4.1 Cryogenic temperature attack to concrete

2.4.1.1 Static performance of concrete at low/cryogenic temperature

Numerous researchers have investigated the concrete's mechanical properties at low and super-low temperatures to facilitate the scientific, rational, and cost-effective design of structures while ensuring their performance and safety in extreme cold environments [91-95]. Van de Veen [96] had a comprehensive review on the properties of concrete such as the compressive strength, tensile strength, modulus of elasticity at low and cryogenic temperature and after FT cycles. It revealed that the mechanical properties of concrete could be affected by the type of aggregate, cooling condition, water to cement ratio (w/c) and moisture content (MC). Lee *et al.* [97] performed a series of experiments across a temperature range from ambient temperature to -70 °C investigating the compressive and splitting tensile strength, elastic modulus as well as Poisson's ratio of concrete, under both monotonic and cyclic loading conditions. Their findings revealed that as the temperature decreased, the characteristics of aforementioned concrete exhibited an increase as compared to ambient temperature conditions. Specifically, the compressive and splitting tensile strength, elastic modulus, and Poisson's ratio at -70 °C were approximately 2.01, 1.50, 2.07 and 1.47 times greater than those at 20 °C. Lin *et al.* [94] extensively reviewed concrete properties including compressive, splitting tensile strength and elastic modulus etc. under low and cryogenic temperatures. It concluded that concrete properties steadily increased until a critical temperature, after which they stabilised or declined slightly.

Compressive strength peaked below -100 °C, while the critical range for tensile strength was between -30 and -70°C. Huo *et al.* [95] demonstrated that moisture content (MC), aggregate type, water to cement ratio (w/c) etc., influenced concrete properties at low temperatures. Moisture content had the most pronounced impact, with higher levels leading to greater enhancements in performance.

Several reasons can explain such improvement. First and foremost, when water freezes inside concrete at lower temperatures, it forms a solid interconnected mesh of ice veins that exerts pressure on the concrete, prestressing it and consequently improving its compressive strength due to the presence of a multiaxial stress state [94]. Furthermore, when water freezes within the tiny pores and capillaries present in the concrete, the ice thoroughly occupies and fills these micro-sized voids throughout the material. This complete filling of the capillary pore spaces by ice helps to distribute stresses more evenly within the concrete matrix at low temperatures. By eliminating these microscopic voids, the formation of localised stress concentrations is mitigated, thereby preventing the initiation and propagation of microcracks within the concrete when exposed to low-temperature conditions. Wiedemann's [98] pore model explained variations in the internal formation of concrete at low temperatures owing to water freezing. Five critical stages were identified with distinct effects on strength, including 20 °C ~ 0 °C, 0 °C ~ -20 °C, -20 °C ~ -60 °C, -60 °C ~ -90 °C and -90 °C ~ -170 °C: shrinkage, ice formation in larger pores (strength increases), ice in smaller pores (strength slows), ice shrinkage reducing pressure (strength increases), and potential peak strength due to opposing effects at ultra-low temperatures. The model highlighted areas for further research like new testing methods. To gain a deeper insight into the reinforcing effects of low temperatures on concrete, Gong *et al.* [99, 100] utilised micro-scale models to investigate the ice formation within concrete pores and the consequent crack propagation. Through the use

of differential scanning calorimetry (DSC) and thermoporometry (TPM) techniques, Jiang *et al.* [101] discovered that the freezing of water present within the pores of concrete (20 ~ -170 °C), particularly in the temperature range from 0 to -50 °C, played a significant role in enhancing the strength of concrete at cryogenic temperatures. The findings revealed that the formation of ice crystals within both the capillary pores and gel pores contributed to the observed increase in concrete strength when exposed to extremely low temperatures.

Ultra-high performance concrete (UHPC) emerges as a premium alternative to conventional concrete with its exceptional strength, durability and improved resistance to cracking [102]. Some researchers examined the fundamental mechanical properties of UHPC at low and cryogenic temperature. Kim *et al.* [103, 104] investigated the compressive and tensile behaviour of UHPC at -170 ℃. Exposure to extremely low temperatures resulted in a significant enhancement in the mechanical properties of the material. For example, UHPC specimens containing 19.5 mm steel fibres, compressive strength was increased by 46.3%, tensile strength by 34.4% and fracture energy by 52.4% at -170 ℃ compared to values at ambient temperature. To address the negative effects of early-age shrinkage, characterised by microcrack formation [105] due to rapid hydration and water loss of UHPC, Jin *et al.* [106] conducted a study where incorporated 20% coarse aggregate into traditional UHPC with steel fibre content (0-3%) and tested the mechanical properties, across a wide temperature range from room temperature down to -90 °C. Results indicated a significant improvement in compressive (increased by 46.3% at -90 °C with 2% steel fibres compared to 20 °C) and splitting tensile strength (increased by 38.6% at -90 °C with 2% steel fibres compared to 20 °C) with decreasing temperature, attributed to improved material properties at lower temperatures and the formation of ice within pores. While steel fibres enhanced compressive and splitting tensile strength,

excessive fibre content led to weaken the low-temperature enhancement effect, likely due to fibre agglomeration.

Vandewalle [107] used the pull-out test to explore the bonding behaviour between steel and concrete at 20, -40, -80, -120 and -165 °C. The results indicated the ultimate bond strength increased by 33.3%,77.8%, 100.0% and 94.4% at -40, -80, -120 and -165 °C, respectively, in comparison with the ultimate bond strength at ambient temperature. The ultimate bond strength increased with higher moisture content in the test piece. Jin *et al.* [108] and Zhang *et al.* [109] analysed the bond strength at cryogenic temperatures via numerical simulation and pull-out test. A linear increase of 11.8% in the ultimate bond strength was noted as the temperature decreased from 20°C to -120°C. However, the residual bond strength and ultimate slip exhibited linear decline of 51.3% and 15.7%, respectively, while the bond strength reduces after FT cycles.

Fracture energy is another important property that characterises the resistance of concrete against crack growth and failure, which represents the total energy that the concrete absorbs since the crack initiates. Ohlsson *et al.* [110] conducted three-point bending tests to understand the fracture energy and the fatigue strength of concrete across temperatures ranging from 20°C to -35°C, using four different concrete grades: C25, C40, C45, and C100. Fatigue strength refers to the ability of a material to withstand repeated loading and unloading cycles without experiencing failure. It relates to the increased resistance of concrete to fatigue failure under low temperatures. The resistance is attributed to the mechanisms governing crack propagation during cyclic loading. Fatigue failures typically exhibit a more extensive pattern of cracks compared to static failures, resulting in a state where the material is more compromised or "cracked" after experiencing fatigue failure. A higher fracture energy and fatigue strength was observed at -35 °C as compared to that at ambient temperature. Maturana *et al.*[111] employed three-point flexural tests to assess

the fracture energy of concrete over a temperature range spanning from 20°C to -170°C. It found out a remarkable rise in fracture energy as the temperature decreased. At -170°C, the fracture energy was roughly three times higher as compared to that at room temperature. Rocco *et al.* [112] investigated the fracture characteristics of concrete at 20, -20, -70, -120 and -170 °C, and conducted flexure bending and standard cylinder-splitting tests. It indicated that the reduction in the temperature resulted in an increase in fracture energy and splitting tensile strength owing to the freezing of water in the bulk of the concrete.

Meanwhile some of the researchers investigated the flexure bending of reinforced structure at cryogenic temperatures. Liu et al. [113] employed four-point flexural bending tests on six reinforced concrete beams (with dimensions of 40 × 40 × 300 mm in width, height, and length, respectively) within a temperature range spanning from 20 °C to -180 °C, which demonstrated that as the temperature decreased, there was an observable increase in both the load-bearing capacity as well as stiffness of the beams. The results indicated that the ultimate bearing capacity of the beams was significantly higher under low temperatures. Specifically, under the temperatures of -40, -80, -120, -160, and -180 °C, the ultimate bearing capacity of the beams was amplified by 1.3, 1.4, 1.9, 2.1, and 2.6 times, respectively, as compared to the beam tested at ambient temperature. Nevertheless, the test beam sizes used in the previous studies were scaled proportionally, limiting the amount of information they could provide. Yan and Xie [114] conducted larger scale experiments to explore the performance of reinforced concrete beams at 20, -40, -70 and -100 °C. They performed twelve groups of four-point flexural bending tests with reinforced concrete beams (65 × 120 × 1600 in terms of width, height, and length in mm). It indicated that the resistance of reinforced concrete beam improved at low temperature. The ultimate bearing capacity of the beams under the temperatures of -40, -70, and -100

°C was 1.0 times, 1.1 times, and 1.3 times greater than the beam tested at ambient temperature, respectively.

On the other hand, in terms of UHPC, Liu *et al.* [115] conducted three-point and four-point bending tests to find out the flexural and fracture behaviour of UHPC with temperate ranging from 20 °C to -30, -60, -90, -120 and -160 °C. The flexural peak loads were 1.08, 1.26, 1.28, 1.61, and 1.60 times greater at -30, -60, -90, -120 and -160 °C, respectively, compared to the load at 20 °C with specimen dimension 515 × 100 × 100 (length × height × width in mm). In addition, the fracture energy of UHPC increased by 1.53, 1.61, 1.63, 1.85, and 1.87 times at -30, -60, -90, -120 and -160°C, respectively, compared to the value at 20 °C. Compared to the experiment results from Xie *et al.* [116] (who has conducted the three-point bending tests for conventional concrete from 20 °C to -80 °C with the same dimension above), it showed that the fracture energy dramatically increased by 99.38% and 99.49% for UHPC specimens at -30 and -60 °C, respectively. The increased fracture resistance of UHPC was attributed to the freezing of pore water into ice, which can enhance the interfacial adhesion between steel fibres and the UHPC matrix. Zhang *et al.* [117] explored the flexural performance of UHPC under six temperature conditions, ranging from 200 °C to cryogenic temperatures, using acoustic emission (AE) technology to identify cracking characteristics. Results revealed that exposure to in-situ -170 °C signally enhanced flexural strength nearly 2 times greater than the values at room temperature. This improvement was attributed to frozen water acting as a barrier to microcrack propagation, increased frictional resistance from hardened cement grains, and improved bond strength between steel fibres and the cement matrix. However, despite these enhancements, UHPC at -170 °C exhibited reduced ductility, characterised by steeper post-peak load decreased and higher energy release rates. AE results showed stronger signals and a higher proportion of shear cracks

in the linear-elastic stage at -170 °C. While at -170 °C condition significantly boosted strength and toughness, it also led to a trade-off in ductility, with the deflection ductility coefficient decreasing by 53.0% compared to ambient temperature.

2.4.1.2 Dynamic behaviour of concrete at low temperature

With the increasing demand for infrastructure in cold environments and the growing utilisation of LNG storage facilities [15, 118], there is a pressing need to develop concrete materials and structures that withstand extreme low temperatures and dynamic loading conditions. Consequently, a comprehensive evaluation of concrete performances and its failure criteria across a broad spectrum of strain rates is crucial for properly designing structures withstanding dynamic loadings and low temperature condition as along with FT cycles.

So far, only a limit study has focused on the dynamic behaviour of concrete material, especially UHPC at low temperature and cryogenic condition, only a few studies have explored in NSC. MacLean and Lloyd [119] performed experiment to investigate the effects of low temperatures (20, 0, -15, -45 and -70 °C) and low strain rates (average strain rate of 1.2 s^{-1}) on the compressive behaviour of concrete by using a drop mass impactor. It showed that the ratio of dynamic to static peak stress decreased linearly with decreasing temperature, reaching 0.82 at -70 °C. Su *et al.* [120] analysed the dynamic compressive behaviour of concrete via SHPB with strain rate 100 s^{-1} - 300 s^{-1} and built up a mesoscopic model of concrete, including mortar, aggregates, interfacial transition zones (ITZs) as well as ice particles. It emphasised that the improvement of mechanical properties was owing to the effect of ice. The declining temperature led to improved mechanical properties of aggregates and ice, resulting in a gradual decrease in damage rates based on the observation in numerical model. Qiao *et al.* [121] explored the dynamic behaviour of concrete by varying temperature (from 20 °C to -75 °C), strain rate

(approximately from 34 s^{-1} to 64 s^{-1}), water to cement ratio (w/c) (0.5, 0.6), and maximum aggregate size (12 and 22 mm). It was noted that temperature had the most dramatic impact on dynamic compressive strength, followed by strain rate, w/c as well as the maximum aggregate size. Dynamic compressive strength generally increased with decreasing temperature, reaching a maximum increase ratio of 65% at -75 °C. Moreover, specific energy absorption (SEA) increased as temperature decreased, indicating improved impact resistance at lower temperatures. Jin *et al.* [122] developed a 3D meso-scale numerical model to investigate the dynamic compressive strength increase factor at strain rate 10^{-5}~10^{2} s^{-1}, with temperature ranging from 20 to -160 °C. Cryogenic temperatures were observed to magnify strain rate sensitivity.

2.4.2 FT cycles attack to ACLNG storage tanks

2.4.2.1 Static performance of concrete after FT cycles

ACLNG storage tanks pose significant challenges to the durability and performance of concrete structures. Not only cryogenic thermal attack, but also FT cycles resulting from the fluctuating state of LNG storage levels [123] remarkably impact the microstructure and mechanical properties of concrete over time.

Over the last few decades, numerous scholars have explored the mechanical properties of concrete following cycles of low temperature FT exposure. A series of experiments regarding compressive and tensile strength as well as elastic modulus of concrete were conducted by Lee *et al.* [97] at a temperature range from 20 °C to -70 °C both under monotonic and cyclic loadings. The study noted a slight reduction in compressive strength and elastic modulus after FT cycles. Rostásy and Punch [124] examined concrete compressive and splitting tensile strength at low temperatures varying from +20°C to -170°C, and they also tested residual strength after low temperature FT cycles between 20 °C and -85 °C with a cooling rate of 1 °C/min. It was reported that the higher water content

in the concrete resulted in a loss of residual compressive strength up to 38% after 10 times FT cycles and the loss of tensile strength up to 57%. The concrete splitting tensile strength exhibited more prominent reductions after thermal cycles when compared to the compressive strength. Rostásy *et al.* [125] performed a series of experiment to explore the compressive and tensile strength of concrete after FT cycles with temperature ranged from 20 °C to -30 °C, 20 °C to -70 °C and 20 °C to -170 °C, respectively. The findings revealed a gradual decline in the compressive strength of the concrete following each temperature cycle, with the majority of the damage occurring within the FT cycle from 20°C to -170°C. After 12 cycles (temperature range from 20 °C to -170 °C), splitting tensile strength reduced to 18% of initial strength for blast furnace slag mortar and 31% for Portland cement mortar.

Shi *et al.*[126-129] explored the compressive strength, tensile strength and elastic modulus of NSC after cryogenic FT cycles, the temperature ranged from 20 °C to -120 °C, -30 °C to -120 °C, 10°C to -160 °C with cooling rate 1 °C/min. With increased FT cycles, there was a notable cumulative influence of FT damage, resulting in a significant reduction in compressive strength, tensile strength and modulus of elasticity. They also adopted two FT methods to test the residual modulus of concrete. In Method 1, the FT cycle began from ambient temperature and in the Method 2, the FT cycle began from the low temperature limit. The results indicated that with the increase in the number of FT cycles, the elastic modulus of concrete using Method 1 decreased, while the elastic modulus of concrete using Method 2 remained unchanged or even slightly increased. This may be because the remarkable freezing effects of concrete pore water offset the cumulative effects of FT damage. Furthermore, uniaxial and triaxial compression tests were conducted by Zhou *et al.* [130] to evaluate the behaviour of high strength concrete and C60 after ultra-low temperature FT cycles between 20 °C to -165 °C with cooling

rate 2-3 ℃/min. The findings indicated that the strength of both high strength concrete and C60 concrete reduced as the number of ultra-low temperature FT cycles increased. The water–binder ratio (w/b) of C60 and high strength concrete was 0.27 and 0.21, respectively. Compared to C60, high strength concrete with a lower water cement ratio and smaller porosity showed a lower expansion strain. Therefore, the strength loss of high strength concrete after super-low temperature FT cycles was less. After 20 cycles of super-low temperature FT, the number of large and fine pores in the concrete increased significantly, leading to significant deterioration of the concrete structure. On the other hand, in accordance with Sun *et al.* [131], the Poisson's ratio of concrete exhibited relatively low sensitivity to the FT cycles.

Kim *et al.* [104] investigated both normal strength concrete (NSC) and ultra-high performance fibre reinforced concrete (UHPFRC) at cryogenic temperature (-170 °C) and 1 time of FT cycle. The results indicated the compressive and tensile strength for both materials increased significantly under cryogenic temperature, but slightly declined after 1 time FT cycle. He et al. [132, 133] analysed the influence of different fibres including steel, polypropylene (PP), and polyvinyl alcohol (PVA) fibre in UHPC subjected to 1 FT cycle from 20 ℃ to −170 ℃ and increased to room temperature. Specimens with PVA and PP fibres experienced a more evident reduction in flexural strength after cryogenic attack, and this is because PVA and PP fibres were more prone to agglomeration and insufficient hydration (which occurred in concrete when there was not enough water available for all cement particles to fully react) due to water absorption of these two fibres, reducing their reinforcing effects. He et al. [134] conducted steel fibre pull-out tests on straight as well as hooked-end steel fibres embedded in UHPC specimens to FT cycles (herein one FT cycle was defined as temperature dropping from 20 °C to -170 °C and then elevating to 200 °C before returning to 20 °C). The results demonstrated that in the

scenario of specimens with hooked-end steel fibres, the compressive strength, bond strength and pull-out energy after 5 FT cycles decreased approximately 7.0%, 6.7% and 9.8%, respectively, as compared to after 3 FT cycles. This indicated that the fibre-matrix interface may be negatively affected by prolonged temperature cycling.

A number of researchers have managed to explain the concrete deterioration after FT cycles via microstructure analysis. He et al. [135] analysed internal pore structure and micro-morphology after cryogenic FT cycles. It demonstrated that cryogenic FT cycles caused remarkable changes in concrete's microstructure. The process involved complete freezing of pore water, water migration, and increased surface absorption. This led to the formation of tiny microcracks (smaller than 20 nm), which gradually expanded owing to crystallisation pressure. Over time, these microcracks developed into medium-sized capillary pores (size ranging from 10 to 50 μm), explaining the progressive deterioration of concrete under repeated FT cycles. The mechanical characteristics of concrete at cryogenic temperatures and after cryogenic FT cycles were thoroughly studied and analysed by Liu et al. [136]. It summarised the main specific mechanisms for cryogenic FT cycles, including stress concentration in the Interfacial Transition Zone (ITZ) stemmed from the variations in the thermal expansion coefficients between mortar and aggregates, nanoscale deterioration of C-S-H gel, causing microcracks within or between C-S-H grains, exacerbated volume expansion from pore water freezing leading to pore wall extrusion and cracking, as well as increased water absorption from the external environment accelerating deterioration.

Some scholars have conducted experimental and numerical simulation studies on the bonding performance of reinforced concrete after ultra-low temperature FT cycles. Lee *et al.* [97] found out the bond strength declined by 1.1%, 2.5% and 8.5% after 1, 10 and 30 times of FT cycles at which temperature ranged from 20 °C to -70 °C. Xie *et al.* [137]

have conducted a pull-out test with temperature ranging from 20 ℃ to -40 ℃, 20 ℃ to -75 ℃ and 20 ℃ to -120 ℃. As the number of cycles increases, the effect of each cycle on the reduction of bond strength gradually weakens. After three FT cycles, the average bond strength reduced by 6%, 13%, and 14% at FT temperatures of 20~-40 ℃, 20~-75 ℃, and 20~-120 ℃, respectively. However, there is a lack of research on the fracture energy of concrete after FT cycles. Xie *et al.* [138] studied the fracture energy of concrete after the FT cycle in the range from 20 °C to -80 °C via three-point bending tests. The findings indicated that as the lower temperature limit decreased and the number of cycles increased, the fundamental mechanical properties of concrete, along with the toughness of crack initiation and fracture energy, demonstrated a decreasing pattern.

The characteristics of concrete after FT cycles that are mentioned in the introduction part are summarised in Appendix N.

2.4.2.1 Dynamic behaviour of concrete after FT cycles

There is limited research on its dynamic behaviour after FT cycles. Li et al. [139] performed impact tests using SHPB on self-compacting concrete (SCC) specimens before and after 200 FT cycles temperature range varying from (−18 ± 2)°C to (5 ± 2)°C with strain rate between 30 to 210 s^{-1}. It demonstrated that peak stress and strain as well as impact toughness index increased with strain rate, and elastic modulus showed weak strain rate dependence. Gan et al. [140] conducted FT cycle tests with temperature range of 0 °C to -30 °C, cyclic loading tests and dynamic loading tests on concrete specimens and examined concrete behaviour at different strain rates (10^{-5} to 10^{-2} s^{-1}) after 50 FT cycles. The results indicated that compressive strength of FT damaged concrete increased 31.61% as compared to room temperature, while undamaged concrete only increased by 22.92% (at 10^{-2} s^{-1}strain rate) and the rate sensitivity of concrete after FT cycles was generally higher than that of undamaged concrete.

2.5 Summary and Discussion

This chapter comprehensively summarises characterisation of blast wave propagation in the soil medium, impact load, and failure mechanism of pipelines optimised protection design of pipelines in detail. The mechanical properties of concrete at cryogenic temperature and after FT cycles for ACLNG storage tanks are comprehensively reviewed. The conclusion can be drawn as follows:

- Part of the energy released by a surface explosion would act on the ground to form a crater, while far-range blasts might produce shock wave propagation. The effects of the explosion on buried or exposed pipelines were significant.
- Both pipelines and LNG storage tanks are vulnerable to impact loads from various sources such as excavator damage and aircraft collisions, but their structural integrity can be maintained through proper design considerations and protective measures based on comprehensive understanding of failure mechanisms and impact responses.
- Static experiments on concrete demonstrate that as temperature decreases, its compressive strength, tensile strength, elastic modulus, and fracture energy correspondingly increase. However, with temperature reduction, concrete also exhibits increased brittleness, with more visible cracks and spalling becoming apparent at low temperatures.
- As concrete undergoes FT cycles, it experiences progressive mechanical performance degradation characterised by microstructural damage, strength reduction, and cumulative material fatigue.

Based on the above summaries, some issues and suggestions are elaborated for further research:

- Due to unavailability of experimental data in open literature, the ground shock caused by explosion could be calculated by using the empirical formula from TM5-855-1. However, the empirical formula was not applicable when the scale distance was less than 0.4 $\mathrm{m}/kg^{1/3}$. According to the relevant regulations on the buried depth of pipelines in Australia, the range was 300 mm to 1800 mm. The impact value calculated in this way had a large error. Therefore, more accurate results needed to be obtained by numerical simulation or experimental methods.
- Understanding the dynamic mechanical properties of concrete at cryogenic temperatures and after FT cycles is critical for accurately predicting and enhancing the blast and impact resistance of ACLNG storage tanks. By developing more precise numerical simulation models and comprehensive experimental data, researchers can provide crucial insights into infrastructure design, improve safety protocols for LNG facilities, and contribute to the development of more resilient construction materials capable of withstanding potential impact or blast loading scenarios in challenging environmental conditions.

Chapter 3. NUMERICAL SIMULATION OF BURIED STEEL PIPELINES SUBJECTED TO GROUND SURFACE BLAST LOADING

3.1 Introduction

Steel gas pipelines are important component in energy sector. Due to its easy accessibility and importance, shallow-buried pipelines are becoming targets of intentional attack. Therefore, it is urgent to investigate the failure mechanism of buried pipelines subjected to ground surface blast loadings and carry out quantitative damage assessment of pipelines. The present study performs numerical simulation on the resistance of buried pipelines subjected to ground surface explosion. The simulated ground shock propagation in the soil medium was validated with technical manual TM5-855-1 as well as experimental data. The effects of charge weight, stand-off distance, explosive position offset, pipe diameter, pipe wall thickness, buried depth, and steel grade as well as different soil types were investigated. It was found that for the grade X70 pipe with the same buried depth 760 mm, the cross-sectional flattening ratio under charge weight 227 kg (typical sedan bomb) was nearly 544 times greater than the case in 2.3 kg charge weight (typical pipe bomb). The flattening ratio decreased 99.9% because of the buried depth increased from 300 mm to 1800 mm. The decrease in pipe diameter from 860 mm to 350 mm caused 89.6% reduction in flattening ratio. The increase in wall thickness from 4.80 mm to 12.7 mm caused 99.7% decline in flattening ratio. Similarly, it showed the flattening ratio decreased 29.3% when the steel grade increased from X42 (yield strength 290 MPa) to X80 (yield strength 580 MPa). The blast resistance was the worst when the pipeline was buried in clay soil, in which the flattening ratio was 74.8% and 40.3% greater as compared with sandy loam and soil medium. An analytical formula was derived to predict the flattening ratio of pipelines against surface explosion.

3.2 Numerical model development and validation

3.2.1 FSI validation

3.2.1.1 Material model and properties

The air model is commonly simulated by MAT_NULL with EOS LINEAR_POLYNOMIAL, which defines the pressure of air by the following equation [141]:

$$p = C_0 + C_1\mu + C_2\mu^2 + C_3\mu^3 + (C_4 + C_5\mu + C_6\mu^2)E \qquad (3.1)$$

where p stands for air pressure; C_0-$C_6$are the constant coefficients; μ=ρ/ρ_0-1, in which ρ and ρ_0 are the current density and reference density; E is the initial energy of reference specific volume per unit. Air is modelled by an idea gas, which can be achieved by setting C_0=C_1=C_2=C_3=C_6=0, and C_4=C_5=γ-1. The following equation provides the idea gas pressure:

$$p = (\gamma - 1)\frac{\rho}{\rho_0}E \qquad (3.2)$$

where γ is the ratio of specific heats, $\rho_0$is air density. In the simulation, γ=1.4, ρ_0=1.225 kg/m^3 and E is 2.5× 10^5 J/m^3.

High explosive TNT is simulated by MAT_HIGH_EXPLOSIVE_BURN with Jones-Wilkins-Lee (JWL) EOS to describe the pressure generated by chemical explosive, which can be expressed as:

$$P = A(1 - \omega/R_1V)e^{-R_1V} + B(1 - \omega/R_2V)e^{-R_2V} + \omega E/V \qquad (3.3)$$

where P indicates the hydrostatic pressure; V is the initial relative volume; E is the internal specific energy; A, B, R_1, R_2 and ω are equation coefficients regarding explosive. The material properties and the parameters of EOS for TNT are given in Table 3.1.

Table 3.1 Material properties and EOS for TNT [142].

Parameter	Value
ρ_0 (kg/m^3)	1603
v_0 (m/s)	6930
P_{CJ} (GPa)	21
A (GPa)	371.2
B (GPa)	3.231
R_1	4.5
R_2	0.95
ω	0.3
E_0 (J/m^3)	7×10^9

Soil is modelled by MAT_SOIL_AND FOAM, which was a relatively simple material model developed by Krieg [143]. This model is suitable for defining the soil of which the yield stress is low and the behaviour of soil is similar to fluid [144]. There is no strain hardening on the surface for this model [145]. The deviatoric perfectly plastic yield function, ϕ, and the second invariant J_2 can be described as:

$$\phi = J_2 - [a_0 + a_1 p + a_2 p^2] \tag{3.4}$$

where

$$J_2 = \frac{1}{2} s_{ij} s_{ij} \tag{3.5}$$

On the yield surface $J_2 = \frac{1}{3}{\sigma_y}^2$, and the uniaxial yield stress σ_y is defined as:

$$\sigma_y = \sqrt{3(a_0 + a_1 p + a_2 p^2)} \tag{3.6}$$

where $a_0 = a_1 = 0$ and $a_2 = \frac{1}{3}{\sigma_y}^2$ to eliminate the dependence of yield strength on pressure.

In this study, wet sandy clay is selected and the parameters are based on [146] (listed in Table 3.2), where ρ is mass density of soil; G is shear modulus; K_u is bulk modulus; $a_0, a_1,$ and a_2 are the yield function constants for plastic yield function and P_{cut} is the pressure cut-off for tensile fracture [141].

Table 3.2 Material properties of soil model.

Parameter	Value
ρ (kg/m^3)	1760
G (MPa)	11.8
K_u (MPa)	107.5
a_0	0
a_1	0
a_2	0.6
P_{cut}(MPa)	0

3.2.1.2 Finite element model of XYZ

A 1/4 symmetrical FE model was established by LS-DYNA with an air domain of 2 m × 2 m × 1.5 m and soil domain of 2 m × 2 m × 4 m, as shown in Figure 3.1. The explosive was positioned on the ground surface. The element size was 15 mm. The model was symmetrical to XZ and YZ planes where symmetric boundaries were used. The non-reflecting boundaries were applied on the top surface, bottom surface and two lateral surfaces to minimize the stress wave reflection.

In the present study, an ALE multi-material was employed to air, soil and explosive, which was advantageous in the analysis of large deformation problems and avoid seriously distorted of mesh [147]. Moreover, with the aid of a fluid structure coupling algorithm that adheres to the conservation of mass, momentum, and energy, the ALE approach can simulate the fluid-structure interface (FSI) [148].

INITIAL_VOLUME_FRACTION_GEOMETRY was applied for spherical TNT with charge weight 227 kg which was sedan car bomb [149]. DATABASE_TRACER was applied to catch the soil pressure in various depth.

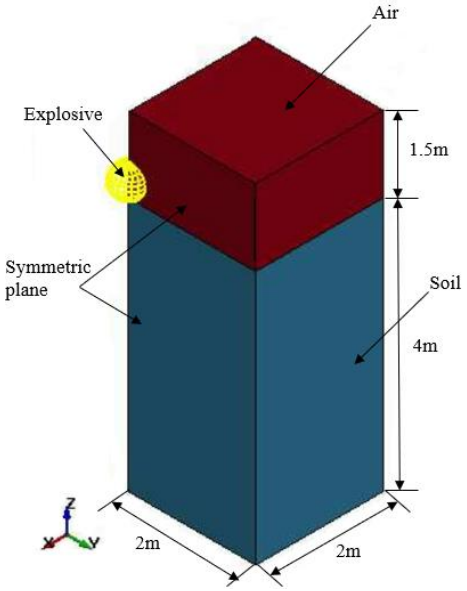

Figure 3. 1 Quarter of ground surface explosion geometrical model.

3.2.1.3 Model validation

Propagation of blast waves in the soil during a 227 kg TNT ground surface explosion is shown in Figure 3.2. The results revealed that the explosion shock wave propagated to the soil in the form of hemispherical wave and created a crater on the surface of ground. A crater was evident on the perimeter of the explosion centre. Figure 3.3 displays the time history of shock load at different depths of soil. The results indicated that ground shock pressure decays rapidly after reaching to peak. With the increase in propagation depth, the ground shock peak pressure attenuated significantly.

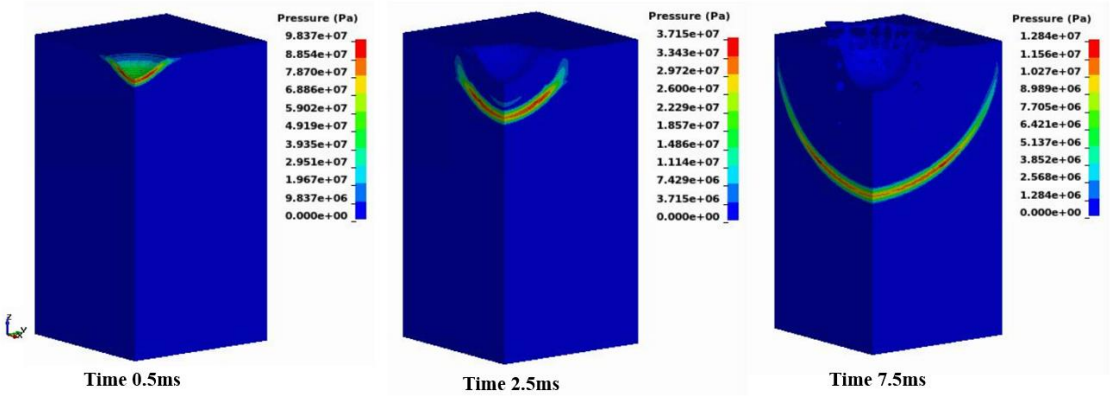

Figure 3. 2 Blast waves propagation in soil under ground surface explosion.

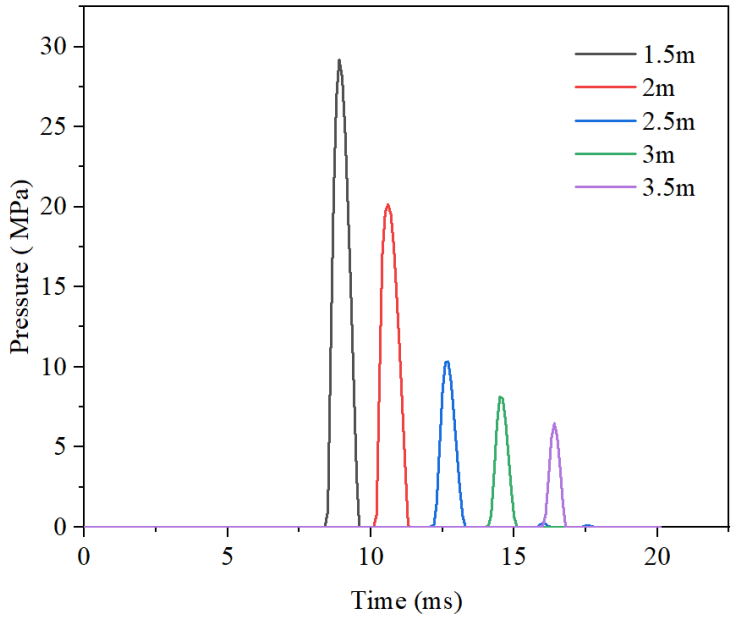

Figure 3. 3 Ground shock pressure time history at varying depth.

The ground shock peak pressure has been forecasted using the US Army Corps of Engineers Manual (TM5-855-1) at various soil depths, and Equation (2.1) was introduced in Section 2.1.2.

Table 3.3 presents the different seismic velocity, acoustic impedance as well as attenuation coefficients with different soil types. Type 5 was similar to represent numerical model soil type. Figure 3.4 demonstrates the differences in peak pressures between simulation results and TM5-855-1 in different scaled distances. TM5-855-1 is applicable to the case where the scaled distance is greater than 0.4 m/kg$^{1/3}$, however, it cannot predict the ground shock peak pressure precisely when the scaled distance is smaller than 0.4 m/kg$^{1/3}$ [53]. It was evident that the numerical simulation results are almost consistent with semi-analytical results. The differences between these two results may be attributed to the different positions of explosive relative to ground level causing energy dissipation in air [148].

Table 3.3 Soil parameters for calculating ground shock [52].

	Soil type	Seismic Velocity, c (fps)	Acoustic Impedance, ρc (psi/fps)	Attenuation coefficient, n
1	Loose, dry sands and gravels with low relative density	600	12	3-3.25
2	Sandy loam, loess, dry sands, and backfill	1,000	22	2.75
3	Dense sand with high relative density	1600	44	2.5
4	Wet sand clay with air voids (>4%)	1,800	48	2.5
5	Saturated sandy clays and sands with small amount of air voids (<1%)	5,000	130	2.25-2.5
6	Heavy saturated clays and clay shales	>5,000	150-160	1.5

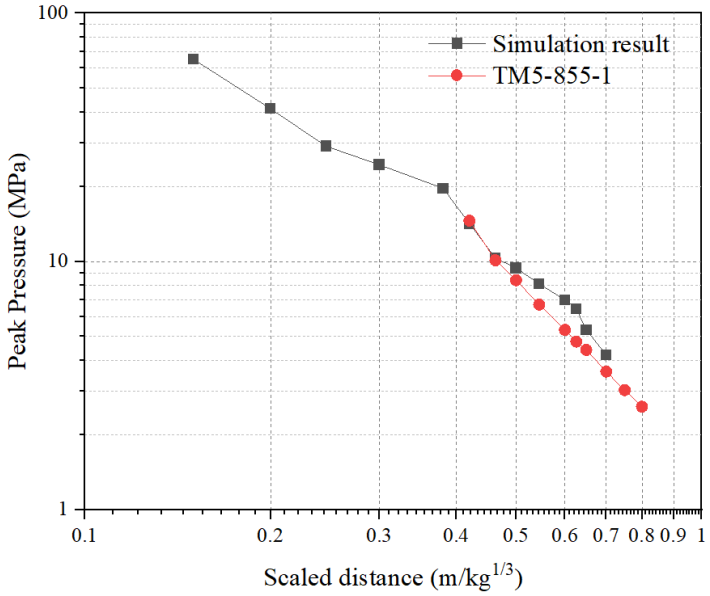

Figure 3. 4 Ground shock peak pressure attenuation comparison between simulation results and TM5-855-1.

3.2.2 Pipe material validation

3.2.2.1 Pipe material model for X70 steel

The material model JOHNSON_COOK is used to define pipe material X70 with GRUNEISEN EOS. This model is suitable for a wide range of strain rates, which can consider strain hardening, strain rate hardening and thermal softening of materials at the same time [150]. The flow stress is defined as:

$$\sigma_y = \left[A + B\left(\overline{\varepsilon}^p\right)^n\right][1 + C\ \ln \dot{\varepsilon}^*][1 - (T^*)^m] \quad (3.7)$$

where A stands for yield stress; B is strain hardening; C is strain rate sensitivity; n is strain hardening exponent; m is temperature softening coefficient; $\overline{\varepsilon}^p$ represents effective plastic strain; $\dot{\varepsilon}^*$ is effective strain and T^* is homologous temperature.

Johnson Cook failure model uses cumulative damage to consider the failure of materials and does not consider the impact of damage on material strength. The stress and strain are taken as zero when the damage degree reaches the critical value. The damage parameter D can be defined by:

$$D = \sum \frac{\Delta\varepsilon_p}{\varepsilon^f} \quad (3.8)$$

The value of D ranges between 0 to 1, when D = 1, material fracture occurs. In Equation (3.8), $\Delta\varepsilon_p$ is equivalent plastic strain increment in one-time step and ε^f is effective failure strain which can also be written as:

$$\varepsilon_f = \left[D_1 + D_2 \exp\left(D_3 \frac{\sigma_m}{\sigma_{eq}}\right)\right][1 + D_4 \ln \dot{\varepsilon}^*][1 + D_5 T^*] \quad (3.9)$$

where D_1 to D_5 are the failure model constants of material, σ_m and σ_{eq} represent mean stress and equivalent stress, respectively. The parameters of X70 pipeline are: density ρ = 7,850 kg/m^3, Poisson's ratio = 0.3, Young's modulus E_P = 210 GPa, A = 560 MPa, B = 510 MPa, C = 0.0044, n= 0.48 [40]. D_1 to D_5 are equal to 0.01, 3.1, -1.4, 0 and 0, respectively [151].

The GRUNEISEN EOS is utilised for steel model, which can define the pressure of the material under compression as:

$$P = \frac{\rho_0 C^2 \mu[1+\left(1-\frac{\gamma_0}{2}\right)\mu-\frac{a}{2}u^2}{[1-(S_1-1)\mu-S_2\frac{\mu^2}{\mu+1}-S_3\frac{\mu^2}{(\mu+1)^2}]^2} + (\gamma_0 + a\mu)E \quad (3.10)$$

and for the pressure when the material expands as:

$$P = \rho_0 C^2 \mu + (\gamma_0 + \alpha\mu)E \tag{3.11}$$

where C is the intercept of the curve (u_s-u_p) regarding shock velocity; S_1, S_2, S_3 are the coefficients of (u_s-u_p) curve slope; γ_0 is the constant; E is internal energy of denotes and μ is volume change rate which is equal to $\frac{\rho}{\rho_0} - 1$ (ρ and ρ_0 are material density and initial material density, respectively). The GRUNEISEN equation of state parameters: C=4569 m/s, S_1=1.49, S_2=0, S_3=0, γ_0=2.17, α = 0.46 [152].

3.2.2.2 Finite element model of XYZ

The model was established based on the experimental investigation by Song et al. [40]. The explosive was placed on the top surface of the X70 steel pipeline. In this study, the full finite element models were developed in LS-DYNA with dimension of 4 m × 2 m × 2.5 m in X, Y, Z directions (shown in Figure 3.5). The model consists of three parts with air, explosive and X70 steel pipeline. The total length L of pipeline is 3 m, diameter ϕ is 1.016 m and wall thickness δ =0.0262 m. The mesh size for air and X70 steel pipeline were 10 mm and 5 mm, respectively, which can be more efficiency and accuracy according to the convergence study from He et al. [153].

The air and explosive were modelled by Arbitrary Lagrangian-Eulerian (ALE)_ MULTI_MATERIAL_GROUP, while the pipeline was developed by Lagrangian mesh. The pipeline was meshed with shell element, and CONSTRAINED_LAGRANGE_IN_SOLID was utilised for coupling ALE multi-material group and pipeline interaction.

INITIAL_VOLUME_FRACTION_GEOMETRY was applied for rectangular box explosives with charge weight 5 kg and 10 kg, which contact area was 0.25 m × 0.2 m

according to Song et al. [40]. For the entire model, the top, bottom, and four lateral faces all used the non-reflecting boundary. Three groups of mesh size sensitivity tests have been done, including the first group with 1 mm steel pipe and 5 mm air; the second group with 5 mm steel pipe and 10 mm air; the third group with 10 mm steel pipe and 15 mm air (the magnitude of the charge weight was 5 kg for all trials). Compared with experimental data from Table 3.4, the differences for the length of axially directed tear and circumferentially directed between experimental data and simulation results were 0.34% and 0.00% for group 1, -4.14% and 0.48% for group 2, 10.34% and 14.29% for group 3, respectively. As can be seen from Figure 3.6, although group 1 may get a more precise result, the simulation time for group 1 was approximately 1 time and 10 times greater than groups 2 and 3. To balance the accuracy and computational cost, the element mesh size with the second group was chosen.

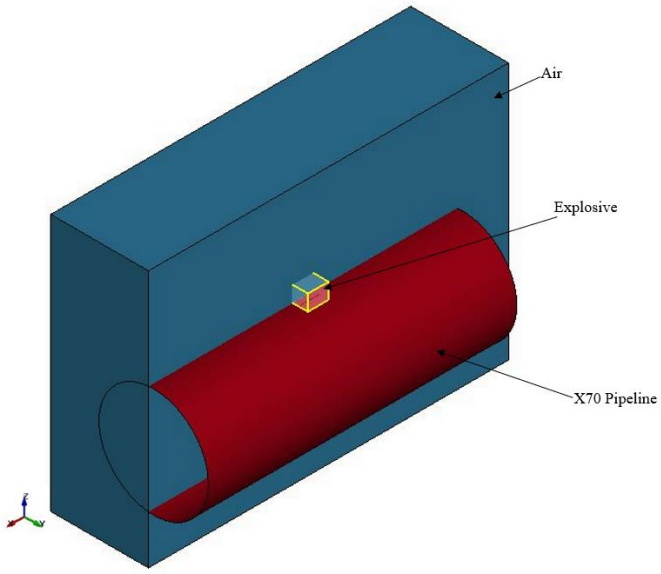

Figure 3. 5 Finite element model for X70 steel pipeline material calibration.

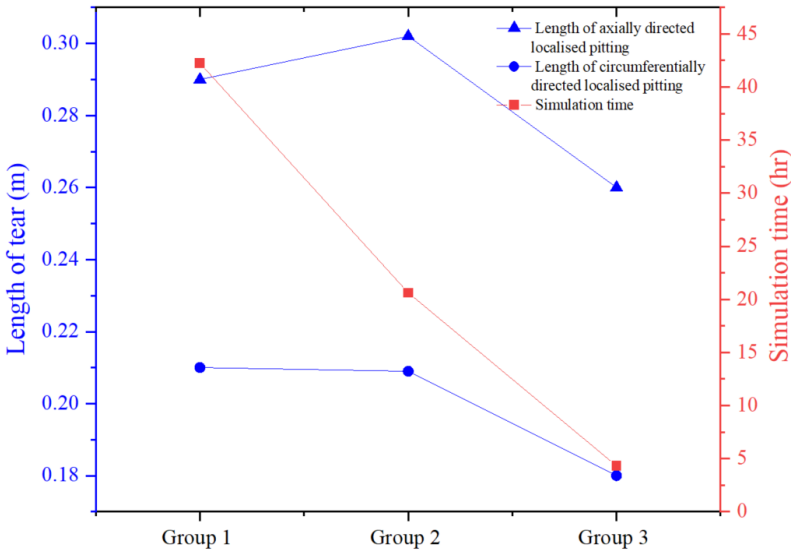

Figure 3. 6 Mesh convergence results of length of tear and simulation time.

3.2.2.3 Model validation

The results of both numerical simulation and experimental test [40] are shown in Figures 3.7 and 3.8. The deformation for the top side of the pipeline in both two scenarios are in good accordance with the experimental results. On the upper side of the pipeline, the distortion had an almost rectangular shape. In addition to this, a comparison between the numerical and experimental results with respect to local pitting length for both axial and circumferential direction are listed in Table 3.4. The errors in the axial and circumferential directions between the numerical and experimental data were approximately 4.14% and -0.476%, respectively when the charge weight was 5 kg. While the errors in the axial and circumferential directions were about 3.45% and 8.57%, respectively with 10 kg TNT. It could be clearly seen that the numerical results were consistent with the experimental measurements. The pipe material model for X70 steel can be utilised to investigate the response of buried pipelines against blast loadings.

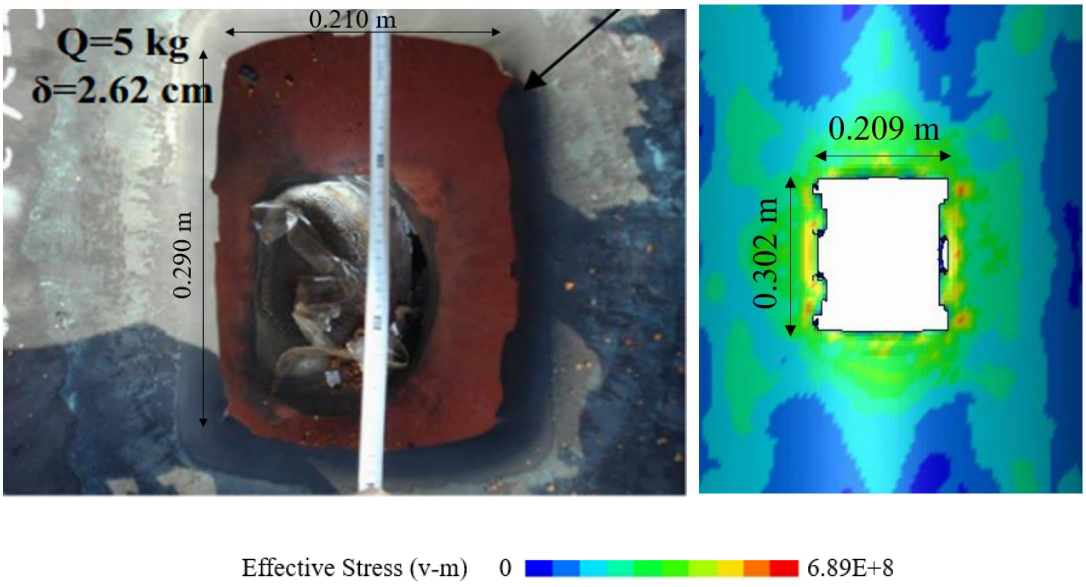

Figure 3. 7 Deformation of X70 pipeline with 5 kg TNT.

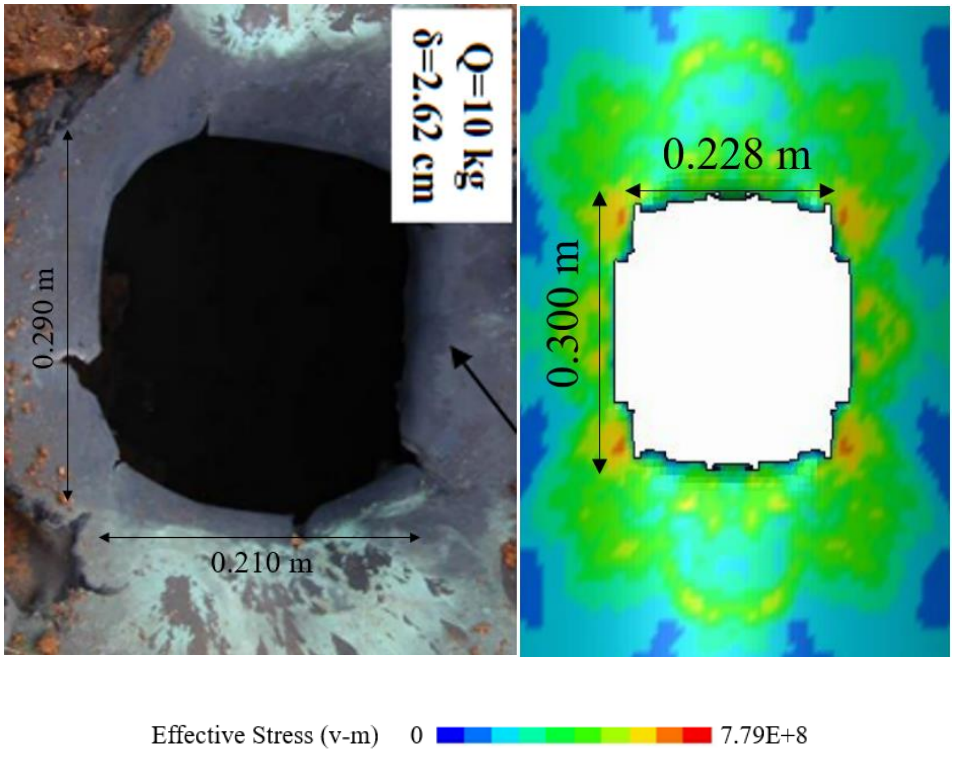

Figure 3. 8 Deformation of X70 pipeline with 10 kg TNT.

Table 3.4 Comparison of numerical and experimental results in relation to pipeline damage area on length of local pitting on different directions.

Numerical Test Trial	Numerical results (m)		Experimental results (m)		Error (%)	
	Axial direction	Circumferential direction	Axial direction	circumferential direction	Axial direction	Circumferential direction
5 kg TNT	0.302	0.209	0.290	0.210	4.14	-0.476
10 kg TNT	0.300	0.228	0.290	0.210	3.45	8.57

3.3 Buried steel pipeline response to blast loads

3.3.1 Material properties

Table 3.5 and Table 3.6 display the input data for different soil types and the material properties in various steel types, respectively. The alphabet prior to the two digital number stood for the condition of manufacturing and chemical and physical properties, while the two digital number represented the minimum yield strength of that pipeline in 000's psi to this grade [9].

Table 3.5 Input parameters of backfilled soil.

Parameter	Sandy loam [154]	Soil medium [155]	Clay soil [156]
ρ (kg/m^3)	1255	1762	1963
G (MPa)	1.724	24	2.524
K_u (MPa)	5.516	142	4673
a_0	0	0.34	0.001
a_1	0	0.7	0.0049
a_2	0.8702	0.3	0.0079
P_{cut}(MPa)	0	0	-0.005

Table 3.6 Material properties in different types of steel pipelines [9, 157, 158].

Parameter	API X42	API X52	API X65	API X80
Poisson's ratio	0.3	0.3	0.3	0.3
Elastic modulus (GPa)	210	210	210	206.04
Yield strength (MPa)	290	360	500	580
Tensile strength (MPa)	415	460	535	674

3.3.2 Finite element model

A half model was established in LS-DYNA with dimensions 6.5 m × 2.5 m × 3 m in X, Y, Z directions in the present study as shown in Figure 3.9. The total length L of X52 pipeline is 12 m with diameter ϕ 660 mm, wall thickness δ 5.56 mm and buried cover 760 mm in sandy loam. The pipeline was modelled by Lagrangian mesh, while air, soil and explosive were applied by ALE multi material. CONSTRAINED_LAGRANGE_IN_SOLID was employed for soil-structure interaction.

INITIAL_VOLUME_FRACTION_GEOMETRY was applied for spherical explosives with charge weight 23 kg. The explosive was located above the crown of the pipeline on the ground surface. The model was symmetrical to YZ plane. The non-reflecting boundaries were applied on the top surface, bottom surface and three lateral surfaces.

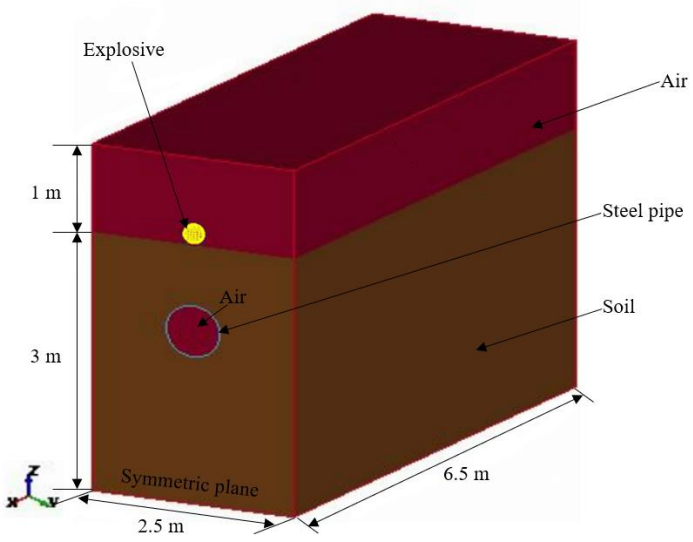

Figure 3. 9 Schematic view of buried pipeline subjected to blast loadings.

3.4 Results and discussion

Based on the model established in Section 3.2, the parametric analysis was developed herein to study the surface explosion induced dynamic response of steel pipelines with different parameters. In this section, the investigated parameters included internal pressure, charge weight, detonation height, explosive offset, pipe diameter, pipe wall thickness, buried cover, and steel grade as well as different soil types. All the parametric data was based on the Dampier to Bunbury natural gas pipeline system in Western Australia (see Appendix D) [159].

3.4.1 Internal pressure

To evaluate the behaviour of pipelines in various internal pressure, internal pressures of 0, 1.50, 2.50, 4.50 and 12.0 MPa were considered, and a uniformly distributed pressure was added on the inner surface of the pipeline.

The deformed shape and the effective plastic strain for the X52 pipeline with various internal pressures under 23 kg TNT explosion are shown in Figure 3.10. It was obvious that the maximum deformation point and the maximum equivalent strain were located on the crown of the pipeline. In addition, the increase in internal pressure caused the lower deformation of cross section.

Ovalisation is one of the most important mechanical response features for pipe structures. The critical flattening of pipelines can be determined by analytical methods or physical test, based on the Canadian standard and regulation CSA Z662: Oil & Gas Pipeline Systems [160]. According to Gresnigt [161], cross-sectional flattening of pipelines is equal to the ratio between the outer diameter of the pipeline (D) and the change in outer diameter (ΔD), and the maximum allowable ovalisation factor is 0.15. Figure 3.11 shows the cross-sectional flattening of the pipeline in various internal pressures. The flattening

ratios of steel pipelines under 0, 1.50, 2.50, 4.50 and 12.0 MPa internal pressure were 0.199, 0.167, 0.060, 0.015 and 0.005, respectively. The increase in internal pressure results in a lower cross-sectional flattening ratio of pipelines. However, the numerical simulation results obtained by this method were not conservative. When the internal pressure increases from 0 to 12.0 MPa, the flattening ratio decreased 97.5%. Differences in simulation findings were caused by an increase in internal pressure. Therefore, to get much more conservative and safe results, the internal pressure of the pipeline was set to 0 MPa in the subsequent parameter analysis.

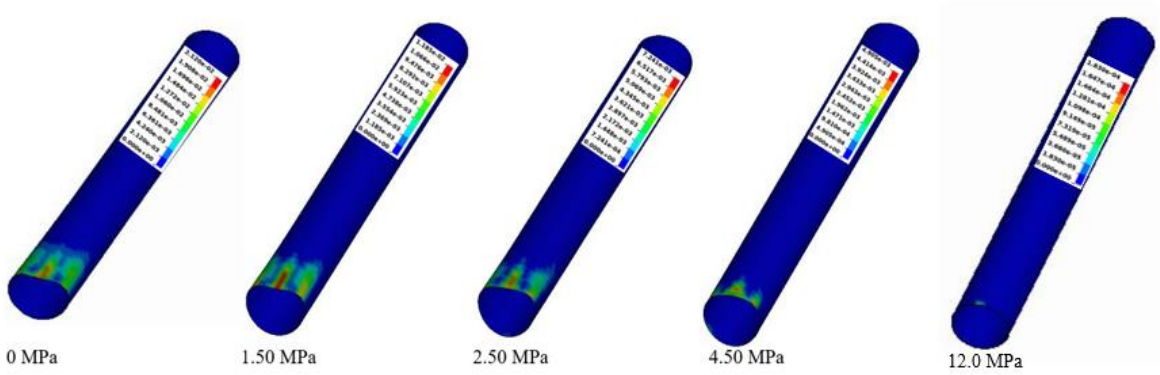

Figure 3. 10 Deformed shape and effective plastic strain of pipelines in different internal pressures.

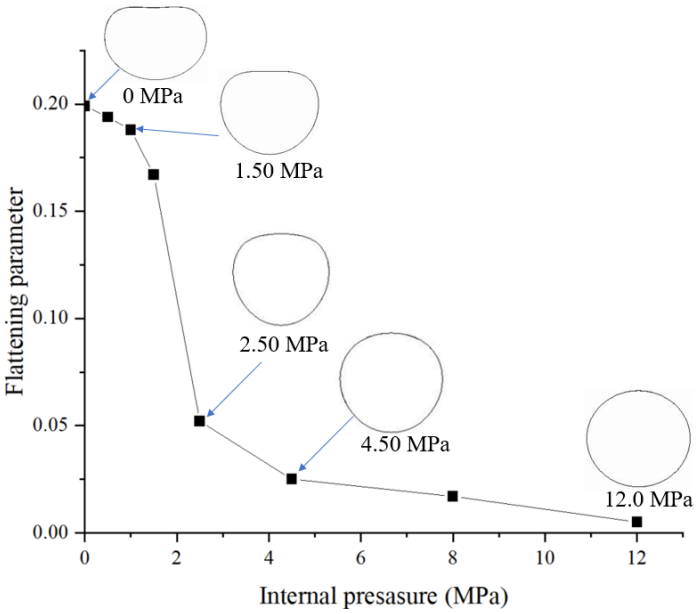

Figure 3. 11 The flattening of pipeline in various internal pressures.

3.4.2 Charge weight

To explore the effect of charge weight for buried pipelines subjected to ground surface explosion, five different charge weights were tested, including 2.3 kg, 4.5 kg, 23 kg, 50 kg and 227 kg. The magnitude of charge weight that investigated was based on equivalent TNT of typical pipe bomb, briefcase bomb and compact sedans [162]. All of the tested specimens were buried in sandy loam with the length of 6 m (half model), ϕ = 660 mm, wall thickness δ = 5.56 mm and buried cover 760 mm. The plastic strain distribution with different angles for the cross section and the cross-sectional flattening of pipelines are presented in Figure 3.12 (a) & (b), respectively. The maximum effective plastic strain typically located on the crown of the pipeline as can be seen from Figure 3.12 (a). The flattening of pipeline was 0.948 when the charge weight was 227 kg, which is 1.91 times, 4.72 times, 103 times, 545 times higher than 50 kg, 23 kg, 4.5 kg and 2.3 kg, respectively. Based on the allowable maximum ovalisation criteria from Gresnigt [161], only the cases 2.3 kg and 4.5 kg were within the allowable flattening ratio.

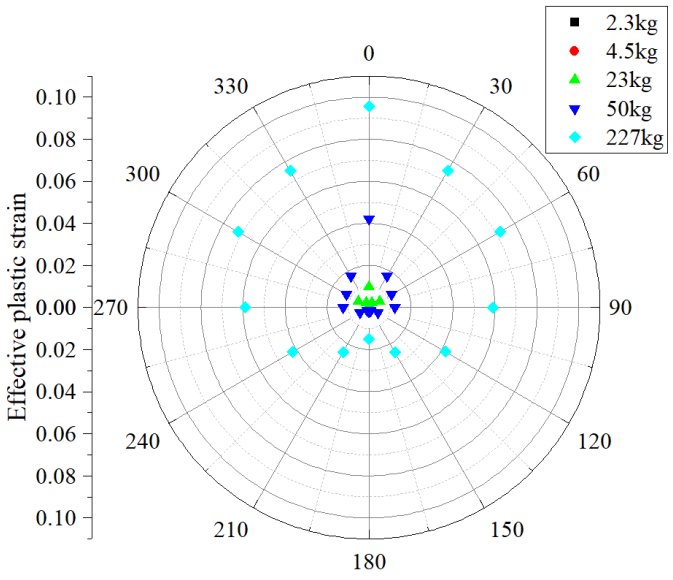

(a)

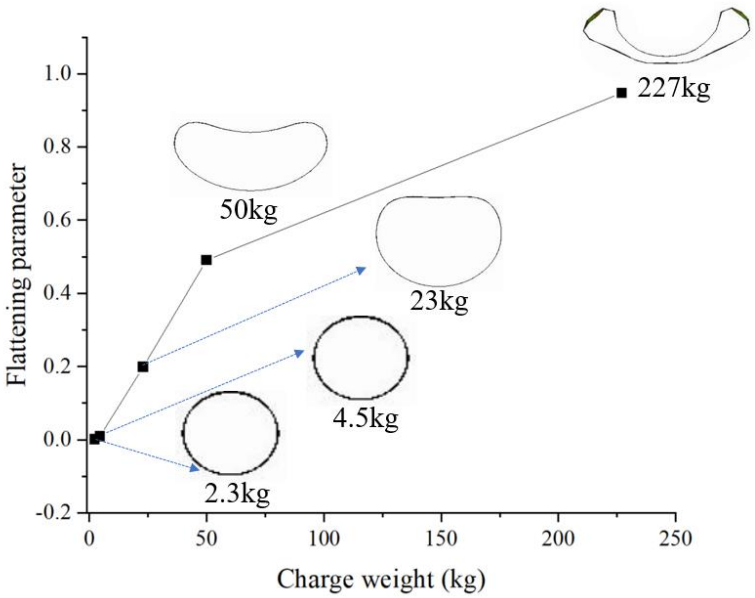

(b)

Figure 3. 12 Pipeline behaviour caused by various charge weight. (a) Effective plastic strain developed in wall and (b) the cross-sectional flattening ratio of pipeline

3.4.3 Detonation height

To evaluate the effect of stand-off distance, five different groups with 0 mm, 100 mm, 150 mm, 250 mm and 500 mm were developed in LS-DYNA. The explosive, which charge weight was 23 kg, was taken place directly above the pipeline. The length (6 mm half model), diameter (660 mm), wall thickness (5.56 mm), steel grade (X52), and buried cover (760 mm) as well as the soil type (sandy loam) remained the same. Figure 3.13 (a) displays the effective plastic strain of the pipeline around the cross section. It demonstrated that when the stand-off distance was 0 mm, the plastic strain was the largest of the five. The effective plastic strain was 0.00985 at the crown of the pipeline when the stand-off distance was 0 mm at the pipe crown, which was 36.7%, 74.3%, 90.4% and 100% higher than the cases with 100 mm, 150 mm, 250 mm and 500 mm stand-off distance, respectively. When the stand-off distance was 0 mm, the cross-sectional flattening of the pipeline was 0.2, which was 2.8 times, 3.1 times, 5.0 times and 22.7 times greater than

that at stand-off distance 100 mm, 150 mm, 250 mm and 500 mm, respectively (see Figure 3.13 (b)). Based on the failure criteria of ovalisation above, it could estimate that the pipeline cannot operate normally when the sand-off distance was 0 mm with 23 kg charge weight.

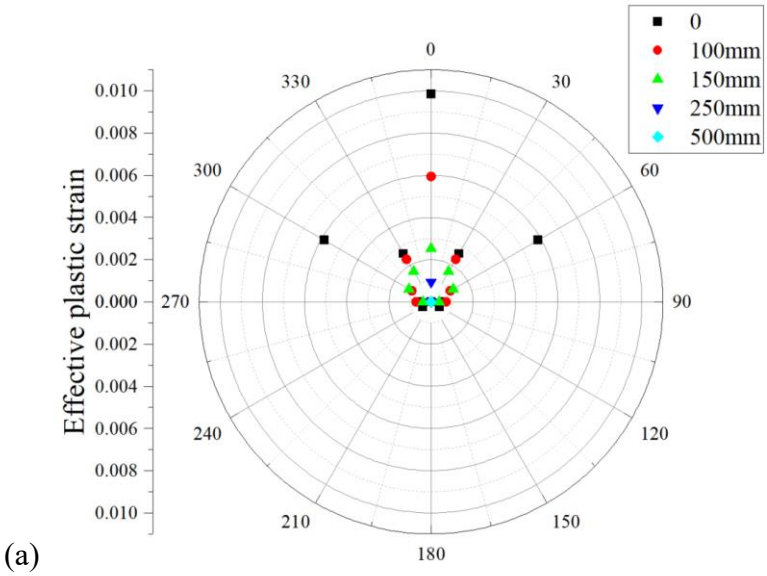

(a)

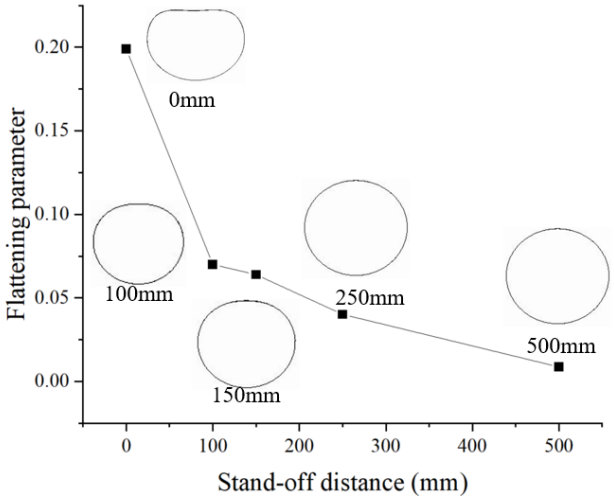

(b)

Figure 3. 13 Pipeline behaviour caused by different stand-off distances. (a) Effective plastic strain developed in wall and (b) the cross-sectional flattening ratio of pipeline

3.4.4 Explosive offset

Explosive offset can also affect the mechanism of pipelines under blast loading. Four different explosive offset groups were built up, including 0 m, 0.15 m, 0.30 m and 0.45 m. Meanwhile, the explosive charge weight (23 kg), the length (6 mm half model), diameter (660 mm), wall thickness (5.56 mm), steel grade (X52), and buried cover (760 mm) as well as the soil type (sandy loam) retained the same. As shown in Figure 3.14 (a), the maximum deformation did not occur at the crown of the pipeline when the explosive was not directly above the pipe. The increase in offset distance resulted in a decline in deformation in the pipe. The flattening ratio was 0.199. 0.173, 0.159 and 0.123 when the offset distance was 0 m, 0.15 m, 0.30 m and 0.45 m, respectively. It was obvious that due to the increase in offset distance, the flattening ratio decreased progressively (see Figure 3.14 (b)). With increase in offset distance, the effective plastic strain declined gradually (see Figure 3.14 (c)).

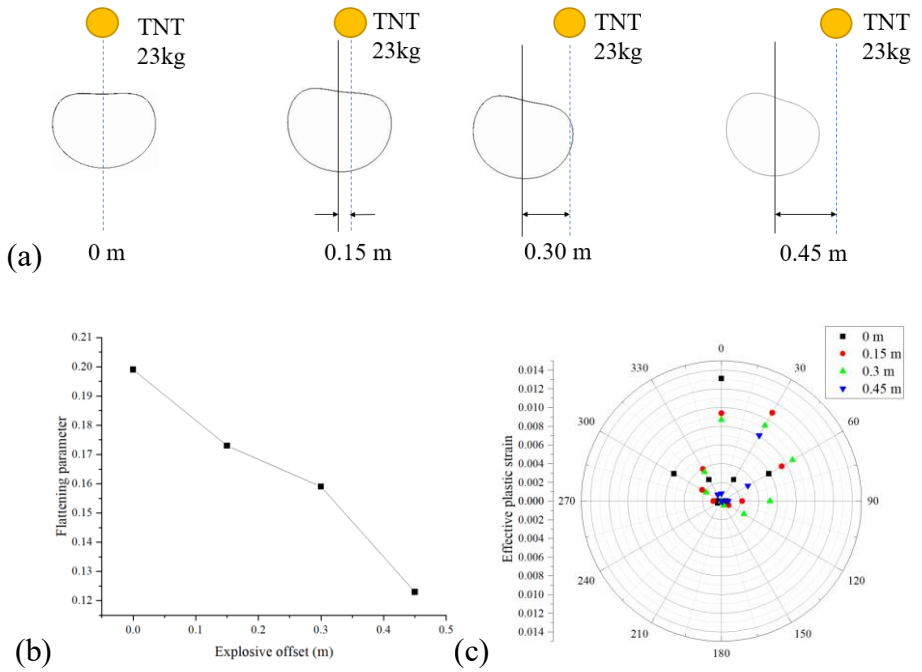

Figure 3. 14 Pipeline behaviour caused by explosive offset. (a) The cross-sectional deformation (b) cross-sectional flattening ratio and (c) effective plastic strain developed in wall

3.4.5 Pipe diameter

In this case, five different pipe diameters 350 mm, 450 mm, 550 mm, 660 mm and 860 mm were considered to evaluate the effect of pipe diameter on mechanical response of steel pipelines subjected to ground surface explosion. The pipe wall thickness was 5.56 mm and the buried cover was 760 mm with sandy loam. The 23 kg TNT was located above the pipe crown on the ground surface. The plastic strain peaked on the crown of the pipe. When the pipe diameter increased, the effective plastic strain increased. The effective plastic strain was 0.01 when the pipe diameter was 860 mm at the crown of the pipe, which was 1.05 times, 2.54 times, 2.61 times and 2.87 times greater than that for 660 mm, 550 mm, 450 mm and 350 mm pipe diameter, respectively. The cross-sectional flattening ratio was 0.24, which was 1.23 times, 3.23 times, 4.89 times and 9.64 times larger than that for 660 mm, 550 mm, 450 mm and 350 mm pipe diameter, respectively. Based on the failure criteria of ovalisation, when the pipe diameter was over 600 mm (with the same condition of pipe wall thickness, buried cover, soil types and charge weight), the pipeline was considered as structural failure at this time (see Figure 3.15 (b)).

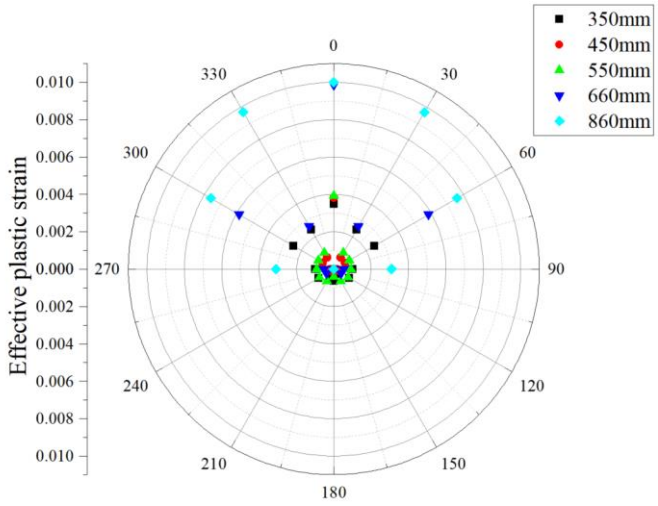

(a)

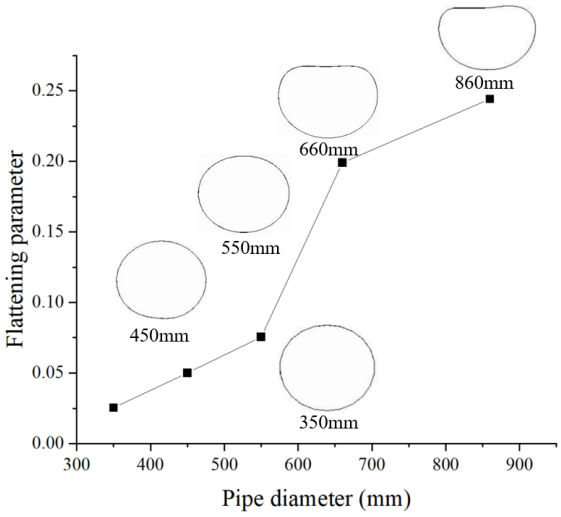

(b)

Figure 3. 15 Pipeline behaviour caused by different pipe diameters. (a) Effective plastic strain developed in wall and (b) the cross-sectional flattening ratio of pipeline

3.4.6 Pipe wall thickness

Pipe wall thickness was also important when analysing the mechanism of buried steel pipelines under blast loadings. Pipe wall thickness was set as 4.80 mm, 5.56 mm, 7.92 mm, and 8.7 mm as well as 12.7 mm in this section. The diameter of the pipe was 660 mm, buried cover was 760 mm, the steel grade was X52 and the magnitude of TNT was 23 kg in this case. As can be seen from Figure 3.16 (a) & (b), the decrease in pipe wall thickness resulted in a higher effective plastic strain on the pipe wall and a higher cross-sectional flattening ratio of pipelines. The effective plastic strain was approximately 0.03, which was 2.44 times, 2.89 times, 3.33 times and 8.48 times higher than that for 5.56 mm, 7.92 mm, 8.7 mm and 12.7 mm pipe wall thickness, respectively. The flattening ratio was 0.30 when the pipe wall thickness was 4.80 mm, which was 1.50 times, 2.50 times, 5.45 times and 38.07 times greater than that for 5.56 mm, 7.92 mm, 8.7 mm and 12.7 mm pipe wall thickness, respectively. Based on the failure criteria of ovalisation, when the pipe wall thickness was over 7.00 mm (with the same condition of pipe diameter, buried cover,

soil types and charge weight), the pipeline can retain normal operation (see Figure 3.16 (b)).

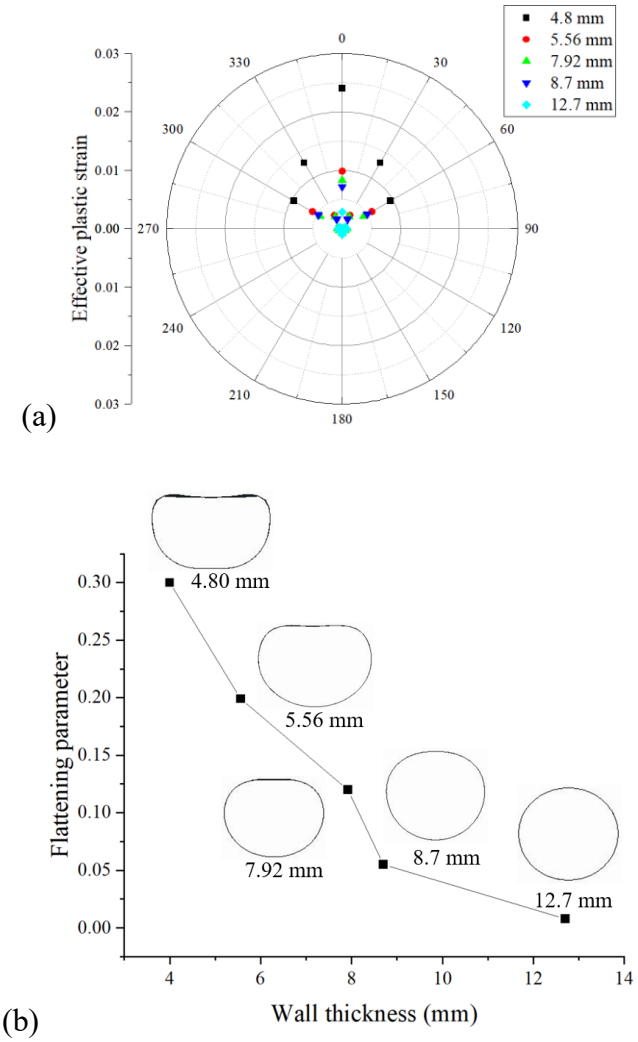

Figure 3. 16 Pipeline behaviour caused by different pipe wall thickness. (a) Effective plastic strain developed in wall and (b) the cross- sectional flattening ratio of pipeline

3.4.7 Buried depth

In this section, the effect of buried depth was investigated based on AS/NZS 2885:2018 *Pipeline - Gas and liquid petroleum* [163] and ATCO [13], which stated that the depth of burial pipeline cover ranged from 300 mm to 1800 mm in Australia in order to access in emergency situation. Therefore, the buried depth of pipelines was set as 300 mm, 760 mm, 900 mm, 1200 mm and 1800 mm. The diameter of the pipe was 660 mm, the wall

thickness was 5.56 mm and the steel grade was X52 in this case. The magnitude of TNT was 23 kg, which was located directly above the pipeline on the ground surface. With the increase in buried depth of pipes, the effective plastic strain distribution diminished significantly (see Figure 3.17 (a)). The effective plastic strain was 0.06 when the buried cover was 300 mm at the pipe crown, which was 83.5%, 94.2%, 98.6% and 100% higher than buried depth with 760 mm, 900 mm, 1200 mm and 1800 mm, respectively. The cross-sectional flattening of pipes was 0.743 when the buried depth was 300 mm, which approximately 5.0 times exceeded the maximum allowable ratio of ovalisation. The flattening ratios were 0.20, 0.075, 0.018 and 7.6E-5 when the buried depth was 760 mm, 900 mm, 1200 mm and 1800 mm, respectively.

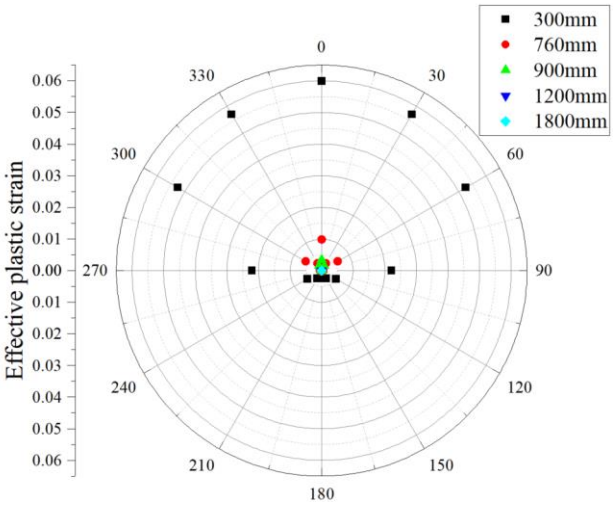

(a)

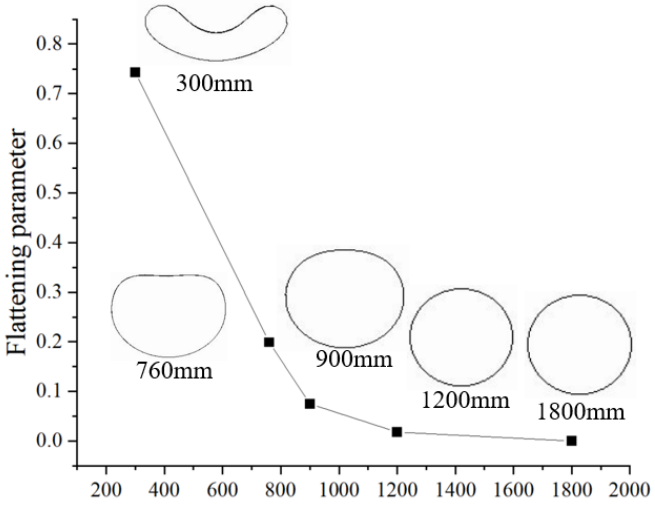

(b)

Figure 3. 17 Pipeline behaviour caused by various buried depths. (a) Effective plastic strain developed in wall and (b) the cross-sectional flattening ratio of pipeline

3.4.8 Steel material

Steel material was another important factor that affected the mechanical response of buried pipelines due to ground surface explosion. Five different steel material API X42, X52, X65, and X70 as well as X80 were explored with the same pipe diameter 660 mm, pipe wall thickness 5.56 mm, and buried depth 760 mm as well as the same soil type sandy loam under 23 kg TNT explosion. Different steel grades had different material properties (see Table 3.6). Due to the lower minimum yield of X42 steel, it demonstrated that the effective plastic strain was the highest of the five (see Figure 3.18 (a)). At the same time, the cross-section flattening ratio was 0.215, which was 1.08 times, 1.11 times, 1.33 times and 1.41 times greater than that for X52, X65, X70 and X80 steel, respectively (see Figure 3.18 (b)). The higher the steel grade, the lower cross-sectional flattening of the pipe. When the steel grade was X80, the flattening ratio was 0.15, which reached the maximum allowable ovalisation value, while the rest of the groups were considered as failures during the operation.

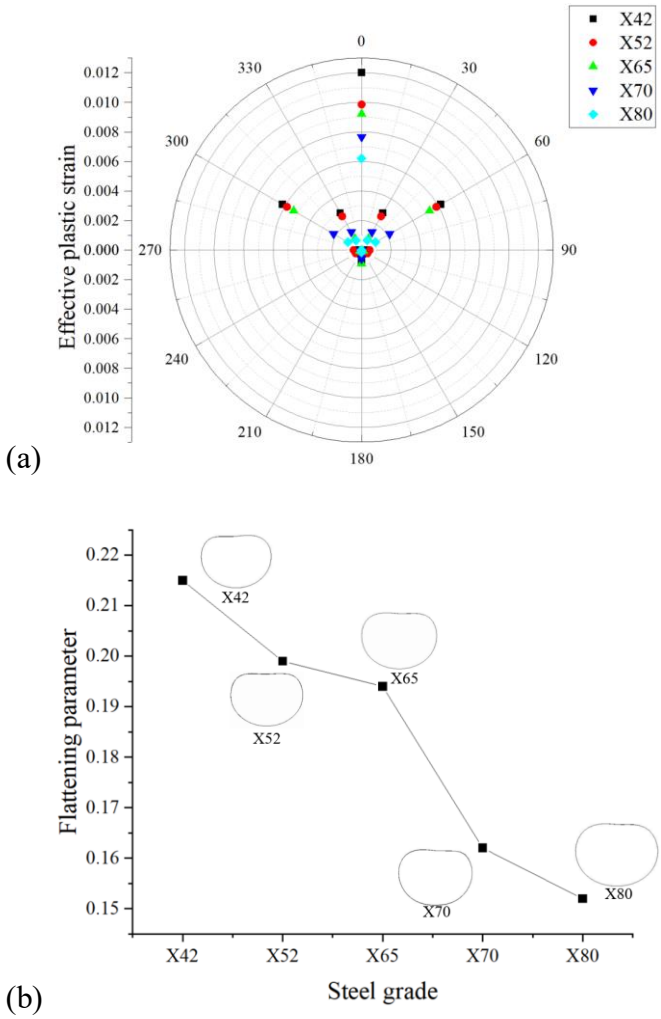

Figure 3. 18 Pipeline behaviour caused by various steel grades. (a) Effective plastic strain developed in wall and (b) the cross-sectional flattening ratio of pipeline

3.4.9 Soil types

The behaviour of the buried pipelines against ground surface explosion was also affected by different soil types. Three different soil types including sandy loam, soil medium and clay soil were considered in this case. The material properties such as soil density, shear modulus and bulk modulus for different soil types are listed in Table 3.5. Pipe diameter, wall thickness, buried depth, steel grade and charge weight were 660 mm, 5.56 mm, 760 mm, X52 and 23 kg, respectively. The clay soil demonstrated the highest effective plastic strain compared with soil medium and sandy soil, which was approximately 0.0775 (see Figure 3.19 (a)). This phenomenon was ascribed to the different water content for soil.

According to Wang et al, [49], the peak pressure and particle velocity in saturated soil were higher than those in unsaturated soil and the wave propagation speed in saturated soil was faster than that in unsaturated soil because of the deformation mechanism and three-phase soil structure. The cross-sectional flattening ratio was 0.35, which was 1.41 times and 1.76 times greater than that for soil medium and sandy loam, respectively (see Figure 3.19 (b)). All of three specimens were over the allowable ovalisation criteria, and clay soil was the worst. It could be inferred that different moisture contents in soil, soil density and other factors such as shear modulus and bulk modulus may aggravate the deformation of the pipeline, thus affecting the normal operation of the pipeline.

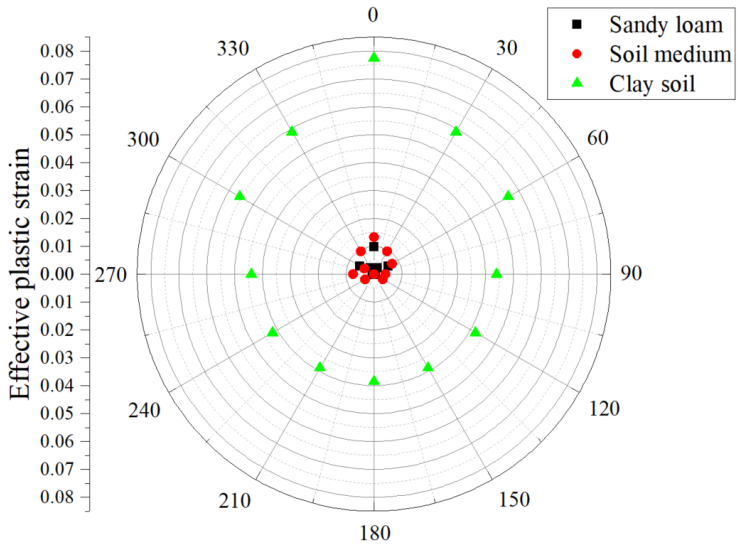

(a)

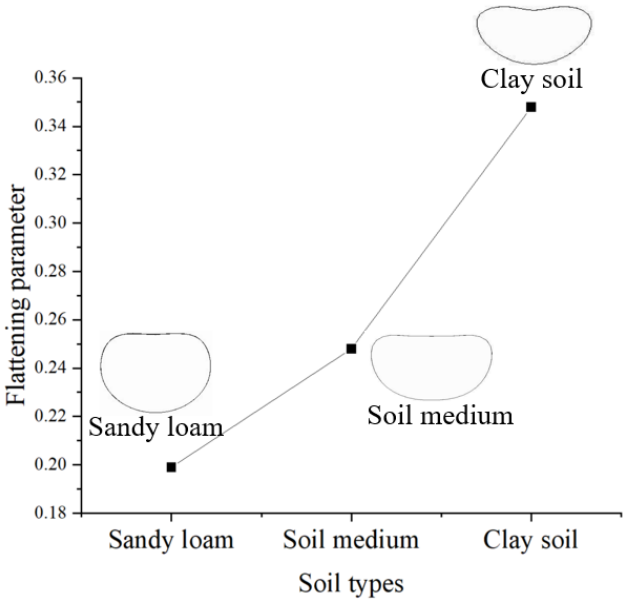

(b)

Figure 3. 19 Pipeline behaviour caused by different soil types. (a) Effective plastic strain developed in wall and (b) the cross-sectional flattening ratio of pipeline

3.5 Derivations of the empirical formula

To predict whether the pipeline structure was failure or not, an empirical formula was derived based on the simulation results above:

$$f = 3.98\left(\frac{W}{1000}\right) - 4.94\left(\frac{S}{10000}\right) - 3.95\left(\frac{D_{bd}}{10000}\right) + 2.73\left(\frac{\phi}{10000}\right) - 3.09\left(\frac{\delta}{100}\right) - 1.89\left(\frac{\sigma}{10000}\right) - 1.04\left(\frac{\rho}{10000}\right) + 1.20\left(\frac{G}{1000}\right) + 4.52\left(\frac{K_u}{100000}\right) + 0.606 \quad (3.12)$$

where f is the cross-sectional flattening ratio of pipeline; W stands for the magnitude of charge weight in kg; S is the stand-off distance in mm; D_{bd} represents the buried depth of pipe in mm; ϕ is pipe diameter in mm; δ is pipe wall thickness in mm; σ is the minimum yield strength for different steel grade in MPa ; while ρ, G and K_u are the soil properties, which stand for soil density (kg/m^3), shear modulus in MPa and bulk modulus in MPa, respectively.

The equation is applicable in cases in the following constraints: $2.3 < W < 227$ kg, $0 < S < 500$ mm, $300 < D_{bd} < 1800$ mm, $350 < \phi < 860$ mm, $4 < \delta < 12.7$ mm,

$290 < \sigma < 580$ mm, $1255 < \rho < 1963$ kg/m^3, $1.724 < G < 24$ MPa and $5.516 < K_u < 4673$ MPa.

Randomly select different values within the above range for different parameters and calculate the estimated flattening ratio of pipeline by using Equation (3.12). Figure 3.20 compares the numerical simulation data and the outcomes of the empirical formula. As can be observed, the curves and data match up well (R^2=0.76). Therefore, the flattening ratio of underground pipelines exposed to group surface explosion can be better predicted using this empirical formula.

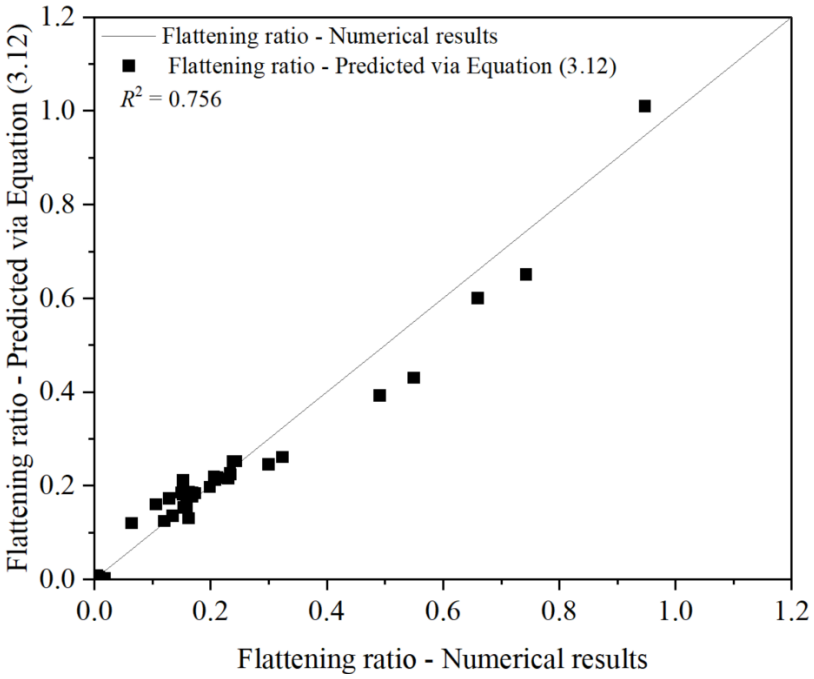

Figure 3. 20 Comparison of predicted flattening ratio to numerical results.

3.6 Limitations

Despite the comprehensive nature of this investigation, several limitations should be acknowledged. The empirical formula (Equation 3.12) is constrained to specific parameter ranges. The model primarily evaluated cross-sectional ovalisation as the failure criterion but did not account for alternative failure modes such as fracture propagation or joint failures. The simulation excludes aging effects, pre-existing damage, environmental

factors (temperature variations, groundwater conditions), and interactions between multiple pipelines or with other underground infrastructure. While the model demonstrated good correlation with experimental data within the tested range, full-scale field validation across all parameter combinations remains outstanding. Future research should address these limitations to enhance the robustness and applicability of the findings.

3.7 Summary

Steel gas pipelines play a very important role in urban energy distribution. Ground surface explosion is a main threat for urban buried steel pipelines. The behaviour of buried steel pipelines subjected to ground surface explosion was investigated in the present study. Failure criteria based on ovalisation were discussed. Parametric study was conducted to evaluate the effect caused by different factors, including charge weight, stand-off distance, pipe diameter, pipe wall thickness, buried cover, and steel grade as well as different soil types. The following inferences are made in light of this study:

- With increase in the internal pressure on the inner surface of the pipe, the damage of the pipe decreased in a certain extent. To get much more conservative results, the internal pressure was set as 0 in the present study.
- The maximum plastic strain and the maximum deformation were always located on the crown of the pipe if the explosive was taken place directly above the pipelines. The higher plastic strain distributed on the pipe, the more significant cross-sectional flattening ratio of the pipe.
- With increase in TNT magnitude and pipe diameter, the effective plastic strain distributed on pipe wall and flattening ratio increased. That means, buried

pipelines were much more dangerous when increasing the charge weight and pipe diameter.

- With increase in stand-off distance, pipe wall thickness and buried depth, the effective plastic strain distributed on pipe wall and flattening ratio declined.
- Due to the different steel properties such as the minimum yield strength and tensile strength for different steel grade, the plastic strain distribution and cross-sectional flattening ratio may be different. API X80 had a better performance against blast loadings, comparing with X42, X52, X65 and X70 when other parameters remained the same.
- Different soil types affected the mechanical response of buried pipelines subjected to blast loading, which was caused by different properties of soil such as moisture content, soil density, and shear modulus as well as bulk modulus.
- An empirical formula was established to predict the cross-sectional flattening ratio of the pipeline for further safety assessment and serviceability.

Chapter 4. EXPERIMENTAL STUDY ON DYNAMIC BEHAVIOUR OF NORMAL STRENGTH MORTAR AT CRYOGENIC TEMPERATURES AND AFTER FREEZE-THAW CYCLES

4.1 Introduction

Concrete structures employed for the storage of LNG currently undergo temperature as low as -170 °C. These critical engineering structures may also experience dynamic loads such as impact or explosion during service life. Therefore, it is crucial to explore the mechanical response of concrete at intermediate to high strain rates together with low temperatures or cryogenic FT cycles. This chapter presents experimental research into the combined effects of low temperatures and strain rate on normal strength mortar, providing a preliminary analysis of the dynamic performance of concrete at low and cryogenic temperatures. A Split Hopkinson Pressure Bar (SHPB) device was used to investigate the characteristics of dynamic compression (at strain rates of 40, 80, 120 and 160 s^{-1}) and dynamic split tension (at strain rates of 20, 40, 60 and 80 s^{-1}) of Normal Strength Mortar (NSM) at different low temperatures. In addition, the dynamic compression (at strain rates of 80, 130 and 180 s^{-1}) after cryogenic FT cycles was also explored. The findings revealed that the failure pattern of NSM samples exposed to coupled low temperature or cryogenic FT cycles and high strain rate loading notably varied from that observed under room temperature condition. Both the dynamic compressive and split tensile strengths of NSM increased with the strain rates at all temperatures. At -160 °C, the dynamic compressive and splitting tensile strengths of NSM specimens were greater than those at room temperature (by 10.94% and 28.29%, respectively) and -70 °C (by 3.13% and 4.12%, respectively). Cryogenic freeze-thaw cycles evidently impacted the material static and dynamic performance. An empirical model was developed to predict the dynamic

increase factors (DIFs) for both dynamic compression and splitting tensile strengths of NSM at low/cryogenic temperatures and after freeze-thaw cycles. Scanning electron microscopy (SEM) technique was performed to study and comprehend the microscopic processes and microstructural changes after FT cycles.

4.2 Details of experiment

4.2.1 Materials and specimen preparation

The mix proportion of NSM employed in this experiment is presented in Table 4.1. The particle size distribution of the sand used in this study is illustrated in Figure 4.1 and the sand passed through a 4.75 mm sieve. The physical and chemical properties of cement and coal ash are listed in Table 4.2. Polycarboxylate ether-based superplasticiser was utilised in mixtures to improve the flowability and workability of mortar. The mixture was poured into the Polyvinyl Chloride (PVC) tube mould with inner diameter of 70 mm. Following initial curing at room temperature (20 ± 2 °C) for 24 hours, the cylindrical specimens were taken out of the PVC tube. After a curing period of 28 days, the specimens were grounded flat on both ends to ensure uniform stress distribution during SHPB testing. The dimensions of the specimen in the dynamic experiment were 70 mm in diameter and 35 mm in height, which is depicted in Figure 4.2.

Table 4. 1 Mix composition of NSM (kg/m^3)

Cement	Water	Coal ash	Superplasticizer	Sand
893	370	70	3	850

Table 4. 2 Chemical composition and physical properties of Portland cement and coal ash.

Materials	Oxide composition % by weight								Physical properties	
	CaO	SiO_2	Al_2O_3	Fe_2O_3	MgO	SO_3	K_2O	Na_2O	Specific gravity	Avg. particle size (mm)
Cement	63.43	18.51	5.81	3.45	2.37	3.14	0.52	0.45	3.13	0.1
Coal ash	4.73	55.12	25.56	9.28	1.51	0.55	0.89	1.50	2.27	0.05

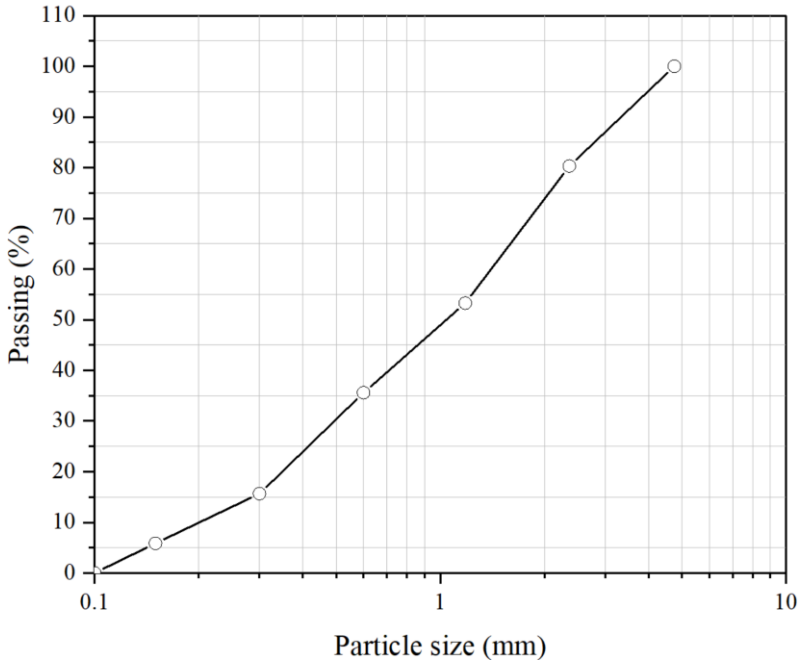

Figure 4. 1The sieving curve of the sand.

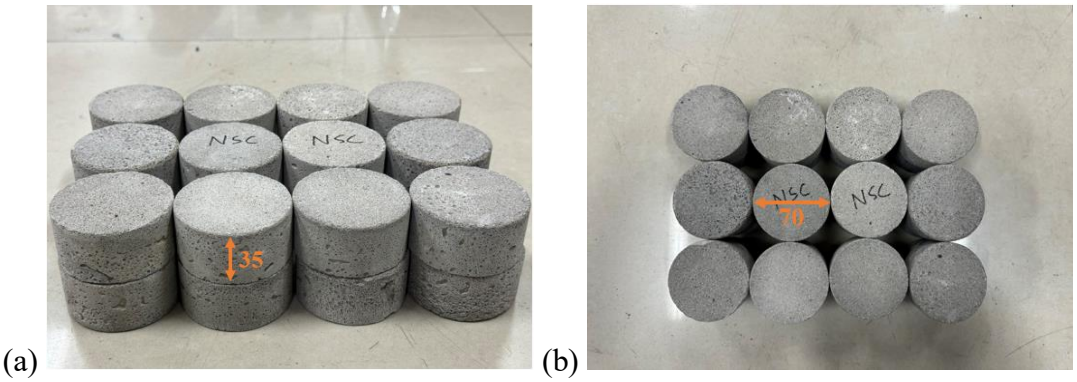

(a) (b)

Figure 4.2 Cylindrical samples after curing (unit: mm).

4.2.2 Experimental setup and methodology

4.2.2.1 Low-temperature test technology

In this experiment, the dynamic compression and splitting tension performance of NSM were investigated at low temperatures of -70 °C and -160 °C. To achieve the desired temperature, the specimens were initially placed inside a low-temperature cooling chamber (depicted in Figure 4.3(a)). The inner cooling area of the chamber measured 383 × 228 × 150 mm in length, width and height (as depicted in Figures 4.3(b) and (c)), and had the capacity to accommodate 16 specimens simultaneously. Subsequently, the liquid nitrogen Dewar valve was opened, and liquid nitrogen (with a temperature of -196 °C) was gradually introduced into the insulation box, maintaining a cooling rate of 1 °C per minute. The cooling rate could be precisely regulated by a temperature controller, and the temperature change inside the low-temperature chamber was monitored and recorded (refer to Figure 4.4). Upon reaching the target temperature, it retained constant for 4 hours to ensure uniform internal and external temperatures of the specimens [164]. Following this, the specimens were expeditiously affixed within the SHPB device to conduct dynamic compressive and splitting tensile experiments.

In terms of the cryogenic FT cycles, specimens were placed in the low-temperature chamber with cooling rate 1 °C/min and stayed for 4 hours after reaching the target temperature. Subsequently, the specimens were removed from the chamber and stored indoors at ambient temperature for 24 hours to ensure complete thawing and thermal equilibrium. Herein, one complete FT cycle was defined as the process of cooling the specimen from room temperature down to -160 °C and then allowing it to return to room temperature. The experiment was conducted by varying FT cycles, specifically 2, 4 and 8 cycles, to examine the cumulative effects of repeated cryogenic temperature exposure on the specimens.

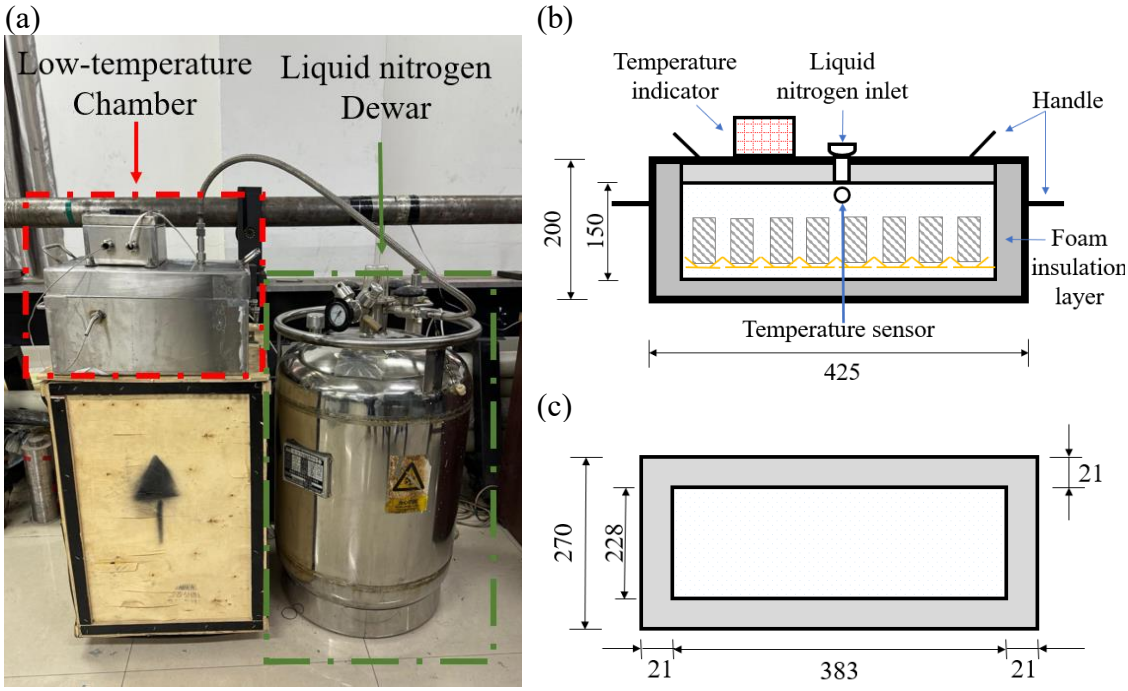

Figure 4.3 Test setup of NSM at low temperature (a) Cryogenic cooling system (b) Front view of low-temperature chamber (c) Top view of low-temperature chamber (unit: mm).

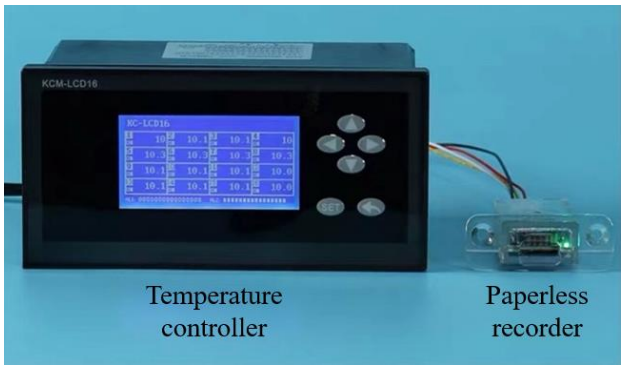

Figure 4.4 Temperature controlled and paperless recorder.

4.2.2.2 Static compressive and splitting tensile test of NSM

The mortar specimens, measuring 70 mm in diameter and 35 mm in height, underwent uniaxial compressive and splitting tensile tests to obtain the basic mechanical properties at 20, -70, and -160 °C. Similarly, the uniaxial compressive strengths of specimens after 2, 4 and 8 number of cryogenic FT cycles (from 20 to -160 °C) were explored. The experiments were carried out by utilising a 300-ton hydraulic testing machine, with

loading applied at a speed of 0.5 mm/min. For the splitting tensile test, the cylindrical specimens were positioned horizontally between the loading surfaces of the compression testing machine. A compressive load was applied along the length of the cylinder with 0.02 mm/min loading rate, diametrically across its width, until the specimen underwent failure by splitting vertically along its diameter.

4.2.2.3 Dynamic compression and splitting tensile test

The experiment involved different strain rates for compressive and splitting tensile tests: 40, 80, 120, and 160 s^{-1} for compression, and 20, 40, 60, and 80 s^{-1} for splitting tensile test at 20, -70, and -160 °C, as well as dynamic compressive test with strain rate 80, 130 and 180 s^{-1} after 2, 4 and 8 number of cryogenic FT cycles. Figure 4.5 illustrates the setup for dynamic compressive and splitting tensile SHPB tests. The SHPB bar had a diameter of 100 mm and a striker bar length of 500 mm. To enhance the rise time of the incident wave, a pulse shaper was placed between the striker bar and the incident bar as a waveform shaper (refer to Figure 4.6) to facilitate the attainment of a uniform stress state within the specimens during dynamic loading, enhancing experimental accuracy and reliability. The strain gauges should be installed at a distance at least 10 times of the bar diameter from the initial impact point [165]. In this experiment, the strain gauges were placed at the midpoint of the bar. Strain gauges captured stress wave pulses throughout the testing procedure. Utilising SHPB experimental data, the stress-strain relationship can be derived using the equations [166-168] as below.

$$\sigma = \frac{EA_e}{A_s}(\varepsilon_i + \varepsilon_r + \varepsilon_t) \tag{4.1}$$

$$\varepsilon(t) = -\frac{2C_0}{L}\int_0^t \varepsilon_r(t)dt \tag{4.2}$$

$$\dot{\varepsilon}(t) = -\frac{2C_0}{L}\varepsilon_r(t) \tag{4.3}$$

where σ is the stress acting at the interface region between the specimen and the loading bar; E denotes the elastic modulus of the incident/transmission bars; A_e and A_s represent the cross-section area of the pressure bar and specimen, respectively. $\varepsilon_i, \varepsilon_r$ and ε_t are the incident, reflected, and transmitted wave pulses, respectively. C_0, L and t denote the velocity at which the longitudinal wave propagates along the incident/transmission bars, the initial length of the specimen and time, respectively.

Unlike dynamic compressive testing, during dynamic splitting tensile testing, the specimen was placed radially, with the incident bar and the transmitting bar gripping the two sides of the specimen, respectively. Considering that during the splitting test, a line surface contact between the sample and the bar weakened the transmitted wave signal, a semiconductor strain gauge with a higher sensitivity coefficient was installed on the transmitted bar. Simultaneously, a pair of resistance strain gauges were attached to the transmission bar to calibrate the sensitivity coefficient of the semiconductor strain gauges. Based on the one-dimensional stress wave theory, stress, strain and strain rate can be derived for the SHPB splitting tensile test as follows.

$$\sigma = \frac{2P(t)}{\pi DL} = \frac{2EA_e\varepsilon_t(t)}{\pi DL} \tag{4.4}$$

$$\varepsilon(t) = -\frac{2C_0}{D}\int_0^t \varepsilon_r(t)dt \tag{4.5}$$

$$\dot{\varepsilon}(t) = -\frac{2C_0}{D}\varepsilon_r(t) \tag{4.6}$$

where D represents the initial diameter of the specimen and other parameters have mentioned above.

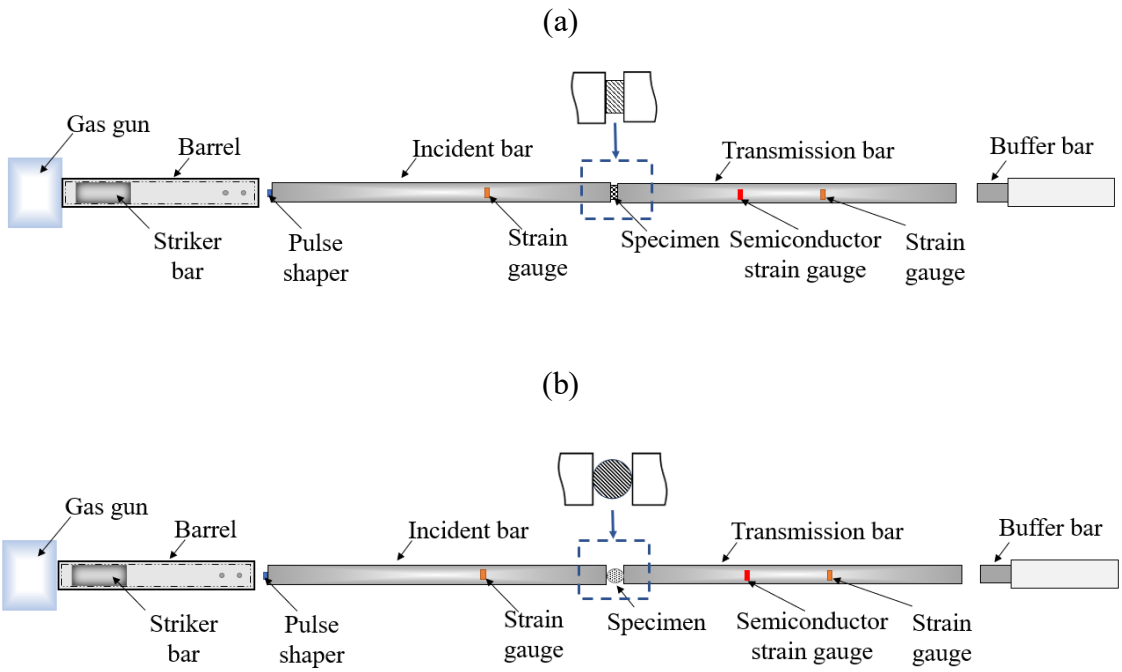

Figure 4. 5 Dynamic testing schematic (a) Compression test (b) Splitting tensile test.

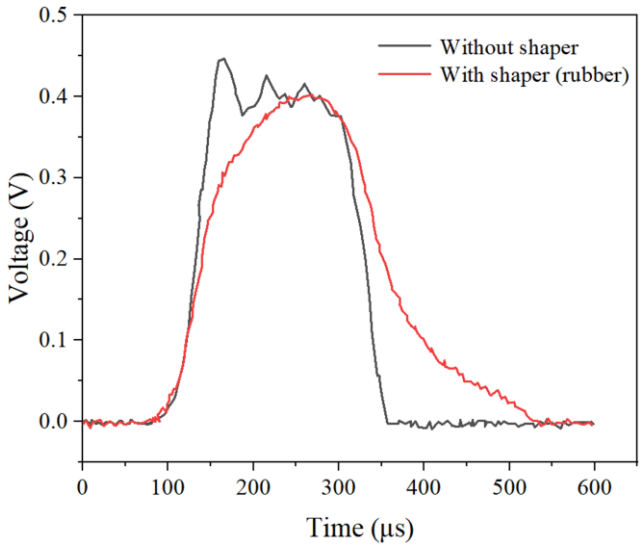

Figure 4.6 Influence of pulse shaper on incident wave.

During testing, an ultra-high-speed video camera at frame rates of 5 million frames per second was utilised to capture the behaviour of concrete samples (see Figure 4.7). The ultra-high-speed video camera replicated the failure processes for NSM specimens under various temperature and strain rate conditions and provided a wealth of qualitative information. By directly observing the damage progression, crack propagation and fragmentation patterns, it could gain critical insights that complemented the quantitative

data from the mechanical tests. This comprehensive visual documentation, paired with the comprehensive mechanical test data, enabled a holistic understanding of the complex interactions between temperature, strain rate and the failure mechanisms of concrete materials.

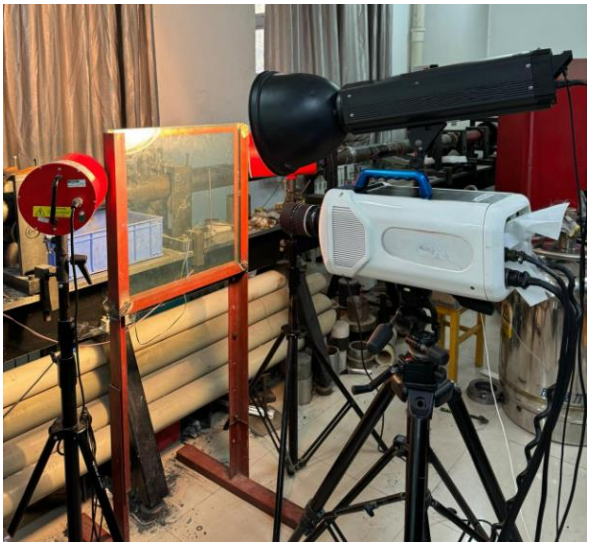

Figure 4. 7 High-speed video camera.

4.3 Experimental results and discussions

4.3.1 Static compressive and tensile behaviour of NSM

The results of uniaxial compressive and splitting tensile strength for NSM at 20, -70, and -160 °C were determined using static tests in Section 4.2.2.2. The static test results at various temperature are listed in Table 4.3. When the testing temperature dropped from 20 °C to -70 and -160 °C, the compressive strength was almost linearly increased from 35.26 MPa to 43.19 and 51.76 MPa, with increase of 22.4% and 46.80%, respectively. Likewise, as the temperature declined from 20 °C to -70 and -160 °C, the splitting tensile strength rose from 2.52 MPa to 2.81 and 3.10 MPa, respectively, rendering an increase of 11.5% and 23.02%. 67, which declined by 5.7%, 14.6% and 27.28% as compared to the room temperature. In terms of static test after cryogenic FT cycles, the uniaxial compressive strength was 33.25, 30.11 and 25.64 MPa after 2-, 4- and 8-times FT cycles,

which declined by 5.7%, 14.6% and 27.28% as compared to the room temperature (see Table 4.4). The uniaxial compressive stress-strain curve of NSM under low temperature and after FT cycles is presented in Figure 4.8.

Table 4. 3 Static test results under low temperature.

Temperature (℃)	Uniaxial compressive strength (MPa)	Splitting tensile strength (MPa)
20	35.26	2.52
-70	43.19	2.81
-160	51.76	3.10

Table 4. 4 Static test results after cryogenic FT cycles.

Number of FT cycles	Uniaxial compressive strength (MPa)
2	33.25
4	30.11
8	25.64

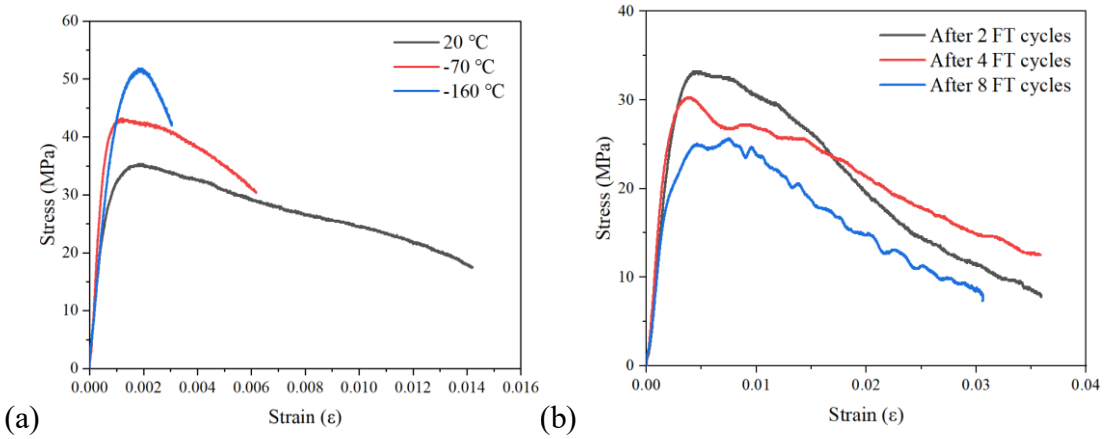

(a) (b)

Figure 4.8 Uniaxial compressive stress-strain curve of NSM. (a)under different low temperatures (b) after various FT cycles.

4.3.2 Dynamic compressive strength under low temperature

4.3.2.1 Damage mode of specimens subjected to combined loading

Under combined loading conditions at temperatures of 20, -70 and -160 °C together with strain rates of approximately 40, 80, 120 and 160 s^{-1}, remarkable variations in the damage appearance of the specimens were observed, indicating a correlation between temperature and strain rate. Figure 4.9 displays the damage forms of NSM at various strain rates under temperatures of 20, -70, and -160 °C, respectively. It was evident that the damage phenomenon of NSM became more pronounced with rising strain rate, and the crushed pieces of damaged concrete gradually decreased in size at the same temperature. The main reason for this phenomenon was that the water freeze forming an ice mesh acted as an internal reinforcement, helping to resist the propagation of cracks and damage through the material. The prestressed state induced by the ice veins can delay or impede the initiation and growth of cracks at lower temperatures. The stiffness of the material increased at lower temperatures, rendering it more resistant to deformation and damage.

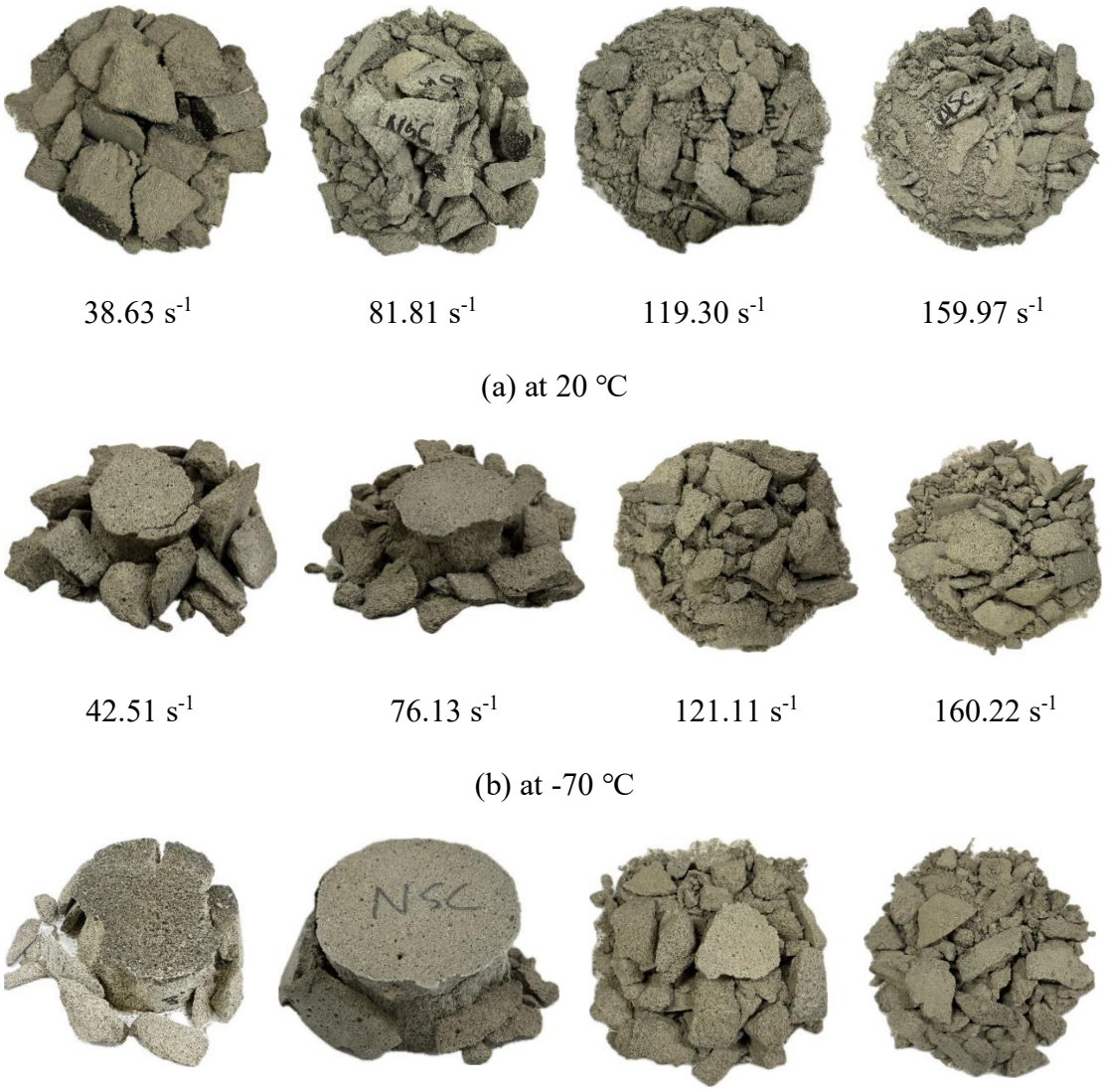

Figure 4. 9 Dynamic compressive failure modes of specimens at different temperatures.

To further elucidate the damage evolution and deformation mechanisms of the specimens under combined loading conditions of varying temperatures (20, -70, and -160 °C) and strain rates (about 40, 80, 120 and 160 s^{-1}), detailed images of the testing process were captured using the ultra-high-speed video camera. Figure 4.10 displays the dynamic failure of NSM specimens at temperatures of 20, -70 and -160°C, respectively, along with a strain rate of around 80 s^{-1}. As compared to the specimens underwent failure at -70 °C,

the longitudinal splitting of specimens experienced failure at 20 °C was more severe. It was noteworthy that at -160 °C, the number and depth of cracks were more significant and apparent in comparison with room temperature and -70 °C, as shown in Figure 4.10(c). This phenomenon, combined with Figure 4.9(c), at which the strain rate was 79.38 s^{-1}, suggested that the stiffness of NSM specimens at -160 °C was high, essentially retained the original appearance after the impact, but accompanied by its more brittle characteristics. This observation aligned with the conclusions drawn by Yan and Xie [114] regarding the low-temperature performance of concrete. In general, when the compressive strength of the material rose, the specimen became more brittle. The temperature gradually decreased, the compressive strength of the specimen improved, thus exhibiting brittleness.

In fact, concrete at -160 °C was more brittle than at -70 °C owing to the water freeze in pores. At -160 °C, more water in the concrete pores froze than at -70 °C. The water-to-ice phase transition resulted in a volume expansion of around 9% as mentioned above, which induced hydraulic pressure and stresses at the ice-pore interfaces [169]. This produced damage and cracks in the concrete microstructure, leading to increased brittleness. In addition, in accordance with Zhang *et al.* [169], temperatures of -90 °C and lower led to a reduction in the quantity of larger pores and an increase in the quantity of smaller pores. This was because the large pores were collapsed or filled due to the inward deformation caused by the uneven contraction and expansion between different concrete constituents at ultra-low temperatures. The loss of these larger pores rendered the concrete more brittle. Furthermore, Jiang *et al.* [170] stated that thermal expansion mismatch was also a main reason causing the brittleness at lower temperatures. The thermal expansion coefficients of the concrete components were different from those of ice. As the temperature declined further from -70 to -160 °C, the inconsistent thermal deformations

between these materials accumulated, resulting in higher internal stresses and cracking, which increased the brittleness.

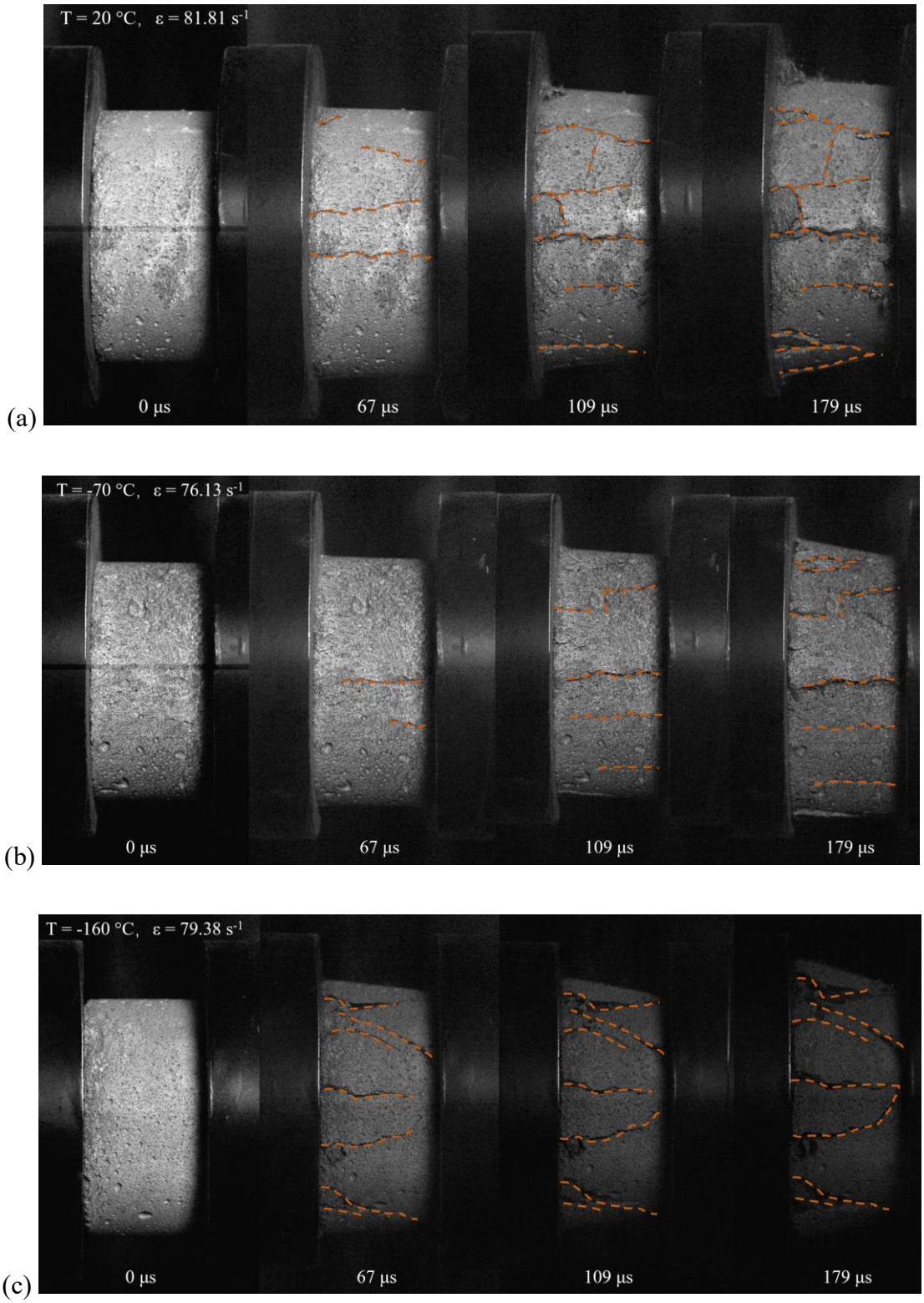

Figure 4.10 Compression failure process of specimens under different temperature. (a) at room temperature (b) at -70 °C (c) at -160 °C

4.3.2.2 Influence of low temperature on the dynamic compressive strength

Figure 4.11 illustrates stress-strain curves with different strain rate at 20, -70 °C and -160 °C. It revealed a consistent trend wherein the dynamic compressive strength of concrete exhibited an upward trajectory as the average strain rate increased. Under room temperature conditions, for instance, the dynamic strength of NSM specimens exhibited signal enhancements in contrast with those subjected to lower strain rates. Specifically, when the strain rate escalated from 40 s^{-1} to 80, 120 and 160 s^{-1}, the dynamic compressive strength experienced increments of 5.27%, 18.02% and 23.91%, respectively. This trend retained consistent across varying temperatures. In environments as extreme as -70 and -160 °C, the dynamic compressive strength also showcased notable improvements with escalating strain rates. For example, at -70 °C, the strength increased by 10.53%, 24.33% and 28.60% at 80, 120 and 160 s^{-1}, respectively, when compared to 40 s^{-1}. Similarly, at -160 °C, the strength rose by 4.10%, 17.22% and 22.57% with the same increment in strain rates. These data indicated that at the identical temperature, the dynamic strength of concrete dramatically increased with strain rate.

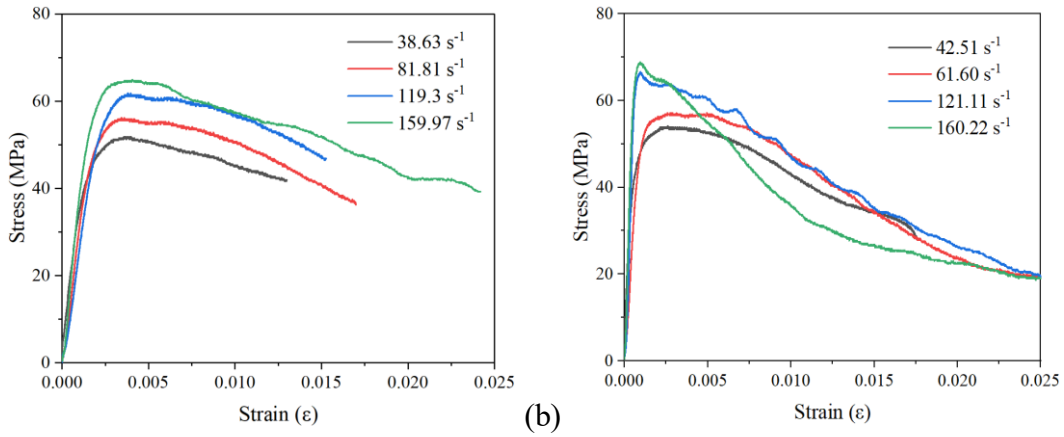

(a) (b)

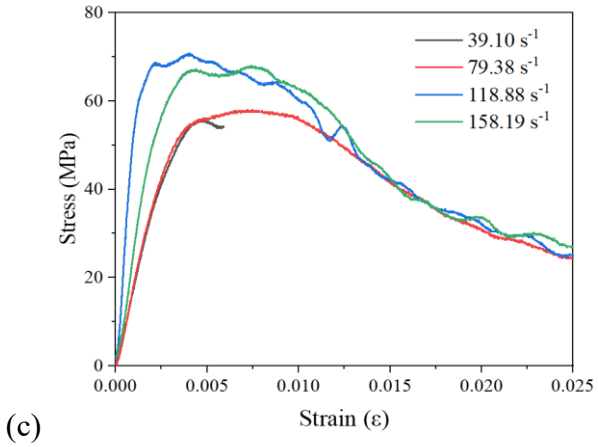

(c)

Figure 4.11 Compression strain-stress curve at different temperatures with various strain rates. (a) at 20 ℃ (b) at -70 ℃ (c) at -160 ℃.

Studying the elastic modulus of NSM under dynamic experiments held significant importance as it constituted a vital mechanical characteristic of concrete materials. Figure 4.12 shows a comprehensive overview of the dynamic compressive strength and elastic modulus variations observed in NSM specimens subjected to different temperatures and strain rates. It was evident that, at the same average strain rate, the dynamic compressive strength gradually increased with decreasing temperature. The elastic modulus representing the proportional relationship between stress and strain could be estimated through the slope between 30% and 50% of the peak strength from Figure 4.11. Notably, at the same average strain rate, the elastic modulus at -70 °C was greater than that at room temperature and -160 °C. For instance, at an average strain rate of 80 s^{-1}, the elastic modulus at -70 °C was 1.76 times that that at room temperature and 1.98 times than that at -160 °C. When the average strain rate was up to 160 s^{-1}, the elastic modulus at -70 °C was 1.56 times and 1.01 times greater than that at 20 and -160 °C, respectively. Similar findings have been observed in low-temperature static tests conducted by a few scholars [169, 171]. Zhang *et al.*[169] explained this phenomenon by employing CT scanning to explore the microstructural alterations of concrete before and after exposure to low temperatures. It was noted that as temperatures declined within the -90 to -30 °C range,

the elastic modulus enlarged due to the transition of a substantial volume of nanoscale pores' water to ice. However, when temperatures plummeted below -90 °C, these pores were entirely filled with ice, resulting in the formation of thermal cracks at the interfaces of ice and cement paste. Consequently, as temperatures decreased, the elastic modulus diminished.

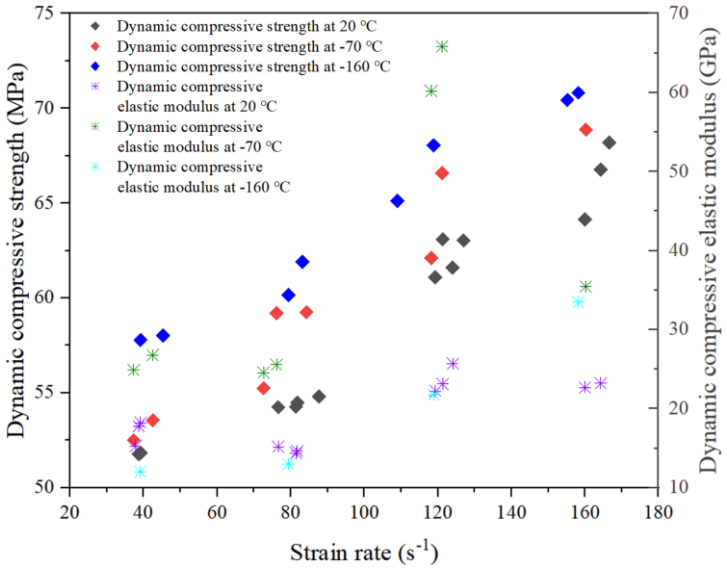

Figure 4.12 Dynamic compressive strength and elastic modulus variation with temperature and strain rate.

4.3.3 Dynamic splitting tensile strength under combined loading

4.3.3.1 Damage mode of specimens subjected to combined loading

Under various combinations of loading conditions with strain rates ranging from 20 to 80 s^{-1} and temperatures of 20, -70, and -160 °C, significant changes in the dynamic splitting damage appearance of the specimens were observed, indicating a clear relationship between temperature and strain rate. Figure 4.13 presents the damage patterns of NSM under dynamic splitting tension in different temperatures and strain rate scenarios. Specifically, at a strain rate of around 20 s^{-1}, secondary micro-cracks as well as small triangular fracture zones emerged at both ends of the specimen along the centre main crack, leading to its division into two parts. With further increase in strain rate, the

triangular fracture area expanded gradually at both ends of the sample, accompanied by increased overall deformation. Notably, comparative analysis revealed that at equivalent strain rates, the damage severity at -70 °C surpassed that at room temperature.

18.92 s^{-1} 41.08 s^{-1} 59.38 s^{-1} 81.14 s^{-1}

(a) at 20 ℃

21.39 s^{-1} 37.95 s^{-1} 60.86 s^{-1} 78.02 s^{-1}

(b) at -70 ℃

24.99 s^{-1} 41.26 s^{-1} 58.06 s^{-1} 78.97 s^{-1}

(c) at -160 ℃

Figure 4.13 Dynamic splitting tensile failure modes at different temperatures.

When subjected to a temperature of -160 °C, the specimen exhibited increase brittleness as compared to its behaviour at room temperature. This heightened brittleness is clearly illustrated in Figure 4.14, which depicted the dynamic fracturing process of NSM specimens under varying temperatures (20, -70, and -160 °C) with a strain rate of nearly 60 s^{-1}, captured using the ultra-high-speed video camera. At 55 µs, a primary crack formed along the loading and transmission rod directions. Notably, at -160 °C, the crack observed in the specimen was considerably larger than those observed at room temperature and -70 °C. Furthermore, secondary micro-cracks as well as small triangular fracture zones developed at the ends of the specimen along the primary crack, and the extent of damage intensified with time.

(a)

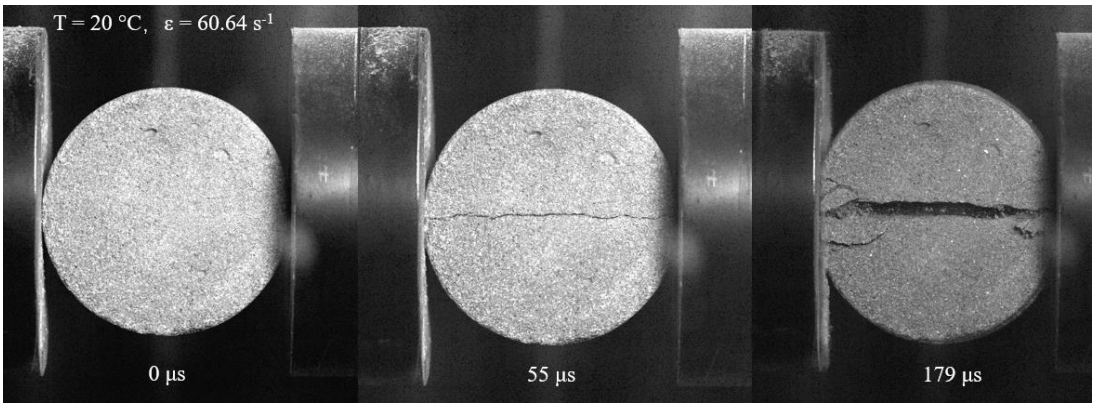

(b)

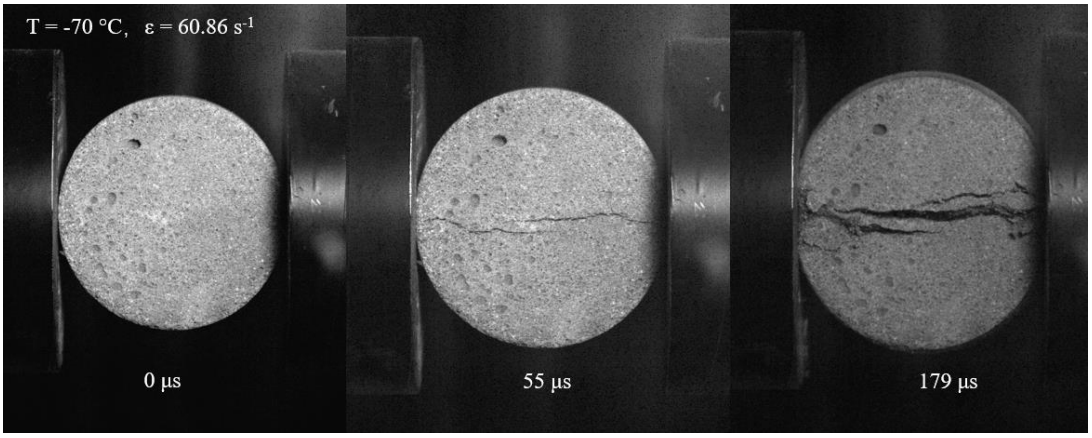

(c) 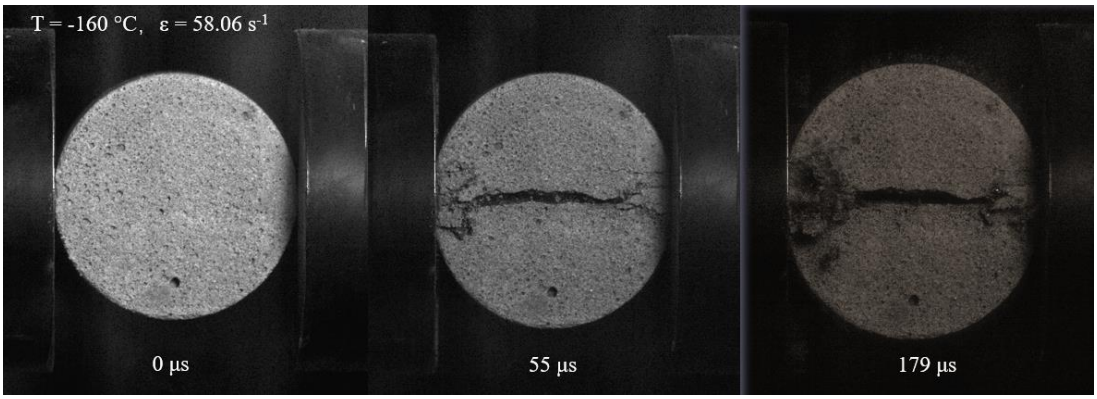

Figure 4.14. Splitting tensile failure process of specimens under various temperatures. (a) at ambient temperature (b) at -70 °C (c) at -160 °C.

4.3.3.2 Influence of low and cryogenic temperature on dynamic splitting tensile strength

The peak splitting tensile strength obtained from dynamic splitting tests at temperatures of 20, -70 and -160 °C along with strain rates of 20, 40, 60 and 80 s^{-1} is depicted in Figure 4.15. It was observed that at the same temperature, the splitting strength increased with strain rate. More specifically, at room temperature, the splitting strength increased by 17.03%, 21.44% and 31.40% when the strain rate rose from approximately 20 s^{-1} (18.92 s^{-1}) to 40 s^{-1} (41.08 s^{-1}), 60 s^{-1} (59.38 s^{-1}) and 80 s^{-1} (81.14 s^{-1}), respectively. At -70 °C, the splitting strength increased by 25.36%, 45.07% and 51.58%, with the strain rate increasing from approximately 20 s^{-1} (21.39 s^{-1}) to 40 (37.95 s^{-1}), 60 (60.86 s^{-1}) and 80 s^{-1} (78.02 s^{-1}), respectively. Likewise, at -160°C, the splitting strength escalated by 13.35%, 27.57% and 35.74% as the strain rate increased from approximately 20 s^{-1} (24.99 s^{-1}) to 40 (41.26 s^{-1}), 60 (58.06 s^{-1}) and 80 s^{-1} (78.97 s^{-1}), respectively. Overall, these findings revealed that both temperature and strain rate visibly influenced the dynamic splitting strength of concrete, with lower temperatures and higher strain rates generally leading to higher splitting strength. Additionally, the rate and magnitude of strength increase varied with temperature, indicating complex temperature-dependent behaviour in dynamic splitting strength.

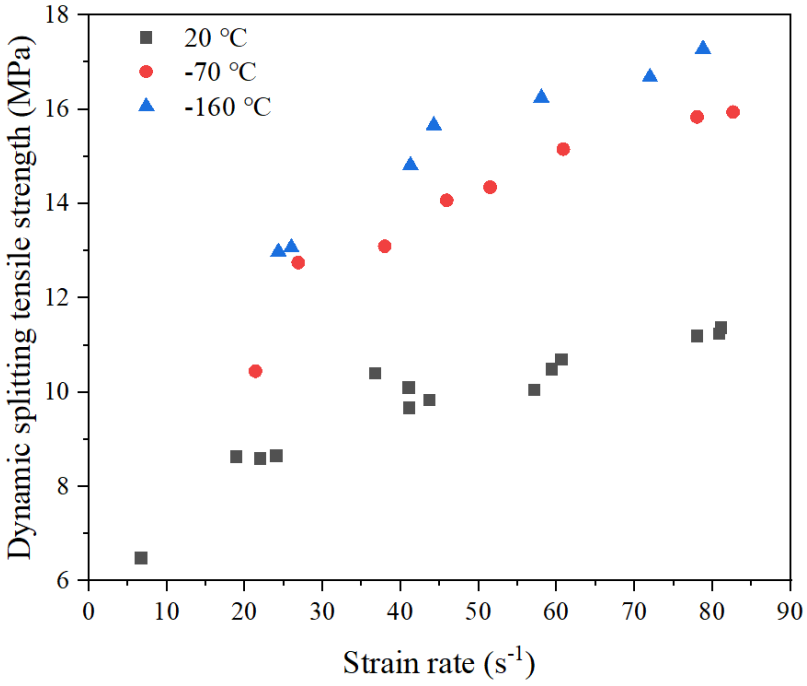

Figure 4. 15 Dynamic splitting tensile strength at different temperatures.

4.3.4 Dynamic behaviour NSM after cryogenic FT cycles

Understanding the dynamic behaviour of NSM subjected to cryogenic temperatures and FT cycles was essential for ensuring the safety and durability of structures cryogenic environments. In the current study, the dynamic compressive behaviour after 2, 4 and 8 FT cycles in the temperature range from -160 to 20 ℃ at high strain rate of 80, 130 and 180 s^{-1} was investigated. Figure 4.16 presents dynamic compressive strain-stress curves for mortar experienced different numbers of FT cycles. Figure 4.16(a) shows the strain-stress curves after 2 FT cycles, with strain rates of 82.76, 131.36 and 185.44 s^{-1}, whose peak strength was 51.53, 56.06 and 66.80 MPa, respectively. Figure 4.16(b) exhibits the strain-stress plots subsequent to 4 FT cycles, showcasing strain rates of 79.29, 127.77 and 175.17 s^{-1}, corresponding to peak strengths of 52.55, 53.79 and 62.72 MPa, respectively. Figure 4.16(c) illustrates the strain-stress curves following 8 FT cycles, featuring strain rates of 82.96, 128.56 and 180.29 s^{-1}, with peak strengths of 52.61, 54.19 and 58.46 MPa, respectively. A further reduction in peak stress can be observed with increased number

of cryogenic FT cycles and a more gradual softening behaviour as compared to after 2 and 4 FT scenarios. For example, the dynamic compressive strength at strain rate around 180 s^{-1} approximately reduced by 8.30% and 14.57% after 4 and 8 FT cycles, as compared to after 2 FT cycles.

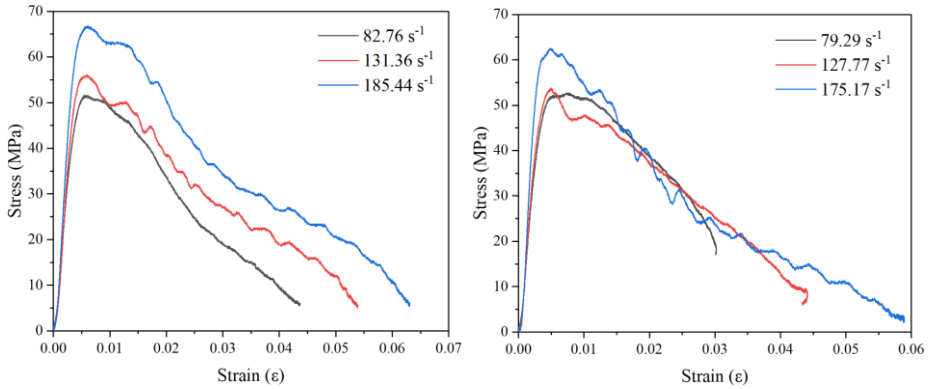

(a) 2 FT cycles (b) 4 FT cycles

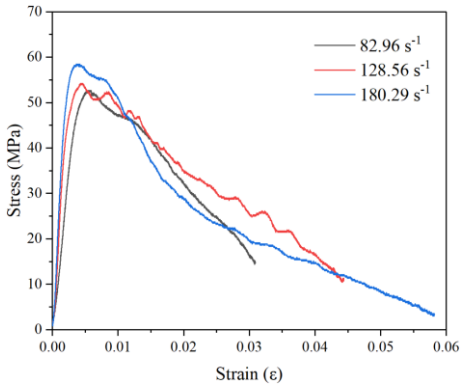

(c) 8 FT cycles

Figure 4. 16 Dynamic compressive strain-stress curve after various number of FT cycles.

4.3.5 Strain rate sensitivity

4.3.5.1 Dynamic increase factor at low temperature

The influence of loading rate on material behaviour can be effectively quantified by the DIF at various strain rates. The DIF expresses the ratio of the material's strength under dynamic loading (e.g., impact or blast) to its static strength. This concept examines the

material response and identifies the critical loading rates experienced during high-velocity events.

The dynamic increase factor in compression (CDIFs) and dynamic increase factors in split tension (TDIFs) with temperature were examined, and an empirical formula was proposed to evaluate CDIFs and TDIFs of concrete at low temperatures in the range of 20 to -160 °C.

Extensive research has been done to explore the DIF of concrete material at ambient temperatures, such as CEB-FIP [172], Malvar and Crawford [173], Malvar and Ross [174] and Bischoff and Perry [175] etc. The DIF equation in compression for CEB-FIP [172] at 20 °C can be expressed as Equations (4.7) and (4.8). The equation demonstrated a bilinear relationship between DIF and the logarithm of strain rate, with a change in slope happening at a strain rate of 30 s^{-1} with strain rate up to 300 s^{-1}.

$$DIF = \left(\frac{\dot{\varepsilon}}{\varepsilon_s}\right)^{1.026\alpha} \quad \text{for } \dot{\varepsilon} \leq 30\ s^{-1} \tag{4.7}$$

$$DIF = \gamma\left(\frac{\dot{\varepsilon}}{\varepsilon_s}\right)^{1/3} \quad \text{for } \dot{\varepsilon} > 30\ s^{-1} \tag{4.8}$$

where ε_s is equal to 3×10^{-6} s^{-1}, $\alpha = \frac{1}{10+6f'_c/10}$ and f'_c is uniaxial compressive strength in MPa, $\gamma = 10^{(7.11\alpha-2.33)}$.

Grote *et al.* [176] conducted an experiment to analyse CDIF of mortar specimens whose diameter was 12.7 mm with a high strain rate from 250 to 1700 s^{-1}, as shown in Figure 4.17. In addition, Zhang *et al.* [177] carried out CDIF of mortar with a specimen diameter of 37 mm. Chen *et al.* [178] also conducted a SHPB test to explore CDIF of mortar with a specimen diameter of 75 mm. It revealed that the strain rate sensitivity was lower for mortar as compared to NSC. Hao *et al.* [179] stated that increasing the volume fraction

and size of aggregates in concrete led to higher heterogeneity, which resulted in a higher CDIF under high strain rates in contrast with concrete without or with smaller aggregates.

The data provided by Zhang *et al.* [177] and Chen *et al.* [178] were utilised for comparative analysis and validation. It could be observed that the experimental data at room temperature agreed well with the results from Zhang *et al.* [177] and Chen *et al.* [178], as shown in Figure 4.17. Additionally, as the temperature decreased, the CDIFs also decreased. Specifically, at -70 °C and -160 °C, the CDIFs decreased by 13.45% and 22.81%, respectively, as compared to room temperature when considering a specific strain rate of 120 s^{-1}. This indicated that the sensitivity of concrete to loading rate decreased significantly at cryogenic temperatures as compared to room temperature. As the temperature declined, the compressive strength of concrete exhibited an increasing trend, whereas the CDIF displayed a decreasing pattern, lending support to the notion that the higher strength of the material was, the lower degree of rate sensitivity exhibited.

Moreover, this phenomenon could be explained by the formation of ice within the pore formation of the mortar. There was no ice in the pores of the mortar at ambient temperature. The behaviour of this material depended on its inherent characteristics, and the compressive strength was mainly influenced by the mortar composition and the strain rate applied during the testing process. While the temperature dropped to -70 °C, water in the mortar pores began to freeze, forming ice. The compressive and splitting strengths of ice were approximately 25 MPa and 3.1 MPa [180], which were similar to the static strength of mortar. The presence of ice raised the overall stiffness of the mortar. As the temperature of ice dropped from -15 to -125 °C or lower, the CDIF decreased [181]. However, at this time, ice has not yet fully dominated the influence on compressive strength. When the temperature dropped to -160 °C, the ice in the pores was much lower

than the freezing point and became harder. At such low temperatures, ice signally affected the mechanical properties of mortar, resulting in lower CDIF as compared to -70 °C.

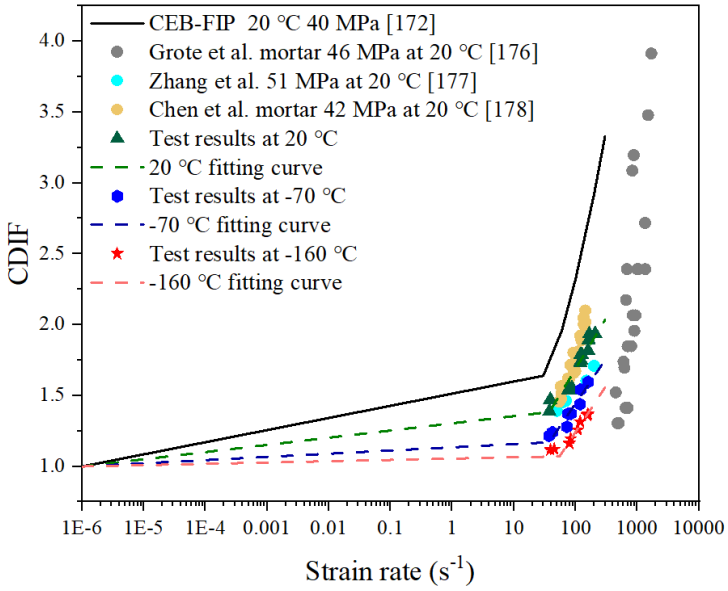

Figure 4. 17 Variation of CDIFs with strain rate at low and cryogenic temperature.

Following the fitting of the data points depicted in Figure 4.17, Equations (4.9), (4.10) and (4.11) were formulated to plot the CDIF curves of NSM at room temperature, -70 and -160 °C, correspondingly. These derived curves were then compared with experimental data, illustrated in Figure 4.17. It was worth noting that as the temperature decreased, the DIF decreased in compression. Furthermore, the transition strain rate was approximately 37.87 s^{-1} at 20 °C, the change point occurred in 37.28 s^{-1} at -70 °C, additionally, the transition strain rate exhibited in 55.21 s^{-1} at -160 °C.

$$\text{CDIF at } 20\,^{\circ}\text{C} = \begin{cases} 0.051 \log \dot{\varepsilon} + 1.305 & \dot{\varepsilon} \leq 37.87\ s^{-1} \\ 0.721 \log \dot{\varepsilon} + 0.247 & \dot{\varepsilon} > 37.87\ s^{-1} \end{cases} \tag{4.9}$$

$$\text{CDIF at } -70\,^{\circ}\text{C} = \begin{cases} 0.021 \log \dot{\varepsilon} + 1.128 & \dot{\varepsilon} \leq 37.28\ s^{-1} \\ 0.644 \log \dot{\varepsilon} + 0.148 & \dot{\varepsilon} > 37.28\ s^{-1} \end{cases} \tag{4.10}$$

$$\text{CDIF at } -160\,^{\circ}\text{C} = \begin{cases} 0.092 \log \dot{\varepsilon} + 1.550 & \dot{\varepsilon} \leq 55.21\ s^{-1} \\ 0.661 \log \dot{\varepsilon} - 0.081 & \dot{\varepsilon} > 55.21\ s^{-1} \end{cases} \tag{4.11}$$

Figure 4.18 displays the TDIFs at 20, -70, and -160 °C together with different strains. The experimental data of TDIFs at ambient temperature fitted well with those from Liu *et al.* [182] and Chen *et al.* [183], which demonstrated the accuracy and reliability of the tests. It was noteworthy that unlike CDIFs, TDIFs increased as the temperature decreased. TDIFs were enhanced at lower temperatures. Compared to room temperature, TDIFs at -70 and -160 °C increased by 30.36% and 30.84%, respectively, for a specific strain rate of 60 s^{-1}. In addition, the TDIFs were slightly greater at -160 °C than at -70 °C. This suggested that NSM exhibited a more sensitive strain rate response under dynamic splitting, highlighting the material's increased brittleness at lower temperatures.

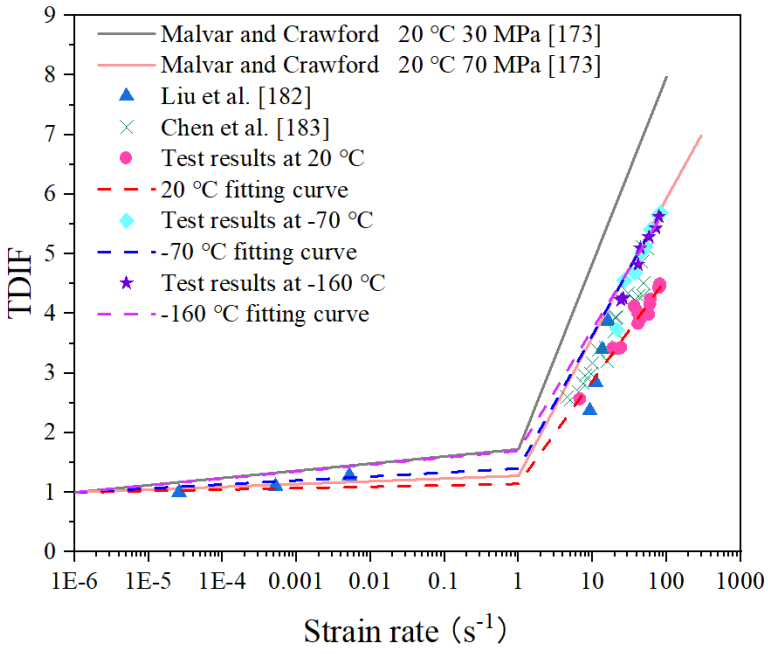

Figure 4. 18 Variation of TDIFs with strain rate at low temperature.

After curve fitting the experimental data points at 20, -70 and -160 °C, the TDIF curves for the NSM at room temperature and -70 and -160 °C temperatures were developed separately in Equations (4.12), (4.13), (4.14), as shown in Figure 4.18. The transition point for TDIF was set as 1 s^{-1}, which was the same as CEB-FIP [172] at 20 °C.

$$\text{TDIF at } 20\,^{\circ}\text{C} = \begin{cases} 0.042\log\dot{\varepsilon} + 1.254 & \dot{\varepsilon} \le 1\ s^{-1} \\ 1.726\log\dot{\varepsilon} + 1.145 & \dot{\varepsilon} > 1\ s^{-1} \end{cases} \tag{4.12}$$

$$\text{TDIF at} - 70\ ℃ = \begin{cases} 0.083\log\dot{\varepsilon} + 1.500 & \dot{\varepsilon} \le 1\ s^{-1} \\ 2.548\log\dot{\varepsilon} + 0.804 & \dot{\varepsilon} > 1\ s^{-1} \end{cases} \quad (4.13)$$

$$\text{TDIF at} - 160\ ℃ = \begin{cases} 0.175\log\dot{\varepsilon} + 2.053 & \dot{\varepsilon} \le 1\ s^{-1} \\ 1.949\log\dot{\varepsilon} + 1.872 & \dot{\varepsilon} > 1\ s^{-1} \end{cases} \quad (4.14)$$

4.3.5.2 Dynamic increase factor after cryogenic FT cycles

Figure 4.19 illustrates the DIFs with respect to strain rate (ranging from approximately 80 to 180 s^{-1}) after different numbers of cryogenic FT cycles. The regression equation for the fitting curve after 2 FT cycles was expressed as y = 1.207log $\dot{\varepsilon}$ - 0.768. It was notable that the CDIF values following 2 FT cycles exhibited a slight elevation as compared to those at 20 °C. The fitting curve after 4 FT cycles followed the equation y = 0.774log $\dot{\varepsilon}$ + 0.272. These CDIF values further rose as compared to those after 2 FT cycles, suggesting continued degradation in the material with increase FT cycles. The test results after 8 FT cycles were shown in the figure below, and the fitting curve was given by the equation y = 0.598log $\dot{\varepsilon}$ + 0.839. The CDIF values after 8 FT cycles were the highest among the tested conditions, indicating the greatest strain rate sensitivity after 8 FT cycles, along with the most significant reduction of mortar owing to the cumulative effects of the FT cycles. The CDIFs after 4 and 8 cryogenic FT cycles increased approximately 11.63% and 28.31%, respectively, in contrast with that after 2 cryogenic FT cycles. The dynamic increase factors measured at a strain rate of 180 s^{-1} following 8 FT cycles exceeded those observed after 2 and 4 FT cycles by approximately 13.43% and 9.62%, respectively. Overall, the CDIF increased with the number of FT cycles, implying a reduction in the material's capability to resist dynamic loading after cryogenic FT cycles. During each FT cycle, water within the pore structure of concrete froze and expanded, resulting in the development of internal stresses. When the ice melted, it left behind microcracks and damage in the mortar. As the number of FT cycles increased, the extent of microcracking and internal damage accumulated, causing a higher CDIF.

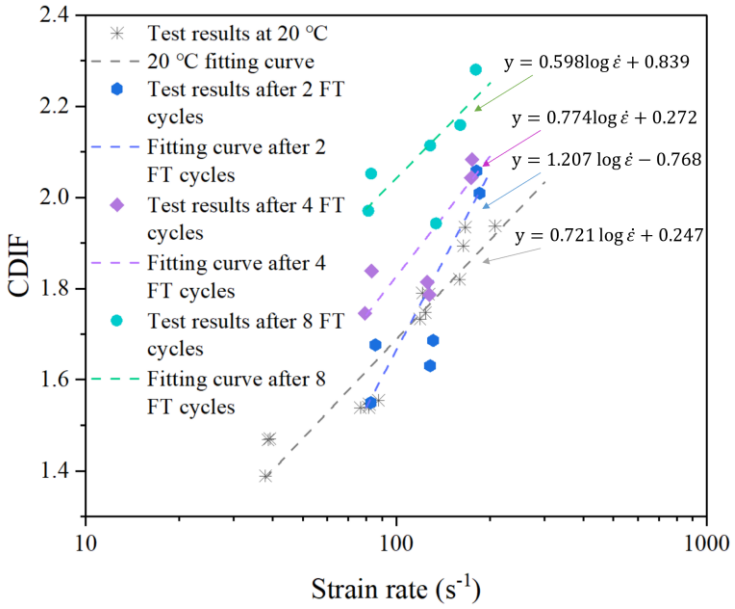

Figure 4. 19 Variation in CDIFs with strain rate after different numbers of FT cycles.

4.4 SEM analysis after FT cycles

SEM was utilised to examine the microstructural changes and crack formation in fragments of samples after 2, 4 and 8 times of FT cycles (see Figure 4.20). The microstructure appeared relatively intact with some pores and voids present when the sample without FT cycles. It was observed that, in comparison to the samples in the unfrozen state at room temperature, the samples subjected to 2 FT cycles exhibited an increase in the number of microscopic pores. After 4 FT cycles, the quantity and diameter of pores increased significantly, leading to severe deterioration of the mortar matrix (showing a fibrous texture), and the formation of microcracks was evident. Following 8 FT cycles, the number and diameter of pores continued to escalate, accompanied by an increase of microcracks. The loosened texture of the material after 8 FT cycles provided a key explanation for its heightened vulnerability to FT damage from a mechanistic standpoint. The observations aligned with the experimental results obtained by Xie and Wu [184] and Wei *et al.* [185]. To better understand the changing patterns of concrete pore characteristics, Zhou *et al.* [130] performed mercury intrusion porosimetry (MIP)

and nuclear magnetic resonance (NMR) tests to analyse ordinary C60 concrete both before and after 20 FT cycles. The MIP results revealed a significant increase in pore volume in the concrete after 20 FT cycles, highlighting that internal pore water was a key factor influencing the mechanical behaviour. Similarly, the NMR results indicated a marked rise in the number of large capillary pores and considerable structural deterioration in the concrete. This consistency in observed trends and damage mechanisms across different studies reinforces the validity of the findings from SEM.

In conclusion, it emphasised that FT cycles had a significant and progressive effect on the microstructure of the samples, leading to increased porosity, deterioration of the mortar matrix, and the formation and propagation of microcracks. These microstructural changes can have detrimental effects on the mechanical properties and durability of the material, potentially compromising its performance and service life in environments subjected to freezing and thawing conditions.

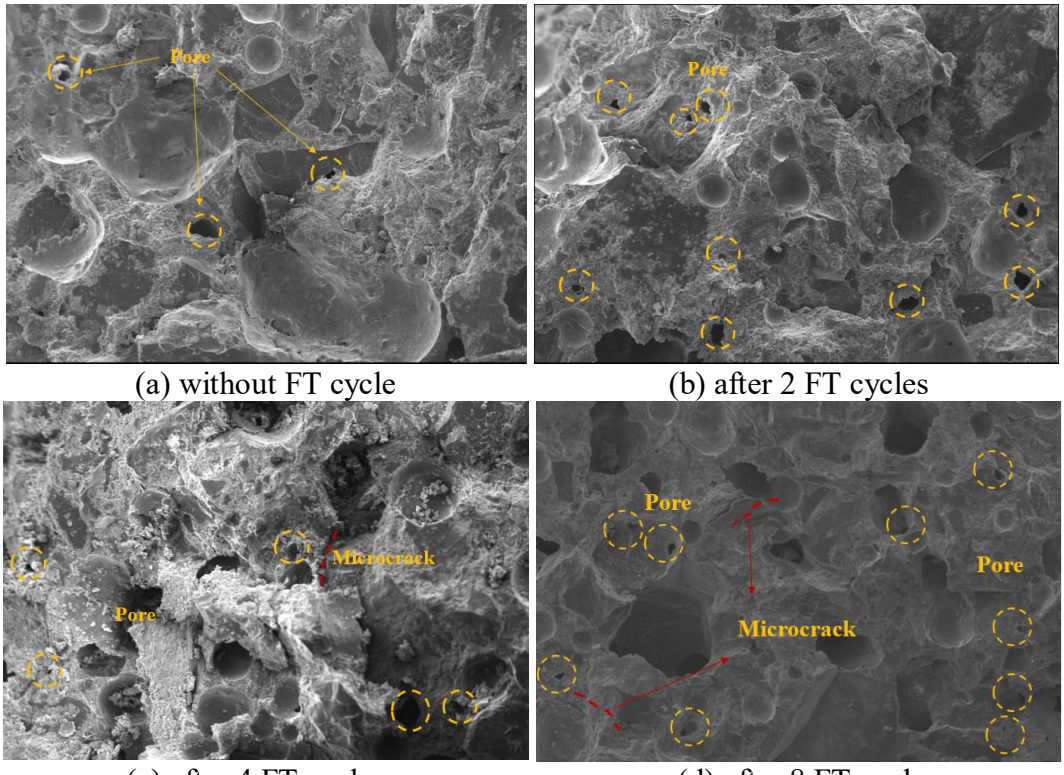

(a) without FT cycle (b) after 2 FT cycles

(c) after 4 FT cycle (d) after 8 FT cycles

Figure 4. 20 Microscopic image of samples after various number of FT cycles.

4.5 Limitations

Although this study provides information of the dynamic behaviour of NCM at cryogenic temperature and after FT cycles, there are several limitations that should be addressed in future research. Firstly, while this study considered a range of FT cycles, additional cycles should be investigated to further understand the long-term effects of FT exposure (e.g., 10~50 cycles) on mechanical properties. Furthermore, the microstructural changes resulting from FT cycles were qualitatively examined, but future studies could utilise more advanced techniques such as CT scanning or mercury intrusion porosimetry to quantitatively analyse the porosity and correlate it with the observed mechanical behaviour. This would enable a more comprehensive understanding of the relationship between the microstructure and mechanical performance of NSM under extreme conditions. Additionally, the tested strain rate range (up to 180 s^{-1}) may not encompass all possible loading scenarios, particularly those encountered in extreme events such as blasts, therefore, higher strain rates needs exploration in the future.

4.6 Summary

This study investigated the dynamic mechanical properties of NSM under extreme temperature conditions (20, -70 and -160 °C) and after cryogenic FT cycles in temperature range from -160 to 20 °C using SHPB tests. The following particular conclusions can be drawn:

- At -70 and -160 °C, the severity of damage decreased as compared to room temperature, indicating improved impact resistance. Additionally, the stiffness of the material increased at lower temperatures, leading to reduced deformation and damage.

- Dynamic compressive strength increased with strain rate at all temperatures, with higher strain rates resulting in considerable enhancements in strength. The modulus of elasticity also increased at lower temperatures, indicating a more rigid response of NSM at extremely cold temperatures.
- The splitting strength increased with strain rate and decreasing temperature. Lower temperatures (-70 °C and -160 °C) led to higher splitting strength than room temperature, indicating enhanced resistance to dynamic tensile loading at extremely cold temperatures.
- While dynamic strengths generally increased with higher strain rates, the sensitivity to strain rate decreased significantly at cryogenic temperatures for compression, as evidenced by decreasing CDIFs. The results showed that the CDIFs at -70 and -160 °C decreased by about 12.63% and 24.7% compared to at 20 °C when the strain rate was 160 s^{-1}. Conversely, dynamic splitting exhibited heightened sensitivity to strain rate at lower temperatures, reflected in increasing TDIFs. The experimental results indicated that the TDIFs at -70 and -160 °C had a rise of 16.71% and 29.72% compared to 20 °C when the strain rate was approximately 40 s^{-1}.
- The increase number of cryogenic FT cycles resulted in a notable increase in the strain rate sensitivity of concrete and decrease its ability to withstand dynamic loading. At the strain rate of 180 s^{-1}, the DIFs after 8 FT cycles were approximately 13.43% and 9.62% greater than after 2 and 4 times FT cycles, respectively.

The findings of this study have several important implications for the design and maintenance of LNG storage facilities. First, the observed increase in compressive strength at cryogenic temperatures suggests that standard safety factors for material selection may need reassessment, as certain concrete compositions might perform better than traditionally assumed. However, the reduction in elastic modulus at -160 °C indicates a potential decrease in structural stiffness, necessitating careful consideration of thermal gradient effects in different regions of an LNG containment system. The progressive deterioration after multiple FT cycles underscores the importance of durability-enhancing measures to mitigate pore pressure-induced microcracking. Additionally, the differing strain rate effects in compression and tension highlight the need for impact-resistant design modifications, as brittle fracture risks could be elevated under high strain-rate tensile loading. The DIF variations at low temperatures further suggest that rate-dependent design criteria should be refined to account for cryogenic conditions. Finally, incorporating these experimental results into lifespan prediction models could improve maintenance scheduling by enabling more accurate estimations of structural degradation over time, ensuring the long-term safety and reliability of ACLNG storage infrastructure.

Chapter 5. EXPERIMENTAL EXPLORATION ON DYNAMIC CHARACTERISTICS OF CEMENT BASED ULTRA-HIGH PERFORMANCE CONCRETE AT LOW AND CRYOGENIC TEMPERATURE

5.1 Introduction

This study presents an experimental investigation on the dynamic compressive and splitting tensile behaviour of CUHPC subjected to low temperatures of -70 °C and -160 °C. The compressive and splitting tensile strengths of CUHPC were examined at various strain rates (40 ~ 160 s^{-1} for compression, 20 ~ 80 s^{-1} for splitting tension) and temperature conditions (at 20, -70 and -160 °C) via SHPB device. The dynamic compressive as well as splitting tensile strengths of UHPC increased significantly with the strain rate. The CDIFs decreased with the decline in temperature. The compressive strengths under a strain rate of 120 s^{-1} at ambient temperature were approximately 1.09 and 1.16 times higher than at -70 and -160 °C, respectively. On the other hand, an opposite behaviour was observed for the TDIFs of CUHPC, i.e., TDIFs rose as the temperature decreased. Based on the experimental data, it showed that the TDIFs at -70 and -160 °C were nearly 1.16 and 1.21 times higher than at 20 °C at the specified strain rate 60 s^{-1}.

5.2 Experimental Methodology

The experimental investigation of CUHPC dynamic behaviour under low and cryogenic temperatures followed the process in Figure 5.1. CUHPC specimens were initially produced and subsequently cooled to target temperatures of -70 and -160 °C to simulate low and cryogenic temperature conditions. Two different tests were employed to evaluate the material's mechanical response: static testing and SHPB testing, both focusing on compression and splitting tension properties. The static tests provided baseline

mechanical properties, while the SHPB tests characterised the dynamic behaviour of CUHPC under high strain rates. This dual testing approach enabled a thorough comparison between static and dynamic responses at these extreme temperatures. All experimental data were acquired and analysed to understand the temperature-dependent mechanical properties and strain rate effects on the behaviour of CUHPC under these harsh environmental conditions.

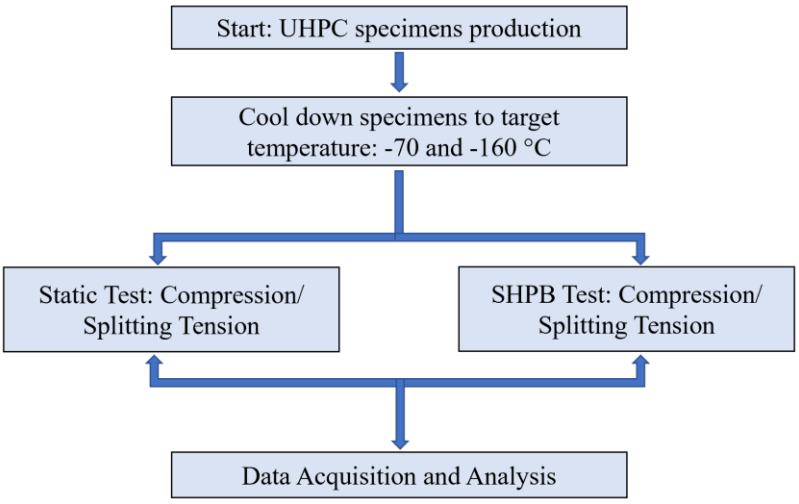

Figure 5.1 Experimental methodology for CUHPC testing at low and cryogenic temperatures.

5.2.1 CUHPC specimen preparation and composition

The CUHPC specimens were reinforced with 2% steel fibres. The properties of steel fibre are listed in Table 5.1. Table 5.2 provides detailed material proportions. Figure 5.2 illustrates the comprehensive particle size distributions of the four solid materials utilised in this CUHPC mixture. To ensure optimal dispersion and random orientation of the steel fibres while preventing agglomeration, manual distribution was employed during the fibre incorporation process. Following this step, the concrete mixture was carefully transferred into PVC pipe moulds, each with an internal diameter measuring 70 mm. After appropriate curing in the PVC moulds, the samples were cut into cylindrical shapes with

a diameter of 70 mm and a height of 35 mm (see Figure 5.3). To achieve uniform load distribution during the loading test, the end faces were grinded.

Table 5.1 Material properties of steel fibre.

Diameter (mm)	Length (mm)	Density (kg/m^3)	Modulus of elasticity (GPa)	Tensile strength (MPa)
0.12	15	7800	210	>2850

Table 5.2 CUHPC composition ratios (kg/m^3)

42.5 Cement	Water	Fine sand	Steel fibre	Superplasticiser	Fly ash	Silica fume
925	230	963	160	26	340	130

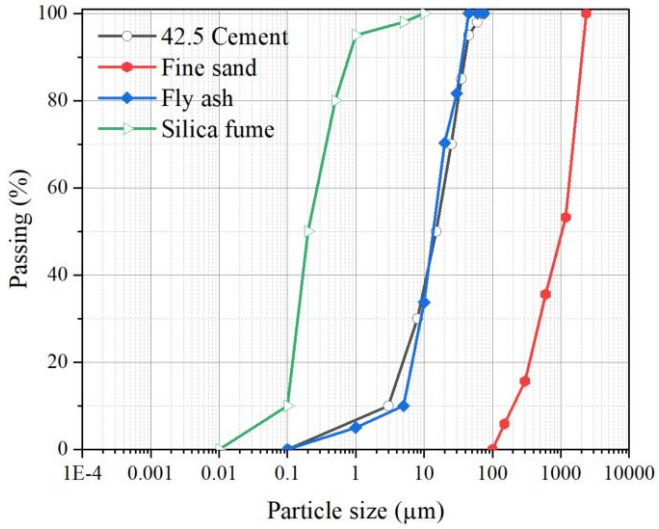

Figure 5. 2 Particle size distribution of used materials.

(a) 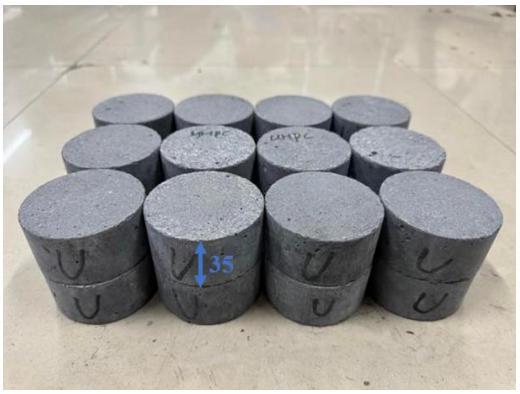

(b) 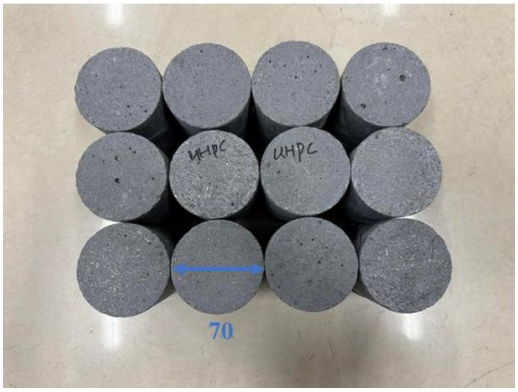

Figure 5.3 CUHPC specimens for testing (unit: mm).

5.2.2 Experimental setup under cryogenic temperature

The proposed experiment aims to examine both the static and dynamic compressive and splitting tensile behaviour of CUHPC under extreme low temperatures of -70 and -160

°C. To attain the target temperatures, a cooling apparatus as depicted in Figure 4.3 was employed. The specimens were put into a low-temperature chamber, which can accommodate 14 specimens simultaneously. The liquid nitrogen was slowly flowed into the low-temperature chamber. During the experiment, the rate of temperature drop was controlled at 1 °C per minute to make sure the uniform temperature distribution within the specimens. The target temperature maintained for 4 hours to guarantee thermal equilibrium. The temperature was accurately recorded and regulated within the low-temperature chamber. Figure 5.4 illustrates the cooling curve within the low-temperature chamber.

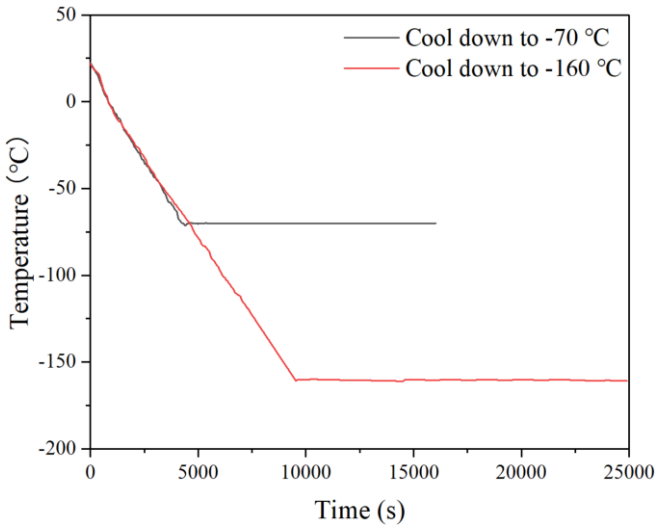

Figure 5. 4 Cooling curves in the test.

5.3 Static test results

The quasi-static experiments were conducted at three distinct temperature conditions, including 20, -70 and -160 °C. A 300-ton hydraulic testing machine was employed to perform these tests. For the compressive tests, the loading rate was set at 0.5 mm/min. In the case of splitting tensile tests, the cylindrical specimens were placed horizontally between the loading surfaces of the compression testing machine. The compressive load was applied diametrically along the cylinder's length at a slower rate of 0.02 mm/min. This loading continued until failure initiated along the vertical diameter of the specimen.

The static compressive and splitting tensile strengths of CUHPC at 20, -70 and -160 °C are shown in Figure 5.5. The compressive strength exhibited an almost linear increase when the temperature decreased from 20 °C to -70 and -160 °C, from 161.20 MPa to 193.56 MPa and 211.58 MPa, respectively, corresponding to an increase of 20.07% and 31.25%. Likewise, the splitting tensile strength increased from 7.20 MPa at room temperature to 10.13 MPa and 11.25 MPa at -70 and -160 °C, respectively, representing an increase of 40.69% and 56.25%.

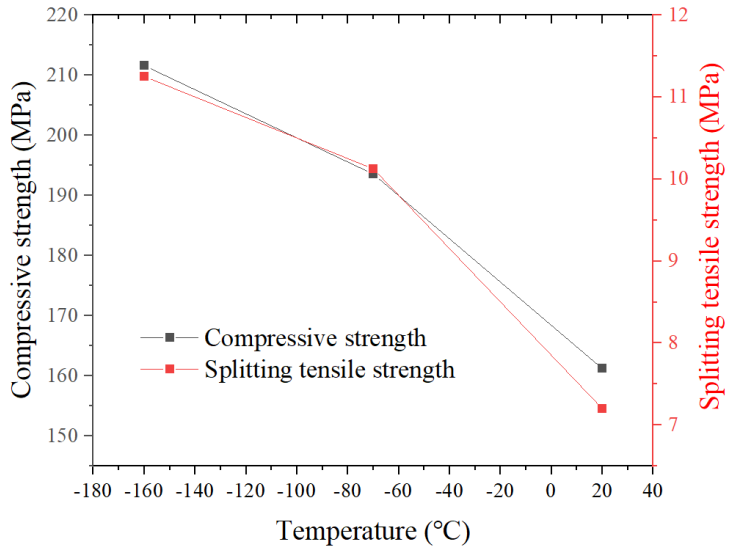

Figure 5.5 CUHPC Compressive and splitting tensile strength at low temperature.

5.4 SHPB test setup

The behaviour of CUHPC under dynamic compression and splitting tensile loading at various strain rates and low/cryogenic temperatures was explored experimentally. Dynamic compressive tests were conducted at strain rates of 40, 80, 120 and 160 s^{-1}, while splitting tensile tests were performed at strain rates of 20, 40, 60 and 80 s^{-1}. Notably, these tests were carried out at three distinct temperature conditions, including 20, -70 as well as -160 °C. The specimens employed for the experiment were cylindrical, having dimensions of 35 mm in height and 70 mm in diameter. Section 4.2.2.3 provides a comprehensive description of the SHPB test methodology.

5.5 Results and discussions of experiments

5.5.1 Dynamic compressive test

5.5.1.1 Damage appearances of specimens subjected to coupled loading

Figure 5.6 presents the dynamic compressive failure modes of CUHPC specimens at different temperatures and strain rates. At 20 °C (see Figure 5.6(a)), the specimens exhibited a progressive increase in damage severity as the strain rate rose. At the lowest strain rate of 40.7 s^{-1}, the specimen showed moderate damage with some cracking and chipping. When the strain rate rose to 81.4 s^{-1}, the sample exhibited pronounced cracking and fragmentation. At 120.1 s^{-1}, the specimen appeared severely damaged, with substantial fragmentation and the formation of smaller debris, CUHPC demonstrated superior damage resistance as compared to Normal Strength Mortar (NSM) [186], as evidenced by its central core remaining relatively intact, which was caused by the effect of steel fibres. Finally, at the highest strain rate of 158.2 s^{-1}, the specimen disintegrated into powdery fragments, indicating complete failure. At -70 °C (see Figure 5.6(b)), a similar trend was observed, but the overall damage appeared less severe with respect to the state of ambient temperature. The specimens at lower strain rates (39.1 s^{-1} and 81.6 s^{-1}) showed moderate cracking and edge chipping, while the core retained relatively intact. At 121.3 s^{-1}, the specimen exhibited more significant fragmentation, with the formation of granular debris. At the highest strain rate of 162.6 s^{-1}, the specimen disintegrated into smaller fragments, but less severe damage occurred in contrast with the corresponding specimen at 20 °C. While at -160 °C (see Figure 5.6(c)), the specimens demonstrated even higher resistance to dynamic compressive failure. The specimens at lower strain rates (45.2 s^{-1} and 82.3 s^{-1}) exhibited minimal damage, with only minor cracking visible. At 119.2 s^{-1}, the specimen showed moderate fragmentation, but the core remained largely intact owing to simultaneous action of steel fibres, albeit with signal cracking and

fragmentation. However, at the highest strain rate of 161.5 s^{-1}, the specimen exhibited more severe damage and disintegration in comparison with the corresponding specimens at 20 °C and -70 °C. This may show the increased brittleness of CUHPC at lower temperature at higher strain rate.

Overall, it highlighted the significant impact of both thermal conditions and strain rate on the dynamic compressive failure mechanisms of CUHPC. Lower temperatures especially at -160 °C resulted in improved resistance to damage and fragmentation at the lower strain rates (40 and 80 s^{-1}), but more brittle at higher strain rate.

40.7 s^{-1} 81.4 s^{-1} 120.1 s^{-1} 158.2 s^{-1}

(a) at 20 °C

39.1 s^{-1} 81.6 s^{-1} 121.3 s^{-1} 162.6 s^{-1}

(b) at -70 °C

45.2 s^{-1} 82.3 s^{-1} 119.2 s^{-1} 161.5 s^{-1}

(c) at -160 °C

Figure 5.6 Dynamic compressive failure patterns of CUHPC across various temperatures.

The dynamic failure process of CUHPC specimens under compressive loading at different temperatures (20, -70 and -160 °C) was captured via ultra-high-speed video camera (see Figure 5.7). It can be observed that at 57 μs, more obvious cracks appeared in the -160 °C sample, as compared to room temperature and -70 °C. Over time, the damage to the sample at -160 °C became more severe, accompanied by a large amount of powder and small fragments. This observation highlighted the impact of temperature on the mechanical properties and failure behaviour of CUHPC, with lower temperatures resulting in a more brittle and catastrophic failure mode at higher strain rate.

CUHPC was a dense, homogeneous material [187] with a tightly packed microstructure and a high degree of hydration, which contributed to its superior mechanical performances and resistance to cracking and fragmentation under impact loading. Wu *et al.* [188] examined the microstructure of the matrix by MIP and showed that after adding fly ash and other substances, the total porosity of the CUHPC matrix decreased by about 5%. The filling effect of supplementary cementitious materials (SCMs) densified the CUHPC matrix, resulting in improved mechanical properties. At lower temperatures, the stiffness of CUHPC increased due to the phase change in the free water, resulting in the enhancement of compressive strength. However, it should emphasise that as concrete's strength increased, it typically became more prone to brittle failure [189]. Even when steel fibres were incorporated into mixtures, CUHPC still exhibited brittle failure modes when subjected to extremely low temperatures [104, 190]. Therefore, it showed noticeably more brittle failure characteristics at -160 °C as compared to room temperature and -70 °C.

The frozen-pore water effect at cryogenic temperatures enhanced the bond between steel fibres and the cement matrix, thereby restricting crack propagation. Kim and Yoo [191] examined how cryogenic temperatures affected the pull-out characteristics of individual

steel fibres embedded in CUHPC matrix. They pointed out that exposure to extremely low temperatures considerably improved both the average bond strength and slip capacity, contributing to the strength enhancement. Overall, it exhibited the superior performance of CUHPC in terms of damage resistance and controlled failure modes.

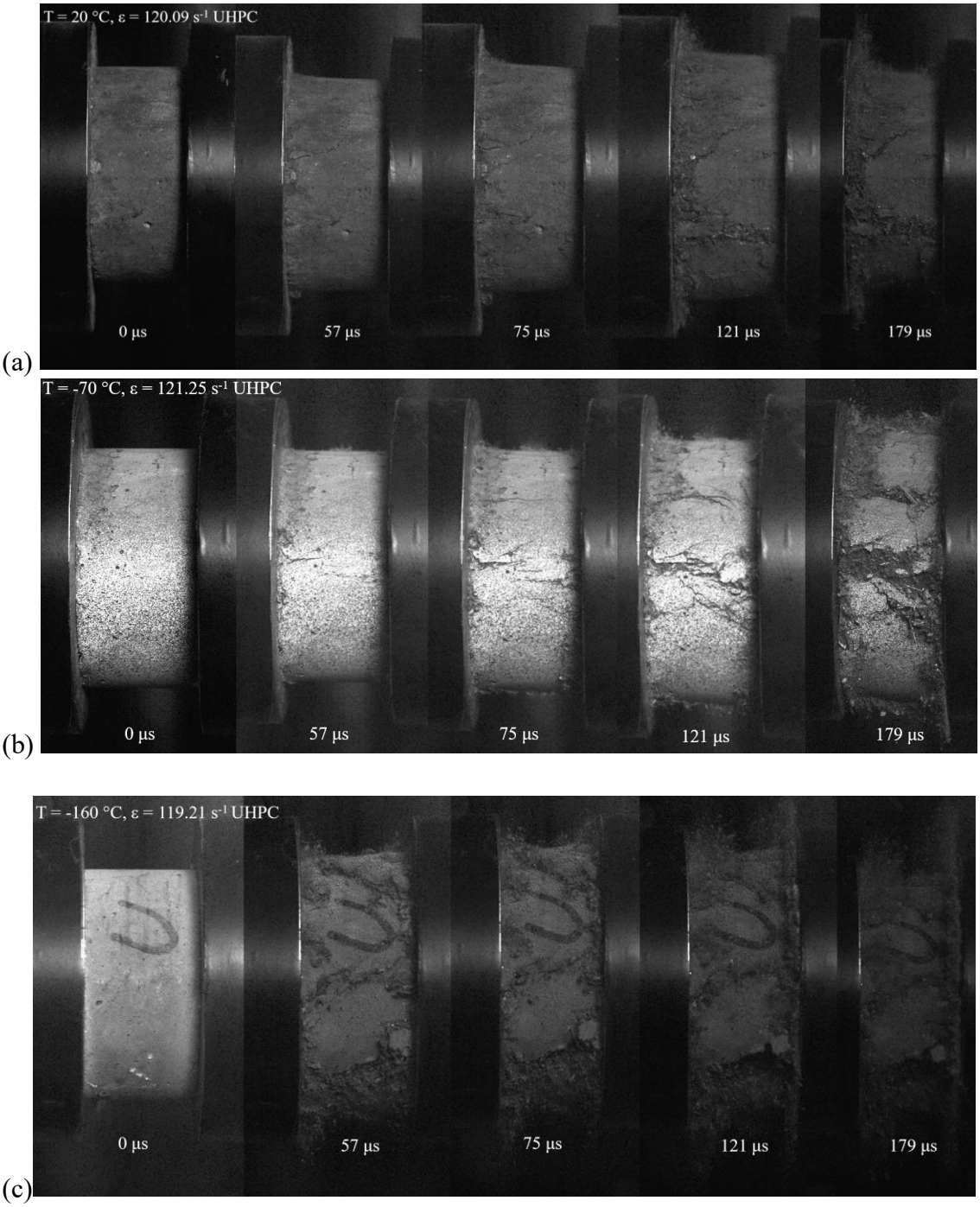

Figure 5.7 Failure process of CUHPC at various temperature. (a) at 20 °C (b) at -70 °C (c) at -160 °C.

5.5.1.2 Effect of low temperature on compressive strength and modulus of elasticity

Figure 5.8 demonstrates the relationship between dynamic compressive stress and strain for CUHPC specimens tested at various temperatures (20, -70 and -160 °C) and strain rates (ranging from 40 s^{-1} to 160 s^{-1}). At the ambient temperature, the dynamic peak stress of CUHPC increased signally with rising strain rate. Specifically, the f'_c increased by 16.4%, 32.0%, 47.3% and 52.1% at strain rates of 40.7 s^{-1}, 81.4 s^{-1}, 120.1 s^{-1} and 158.2 s^{-1}, respectively, in comparison with the static strength (see Figure 5.8(a)). At -70 °C, the stress-strain curves exhibited a similar trend as those at room temperature, with the peak stresses kept increasing at higher strain rates. By comparing the static strength at -70 °C, the dynamic compressive strength escalated by 5.2%, 22.9%, 34.7% and 35.3% at strain rates of 39.1 s^{-1}, 81.6 s^{-1}, 121.3 s^{-1}, and 162.6 s^{-1}, respectively (see Figure 5.8(b)).

At -160 °C, the stress-strain curves exhibited a more brittle behaviour with a steeper post-peak softening branch as compared to 20 and -70 °C. The f'_c continued to increase with strain rate. At the strain rate of 45.2 s^{-1}, 82.3 s^{-1}, 119.2 s^{-1} and 161.5 s^{-1}, the dynamic compressive strength at -160 °C experienced an increase of 1.66%, 13.1%, 26.7% and 29.8% in contrast to the uniaxial compressive strength at -160 °C. These findings demonstrated that the f'_c of CUHPC specimens increased with strain rate across all temperature conditions. This trend was particularly pronounced at room temperature, where the strength enhancement was more substantial as compared to -70 °C and -160 °C. As the temperature reduced from -15 °C to -125 °C and below, Wu and Prakash [181] observed an increase peak stress of ice, resulting in an enhancement of compressive strength for CUHPC with declined temperature.

Regarding the dynamic compressive modulus of elasticity of CUHPC, a phenomenon similar to that observed in NSM [186] was noted, i.e., the dynamic modulus of elasticity at -70 °C was higher than that at room temperature and -160 °C. According to Zhang *et*

al. [169], this is probably caused by the binding and filling actions of ice in the pores of the concrete in this temperature range. The formation of ice in the pores helped fill the voids and bind the cement paste and aggregates together, causing an increase in the overall stiffness and modulus of elasticity of the CUHPC. Additionally, the thermal contraction of the CUHPC components at -70 °C further contributed to this stiffening effect, as it reduced the volume of the pores and raised the density of the material. However, as the temperature dropped further down to -160 °C, the dynamic elastic modulus started to decrease. This can be explained by the increased thermal expansion mismatch between the different CUHPC constituents (cement paste, aggregates, and ice) at cryogenic temperatures. The inconsistent thermal deformations resulted in the development of microcracks and damage within the CUHPC microstructure, which in turn reduced the overall stiffness and dynamic elastic modulus of the material. At the strain rate of about 120 s^{-1}, the dynamic elastic modulus of CUHPC at -70 °C was approximately 7.16 times and 3.64 times higher than at 20 °C and -160 °C, respectively. This highlighted the markedly influence of the ice filling and binding effects as well as the thermal expansion mismatch on the dynamic mechanical performances of CUHPC at different low and extremely low temperature conditions.

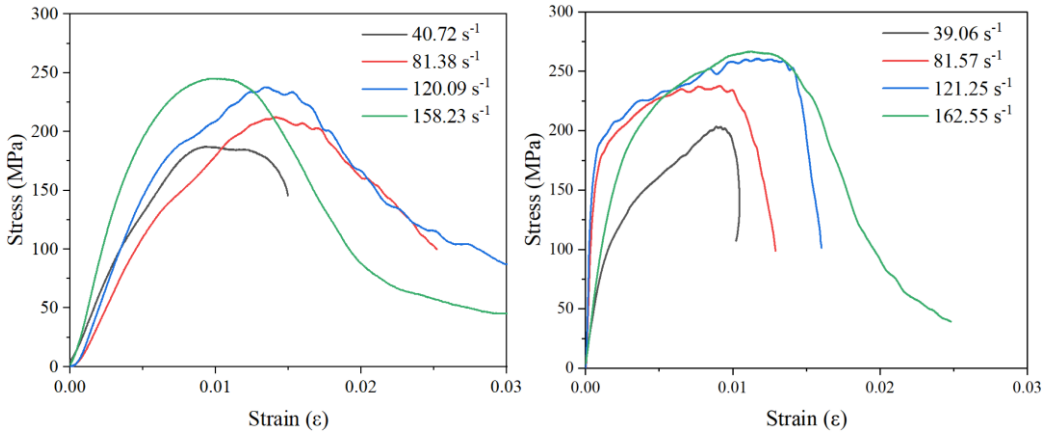

(a) at 20 °C (b) at -70 °C

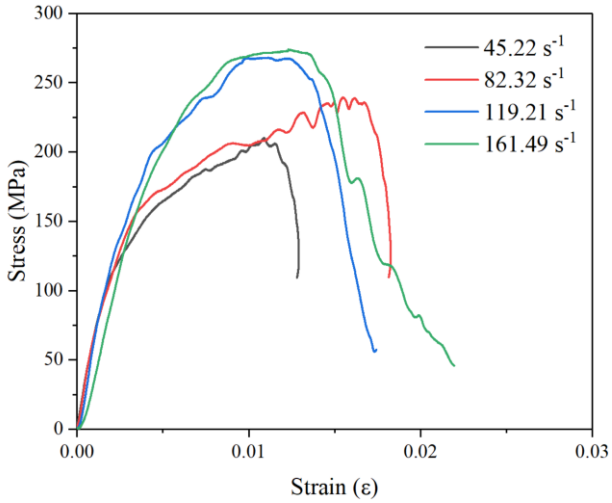

(c) at -160 °C

Figure 5.8 Dynamic compressive stress-strain curve at various temperatures.

5.5.2 Dynamic splitting tensile results

5.5.2.1 Failure modes of specimens under combined loading

Figure 5.9 illustrates the dynamic splitting tensile failure modes of CUHPC specimens at various temperatures and strain rates. The relationship among temperature, strain rate, and the resulting damage patterns in the concrete specimens were examined. At various strain rates (20, 40, 60 and 80 s^{-1}) and temperatures (20, -70 and -160 °C), different failure modes appeared in the specimens. Three primary categories may be used to classify the failure scenarios [192]: Failure Mode I (lower strain rates): The specimen maintains stress equilibrium before cracking, then splits from the centre along the loading axis into two halves that can be reassembled to closely resemble the original shape. Failure Mode II (above 20 s^{-1}): The specimen experiences a fracture along its central axis, resulting in two distinct halves. A minor wedge-shaped zone of crushing is evident at the point of load application. Failure Mode III: The specimen exhibits a more complex failure pattern. Shear damage manifests at both extremities of the specimen. Concurrently, a wedge-shaped crushing zone develops at the loading end. The central region of the specimen displays a substantial zone of tensile damage, often presenting as a band of crushed material. At lower strain rates (around 20 s^{-1}), the specimens exhibit a central crack

damage pattern, where they fracture into two halves along the loading direction. At higher strain rates (above 20 s^{-1}), the specimens display a triangular crack damage pattern, characterised by triangular damage zones, especially at the contact ends (particularly the loading end). The damage level escalated with strain rate, with the triangular fracture area expanding and the overall deformation increasing. Generally speaking, the transition in failure modes observed in the CUHPC specimens, shifting from shear failure to tensile failure, can be primarily attributed to the redistribution of the maximum tensile strain within the material [193]. A comparative assessment revealed that, under identical strain rates, the extent of damage was more severe at -70 °C than at ambient temperature. Furthermore, the damage severity at -160 °C was even worse than at -70 °C.

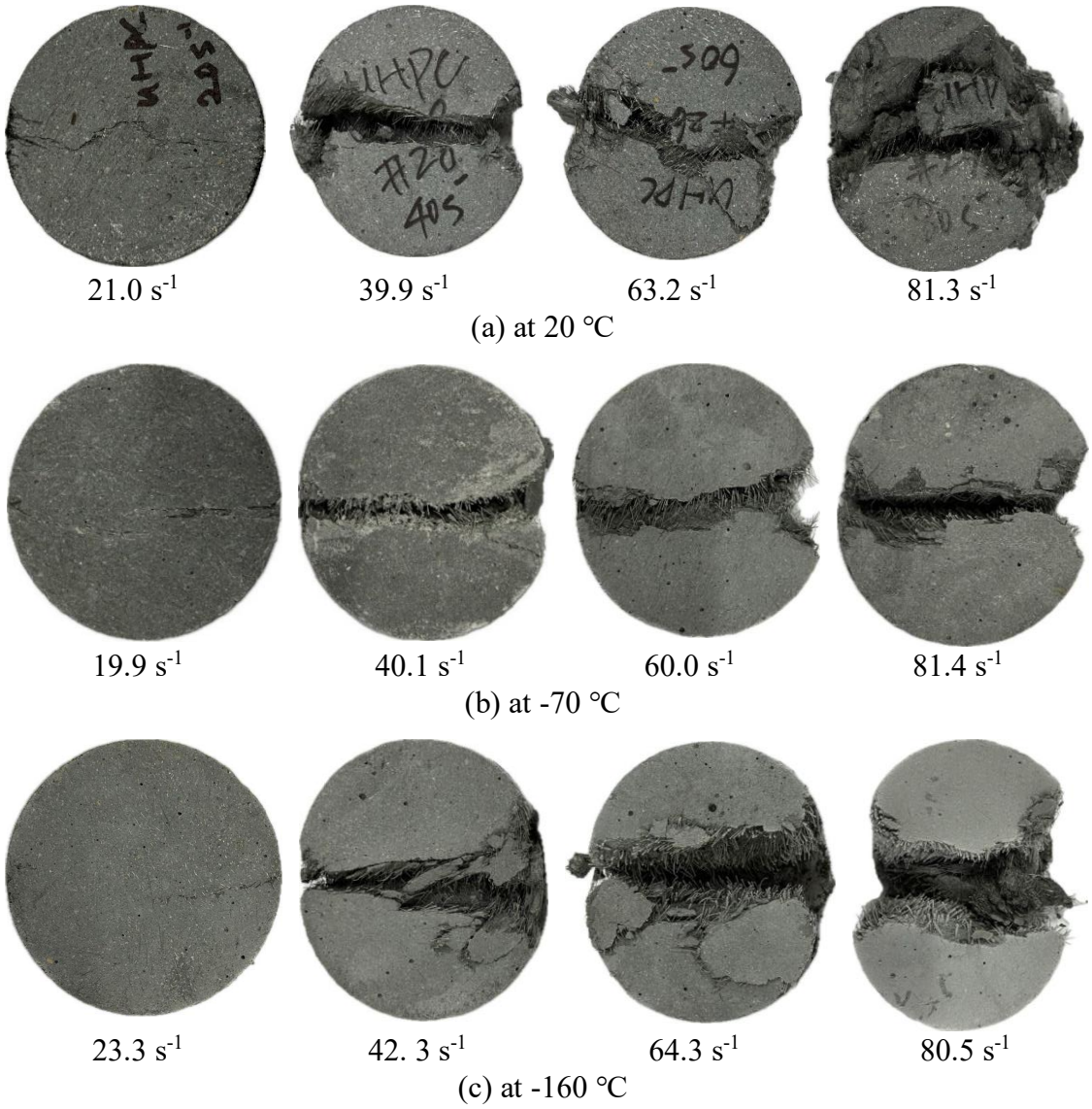

Figure 5.9 Dynamic splitting tensile failure mechanisms of CUHPC at various temperatures.

Figure 5.10 shows the failure process of CUHPC under dynamic splitting tensile tests conducted at approximately 40 s^{-1} strain rate together with temperatures of 20, -70 and -160 °C. As time progressed, the cracks in the CUHPC specimens propagated along the centre of the samples, gradually widening and extending. At -70 ℃, an undamaged sample displayed at 33 μs, while a more rapid and irregular crack propagation pattern demonstrated at the following time step 82 μs, 112 μs and 180 μs in contrast to the state of room temperature. At the temperature of -160 ℃, the failure of CUHPC became more sudden and catastrophic, exhibiting a more brittle behaviour. The crack formation was

visible as early as 8 μs, with subsequent widening and extension of the crack at 33 μs, 112 μs and 180 μs. In summary, as the temperature decreased, the crack initiation and propagation become more rapid, irregular, and catastrophic, indicating a transition from a more ductile failure mode at ambient temperature to a more brittle failure mode at lower temperatures.

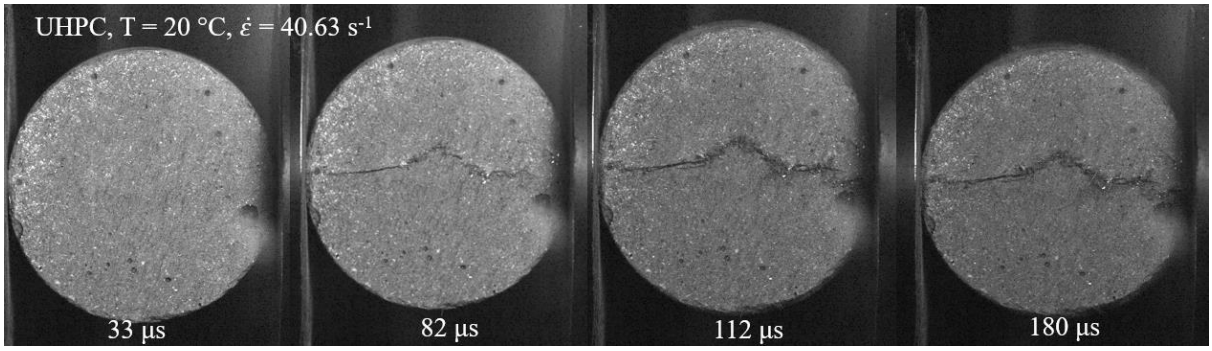

(a) at ambient temperature

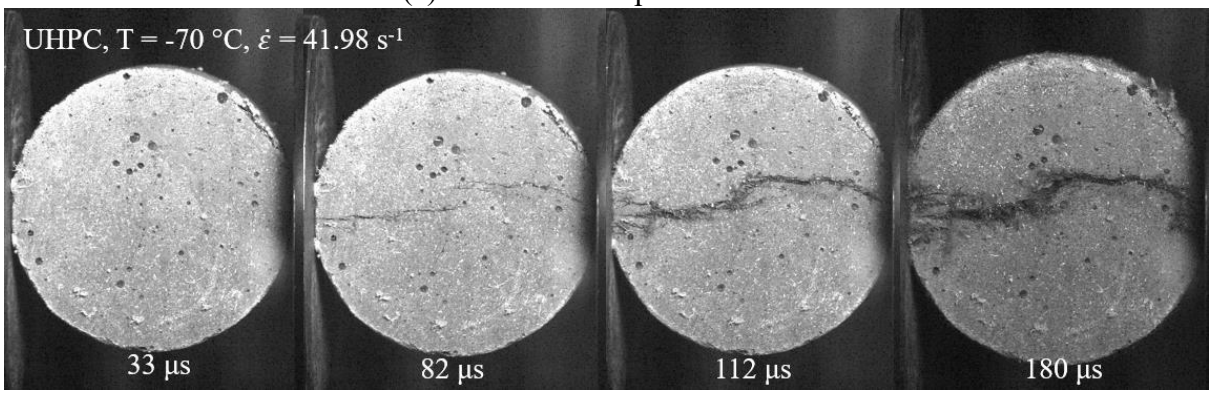

(b) at -70 °C

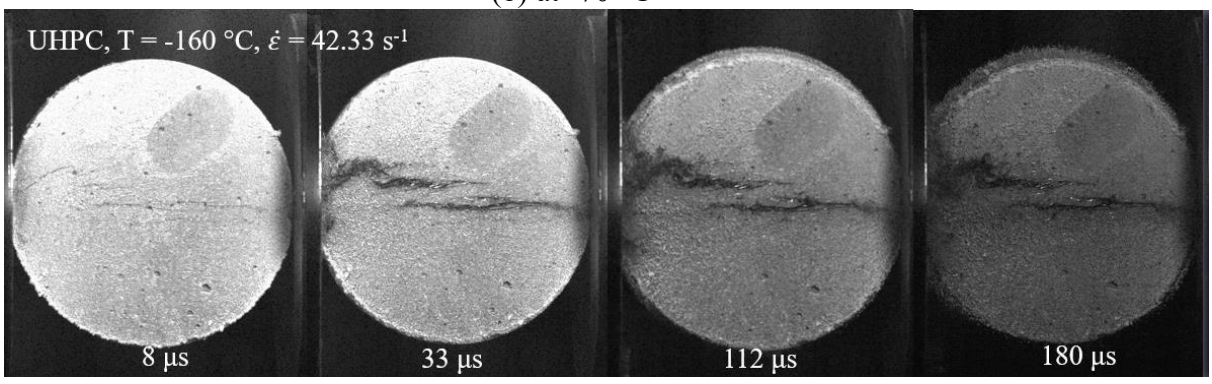

(c) -160 °C

Figure 5. 10 Failure process of CUHPC under dynamic splitting tensile test.

5.5.2.2 Effect of low temperature on splitting tensile strength

The dynamic splitting tensile behaviour of CUHPC was investigated at temperature conditions of 20, -70 and -160 °C, with strain rates ranging from approximately 20 to 80 s^{-1}, and the peak splitting tensile strength of different scenarios is presented in Figure 5.11. At room temperature, as the strain rate increased from 21.0 s^{-1} to 39.9 s^{-1}, 63.2 s^{-1}, and 81.3 s^{-1}, the splitting tensile strength of the CUHPC specimens rose by approximately 108.6%, 141.1%, 172.6% and 188.1%, respectively, in contrast to the static splitting tensile strength at 20 °C. At -70 °C, with increasing strain rates from 19.9 s^{-1} to 40 s^{-1}, 60.0 s^{-1} and 81.4 s^{-1}, the splitting tensile strength showed respective increases of about 122.3%, 156.5%, 204.6% and 224.9% in compared to the static splitting tensile strength at -70 °C. Similarly, at -160 °C, with strain rates rising from 23.3 s^{-1} to 42.3, 63.3 and 80.5 s^{-1}, the splitting tensile strength exhibited increase of around 171.20%, 184.6%, 215.7% and 257.5%, respectively, in contrast with the static splitting tensile strength at -160 °C. It was noted that as the strain rate ascended, the splitting tensile strength of the specimen increased at the same temperature condition. Furthermore, it was evident that under the same strain rate the dynamic splitting tensile strength rose as the temperature decreased. For example, at a strain rate of 40 s^{-1}, the dynamic splitting strength at -70 and -160 °C rose by 52.3% as well as 87.7%, respectively. Likewise, at strain rates of 80 s^{-1}, the dynamic splitting tensile strength at -70 and -160 °C grew to 58.7% as well as 93.9%, respectively, as compared to room temperature.

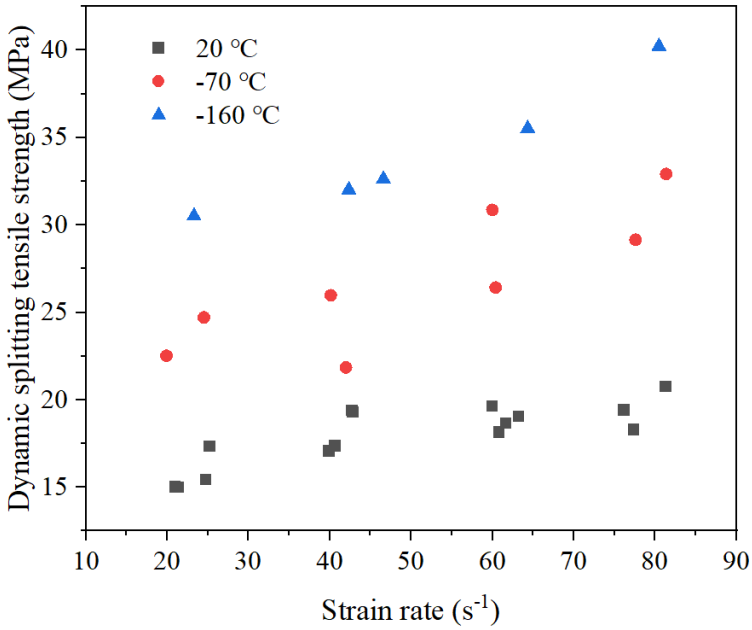

Figure 5.11 Dynamic splitting tensile strength of CUHPC at various temperatures.

5.5.3 Relationship between dynamic compressive and splitting tensile strength

The relationship between dynamic compressive strength and splitting tensile strength at various temperatures and strain rates can be expressed using Equation (5.1). This equation incorporates the effects of strain rate and temperature at 20, -70 and -160 ℃ on the material's mechanical properties. These relationships were established through regression analysis, having high correlation coefficient of determination (R^2), which was 0.87. 0.91 and 0.92 at 20, -70 and -160 ℃, respectively. This indicates a strong fit between the predicted and experimental values. These findings highlight the significant influence of strain rate and temperature on the dynamic compressive and tensile properties of CUHPC, showing their interdependence under varying conditions.

$$f'_{c,d} = \begin{cases} 25.92 \ln \dot{\varepsilon} + 5 \times 10^{-4} f'_{t,d} + 100 & T = 20\ ℃ \\ 33.97 \ln \dot{\varepsilon} + 1 \times 10^{-4} f'_{t,d} + 100 & T = -70\ ℃ \\ 38.27 \ln \dot{\varepsilon} + 1.34 f'_{t,d} & T = -160\ ℃ \end{cases} \quad (5.1)$$

where $f'_{c,d}$ is the dynamic compressive strength in MPa, $\dot{\varepsilon}$ is the strain rate in s^{-1} and $f'_{t,d}$ represents the dynamic splitting tensile strength in MPa.

5.6 Strain rate sensitivity

The DIF is a widely utilised metric that quantifies the enhancement in concrete's strength at high strain rates. The definition of DIF is the proportion of dynamic strength to static strength. Understanding DIF of concrete is crucial for accurately predicting the structural response, designing structural elements to withstand high-strain-rate events, and developing appropriate constitutive models. In accordance with the foregoing experiment results, the relationship between strain rate in compression of CUHPC and CDIF is plotted in Figure 5.12. It is worth noting that with the decline in temperature, CDIFs decreased gradually, which indicated the concrete material was more sensitive at ambient temperature rather than at low or cryogenic temperature in compression.

In fact, a large number of empirical formulas for NSC under different strain rate ranges have been derived and widely used. The predictive curve suggested by CEB-FIP model code [172] for DIF in compression at room temperature is given in Equation (5.2), which also plots in Figure 5.12. However, as mentioned above, this formula can only describe the critical strain rate for NSC at ambient temperature, in other words, it was not suitable for CUHPC at other temperature conditions. Therefore, new empirical formulas were derived for CUHPC at room temperature, -70 and -160 ℃ using experimental data, as shown in Equations (5.3) - (5.5). The derived empirical formulae fit well with the experimental data. In the current study, the inflection points in relation to CDIF were determined to be 30 s^{-1} at 20, -70 and -160 °C, which was the same as CEB-FIP model code [172].

$$CDIF = \frac{f_c}{f'_c} = \begin{cases} (\frac{\dot{\varepsilon}}{\varepsilon_s})^{1.026\alpha} & \text{for } \dot{\varepsilon} \leq 30\ \text{s}^{-1} \\ \gamma(\frac{\dot{\varepsilon}}{\varepsilon_s})^{1/3} & \text{for } \dot{\varepsilon} > 30\ \text{s}^{-1} \end{cases} \quad (5.2)$$

where ε_s = 3× 10^{-6} s^{-1}, $\alpha = \frac{1}{10+6f'_c/10}$ and f'_c is uniaxial compressive strength, γ = $10^{(7.11\alpha-2.33)}$.

The fitting curves of CDIFs for CUHPC at 20, -70 and -160 °C are also displayed in Figure 5.13. It was highlighted that with the decrease in the temperature, the CDIFs of CUHPC diminished. In fact, the material with a higher uniaxial compressive strength shows lower rate sensitivity [194, 195], this aligns with the observation of CUHPC's CDIF at low temperature. The occurrence of a phase transition within the pore network, wherein the pore water crystallised into an ice matrix upon exposure to cryogenic conditions [101]. It is noteworthy that at a temperature of -70 °C, the ice has not yet assumed complete control over its impact on the compressive strength, as the freezing process has merely initiated within the pores [98]. Upon further cooling to -160 °C, the ice within the pores becomes remarkably more rigid, freezing water further expands, leading to microcracking and weakening of the concrete matrix. As temperature decreases, different components of CUHPC contract at different rates, forming the microcrack in the ITZ [15]. Meanwhile, the freezing of water within the concrete's pore structure leads to a volumetric expansion of about 9% [196]. This expansion contradicts the overall shrinkage of the surrounding matrix, exacerbating the development of microcracks. These microcracks serves as initial defects. When subjected to impact loads, these initial defects rapidly coalesce into larger macrocracks, accelerating the path to ultimate failure, hence the CDIF under low temperatures is reduced.

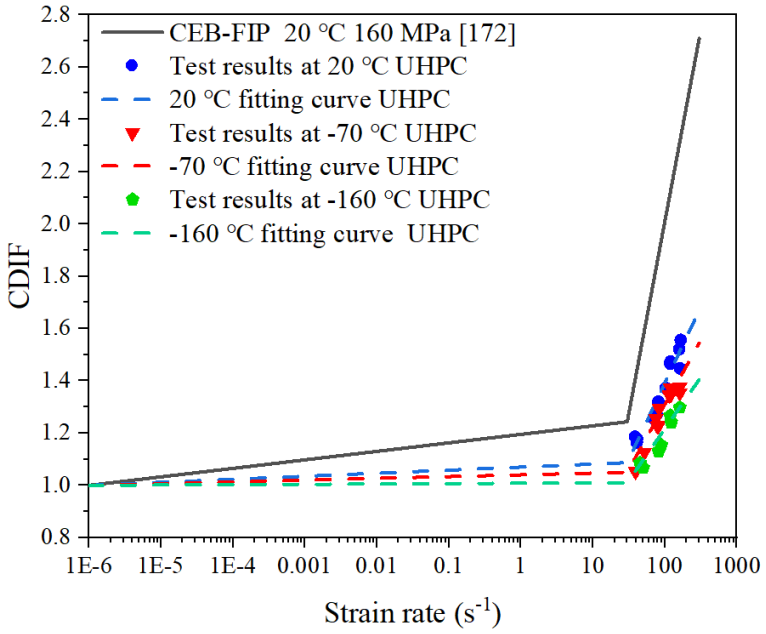

Figure 5.12 CDIFs for CUHPC at low temperature.

$$\text{CDIF at } 20\ ^\circ\text{C} = \begin{cases} 0.012\log\dot{\varepsilon} + 1.070 & \dot{\varepsilon} \le 30\ s^{-1} \\ 0.580\log\dot{\varepsilon} + 0.230 & \dot{\varepsilon} > 30\ s^{-1} \end{cases} \quad (5.3)$$

$$\text{CDIF at } -70\ ^\circ\text{C} = \begin{cases} 0.007\log\dot{\varepsilon} + 1.041 & \dot{\varepsilon} \le 30\ s^{-1} \\ 0.527\log\dot{\varepsilon} + 0.238 & \dot{\varepsilon} > 30\ s^{-1} \end{cases} \quad (5.4)$$

$$\text{CDIF at } -160\ ^\circ\text{C} = \begin{cases} 0.001\log\dot{\varepsilon} + 1.008 & \dot{\varepsilon} \le 30\ s^{-1} \\ 0.427\log\dot{\varepsilon} + 0.349 & \dot{\varepsilon} > 30\ s^{-1} \end{cases} \quad (5.5)$$

A unified model was utilised to gain a single equation to understand how DIF changed not only with strain rate but also with temperature in a continuous manner. It also enabled to predict CDIF values for temperatures and strain rates that were not directly tested. The following Equation (5.6) was obtained based on the experimental results in Appendix I. Figure 5.13 compares the outcomes of Equation (5.6) with the experimental results presented in Appendix I. The coefficient of determination (R^2) values was 0.96, which indicated a strong correlation between the forecasted and observed CDIFs, supporting a reliability and accuracy of the prediction formula.

$$\text{CDIF} = 0.557 + 0.001\times T + 0.284\times \log\dot{\varepsilon} + 0.059\times (\log\dot{\varepsilon})^2 + 0.0001\times T\times \log\dot{\varepsilon} \quad (5.6)$$

where T symbolises temperature in °C, -160 °C ≤ T ≤ 20 °C; $\dot{\varepsilon}$ represents as the strain rate, 38.5 s^{-1} ≤ $\dot{\varepsilon}$ ≤ 165.81 s^{-1}.

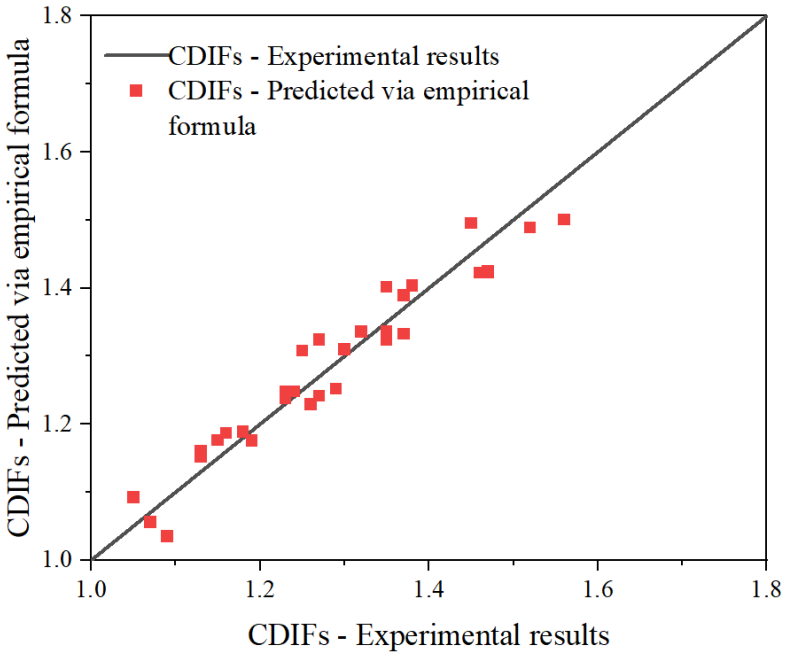

Figure 5.13 Comparison of predicted CDIFs to experimental results.

Figure 5.14 depicts the aggregated data and estimates for the TDIFs of CUHPC. The figure also compared the experimental data with the models proposed by CEB-FIP model code [172] as Equation (5.7) and Malvar and Crawford [173] as Equation (5.8), both of which used uniaxial compressive strength of 160 MPa at room temperature. It revealed that neither the CEB-FIP model code [172] nor Malvar and Crawford [173] adequately described the TDIFs of CUHPC at high strain rates. The inflection points, which represented the transition from the static to the dynamic regime, also did not align well with the observed data. The CEB-FIP model predicted an inflection point at 30 s^{-1}, while the Malvar and Crawford model suggested an inflection point at 1 s^{-1}, both of which did not match the experimental findings. In contrast, Park *et al.* [197] proposed a different relationship for the TDIFs of CUHPC, with a reported transition strain rate of 25 s^{-1}. Furthermore, Yang *et al.* [198] have pointed out that the inflection point in the TDIF-strain rate relationship can be influenced by various factors, like the fibre shape (straight, twisted, or hooked), matrix strength and fibre volume fraction. In the current study, the

inflection points were determined to be 1 s^{-1} at 20, -70 and -160 °C, the same as Malvar and Crawford [173].

$$TDIF = \frac{f_T}{f_{Ts}} = \begin{cases} (\frac{\dot{\varepsilon}}{\varepsilon_s})^{1.016\alpha} & \text{for } \dot{\varepsilon} \leq 30\ s^{-1} \\ \gamma(\frac{\dot{\varepsilon}}{\varepsilon_s})^{1/3} & \text{for } \dot{\varepsilon} > 30\ s^{-1} \end{cases} \quad (5.7)$$

where ε_s is equal to 3× 10^{-6} s^{-1}, $\alpha = \frac{1}{10+6f'_c/10}$ and f'_c is uniaxial compressive strength, $\gamma = 10^{(7.11\alpha-2.33)}$.

$$TDIF = \frac{f_T}{f_{Ts}} = \begin{cases} (\frac{\dot{\varepsilon}}{\dot{\varepsilon}_s})^{\delta} & \text{for } \dot{\varepsilon} \leq 1\ s^{-1} \\ \beta(\frac{\dot{\varepsilon}}{\dot{\varepsilon}_s})^{1/3} & \text{for } \dot{\varepsilon} > 1\ s^{-1} \end{cases} \quad (5.8)$$

where f_T and f_{Ts} represent the dynamic as well as static tensile strength, respectively. $10^{-6} \leq \dot{\varepsilon} \leq 160$ s^{-1}, $\dot{\varepsilon}_s$ = 1× 10^{-6} s^{-1}, $\delta = \frac{1}{1+8f'_c/10}$, f'_c is uniaxial compressive strength and $\log\beta = 6\delta - 2$.

The empirical formulae of TDIFs for CUHPC at 20, -70 and -160 °C were derived and showed in Equations (5.9) - (5.11). The fitting curve for each temperature presents in Figure 5.14. It demonstrated that the empirical formula derived in the study could accurately match the experimental data for the TDIFs of CUHPC, indicating a high degree of precision and reliable predictive capabilities for model. It can be observed that with decrease in temperature, the TDIFs increased dramatically for CUHPC, showing the highest rate sensitivity at -160 °C. At a strain rate of approximately 20 s^{-1}, the TDIFs of CUHPC at ambient temperature were 11.00% and 35.50% lower than at -70 and -160 °C, respectively. In addition, the TDIFs of CUHPC at -70 and -160°C exceeded those at ambient temperature by 11.26% and 23.38% at a strain rate nearly 40 s^{-1}. Similarly, at a strain rate of around 60 s^{-1}, the TDIFs of CUHPC were 7.19% lower at ambient temperature than at -70°C, and 28.01% lower than at -160°C. The TDIFs of CUHPC in specific strain rate 80 s^{-1} at -70 and -160 °C had a spectacular rise of nearly 17.33% and

29.24% compared with those at the room temperature, respectively. The TDIFs of CUHPC showed an increasing tendency as the temperature decreased, indicating a high sensitivity to strain rate under lower temperature conditions.

The hypothesis for this phenomenon is as follows. As temperatures drop, ice crystals progressively form within the micro-cracks and pores of the concrete. These ice formations act as natural bridges across the micro-cracks and strengthen the bond between aggregate particles and the surrounding cement paste [101]. As water in the pores freezes, it forms an ice skeleton within the concrete microstructure. This ice network can effectively enhance the internal structure of the concrete at low temperatures. The pre-stressed state induced by the formation of the ice veins can retard or inhibit the initiation and growth of internal cracks within the material. On the other hand, the bond between steel fibres and the concrete matrix improves at lower temperatures [104, 191]. This enhancement is primarily attributed to the increased frictional resistance that develops under cryogenic conditions. A comparison between NSM [186] and CUHPC at cryogenic conditions (-160 °C) and a high strain rate (80 s^{-1}) revealed a significant difference in the TDIF. It found that the TDIF of NSM which data based on the results from Chi *et al.* [186] was 1.61 times greater than that of CUHPC under -160 °C at the strain rate of 80 s^{-1}. It was important to note that the primary distinction between these two materials was the presence of steel fibres in CUHPC, as neither contained coarse aggregates. Kim et al. [191] found out that deeper and more severe scratches on the surface of the fibres after testing them under cryogenic conditions, which indicated an improvement of their ability to resist being pulled out of the concrete.

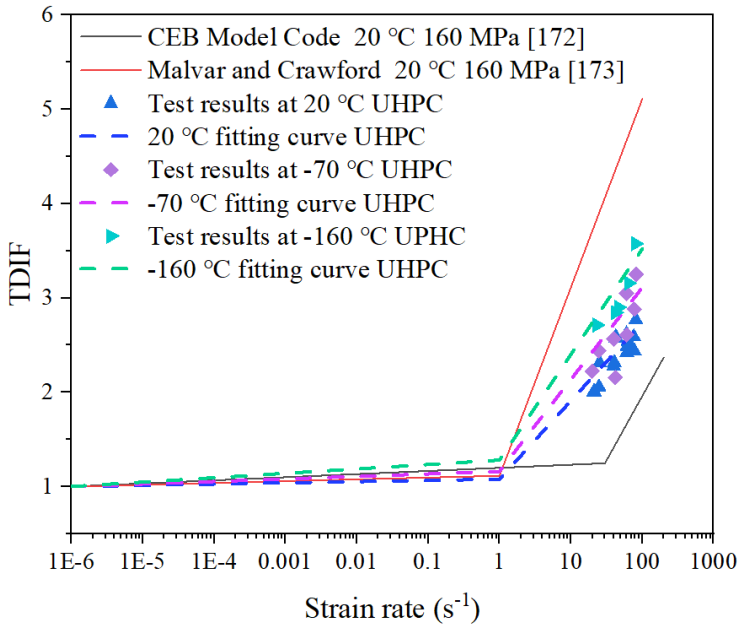

Figure 5.14 TDIFs for CUHPC at low temperature.

$$\text{TDIF at } 20\ ^\circ\text{C} = \begin{cases} 0.013\log\dot{\varepsilon} + 1.078 & \dot{\varepsilon} \le 1\ s^{-1} \\ 0.975\log\dot{\varepsilon} + 0.790 & \dot{\varepsilon} > 1\ s^{-1} \end{cases} \quad (5.9)$$

$$\text{TDIF at } -70\ ^\circ\text{C} = \begin{cases} 0.027\log\dot{\varepsilon} + 1.160 & \dot{\varepsilon} \le 1\ s^{-1} \\ 1.356\log\dot{\varepsilon} + 0.395 & \dot{\varepsilon} > 1\ s^{-1} \end{cases} \quad (5.10)$$

$$\text{TDIF at } -160\ ^\circ\text{C} = \begin{cases} 0.047\log\dot{\varepsilon} + 1.281 & \dot{\varepsilon} \le 1\ s^{-1} \\ 1.489\log\dot{\varepsilon} + 0.544 & \dot{\varepsilon} > 1\ s^{-1} \end{cases} \quad (5.11)$$

Like CDIFs, a single equation to predict TDIFs of CUHPC was created based on experimental data in Appendix J. Figure 5.15 shows the results of comparing the empirical formula with the experimental data. The coefficient of determination (R^2) for Equation (5.12) was 0.95, demonstrating a greater level of accuracy in predicting the TDIFs of CUHPC at low temperature with various strain rate.

$$\text{TDIF} = 0.9614 - 0.002\times T + 0.702\times\log\dot{\varepsilon} + 0.119\times(\log\dot{\varepsilon})^2 - 0.0005\times T\times\log\dot{\varepsilon} \quad (5.12)$$

where T stands for temperature in °C, -160 °C $\le T \le$ 20 °C; $\dot{\varepsilon}$ represents as the strain rate, 19.89 $s^{-1} \le \dot{\varepsilon} \le$ 81.32 s^{-1}.

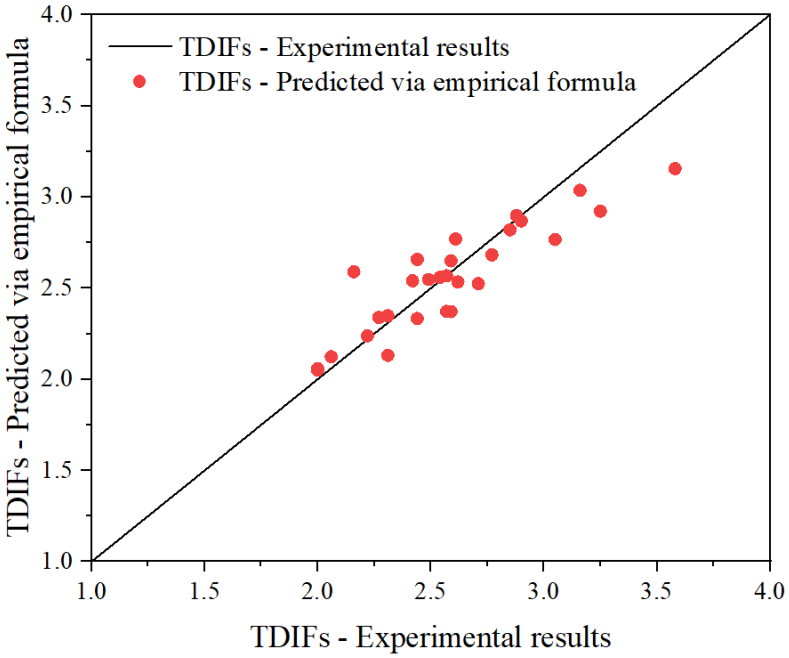

Figure 5.15 Comparison of predicted TDIFs to experimental results.

5.7 Limitations

While this study provides valuable information about CUHPCs' dynamic behaviour at low and cryogenic temperatures, it is important to acknowledge its limitations. The research primarily focused on macroscopic mechanical properties and did not delve deeply into the microstructural mechanisms underlying the observed dynamic behaviour. Advanced microstructural characterisation techniques such as X-ray computed tomography (CT) scanning and SEM would be beneficial for future studies to provide a more comprehensive understanding of the material's behaviour. CT scanning could enable three-dimensional visualisation and quantification of internal void distribution, crack propagation patterns, and pore structure evolution at different temperatures. Similarly, high-resolution SEM analysis would allow detailed examination of the ITZ between aggregates and cement paste, revealing potential microstructural changes, ice crystal formation mechanisms, and their impact on bond strength at cryogenic temperatures. Such advanced imaging techniques would help establish direct correlations between microstructural alterations and the observed macroscopic mechanical properties,

particularly in understanding the role of pore size distribution, ice crystallisation patterns, and ITZ degradation in the dynamic response of CUHPC under extreme temperature conditions.

5.8 Summary

In view of the comprehensive experimental investigation presented in the current study, several key conclusions can be drawn regarding the dynamic behaviour of CUHPC at low and cryogenic temperatures:

- CUHPC exhibited superior resistance to damage and fragmentation, especially under dynamic loading conditions at low temperatures. The failure patterns of CUHPC were characterised by more localised cracking and reduced disintegration, even at high strain rates and cryogenic temperatures.
- The dynamic compressive strength of CUHPC increased significantly with strain rate across all temperature conditions. However, the rate of strength increase slowed down at higher strain rates (above 120 s^{-1}). At a given strain rate, the dynamic compressive strength of CUHPC was higher at the lower temperatures, with the highest strength observed at -160 °C.
- The dynamic compressive elastic modulus of CUHPC exhibited a complex relationship with temperature. It was the highest at -70 °C owing to the ice filling and binding effects within the concrete pores, but decreased at -160 °C resulting from the thermal expansion mismatch between the CUHPC constituents.
- Under dynamic splitting tensile loading, CUHPC displayed a transition in failure modes from shear failure at lower strain rates to tensile failure at higher strain rates. The damage severity was more pronounced at lower temperatures (-70 and -160 °C) in comparison with room temperature.

- The relationship between dynamic compressive and splitting tensile strength at various temperature was derived.
- DIFs in compression of CUHPC decreased with decline in temperature, indicating reduced strain rate sensitivity at lower temperatures. In contrast, DIFs in tension of CUHPC increased when the temperature went down.

The experimental investigation of CUHPC under cryogenic conditions yields significant implications for structural design and construction in extreme cold environments. CUHPC demonstrated superior performance in terms of ductility, controlled failure modes, and reduced strain rate sensitivity under dynamic loading conditions at low and extremely low temperatures. The observed enhancement in compressive and tensile strengths at -70 °C and -160 °C facilitates the development of more efficient structural sections while simultaneously providing higher safety factors for specialised infrastructure such as ACLNG storage facilities and arctic installations. This rendered CUHPC a more suitable material for concrete infrastructure subjected to coupled extreme environmental and loading conditions, such as those encountered in cryogenic storage facilities or other harsh environments. However, the documented strain rate sensitivity variations—specifically decreased compressive DIFs and increased tensile DIFs at lower temperatures—necessitate a recalibration of dynamic amplification factors in impact-prone regions. Furthermore, the transition toward more brittle failure modes at cryogenic temperatures, particularly under high strain rates, underscores the requirement for advanced reinforcement strategies and confinement techniques to ensure structural integrity during extreme loading events.

Chapter 6. EXPERIMENTAL STUDY ON DYNAMIC CHARACTERISATION OF CEMENT BASED ULTRA-HIGH PERFORMANCE CONCRETE AFTER CRYOGENIC FREEZE-THAW CYCLES

6.1 Introduction

The increasing demand for advanced construction materials capable of withstanding extreme environmental conditions has prompted extensive research into CUHPC. This study investigated the dynamic compressive properties of CUHPC after FT cycles. CUHPC specimens were exposed to 2, 4 and 8 FT cycles at -160 °C before being tested under dynamic loading conditions at the strain rate of 80, 130 and 180 s^{-1} by the use of a SHPB device. The effects of strain rate and FT cycles on the compressive strength, energy absorption capacity, and microstructural changes of CUHPC were examined. Results revealed that dynamic compressive strength increased with strain rate for all FT cycle conditions. The study also found that the CDIF of CUHPC was influenced by FT exposure, higher CDIFs were observed after more FT cycles. The CDIF after 4 and 8 FT cycles increased 1.31% and 2.61%, respectively, in comparison with 2 FT cycles at the strain rate of 130 s^{-1}. Repeated FT cycles led to progressive deterioration of the CUHPC matrix and fibre-matrix interface, as evidenced by Scanning Electron Microscopy (SEM) analysis. After 8 FT cycles, the Calcium Silicate Hydrate (C-S-H) structure experienced further damage, with noticeable cracks forming between the steel fibres and matrix, indicating a weakening of the bond between these components. The behaviour and durability of CUHPC under extreme environmental and dynamic loading conditions are better understood during this research.

6.2 Experimental setup

6.2.1 Material and specimen preparation

The CUHPC mixture utilised 42.5 grade ordinary Portland cement, supplemented with reactive silica fumes to enhance the formation of calcium silicate hydrate. Micro straight steel fibres, comprising 2% of the mixture by volume, were manually dispersed to ensure uniform distribution and random orientation in the CUHPC matrix. The properties of steel fibre are listed in Table 5.1 and the detailed composition of CUHPC is proportioned as per Table 5.2. The CUHPC was mixed in a lab concrete mixer and then poured into 70 mm inner diameter PVC pipe moulds. Following appropriate curing, the samples were demoulded and precision-cut into cylinders with dimensions of 70 mm in diameter and 35 mm in height for the tests. To guarantee an even distribution of load during the testing process, the end faces of each specimen were machined to a high degree of smoothness and parallelism, achieving a surface roughness of 0.02 mm. This preparation process was essential to obtain reliable and consistent results in the subsequent dynamic compression experiments.

6.2.2 Cryogenic FT cycle procedure

The cryogenic FT cycle procedure for CUHPC specimens was conducted to evaluate the cumulative effects of repeated exposure to extreme low temperatures regarding dynamic compression behaviour. The protocol involved subjecting the samples to a controlled cooling process within a low-temperature chamber (see Figure 4.3). The specimens were cooled at a rate of 1 °C per minute to the target cryogenic temperature of -160 °C. Upon attaining this temperature, the samples were kept in the chamber for additional 4 hours to ensure thermal equilibrium throughout the specimen. Following the cold exposure phase,

the specimens were removed from the chamber and allowed to thaw and equilibrate at ambient room temperature for a period of 24 hours. This process is defined as one complete FT cycle. To assess the progressive impact of cyclic cryogenic exposure, the experiment was designed with 2, 4 and 8 FT cycles. Figure 6.1 shows concrete samples after 2, 4 and 8 times FT cycles.

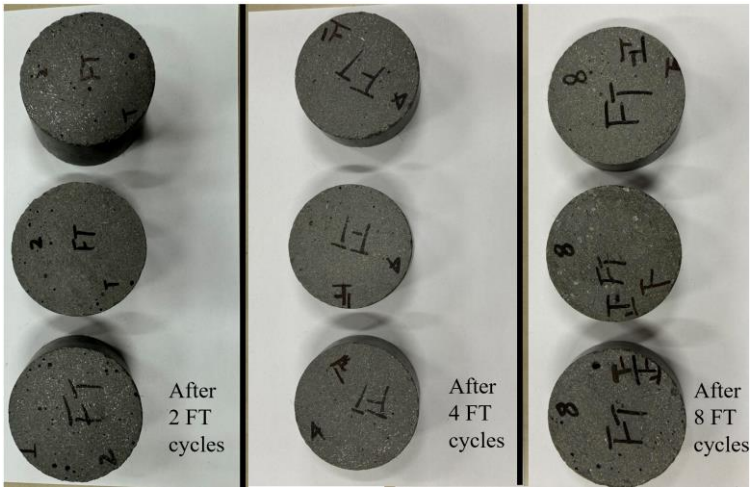

Figure 6.1 Sample specimens after various number of FT cycles.

6.3 Quasi-static tests

The uniaxial compression tests on CUHPC were conducted using cylindrical specimens as mentioned in Section 6.2.1. The samples underwent the cryogenic FT cycle process as previously described. The tests were performed on a 300-ton hydraulic testing machine at a loading rate of 0.5 mm/min.

The uniaxial compressive strength of CUHPC after 0, 2, 4 and 8-times FT cycles were obtained as shown in Figure 6.2. It exhibited a clear correlation between the number of FT cycles and the compressive strength of CUHPC. Without FT cycles, CUHPC demonstrated its compressive strength of 161.46 MPa. A gradual deterioration in its compressive strength was observed as the material was subjected to more FT cycles. The compressive strength after 2 and 4 times of FT cycle was around 159.60 and 155.72 MPa,

respectively. After 8 FT cycles it exhibited the lowest compressive strength, approximately 151.51 MPa, which has lost approximately 6.5% of its initial compressive strength. Similar to conventional concrete, this decline in compressive strength was attributed to the cumulative damage induced by repeated FT cycles. Notably, CUHPC performed better in preserving its mechanical strength after FT cycles when compared against NSC, previous study on NSC lost about 6%, 15% and 27% after 2, 4 and 8 FT cycles [199].

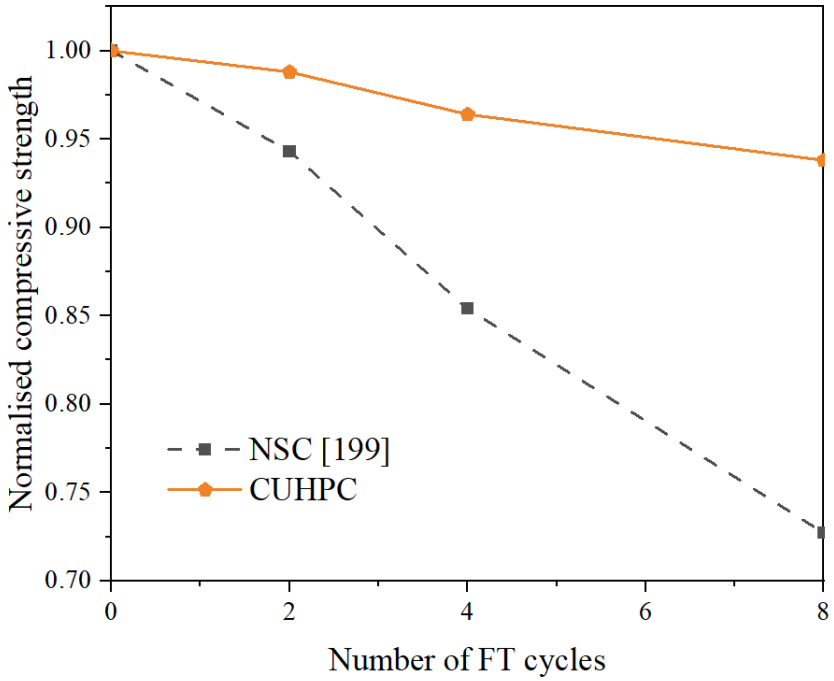

Figure 6.2 The relationship between varying FT cycles and material compressive strength.

6.4 SHPB tests

Prior to conducting the SHPB tests, the CUHPC specimens of the same size as the static compression tests were loaded against the same FT cycles as defined in Section 6.2. More details were mentioned in Section 4.2.2.3. By plotting the calculated stress against strain, stress-strain curves were obtained, allowing for the determination of dynamic

compressive strength, modulus of elasticity and other key mechanical properties of the CUHPC specimens under high strain rate loading conditions.

6.4.1 Test results and analysis

6.4.1.1 Failure characteristics of specimens subjected to combined loading

Figure 6.3 presents final failure patterns of CUHPC specimens subjected to varying numbers of FT cycles (2, 4, and 8) and strain rates (80, 130 and 180 s^{-1}). In terms of 2 FT cycles, the specimen maintained its integrity with minor surface cracks at strain rate of 81.90 s^{-1}. As strain rates increased to 131.14 s^{-1} and 180.29 s^{-1}, progressive damage was observed, culminating in significant fragmentation and spalling at the highest rate. While for 4 FT cycles, the damage pattern was similar to 2 FT cycles, but with enhanced deterioration. At 86.76 s^{-1}, surface cracks were more pronounced. The specimen at 131.72 s^{-1} showed increased fragmentation, while at 175.48 s^{-1}, severe disintegration was evident. The most severe damage was observed after 8 FT cycles. Even at the lowest strain rate (82.99 s^{-1}), significant surface degradation was visible. At 130.31 s^{-1}, large fragments separated from the core. The specimen at 193.61 s^{-1} completely disintegrated into small fragments.

The number of FT cycles played a crucial role in the degradation of CUHPC's dynamic compressive strength. When the number of cycles increased from 2 to 8, the specimens exhibited progressively worse damage at comparable strain rates. This observation suggested that repeated FT cycles caused cumulative damage within the CUHPC microstructure. FT cycles induced expansive forces within the concrete matrix due to water freezing and thawing. The degradation was attributed to the formation of micro cracks within the hardened cement matrix, caused by the expansive forces of water as it transformed into ice. Monteiro et al. [200] provided further evidence for this phenomenon

in their research, which revealed that multiple freeze-thaw cycles led to the development of micro-cracks in close proximity to pore spaces within the hardened cement paste. This process created microcracks and weakened the internal structure of the CUHPC, resulting in microstructure damage.

81.90 s^{-1} 131.14 s^{-1} 180.29 s^{-1}

(a) 2 FT cycles

86.76 s^{-1} 131.72 s^{-1} 175.48 s^{-1}

(b) 4 FT cycles

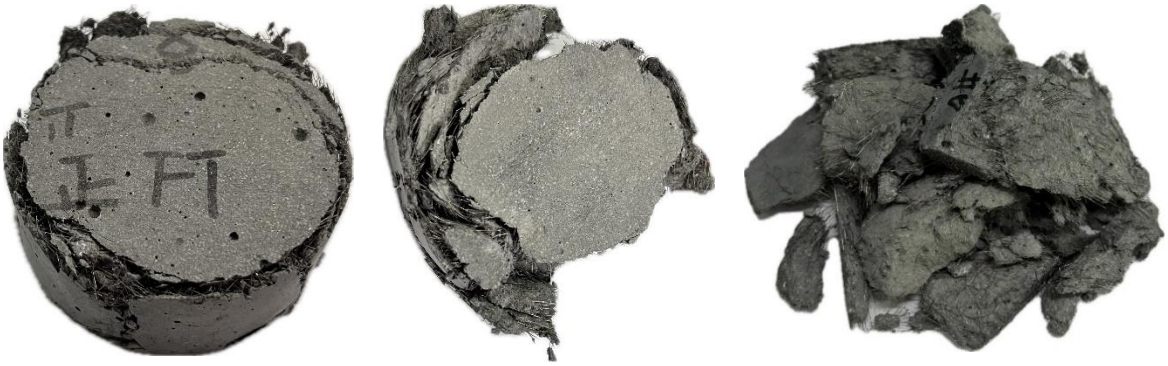

82.99 s^{-1} 130.31 s^{-1} 193.61 s^{-1}

(c) 8 FT cycles

Figure 6. 3 Dynamic compressive failure modes of CUHPC after FT cycles.

Figure 6.4 depicts the failure process of CUHPC after 2, 4 and 8 FT cycles at the strain rate of roughly 130 s^{-1}, as captured by an ultra-high-speed camera. It showed the gradual evolution of damage, with the formation and propagation of cracks becoming increasingly evident over time, culminating in the final failure of the specimen. A more developed network of cracks was evident after 4 FT cycles, indicating a higher degree of damage accumulation as compared to after 2 FT cycles. Also, the CUHPC specimen after 8 FT cycles showed widespread cracking and a highly fragmented internal structure, suggesting advanced deterioration in contrast with 2, and 4 cycles. It is noteworthy that when compared to NSC [199] under ultra-high-speed camera observation, the CUHPC specimens subjected to 2 and 4 FT cycles exhibited less pronounced microcracking at a similar time frame of 65 μs. This reduced prevalence of microcracks in CUHPC may be caused by the bridging effect of steel fibres within the matrix. The inclusion of steel fibre reinforcement in CUHPC potentially contributed to enhanced crack resistance and improved cohesion of the composite material under dynamic loading conditions, even after exposure to FT cycles. The comparison of Figure 6.4 (a), (b) and (c) clearly demonstrated that when the number of FT cycles rose, the crack density and overall damage in the CUHPC material became more severe.

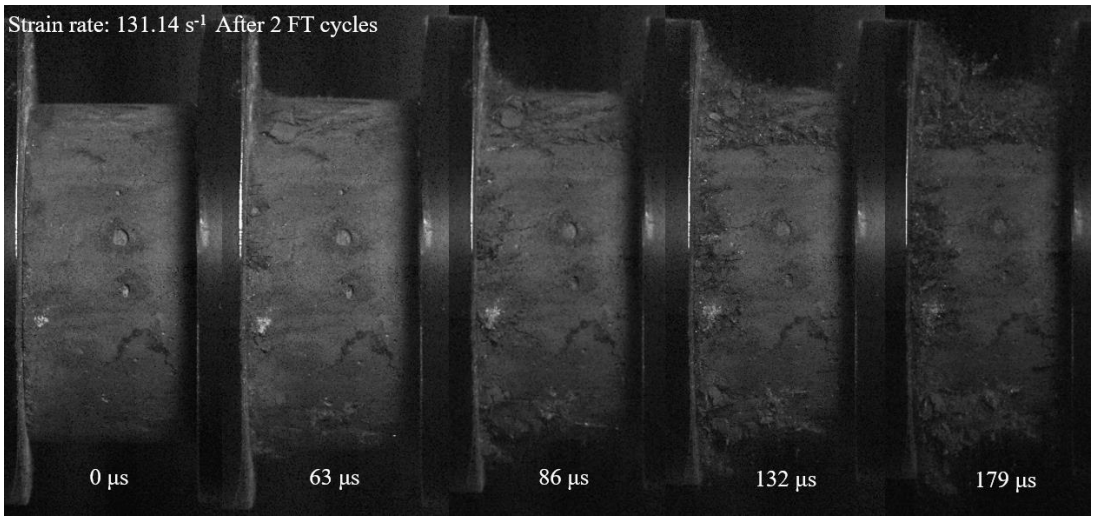

(a)

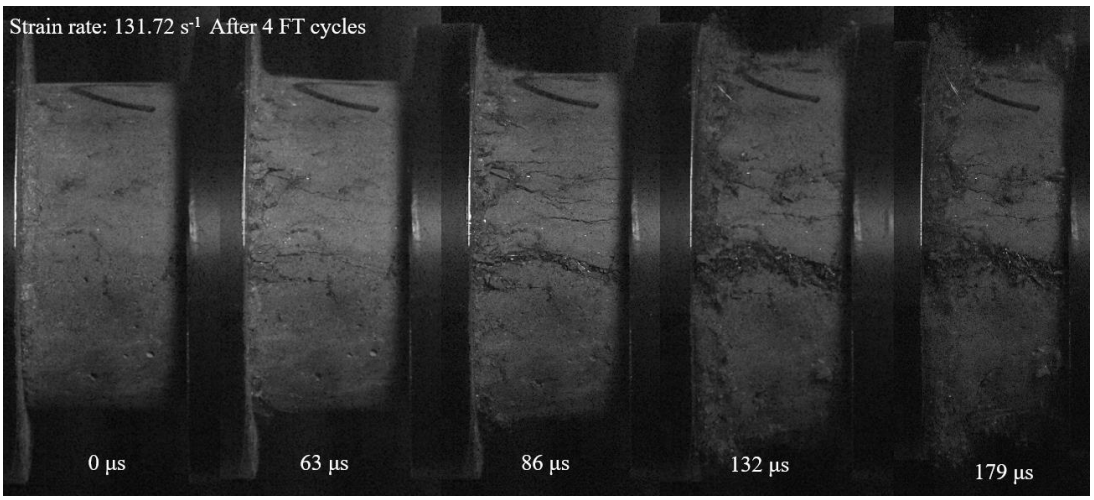

(b)

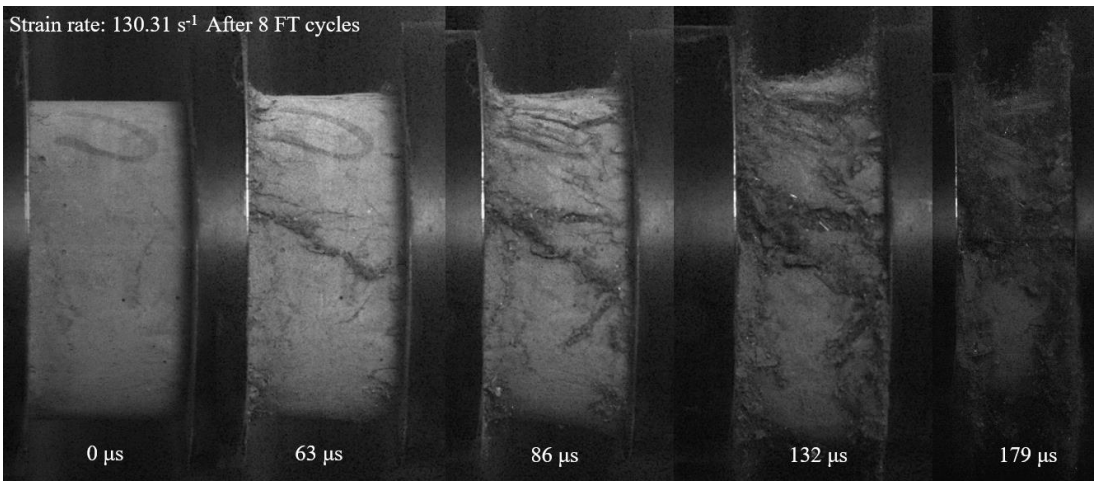

(c)

Figure 6. 4 Failure process of CUHPC after FT cycles under dynamic axial compression.

6.4.1.2 Effect of cryogenic FT cycles on strain rate

This study investigated the influence of strain rate as well as cryogenic FT cycles on the dynamic compressive behaviour of CUHPC. The results, presented in Figure 6.5, demonstrate a remarkable increase in dynamic compressive strength with strain rates. Unsurprisingly, at 20 °C without FT cycle, the specimen showed markedly increases in strength at various strain rates. Specifically, at a strain rate of 78.86 s^{-1}, the strength increased by 31.56%. At 134.13 s^{-1}, a more substantial increase of 54.86% was observed. The most dramatic improvement was seen at the highest strain rate of 177.67 s^{-1}, where the strength increased by 56.27%. These results revealed a clear correlation between increasing strain rates and enhanced dynamic strength.

After 2 FT cycles, the specimen demonstrated substantial enhancements in dynamic strength, with increases of 32.01%, 51.55%, and 60.93% at strain rates of 81.9 s^{-1}, 131.14 s^{-1}, and 179.26 s^{-1}, respectively, when compared to the static strength under identical FT conditions (see Figure 6.5(b)).

After 4 FT cycles, the dynamic stress-strain curves maintained a similar trend to those observed after 2 FT cycles, with peak stresses consistently rising at higher strain rates. The dynamic compressive strength showed signal increases of 43.46%, 49.94%, and 66.99% at strain rates of 82.86 s^{-1}, 131.72 s^{-1}, and 180.81 s^{-1}, respectively, relative to the static strength under the same FT exposure (see Figure 6.5(c)).

After 8 FT cycles, the specimen exhibited dynamic strength increments of 42.55%, 51.45% and 80.48% at strain rates of 80.95 s^{-1}, 130.31 s^{-1}, and 193.61 s^{-1}, respectively, when compared to the uniaxial compressive strength under identical FT conditions.

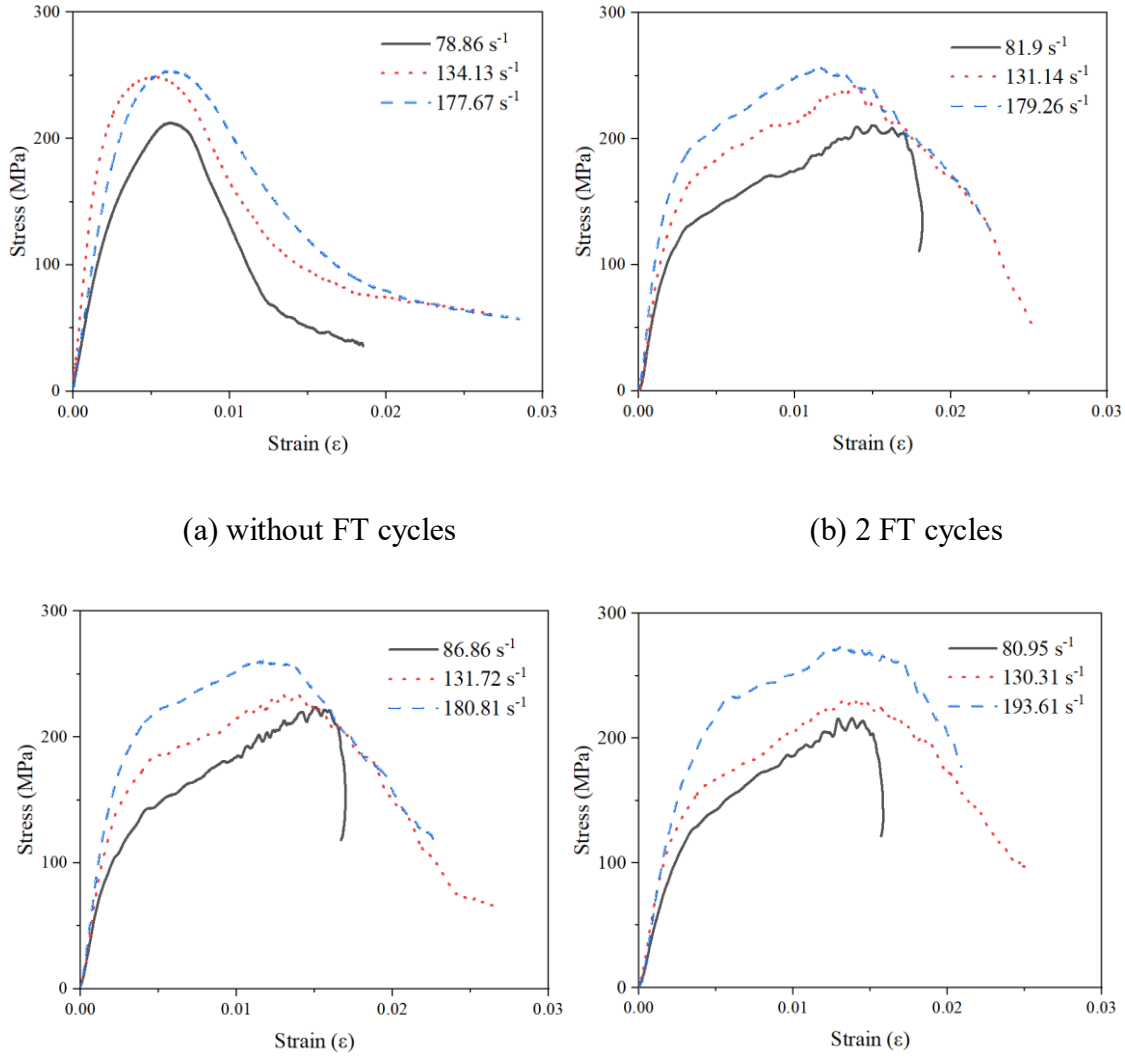

(a) without FT cycles

(b) 2 FT cycles

(c) 4 FT cycles

(d) 8 FT cycles

Figure 6. 5 Dynamic compressive stress-strain curve after various FT cycles.

Figure 6.6 (a), (b) and (c) shows stress-strain curves for CUHPC subjected to different numbers of FT cycles at various strain rates, corresponding to strain rates of approximately 80 s^{-1}, 130 s^{-1}, and 180 s^{-1}, respectively. The stress-strain curves exhibited notable differences between samples subjected to varying FT cycles. As the number of FT cycles increased, a pronounced nonlinearity emerged in the material's response, particularly evident in the early to mid-strain ranges. This FT-induced nonlinearity showed as curved initial responses, multiple inflection points, and regions of varying stiffness throughout the deformation process. The effect was most significant at lower

strain rates and became more pronounced with an increasing number of FT cycles. In contrast, samples without FT exposure demonstrated a more conventional stress-strain relationship, characterised by a distinct linear elastic region followed by yielding and strain softening. The FT cycled specimens exhibited reduced initial stiffness as compared to samples without FT cycle.

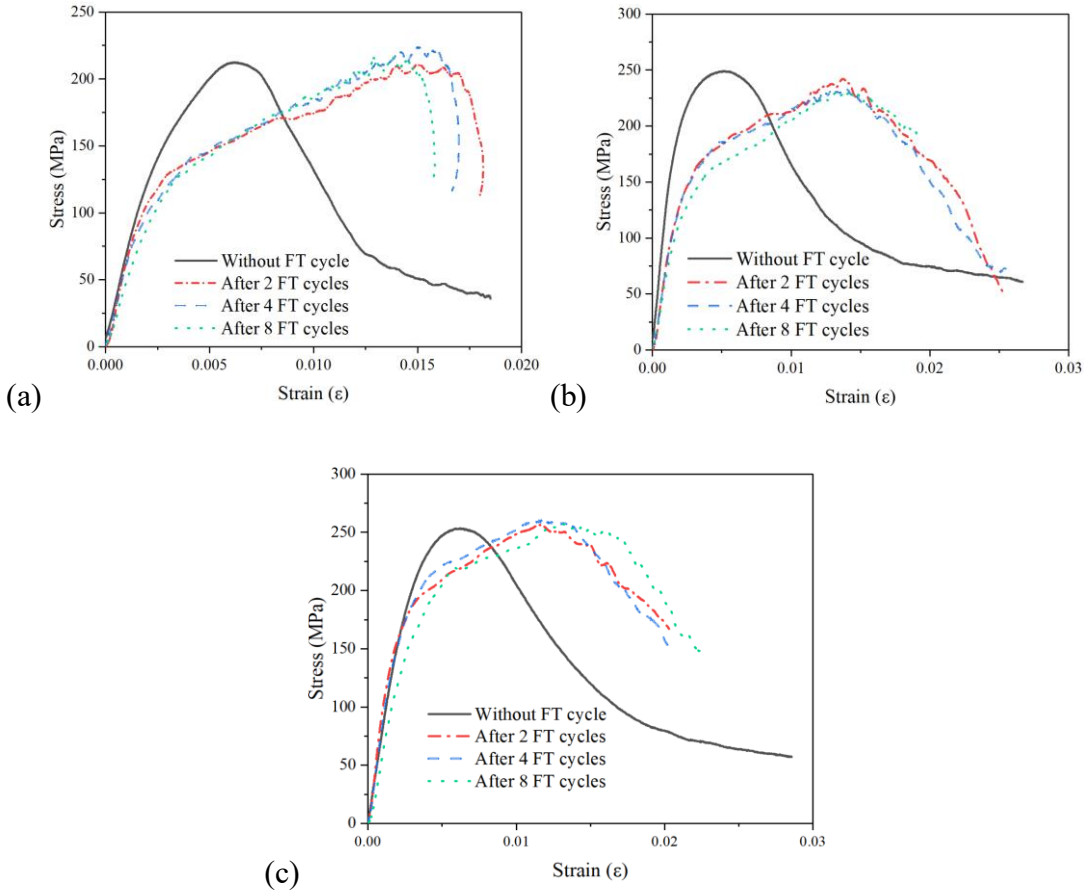

Figure 6. 6 Comparison of stress-strain curve with various FT cycles under same strain rate: (a) 80 s^{-1} (b) 130 s^{-1} (c) 180 s^{-1}.

6.4.1.3 Dynamic constitutive model of CUHPC after FT cycles

The Zhu–Wang–Tang (ZWT) constitutive model [201] was employed to characterise the dynamic stress-strain relationship of CUHPC subjected to FT cycling. The ZWT model is a commonly used model for describing the dynamic behaviour of various materials [202-204]. This model, based on viscoelastic principles, incorporated both nonlinear and linear transient responses [205] to accurately represent material behaviour under dynamic

loading conditions. The mechanical model of the ZWT constitutive equation can be composed of one nonlinear transient response model and two Maxwell models, which can be defined as,

$$\sigma = E_0\varepsilon + \alpha\varepsilon^2 + \beta\varepsilon^3 + E_1\int_0^t \dot{\varepsilon}\exp(-\frac{t-\tau}{\theta_1})d\tau + E_2\int_0^t \dot{\varepsilon}\exp(-\frac{t-\tau}{\theta_2})d\tau \quad (6.1)$$

where σ, ε and $\dot{\varepsilon}$ denote stress, strain and average strain rate; E_0, α, β are elastic constants to explain the nonlinear transient response model; the first Maxwell model (with parameters E_1 (elastic constant 1), θ_1 (relaxation time 1)) is to explain the viscoelastic response at low strain rates (quasi-static compression); the second Maxwell body (with parameters E_2 (elastic constant 2), θ_2 (relaxation time 2)) is to explain the viscoelastic response at high strain rates (dynamic impact).

In dynamic impact scenarios, the short duration of impact experiments did not have sufficient time to relax and can be replaced by an elastic element. As a result, the first Maxwell element can be approximated as a purely elastic spring, allowing the elastic moduli E_0 and E_1 to be combined [202, 206]. Consequently, Equation (6.1) can be simplified as follows,

$$\sigma = E_0\varepsilon + \alpha\varepsilon^2 + \beta\varepsilon^3 + E_2\int_0^t \dot{\varepsilon}\exp(-\frac{t-\tau}{\theta_2})d\tau \quad (6.2)$$

The degradation of concrete is primarily driven by the development of internal damage such as microcracks. These damages, including microcracks, cause a weakening effect on the macroscopic level. The damage parameter D can then be expressed as [207],

$$\sigma_a = \sigma(1 - D) \quad (6.3)$$

when $D = 0$, it indicates the material is undamaged. If D = 1, it signifies the material has completely lost its load-bearing capacity.

According to Wang et al. [208, 209], the cementitious materials' parameter D can be stated as follows,

$$D = \begin{cases} 0 & \varepsilon \le \varepsilon_{th} \\ K_D \dot{\varepsilon}^{(A-1)} (\varepsilon - \varepsilon_{th})^B & \varepsilon > \varepsilon_{th} \end{cases} \tag{6.4}$$

where K_D, A and B are the material parameters; ε_{th} stands for the threshold strain of material cumulative damage.

The dynamic behaviour of CUHPC after exposed FT cycles, accounting for material damage, can be described by the constitutive equation presented in Equation (6.6).

$$\sigma_a = K_D \dot{\varepsilon}^{(A-1)} (\varepsilon - \varepsilon_{th})^B \left[E_0 \varepsilon + \alpha \varepsilon^2 + \beta \varepsilon^3 + E_2 \int_0^t \dot{\varepsilon} \exp(-\frac{t-\tau}{\theta_2}) d\tau \right] \tag{6.5}$$

Based on the updated ZWT constitutive model, the predicted stress-strain curves of CUHPC after varying FT cycles are presented in Figure 6.7. The model matched the experimental data across all FT cycle conditions, indicating its accuracy in predicting CUHPC behaviour. Table 6.1 summarises the constitutive model parameters used to fit the CUHPC behaviour under different FT cycles and strain rates.

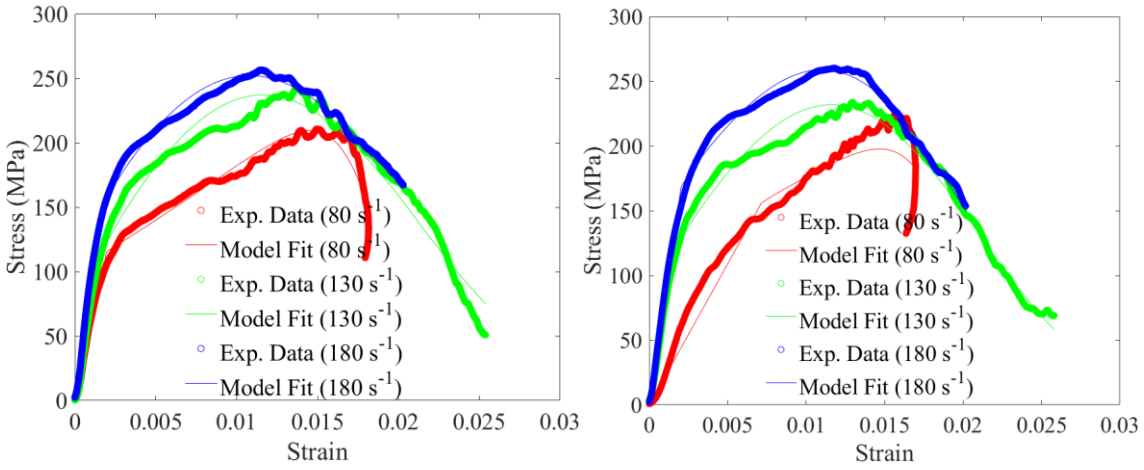

(a) 2 FT cycles (b) 4 FT cycles

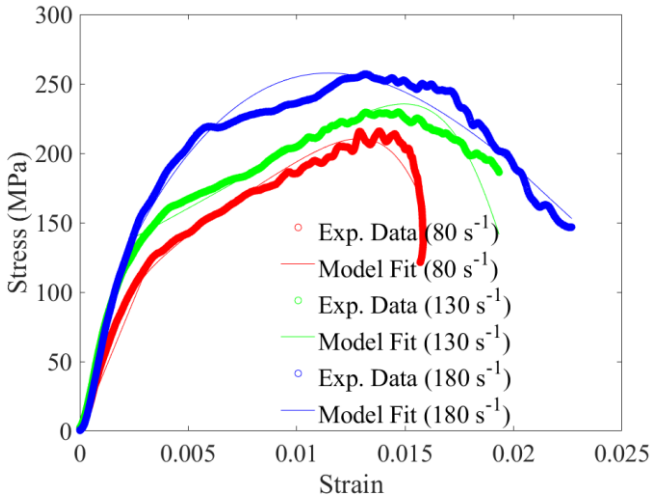

(c) 8 FT cycles

Figure 6.7 Comparison between experimental data and predicted model after FT cycles.

Table 6. 1 Constitutive model parameters for fitting CUHPC under different FT cycles.

No. FT	Strain rate (s^{-1})	E_0 (GPa)	E_2 (GPa)	θ_2 (μs)	K_D	α (GPa)	A	B	ε_{th}	R^2
2	81.90	5.52	41.92	0.04	53	1.63	2.11	0.16	4.19E-3	0.97
2	131.14	5.52	52.45	0.63	50	1.63	2.07	0.04	4.19E-3	0.90
2	179.26	5.52	93.71	0.45	50	1.63	2.03	0.17	4.19E-3	0.93
4	86.86	5.52	34.53	0.21	50	0.97	2.05	0.18	4.19E-3	0.94
4	131.72	5.52	54.38	0.64	50	0.97	2.07	0.62	4.19E-3	0.93
4	180.81	5.52	77.18	0.33	50	0.97	2.03	0.07	4.19E-3	0.98
8	80.95	5.52	62.92	0.27	30	0.61	2.03	0.06	4.19E-3	0.98
8	130.31	5.52	65.94	0.88	30	0.61	1.93	0.07	4.19E-3	0.97
8	193.62	5.52	60.61	0.43	30	0.61	1.43	0.16	4.19E-3	0.88

6.4.1.4 Specific energy absorption

During SHPB test, W_i, W_r, W_t are the energy caused by incident, reflected as well as transmitted wave, respectively. The energy absorbed by the specimen W_s, can be expressed as [210, 211],

$$W_s = W_i - W_r - W_t \tag{6.6}$$

According to Fu et al. [212], Specific Energy Absorption (SEA) refers to the amount of stress wave energy absorbed per unit volume of concrete. It is computed as follows,

$$SEA = \frac{EC_0A_e}{A_sL}[\varepsilon_i^2(t) - \varepsilon_r^2(t) - \varepsilon_t^2(t)]dt \quad (6.7)$$

The parameters in Equation (6.8) have been mentioned previously.

To explore the impact of FT cycles in relation to the dynamic behaviour of CUHPC specimens, the energy absorption capacity of the CUHPC specimens is analysed. Figure 6.8 shows that the *SEA* of CUHPC after 0-, 2,4- and 8-times cryogenic FT cycles. As the strain rate increased, the *SEA* of CUHPC rose in a nearly linear fashion. Without FT cycles, the CUHPC exhibited the highest energy absorption capacity at most strain rates. This could be ascribed to the presence of steel fibres. The limited time for crack propagation might lead to a more effective bridging action by the fibres, enhancing energy dissipation through fibre pull-out and debonding [213]. This would contribute to a higher energy absorption capacity despite the presence of microcracks. Furthermore, the efficiency of fibre pull-out in absorbing energy was highly dependent on the fibre-matrix bond. Stronger bonds, potentially achieved through the use of supplementary cementitious materials [214], can promote more energy absorption during fibre pull-out before interfacial debonding occurs.

However, as the number of FT cycles increased to 2, 4 and 8, there was a slight decline in energy absorption. For example, the *SEA* of CUHPC after 2, 4 and 8 FT cycles was reduced by 18.12%, 27.47% and 32.00% as compared to the scenario without FT cycle with the strain rate approximately 80 s^{-1}. CUHPC's energy absorption capacity diminished with more FT cycles, exhibiting a 7.55% reduction after 2 cycles, a 10.25% decline after 4 cycles and a 15.69% reduction after 8 cycles as compared to 0 cycles, when tested at a strain rate of about 130 s^{-1}. This phenomenon possibly indicated the degradation of the concrete matrix or fibre-matrix interface. Initial FT cycles might induce micro-cracks

[215] that contributes to energy dissipation, potentially creating preferential pathways for crack propagation and reducing the overall energy absorption capacity.

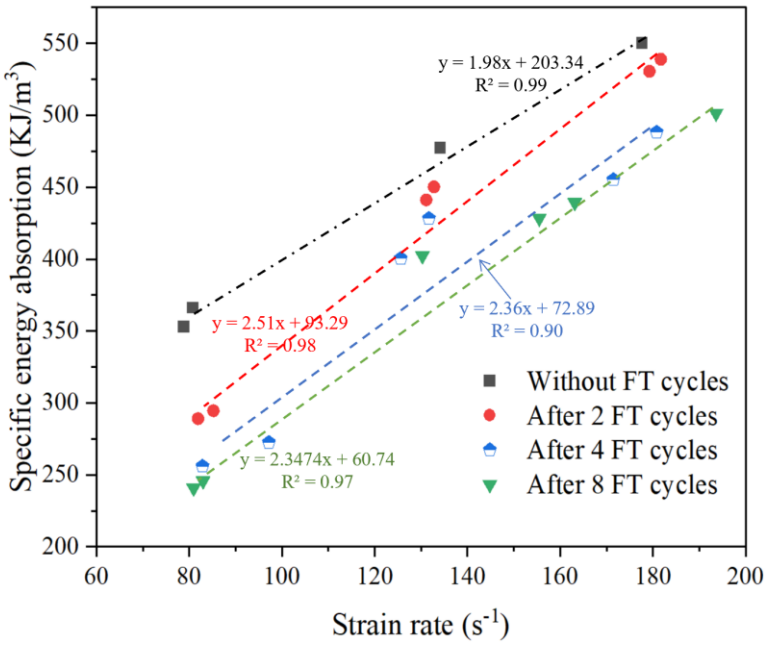

Figure 6. 8 The energy absorption of CUHPC after FT cycles.

6.5 Dynamic increase factors in compression

While the CEB-FIP model code [172] has demonstrated relatively good accuracy in describing the evolution of the CDIF for both NSC and HSC, its application to CUHPC reveals some limitations [213]. The experimental results from the present study aligned well with previous investigations by Hassan and Wille [216], Ren et al. [217] and Hou et al. [218], all of which examined CUHPC with 2% steel fibre reinforcement at room temperature (see Figure 6.9).

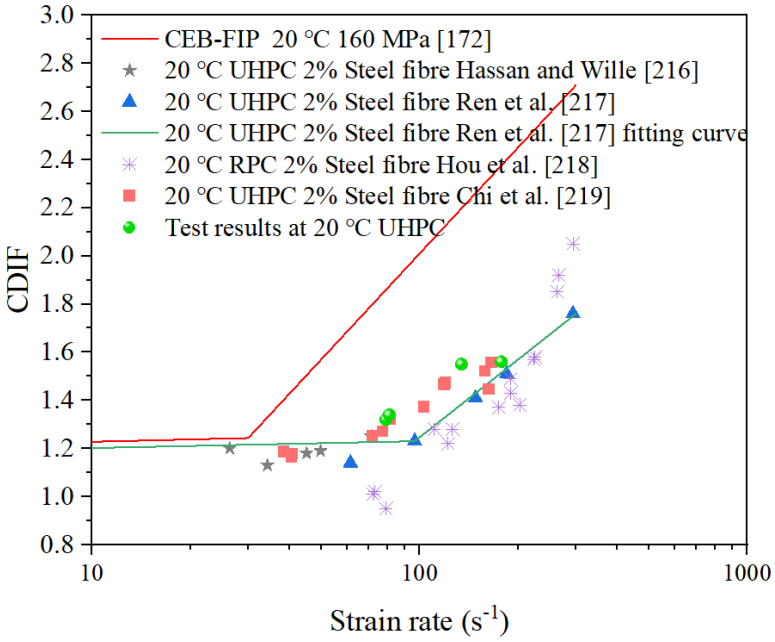

Figure 6. 9 Comparison of CDIFs from different experimental tests and model.

Figure 6.10 presents the variations in CDIF for CUHPC subjected to cryogenic FT cycles ranging from approximately 80 to 200 s^{-1}. The CDIF is a measure of the relative enhancement in dynamic compressive strength as compared to the static strength at a specific strain rate. There were four conditions showed in the figure, including CUHPC at 20 °C (without FT cycle) [219] and after 2, 4 and 8 FT cycles. For all conditions, the CDIFs exhibited a clear increasing trend with higher strain rates. The FT cycles appeared to influence the strain rate sensitivity of CUHPC. After 2 FT cycles, the CDIF values were generally higher than the room temperature condition. For instance, the CDIF of CUHPC increased up to 7.14% after 2 FT cycles in contrast to those at 20 °C with strain rate approximately 130 s^{-1}. With the increase in FT cycles to 4 and 8, the CDIF curves shifted upwards. This indicated that cryogenic FT exposure could lead to a more pronounced rate-sensitive behaviour. Repeated freeze-thaw cycles can induce internal stresses within the CUHPC matrix due to the expansion and contraction of water. This can lead to the formation of microcracks, which act as stress concentrators and weaken the overall material [220]. Under dynamic loading, these pre-existing cracks can

propagate more easily, negating the potential benefit of limited crack propagation time at higher strain rates.

In fact, when compared to NSC [199], the increase ratios of CDIF for CUHPC after FT cycles were much lower (there was no coarse aggregate for both materials). For example, the CDIFs of NSC exhibited an approximate increase of 18.71% and 27.10% after 4 and 8 FT cycles as compared to 2 FT cycles, while CDIFs of CUHPC increased by 8.33% and 10.61% after 4 and 8 FT cycles in comparison with 2 FT cycles both at the strain rate of 80 s^{-1}. This phenomenon was likely contributed to the steel fibres. These fibres could enhance energy absorption and delay crack propagation, especially at high strain rates. The effectiveness of fibres in CUHPC was directly linked to their bonding mechanism with the surrounding matrix [221].

To predict the CDIFs of CUHPC after FT cycles at high strain rates, the fitting curves were obtained and presented in Equations (6.8) - (6.10). The coefficients of determination (R^2) values, which reflected the percentage of variance in the dependent variable that could be accounted for by the independent variables, were 0.92, 0.87 and 0.86, respectively, for these formulae. This indicated a good correlation between the experimental data and the derived equations, demonstrating the reliability in representing the observed behaviour.

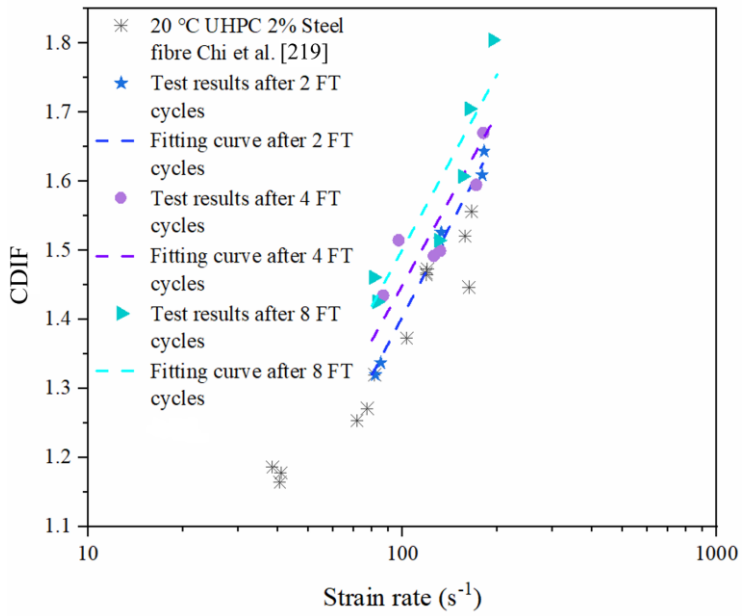

Figure 6. 10 Variations of CDIF for CUHPC after cryogenic FT cycles.

$$\text{CDIF after 2 FT cycles} = 0.877\log\dot{\varepsilon} - 0.352 \quad 81.90 \le \dot{\varepsilon} \le 262.31\ s^{-1} \quad (6.8)$$

$$\text{CDIF after 4 FT cycles} = 0.757\log\dot{\varepsilon} - 0.069 \quad 82.86 \le \dot{\varepsilon} \le 260.04\ s^{-1} \quad (6.9)$$

$$\text{CDIF after 8 FT cycles} = 0.861\log\dot{\varepsilon} - 0.227 \quad 80.95 \le \dot{\varepsilon} \le 273.45\ s^{-1} \quad (6.10)$$

6.6 Microscopy analysis

SEM was employed to examine the microstructure of the CUHPC matrix and ITZ after exposure to 0, 2, 4 and 8 FT cycles (see Figure 6.11). It can be observed from the scenario without FT cycle that the matrix exhibited a dense and compact structure with a continuous C-S-H gel, white flaky calcium hydroxide crystals, and unhydrated cementitious materials. Very fine silica fume and fly ash particles filled the pores between cement particles, and the junction between steel fibres and the concrete matrix exhibited a tight, well-bonded interface, indicating good adhesion. After 2 FT cycles, there was a slight increase in both the size and quantity of pores in contrast with 0 cycles, but the bond between steel fibres and the matrix still showed relatively intact, with no significant visible deterioration, which was in line with the results reported by Kim et al. [104].

Microcracks began to appear in the structure after 4 FT cycles which was owing to the freezing and thawing of free water in the pores. Pores became more visible and numerous. Cracks started to form between the steel fibres and the matrix, indicating the inception of bond degradation. After 8 FT cycles, the C-S-H gel structure exhibited more disruption, and pores were more pronounced and appeared larger as compared to earlier cycles. The significant crack was visible between the steel fibres and the matrix, indicating substantial degradation of the fibre-matrix bond.

Overall, as the number of FT cycles increased, there was a progressive deterioration of both the matrix structure and the fibre-matrix bond. The matrix became more porous and less dense, while microcracks developed and expanded. The interface between steel fibres and the concrete matrix weakened considerably, potentially leading to reduced strength and durability of the CUHPC material over repeated FT cycles.

No. FT	Matrix	ITZ
0	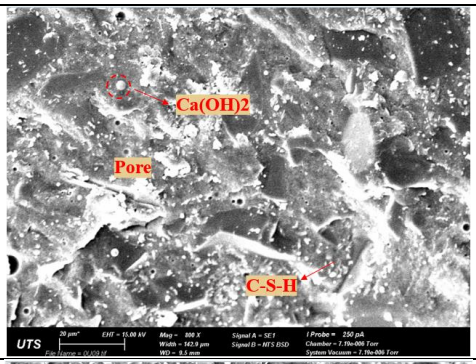	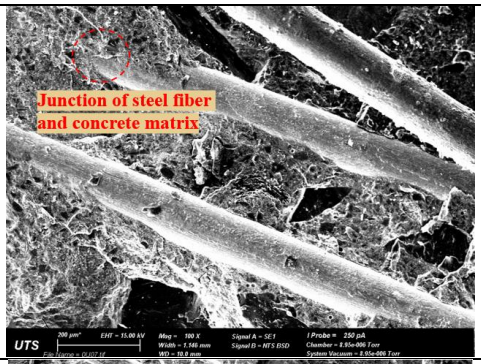
2	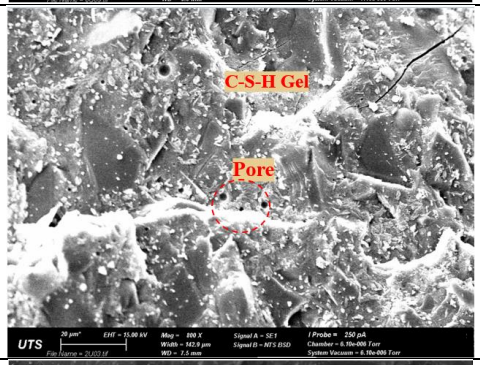	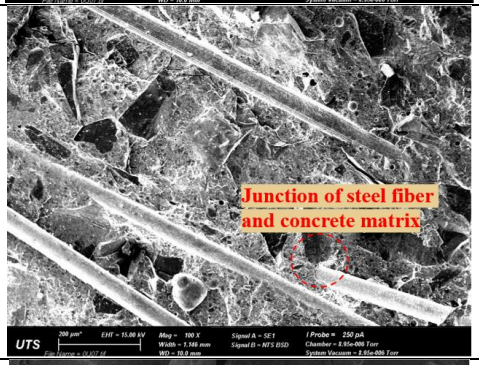
4	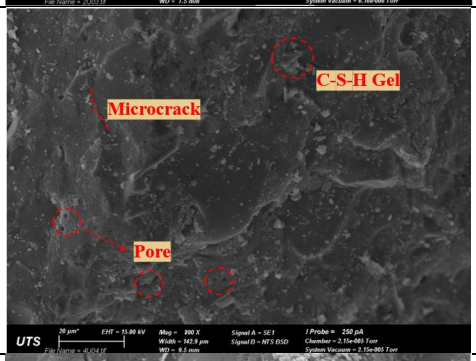	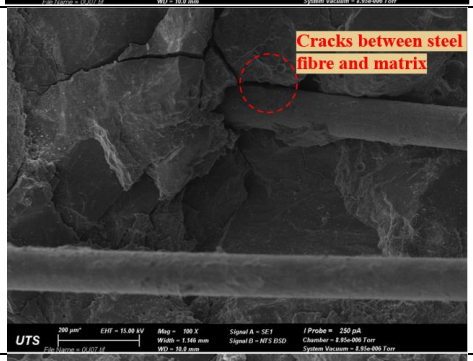
8	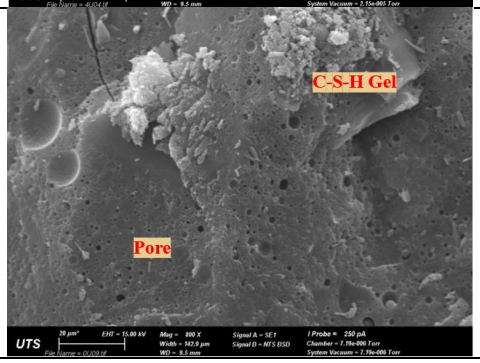	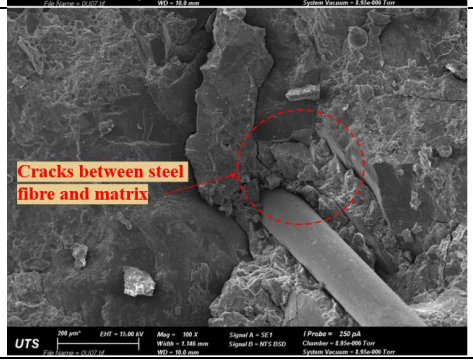

Figure 6. 11 Mortar matrix and ITZ of CUHPC after FT cycles.

6.7 Summary

The investigation into the dynamic compressive behaviour of CUHPC subjected to cryogenic FT cycles via SHPB technique revealed several important findings, which can be drawn as follows:

- The dynamic compressive strength of CUHPC increased with strain rate, regardless of the number of FT cycles experienced. However, the cumulative damage from repeated FT cycles resulted in a progressive deterioration of the material's microstructure.
- The SEA of CUHPC decreased with increased number of FT cycles, which possibly resulted from the degradation of the concrete matrix or fibre-matrix interface. It showed that the C-S-H gel structure within the concrete experienced substantial degradation after 8 FT cycles, characterised by increased porosity and the formation of prominent cracks between the steel fibres and the matrix, suggesting a significant weakening of the fibre-matrix bond.
- CDIFs increased with higher strain rates and exhibited a more pronounced rate-sensitive behaviour after repeated FT cycles. CDIFs of CUHPC after 4 and 8 FT cycles were approximately 1.08 and 1.11 times greater than 2 cycles at a strain rate of 80 s^{-1}.
- SEM analysis indicated progressive deterioration of the CUHPC matrix and fibre-matrix bond with increasing FT cycles. The formation of microcracks and increased porosity were observed, contributing to the overall reduction in mechanical strength.

In conclusion, while CUHPC demonstrates enhanced dynamic performance and energy absorption capabilities, repeated cryogenic FT cycles can significantly impact its

microstructure and mechanical properties. These findings underscore the importance of considering environmental factors in the design and application of CUHPC structures subjected to dynamic loading in extreme conditions.

Chapter 7. DYNAMIC BEHAVIOUR OF GEOPOLYMER-BASED ULTRA-HIGH-PERFORMANCE CONCRETE AT LOW AND CRYOGENIC TEMPERATURE

7.1 Introduction

This study investigates the mechanical behaviour of GUHPC under extreme low temperatures (-160 ~ 20 °C) and dynamic loading conditions. Experiments were conducted at temperatures of 20, -70 and -160 °C, with strain rates ranging from 40 to 160 s^{-1} for compression tests and 20 to 80 s^{-1} for splitting tensile tests. The research utilised a Φ100-mm SHPB apparatus for dynamic testing. Results reveal that both compressive and splitting tensile strengths of GUHPC increase as temperature decreases and strain rate increases. The DIF for both compression (CDIF) and tension (TDIF) was found to be higher at lower temperatures, indicating enhanced rate sensitivity in cryogenic conditions. The CDIF values at -70 °C and -160 °C were approximately 12% and 22% higher, respectively, as compared to the values at 20°C with the strain rate of 160 s^{-1}. The TDIFs at -70 °C and -160 °C were 35% and 47% higher, respectively, in comparison with the room temperature values at a strain rate of 40 s^{-1}. The study also examined the material microstructural change, failure modes, energy absorption capacity, and developed empirical formulae for predicting the DIF at various temperatures. X-ray CT scans revealed distinct microstructural changes in GUHPC under various temperatures, illustrating ice formation, pore structure alterations and microcracking, particularly at cryogenic temperatures. These findings contribute to the understanding of GUHPC behaviour in extreme environments and have implications for its application in cryogenic structures subjected to impact loading.

7.2 Experimental details

7.2.1 Materials and specimen preparation

In this study, GUHPC specimens were prepared using a carefully designed mix of cementitious materials and aggregates. GUHPC specimens were moulded into cylinders with dimensions of 70 mm in diameter and 35 mm in height, as illustrated in Figure 7.1, suitable for standardised testing of mechanical properties. The binder consisted of GGBFS, silica fume and fly ash. The mix proportions, outlined in Table 7.1, show a complex blend of materials including 750 kg/m³ of GGBFS, 100 kg/m³ of fly ash, and 157 kg/m³ of steel fibre, among other components. Quartz sand was used as the primary aggregate, with particle size, ranging from fine grains (0.1 to 0.5 mm), medium sand (0.5 to 1 mm) to coarse grains (up to 2 mm). A mixture of sodium hydroxide (NaOH) powdery (99% purity) and sodium silicate (Na_2SiO_3) solution (40% concentration) was used as an alkaline activator to initiate and accelerate the chemical reaction process in the cementitious materials [222]. Table 7.2 presents the oxide composition of GGBFS, with CaO (39.85%) and SiO_2 (31.70%) as the primary components. To improve strength and reduce brittleness, straight steel fibres measuring 0.12 mm in diameter and 10 mm in length were incorporated, as detailed in Table 5.1.

(a) 

(b) 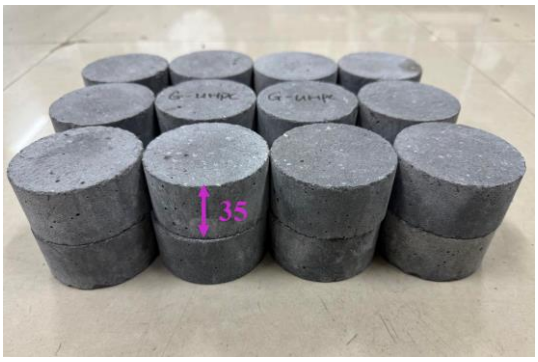

Figure 7. 1 GUHPC specimens for testing (unit: mm).

Table 7.1 Mix proportions of GUHPC (kg/m^3)

GGBFS	Water	Fly ash	Quartz sand	Steel fibre	Alkaline activator	Silica fume
750	71.3	100	910	157	520.6	132

Table 7.2 Oxide composition by weight of GGBFS.

Elements	CaO	SiO_2	Al_2O_3	Fe_2O_3	MgO	SO_3	CO_2	MnO
Content (%)	39.85	31.70	14.60	0.92	8.25	1.85	2.52	0.58

7.2.2 Low-temperature test technology

Low-temperature test setup for GUHPC under cryogenic conditions presents in Figure 4.3. The cooling curves presented in Figure 5.4 demonstrate two distinct target temperatures: -70 and -160 °C. Upon reaching these predetermined temperatures, the specimens maintained at these conditions for a duration of 4 hours. This extended exposure period allowed for thorough temperature equilibration throughout the specimen and enabled the study of GUHPC behaviour under sustained cryogenic conditions. Further detailed of low-temperature test technology can be found in Section 4.2.2.1.

7.2.3 SHPB test setup

The SHPB apparatus was employed to investigate the dynamic properties of GUHPC under high strain rate conditions (20~160 s^{-1}) at 20, -70 and -160 °C. This experimental setup comprised several essential components: a gas gun, which provided the initial impulse; a striker bar; an incident bar; a transmission bar; and a buffer bar. The SHPB apparatus was adaptable for both compression and splitting tension tests, as indicated by Figure 4.6, allowing for comprehensive characterisation of material properties under various loading conditions. More details were mentioned in Section 4.2.2.3.

7.3 Results and discussion

7.3.1 Quasi-static tests at low and cryogenic temperatures

This study investigates the mechanical behaviour of GUHPC under quasi-static loading conditions at low and cryogenic temperatures. Compressive and splitting tensile tests were performed at 20, -70 and -160 °C to evaluate the material's performance across a range of extreme temperature environments. The results, presented in Figure 7.2, demonstrate the temperature-dependent nature of GUHPC's mechanical properties. As the temperature decreased from ambient to cryogenic levels, both the compressive and splitting tensile strengths of the GUHPC specimens exhibited an increase. In terms of compression test, it showed a modest but consistent increase in compressive strength as the temperature decreased. The uniaxial compressive strength of GUHPC increased about 2.91% and 4.86% at -70 and -160 °C, respectively, as compared to room temperature. While the splitting tensile strength showed a more substantial relative increase, which was 18.55% and 50.00% higher when the temperature dropped from room temperature to -70 and -160°C, respectively.

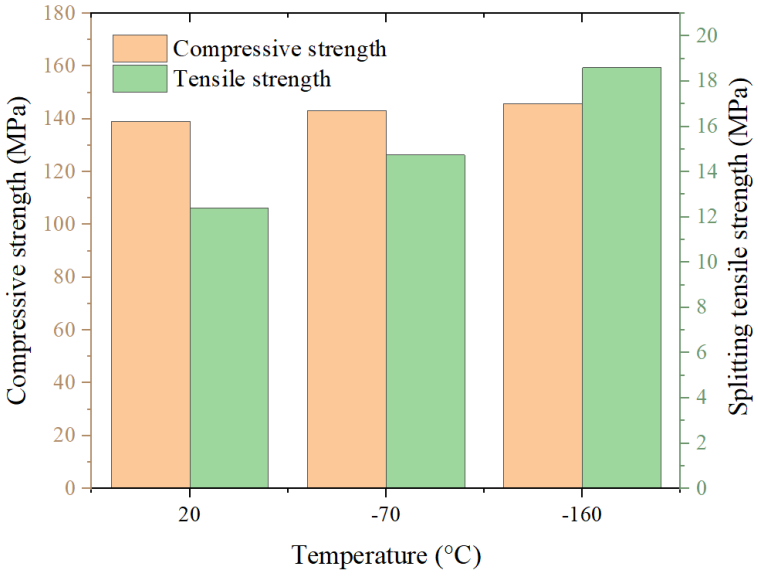

Figure 7. 2 Quasi-static results of GUHPC at low temperature.

7.3.2 SHPB tests under low temperatures in compression

7.3.2.1 Effect of low temperature on strain rate

Figure 7.3 illustrates the relationship between strain rate and dynamic compressive strength at three temperatures, including 20, -70 and -160 °C. It showed that compressive strength generally increased with strain rate, but the effect was most pronounced at cryogenic temperatures. The -160°C condition consistently yielded the highest strength values, followed by -70 °C, and then 20 °C. At room temperature, the compressive strength increased progressively as strain rates increased from 43.78 s^{-1} to 160.41 s^{-1}, with improvements ranging from 16.62% to 38.53% as compared to static strength. In contrast to the static strength at -70 °C, the dynamic compressive strength increased by 24.23%, 43.66%, 46.63%, and 54.76% at strain rates of 40.04 s^{-1}, 80.26 s^{-1}, 122.60 s^{-1}, and 161.41 s^{-1}, respectively. The most pronounced effects were seen at -160 °C. Here, 37.97% to 68.62% strength increase was noted for strain rate 38.05 s^{-1} and 160.30 s^{-1}, respectively, as compared to the static strength at -160 °C. These results demonstrate a consistent trend of increasing compressive strength with strain rate across all temperature conditions tested, with the effect becoming more pronounced at lower temperatures.

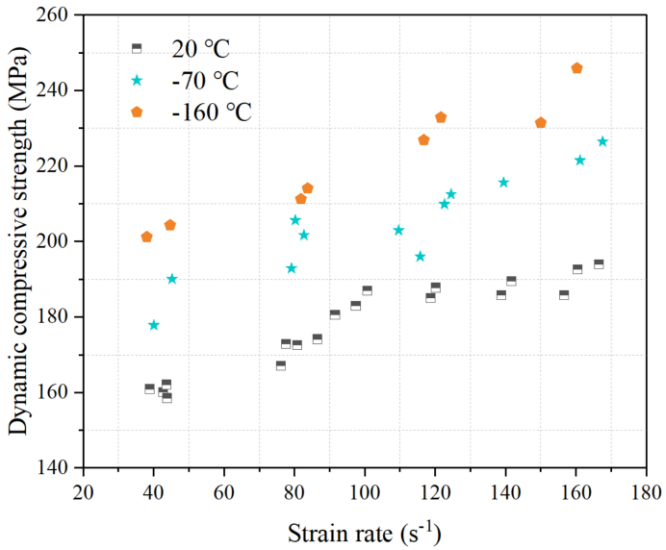

Figure 7. 3 Dynamic compressive stress-strain curve at various temperatures.

The relationship between strain rate and dynamic compressive elastic modulus of GUHPC under different temperature conditions is plotted in Figure 7.4. It was noted that the dynamic compressive elastic modulus increased with strain rate in all temperatures. Notably, the -70 °C condition consistently exhibited the highest elastic modulus values, particularly at higher strain rates, with a peak around 120 GPa. The room temperature data showed a general trend of increasing elastic modulus with strain rate, ranging from about 40 to 60 GPa. The -160°C condition displayed values similar to the room temperature condition. The phenomenon observed in GUHPC was indeed similar to that of cement concrete [199]. The higher elastic modulus at -70 °C and -160°C can be explained by several factors. At -70 °C, pore water froze, increasing overall stiffness as ice fills voids and created internal prestressing. This temperature represented an optimal point for ice formation that enhances stiffness [169]. At the extreme low temperature of -160 °C, the material likely became excessively brittle, potentially experiencing micro-damage due to differential thermal contraction and phase changes between ice and geopolymer binder, which collectively reduced its elastic modulus. Additionally, at the extreme low temperature, volume expansion potentially causing micro-cracking and structural changes [196] that reduce the elastic modulus.

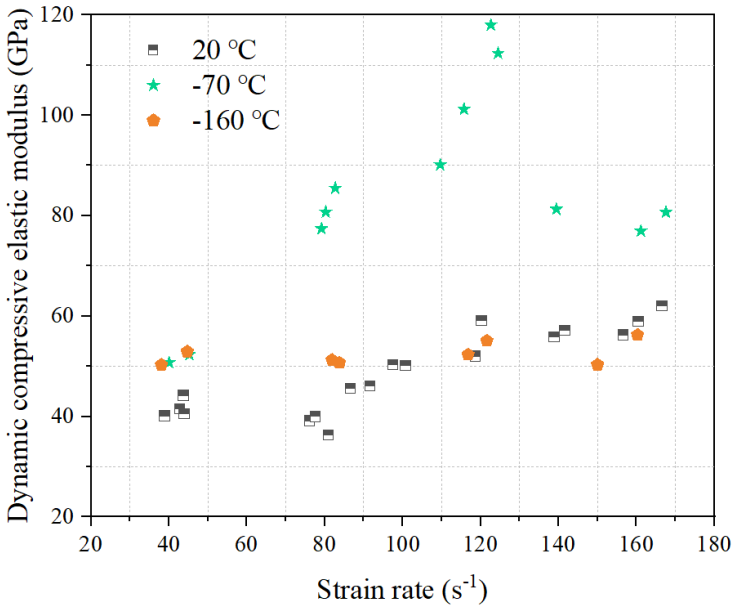

Figure 7.4 Dynamic modulus of elasticity at various temperatures.

7.3.2.2 Comparison of impact toughness at low temperatures

There are normally two different ways to calculate specific energy absorption (*SEA*), including volume-based *SEA* and mass-based *SEA*. Both methods for calculating SEA demonstrated distinct advantages in material characterisation and analysis. The volume-based method (Energy/Volume) excelled in structural design applications by obtaining energy absorption efficiency, facilitating straightforward scaling calculations, and supporting optimisation of structural components where volume was a critical parameter. While the mass-based method (Energy/Mass) offered significant advantages in material comparison by eliminating density effects, enabling direct comparison between materials of different densities, and providing true material efficiency metrics independent of density variations [223]. In this study, volume-based method was utilised to gain the SEA for GUHPC at low/cryogenic temperature, where it can be calculated by Equations (6.7) - (6.8).

The impact toughness of GUHPC specimens at different temperatures was evaluated using dynamic tests via SHPB device. The dynamic compressive stress-strain relationships of GUHPC at 20, -70 and -160 °C are presented in Figure 7.5.

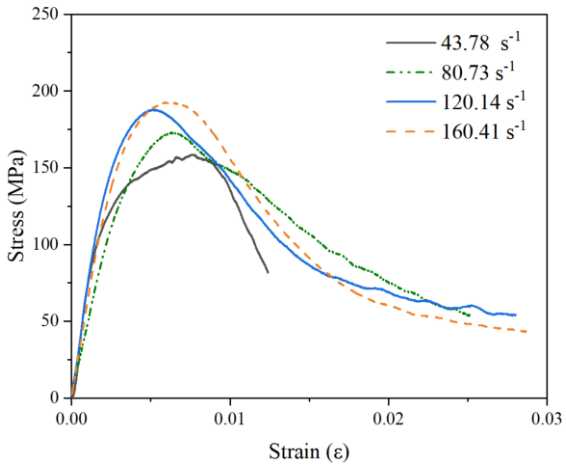

(a) at 20 ℃

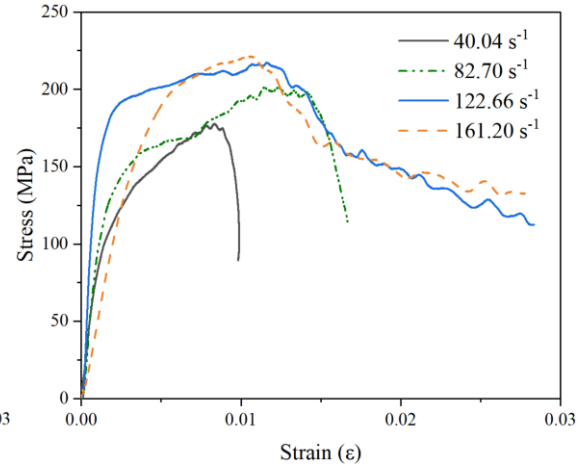

(b) at -70 ℃

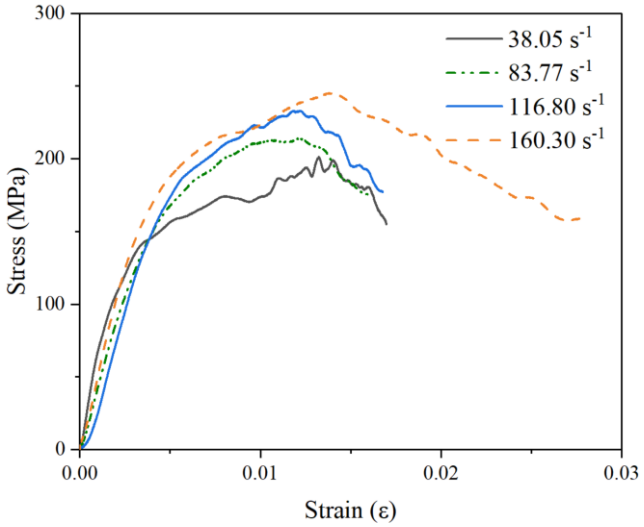

(c) at -160 ℃

Figure 7.5 Dynamic compressive stress-strain curve at various temperatures.

Figure 7.6 illustrates the compressive toughness of GUHPC specimens, represented as specific energy absorption, across a range of strain rates and temperatures. The results demonstrated a clear temperature-dependent behaviour of GUHPC's impact toughness. The observations indicated that with a decrease in temperature, the specific energy

absorption of GUHPC decreased. This phenomenon aligned with the findings of Jin et al. [106], who reported similar temperature-dependent behaviour in CUHPC. This was because that the geopolymer matrix became more brittle at lower temperatures. This increased brittleness reduced the material's ability to deform plastically, leading to lower energy absorption during fracture. On the other hand, the water freeze at low temperature can contribute to the formation of microcracks, which can reduce the material's ability to absorb energy [106].

At room temperature, the specific energy absorption increased significantly with strain rate, ranging from approximately 5.2 MJ/m³ at 40 s^{-1} to 12.9 MJ/m³ at 160 s^{-1}. This trend indicated enhanced energy absorption capability under higher loading rates at ambient conditions. As the temperature decreased, the overall toughness of GUHPC was reduced, but the material still exhibited considerable energy absorption capacity. At -70 °C, the specific energy absorption values were lower than those at 20 °C across all strain rates, but they follow a similar increasing trend with strain rate. The values range from about 4.2 MJ/m³ at 40 s^{-1} to 11.4 MJ/m³ at 160 s^{-1}. Further temperature reduction to -160 °C resulted in additional decrease in toughness, particularly at lower strain rates. However, it was noteworthy that the energy absorption capacity still improved with strain rate, rising from approximately 4.1 MJ/m³ at 40 s^{-1} to 9.45 MJ/m³ at 160 s^{-1}. The specific energy absorption increased with strain rate at all tested temperatures, suggesting that the material retained some capacity for dynamic energy absorption even in cold environments.

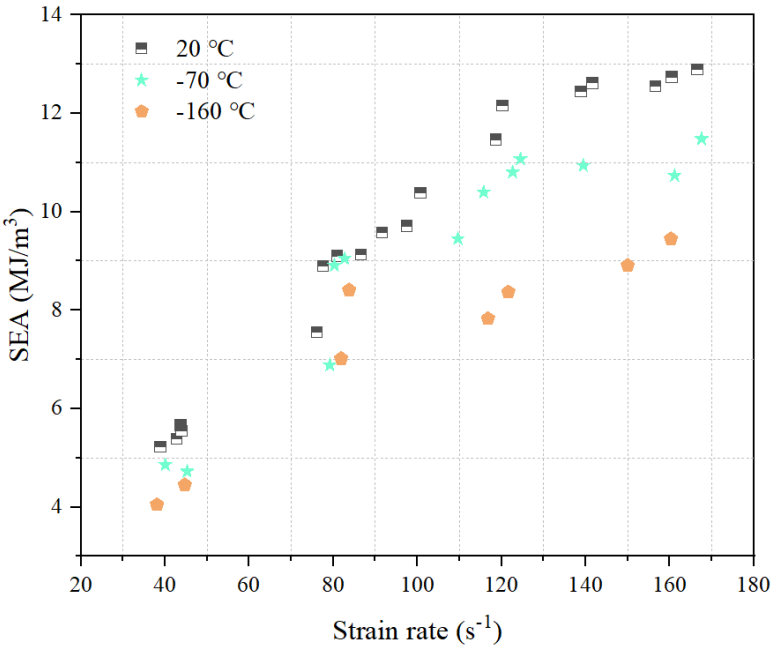

Figure 7.6 Compressive toughness of GUHPC specimens at different temperatures.

7.3.2.3 Comparison of post-test failure patterns in compression

Figure 7.7 presents the dynamic compressive failure modes of GUHPC specimens subjected to various strain rates and temperatures. The specimens exhibited a progressive increase in damage severity with rising strain rates. As seen from Figure 7.7(a), at the highest strain rate of 158.2 s^{-1}, the specimen displayed significant fragmentation, with large pieces detached from the main body, indicating a more catastrophic failure mode at 20°C. At extreme low temperature (-160 °C), the failure patterns revealed significant changes in material behaviour. The specimen at 45.2 s^{-1} showed minimal external damage, indicating high brittleness. As strain rates increased to 82.3 s^{-1} and 119.2 s^{-1}, distinct crack patterns emerge, characterised by larger, more defined fractures as compared to higher temperatures. The specimen at 161.5 s^{-1} exhibited extensive cracking and partial fragmentation, but notably retains more of its original shape as compared to specimens at higher temperatures. Across all temperature conditions, a clear trend of increasing damage severity with strain rates was observed. However, the nature of this damage

evolution differs markedly with temperature. At room temperature, failure tends towards fragmentation and disintegration at high strain rates. In contrast, at lower temperatures, particularly at -160 °C, the specimens exhibited more defined crack patterns and retain their overall shape even at high strain rates, suggesting a transition to a more brittle failure mode.

38.7 s^{-1} 80.7 s^{-1} 120.1 s^{-1} 160.4 s^{-1}

(a) at 20 ℃

40.0 s^{-1} 80.3 s^{-1} 122.7 s^{-1} 162.6 s^{-1}

(b) at -70 ℃

38.1 s^{-1} 82.9 s^{-1} 121.7 s^{-1} 161.5 s^{-1}

(c) at -160 ℃

Figure 7. 7 Dynamic compressive failure modes of GUHPC at different temperatures.

7.3.3 SHPB tests under low temperatures in split tension

7.3.3.1 Effect of low temperature on strain rate

The dynamic splitting tensile properties of GUHPC were evaluated under varying temperatures (20, -70 and -160 °C) and strain rates (approximately 20~80 s^{-1}), with the maximum splitting tensile strengths displayed in Figure 7.8. Under ambient conditions, increasing the strain rate from 20.11 s^{-1} to 85.73 s^{-1} resulted in a 74.90%~145.24% enhancement in splitting tensile strength as compared to static conditions. When tested at -70 °C, the material exhibited strength increases of 91.27-146.07% as strain rates varied from 21.18 s^{-1} to 81.28 s^{-1}. At -160 °C, strength improvements of 84.84%~116.13% were observed when strain rates increased from 19.14 s^{-1} to 81.97 s^{-1}, relative to static conditions. The investigation revealed two key trends: first, at constant temperature, higher strain rates corresponded to increased splitting tensile strength; second, at fixed strain rates, lower temperatures yielded higher dynamic splitting tensile strength values.

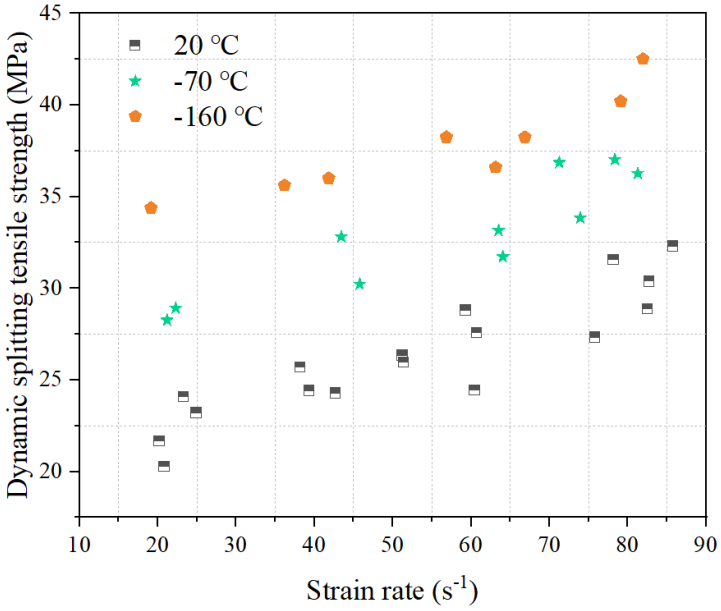

Figure 7. 8 Dynamic splitting tensile strength of GUHPC at different temperatures.

7.3.3.2 Comparison of post-test failure patterns in split tension

Figure 7.9 displays the dynamic splitting tensile failure modes of GUHPC at 20, -70 and -160 °C, with strain rate from 20 to 80 s^{-1}. It was clear to see that the failure modes at this reduced temperature at -70 °C showed distinct characteristics as compared to room temperature. At 19.89 s^{-1}, the specimen exhibited a faint diametral crack. With increasing strain rates (40.11 s^{-1} and 59.99 s^{-1}), the crack became more pronounced, with visible fibre bridging. The specimen tested at 81.38 s^{-1} demonstrated extensive cracking and partial separation along the diametral plane, with significant fibre pull-out evident. When the temperature reached to -160 °C, the specimen at 23.29 s^{-1} showed minimal external damage. As strain rates increased to 42.33 s^{-1} and 64.34 s^{-1}, distinct diametral cracks form with notable fibre bridging. The specimen at 80.48 s^{-1} exhibited the most severe damage, with partial fragmentation and extensive fibre pull-out, and the triangular fracture area expanded at both ends of the sample, accompanied by increased overall deformation.

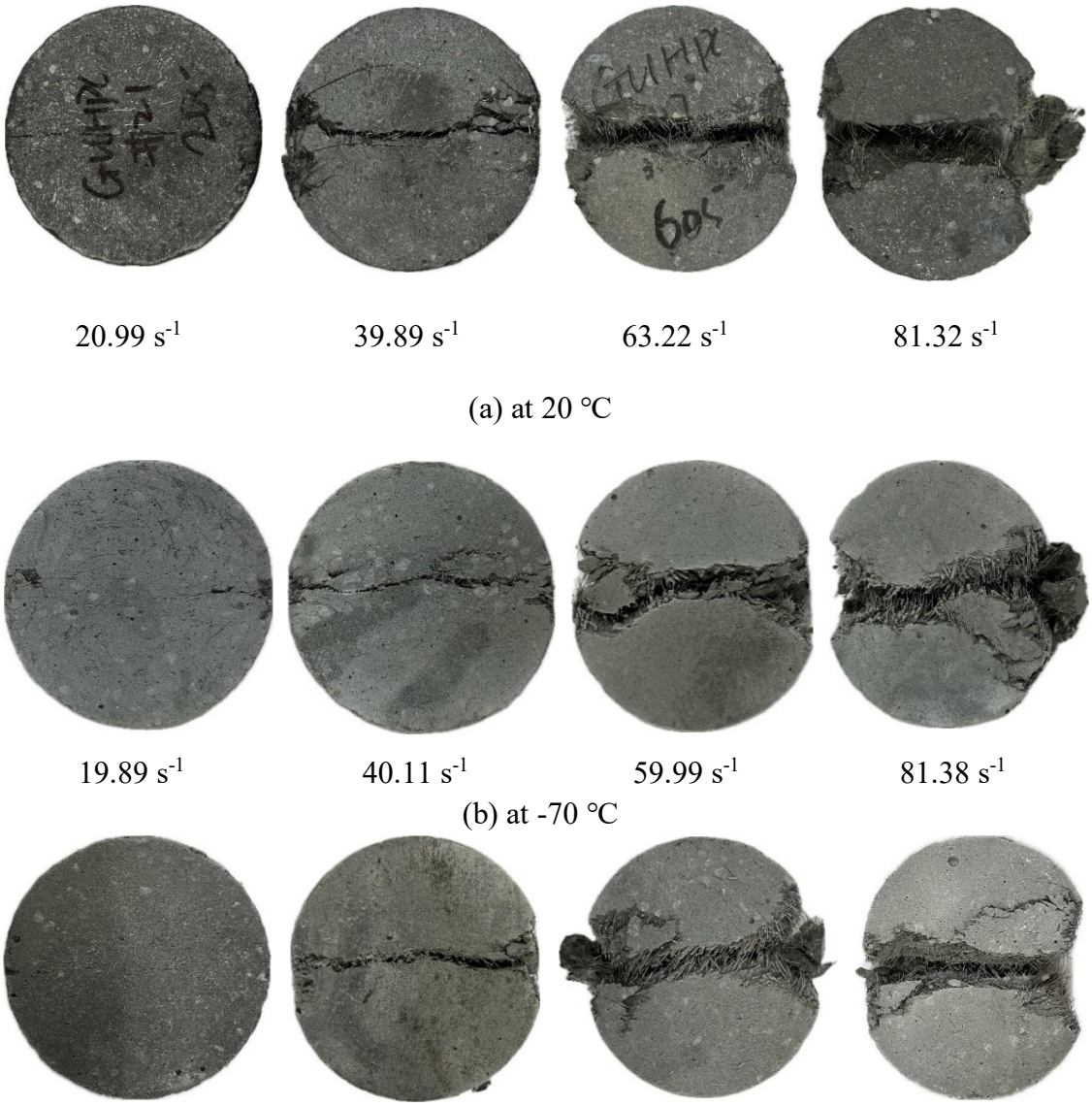

Figure 7. 9 Dynamic splitting tensile failure modes of GUHPC at different temperatures.

7.4 Strain rate effect

The mechanical properties of concrete are known to be sensitive to the rate of loading, a phenomenon referred to as the strain rate effect. As the strain rate increases, concrete typically exhibits higher strength and stiffness in contrast to its quasi-static behaviour. This effect is particularly important in scenarios involving impact or blast loading. To quantify this enhancement, DIF

, defined as the ratio of the dynamic strength to the static strength of the material, was utilised. Mathematically, DIF is expressed as DIF = f_d / f_s, where f_d is the dynamic strength at a given strain rate and f_s is the static strength. The DIF varies depending on whether the concrete is under compression or tension, and it can be influenced by factors such as concrete composition and environmental conditions.

In this section, the dynamic increase factor of GUHPC under both CDIF and TDIF at various temperatures (20, -70 and -160 °C) is summarised. By examining the DIF across these temperature ranges, it showed how the strain rate effect on GUHPC was influenced by extreme temperature condition.

7.4.1 Effect of strain rate on CDIF at low temperature

The CDIF of at low temperatures exhibited notable characteristics. The experimental results revealed that the CDIF of GUHPC was significantly influenced by temperature. It is important to note that the CEB-FIP model code [172], which was developed for conventional concrete, proved unconservative for predicting the behaviour of GUHPC at room temperature. This study made comparisons with two previous research works in the field at room temperature. The first was conducted by Liu et al. [224], who worked with GHPC that contained 2% straight steel fibres. The second was by Khan et al. [225], who studied GUHPC and used a more complex fibre mixture - combining steel and PE fibres with 2% fibre volume. As expected, the material with higher uniaxial compressive strength demonstrated lower rate sensitivity [194, 195], which aligned well with the experimental results obtained at room temperature in the current study. Regarding the temperature effect, the CDIF curves displayed an increasing trend as temperatures decreased from 20 °C to -160 °C, with the most pronounced rate sensitivity observed at -160 °C (see Figure 7.10). This trend suggested that the cryogenic temperatures enhanced the strain rate effect on the compressive strength of GUHPC, potentially due to the altered

microstructure at extremely low temperatures. As temperature decreased, especially to cryogenic levels, the microstructure of the concrete underwent significant changes. The pore water froze, potentially causing microcracks and altering the internal stress distribution. In addition, at reduced temperatures, the interface between steel fibres and the concrete matrix experienced a notable improvement in bond strength. This enhancement was primarily due to the increased frictional forces that develop under cryogenic conditions [104, 191]. It is worth noting that the GUHPC exhibited an inverse relationship in rate sensitivity as compared to CUHPC with the decrease in temperature [219]. The behaviour of GUHPC at low temperatures was characterised by a complex interplay of microstructural changes and ice formation dynamics. GUHPC typically exhibited a more heterogeneous microstructure with a higher porosity as compared to CUHPC [84, 226, 227]. As temperatures dropped, this unique microstructure underwent significant transformations. Ice crystals progressively form within the microcracks and pores, creating natural bridges across these voids [101]. These ice formations strengthen the bonds between aggregate particles and the surrounding geopolymer matrix, effectively enhancing the internal structure of the concrete.

In the current study, empirical formulae for the CDIF of GUHPC were derived for temperatures of 20, -70 and -160 °C, as illustrated in Equations (7.1) - (7.3). These formulae provided a mathematical representation of the CDIF as a function of strain rate, accounting for the significant influence of temperature on the dynamic tensile behaviour of GUHPC. The researchers established a transition point at a strain rate of 30 s^{-1}. The reliability of these empirical formulas was supported by their high coefficient of determination (R^2) values, which indicated a strong correlation between the predicted and observed data. Specifically, the R^2 value at room temperature was 0.93, at -70 °C was 0.82, and at -160 °C was 0.88, demonstrating the robustness of the empirical formulae

across different temperature conditions. These findings underscored the accuracy and reliability of the derived equations in capturing the behaviour of GUHPC under dynamic loading at various temperatures.

The CDIF of GUHPC exhibited notable variations across different temperatures and strain rates. At a strain rate of approximately 40 s^{-1}, the CDIF values at -70 °C and -160 °C were 1.07 and 1.19 times greater, respectively, than those observed at 20°C. As the strain rate increased to approximately 80 s^{-1}, the disparity became more pronounced, with the CDIF at -70 °C and -160 °C being 1.16 and 1.17 times higher than at room temperature. At higher strain rates of approximately 120 s^{-1}, the CDIF at -70 °C and -160 °C surpassed that at 20 °C by factors of 1.09 and 1.18, respectively. The most significant difference was observed at the highest tested strain rate of approximately 160 s^{-1}, where the CDIF values at -70 °C and -160 °C were 1.12 and 1.22 times greater than those at 20 °C. These results demonstrated a consistent trend of increased rate sensitivity at lower temperatures across all strain rates tested. Notably, the enhancement in CDIF was more pronounced at -160 °C as compared to -70 °C, suggesting that the extreme cryogenic condition had a more substantial impact on the dynamic compressive behaviour of GUHPC.

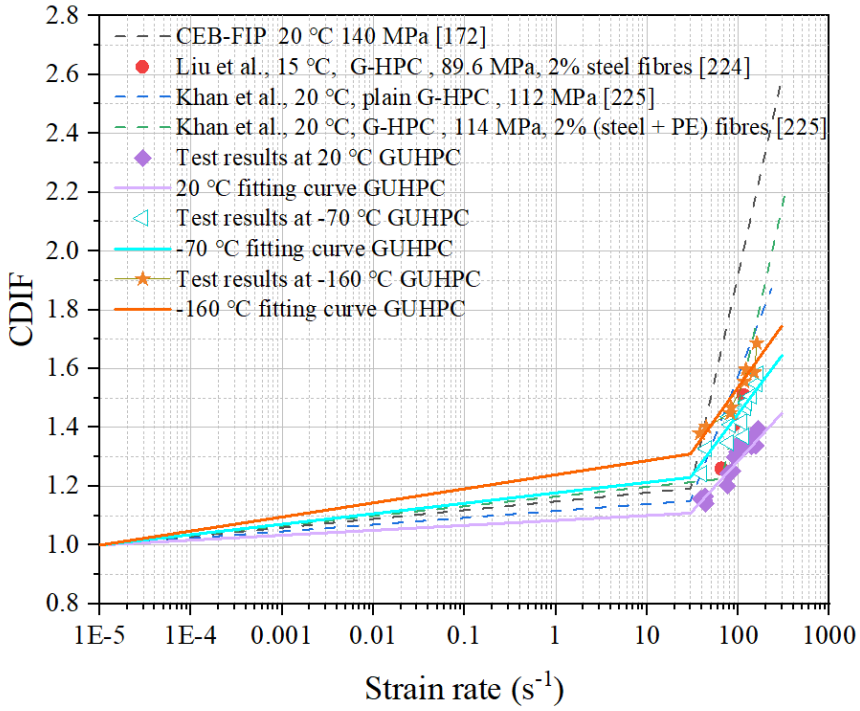

Figure 7. 10 CDIF for GUHPC at low temperature.

$$\text{CDIF at } 20\ ℃ = \begin{cases} 0.015\log\dot{\varepsilon} + 1.087 & \dot{\varepsilon} \le 30\ s^{-1} \\ 0.340\log\dot{\varepsilon} + 0.607 & \dot{\varepsilon} > 30\ s^{-1} \end{cases} \tag{7.1}$$

$$\text{CDIF at } -70\ ℃ = \begin{cases} 0.031\log\dot{\varepsilon} + 1.185 & \dot{\varepsilon} \le 30\ s^{-1} \\ 0.416\log\dot{\varepsilon} + 0.613 & \dot{\varepsilon} > 30\ s^{-1} \end{cases} \tag{7.2}$$

$$\text{CDIF at } -160\ ℃ = \begin{cases} 0.042\log\dot{\varepsilon} + 1.249 & \dot{\varepsilon} \le 30\ s^{-1} \\ 0.434\log\dot{\varepsilon} + 0.669 & \dot{\varepsilon} > 30\ s^{-1} \end{cases} \tag{7.3}$$

7.4.2 Effect of strain rate on TDIF at low temperature

The TDIF of GUHPC at low temperatures exhibited significant variations as compared to room temperature performance. As the temperature decreased, the TDIF values rose, indicating that the material became more sensitive to strain rate under lower temperatures, as shown in Figure 7.11. At a strain rate of approximately 20 s^{-1}, the TDIF values at -70 °C and -160 °C were 1.30 and 1.58 times greater, respectively, than those at 20 °C. As the strain rate increased to 40 s^{-1}, the TDIF at -70 °C and -160 °C surpassed the room temperature values by factors of 1.35 and 1.47. At higher strain rates of 60 s^{-1} and 80 s^{-1}, the enhancement persisted, with TDIF at -70 °C and -160 °C being 1.20 and 1.32 times

(at 60 s^{-1}), and 1.25 and 1.39 times (at 80 s^{-1}) greater than at 20 °C, respectively. This trend indicated a consistent increase in rate sensitivity at lower temperatures across all tested strain rates, with the most significant enhancement observed at -160 °C.

To quantify these relationships, empirical formulae were developed based on the experimental findings, which show in Equations (7.4) - (7.6). In the current study, the inflection points were determined to be 1 s^{-1} at 20, -70 and -160 °C, the same as Malvar and Crawford [173] as well as Tedesco and Ross [228]. The reliability of these models was assessed using R^2, yielding values of 0.85, 0.83, and 0.80 for 20, -70 and -160°C, respectively. These high R^2 values indicated strong correlations between predicted and observed DIF_{ft}, underscoring the models' efficacy in capturing the complex temperature-dependent dynamic tensile behaviour of GUHPC across a wide range of conditions.

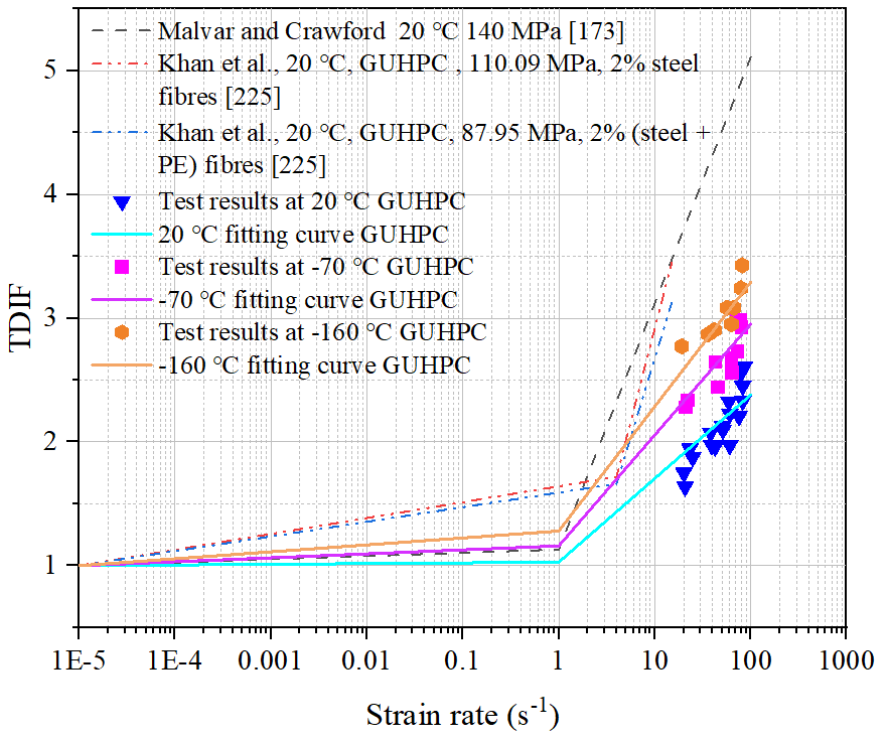

Figure 7.11 TDIFs for GUHPC at low temperature.

$$\text{TDIF at } 20\ ℃ = \begin{cases} 0.005 \log \dot{\varepsilon} + 1.028 & \dot{\varepsilon} \leq 1\ s^{-1} \\ 1.098 \log \dot{\varepsilon} + 0.285 & \dot{\varepsilon} > 1\ s^{-1} \end{cases} \quad (7.4)$$

$$\text{TDIF at } -70\ ℃ = \begin{cases} 0.027 \log \dot{\varepsilon} + 1.160 & \dot{\varepsilon} \leq 1\ s^{-1} \\ 1.031 \log \dot{\varepsilon} + 0.890 & \dot{\varepsilon} > 1\ s^{-1} \end{cases} \quad (7.5)$$

$$\text{TDIF at } -160\ ℃ = \begin{cases} 0.047 \log \dot{\varepsilon} + 1.281 & \dot{\varepsilon} \leq 1\ s^{-1} \\ 0.852 \log \dot{\varepsilon} + 1.587 & \dot{\varepsilon} > 1\ s^{-1} \end{cases} \quad (7.6)$$

7.5 Computed Tomography (CT) scans testing

X-ray CT scanning was conducted using a Siemens Artis Pheno system operating at 125 kV to investigate the microstructural changes in GUHPC specimens subjected to different temperature conditions (20, -70 and -160 °C). This advanced imaging technique provided detailed three-dimensional visualisation of internal structures at the microscale level, enabling non-destructive examination of pore networks, crack formations and phase distributions within the specimens. The high-energy X-ray beam facilitated optimal penetration through the dense GUHPC matrix, while maintaining sufficient contrast to differentiate between various phases including the geopolymer matrix, steel fibres, pores, and ice formations at sub-zero temperatures.

The CT scans at ambient temperature revealed a dense microstructure characteristic of GUHPC, as evidenced in Figure 7.12(a). The images clearly showed steel fibres appearing as bright features due to their high X-ray attenuation, while pores were distinctly visible as darker regions throughout the matrix. The geopolymer matrix exhibited higher porosity than -70 and -160 °C. At -70°C, as shown in Figure 7.12(b), the CT scans revealed emerging microstructural changes. It showed initial formation of ice within the pore structure, identifiable through density variations, utilising the Hounsfield scale which is a standardised quantitative scale used in CT to represent different degrees of X-ray attenuation by various materials (approximately -100 HU for ice) [229] to detect frozen water inside the specimen. The most pronounced microstructural alterations were

observed at -160 °C (Figure 7.12(c)), providing critical information on the freezing mechanisms. It demonstrated ice formations appeared as regions with characteristic grayscale values, distinguishable from the surrounding matrix and also extensive microcrack networks were visible surrounding the frozen regions. The observed crack patterns aligned with Zhu et al. [230] who pointed out the volume expansion and the internal cracking of concrete during freezing. Additionally, this observation confirmed Wiedemann's prediction of concrete embrittlement at cryogenic temperatures [231]. The competing mechanisms of partial ice filling and continued matrix prestressing showed in the CT images as a network of microcracks, particularly visible around ice-filled pores.

Figure 7.13 illustrates the 3D CT scan views of GUHPC specimens at three different temperatures. At room temperature, the cylindrical specimen exhibited steel fibres throughout the matrix. When cooled to -70 °C, the formation of ice became evident within the concrete matrix, while the steel fibres remained visible in the structure. At the cryogenic temperature of -160 °C, the specimen demonstrated the most significant microstructural changes, with more extensive ice formation throughout the matrix. The CT scans effectively captured the progressive changes in the internal structure of GUHPC as temperature decreased, particularly highlighting the interaction between ice formation, steel fibres, and the concrete matrix.

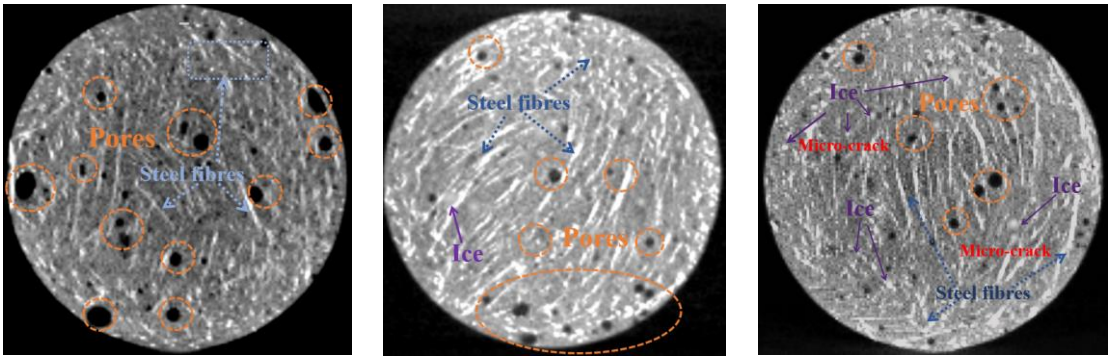

(a) 20 °C (b) -70 °C (c) -160 °C

Figure 7.12 2D views of GUHPC specimen microstructure.

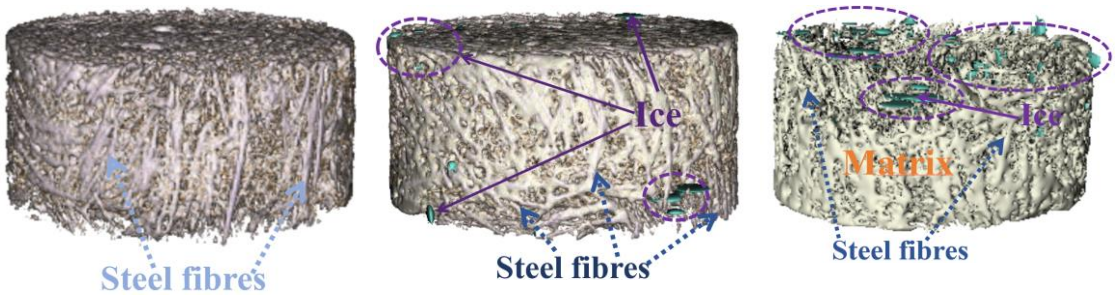

(a) 20 °C (b) -70 °C (c) -160 °C

Figure 7. 13 3D views of GUHPC specimen via CT scan.

7.6 Summary

This comprehensive study on the behaviour of GUHPC under extreme low temperatures and dynamic loading conditions has yielded several significant findings:

- Both the compressive and splitting tensile strengths of GUHPC increased as temperature decreased from 20 °C to -160 °C, the increase in split tensile strength was more evident than the compressive strength.
- GUHPC exhibited increased strength with higher strain rates across all temperature conditions, with this effect being more pronounced at lower temperatures.
- As temperatures decreased, the failure patterns transitioned from fragmentation to more defined crack patterns, suggesting a shift towards more brittle behaviour at extreme low temperatures.
- While the overall toughness decreased at lower temperatures, GUHPC maintained considerable energy absorption capacity, particularly at higher strain rates.
- The DIFs for both compression and tension were found to be higher at lower temperatures, indicating that GUHPC became more sensitive to strain rate effects in cryogenic conditions.

- The study developed empirical formulae for predicting the DIF in both compression and tension, providing valuable tools for future design and analysis.
- The X-ray CT analysis of GUHPC specimens revealed distinct microstructural transformations, where the specimens exhibited a progression from dense matrix structure with visible pores and steel fibres, particularly culminating in microcrack networks surrounding frozen regions at -160 °C.

These results highlight the complex interplay between temperature, strain rate, and mechanical properties in GUHPC. The transition to more brittle behaviour at extreme low temperatures warrants careful consideration in structural design.

Future research should focus on further exploring the long-term durability of GUHPC in cyclic temperature environments could provide insights into its suitability for repeated use in extreme conditions.

Chapter 8. BEHAVIOUR OF REINFORCED CONCRETE PANELS UNDER IMPACT LOADING AFTER CRYOGENIC FREEZE-THAW CYCLES

8.1 Introduction

This study aims to numerically examine the damage caused by impact loading on reinforced concrete panels after exposure to cryogenic FT cycles. A plasticity based continuous surface cap model was adopted to simulate concrete. The material modulus, uniaxial and triaxial strength surface as well as damage parameters were updated to incorporate the effect of cryogenic FT cycles. A numerical model was established to forecast the impact resistance of the reinforced concrete panels after various cryogenic FT cycles. Through the numerical simulation, it was evident that FT cycles exerted detrimental effects on the impact resistance of reinforced concrete panels. With an escalation in the number of FT cycles, there was a pronounced increase in the size of the crater formed on the top surface, accompanied by a corresponding rise in the penetration depth of the panel. The results of this research offer insights into the impact resistance of reinforced concrete structures following cryogenic FT cycles. Such insights are vital for the design and maintenance of critical structures like liquefied natural gas (LNG) storage tanks and other cryogenic facilities.

8.2 Constitutive models and material properties

8.2.1 CSCM Concrete model

Continuous Surface Cap Model (CSCM) is a concrete material model used in LS-DYNA and other finite element analysis programmes. The nonlinear stress-strain response, failure mechanism, and overall structural response of concrete under various load situations can be accurately simulated by the CSCM model. The CSCM model is

available in two versions: MAT_CSCM and MAT_CSCM_CONCRETE. Three parameters need to input for MAT_CSCM_CONCRETE, of the concrete density (ρ), unconfined compressive strength (f'_c) and maximum aggregate size (d_{max}). According to CEB_FIP model code [232], the concrete density (ρ) is 2400 kg/m^3 for plain concrete and 2500 kg/m^3 for prestressed concrete. It is specifically designed for modelling NSC with compressive strength between 28 to 58 MPa and the aggregate sizes between 8 and 32 mm [233]. In this particular study, to conduct simulation analysis on potential damage modes, MAT_CSCM_CONCRETE model is utilised to simulate normal strength concrete under room temperature conditions. It can generate parameters automatically by inputting ρ, f'_c and d_{max}, which incorporate a set of standardised material properties, derived from laboratory test data, to serve as default material properties. However, the performance of concrete will change after cryogenic FT cycles, thus CSCM_ CONCRETE model cannot be simply used to generate parameters. MAT_CSCM model is employed to simulate normal strength concrete exposed to FT cycles, because it can update the parameter such as elastic modulus, compressive strength, fracture energy etc. after FT cycles. The subsequent section will delve into the critical parameters in detail.

8.2.1.1 Shear modulus and bulk modulus after FT cycles

According to Goto and Miura [234], Yamane *et al.* [235], Rostásy and Wiedemann [236], Shi *et al.* [127] and Shi *et al.* [128], Figure 8.1 summarises the loss of elastic modulus of NSC after different low-temperature FT cycles. The term "relative" in Figure 8.1 means that the values are normalised, with 1.0 representing the initial elastic modulus of the material before any freeze-thaw cycles. It is noted that the loss of elastic modulus is related to a number of parameters such as the number of FT cycles, thermal loading, moisture content of concrete specimens, and water-to-cement ratio etc. For a particular concrete, with increased FT cycles, the loss of elastic modulus tends to increase. Based

on the experiments conducted by Goto and Miura [234], Yamane *et al.* [235], when the w/c ratio and moisture content increased, a more rapid decrease in elastic modulus was observed [234]. Rostásy and Wiedemann [236] investigated the influence of a cooling rate on water-saturated concrete subjected to eight FT cycles. Their findings indicated that an increase in the w/c ratio caused a decline in elastic modulus. Generally, the influence on the internal structure of the concrete, characterised by the emergence of microcracks and the breakdown of the bond between cement paste and aggregates, contributed to a reduction in the elastic modulus following FT cycles. Besides, Figure 8.1(b) demonstrates that, when subjected to identical cooling conditions, altering the w/c ratio results in a more significant reduction in the elastic modulus of concrete as compared to changing the moisture content. Furthermore, shock conditions, such as immersing the concrete specimens in liquid nitrogen, resulting in a more pronounced influence on the elastic modulus of concrete. The intense forces generated during shock loading can result in microcracks and structural damage, leading to a substantial decrease in the elastic modulus.

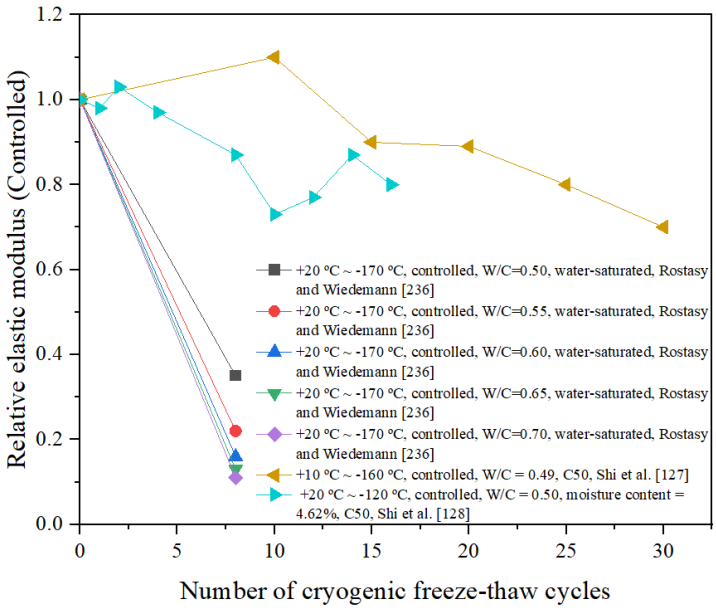

(a)

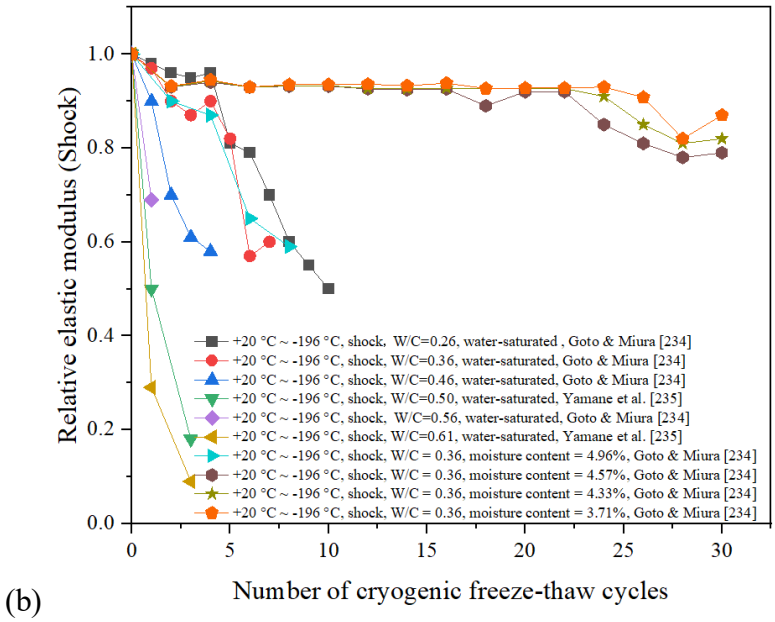

(b)

Figure 8. 1 Relative modulus of elasticity after various number of FT cycles. (a) Controlled (b) Thermal shock

8.2.1.2 Compressive strength after FT cycles

Similar to the elastic modulus, the compressive strength of concrete is influenced by diverse factors such as the number of FT cycles, moisture content, w/c ratio, and cooling techniques. Figure 8.2 presents the experimental results conducted by different researcher [96, 104, 125, 127, 129, 130, 235, 237], which demonstrates the effect of FT cycles on the concrete compressive strength. The data from these studies provide valuable insights into the relationship between FT cycles and the resulting compressive strength reduction in concrete. Most FT cycles range in temperature from room temperature to -170 °C or -196 °C, while FT cycle temperature range for Rostásy and Punch [124] is from room temperature to -85 °C. The observation reveals that lowering the lower limit temperature of the FT cycle leads to a more evident reduction in the compressive strength. Figure 8.2 (b) provides a clear illustration that, when exposed to identical cooling conditions, a higher w/c ratio corresponds to a more pronounced decrease in the relative compressive strength of concrete. Within a specific FT cycle range, using the same cooling method

and w/c ratio, a higher moisture content in the concrete results in a greater decline in compressive strength under the same number of FT cycles. In accordance with the experimental results of Rostásy *et al.* [125], it can be deduced that the compressive strength experiences a more substantial reduction subjected to thermal shock as compared to controlled cooling. It implies that the application of shock cooling methods leads to a more rapid and pronounced decrease in the compressive strength.

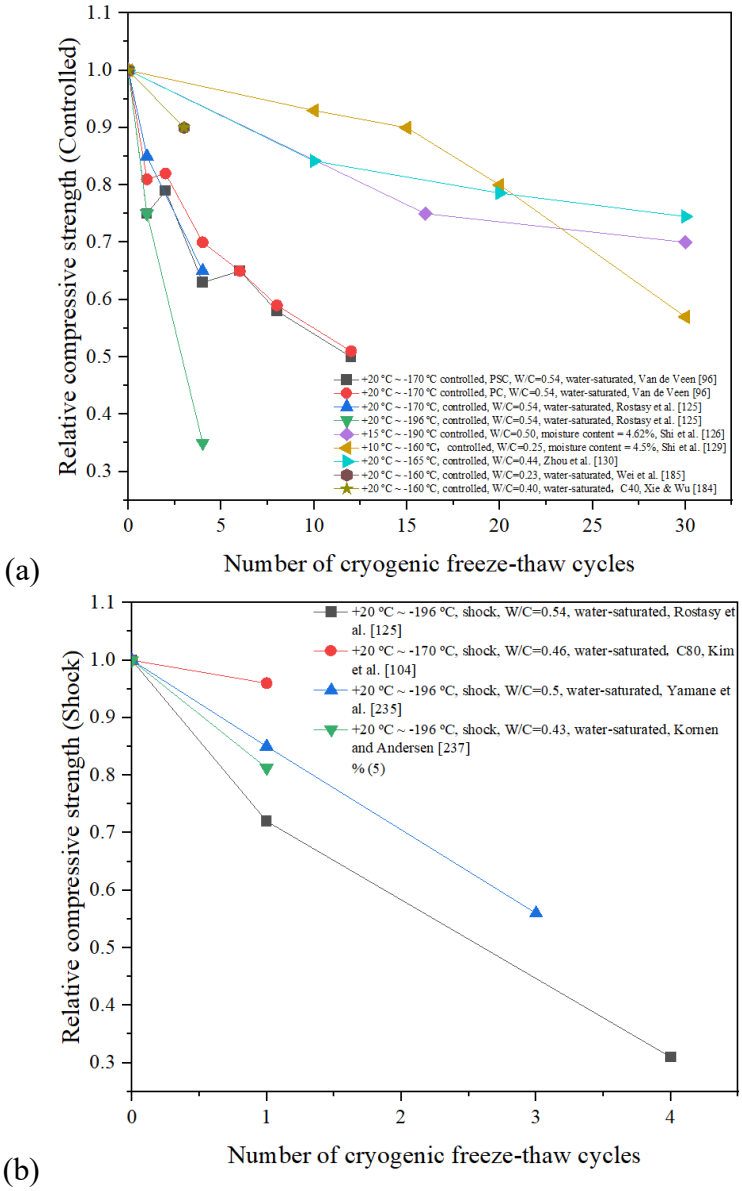

Figure 8. 2 Loss of compressive strength versus the number of thermal cycles. (a) Controlled (b) Thermal shock

8.2.1.3 Splitting tensile strength after FT cycles

The number of FT cycles also influences the splitting tensile strength of concrete. Figure 8.3 presents experimental data from various researchers [96, 104, 124, 125, 184, 185, 238, 239], and reveals the changes in tensile strength of concrete after different FT cycles. It is observed that a decrease in the lower temperature limit in FT cycles causes a rise in the loss of splitting tensile strength. Furthermore, when saturated or highly moist concrete is exposed to sudden thermal shock, the decrease in splitting tensile strength is more significant as compared to slow cooling processes [236]. It should be emphasized that the splitting tensile strength demonstrates more remarkable reductions after thermal cycling as compared to the compressive strength.

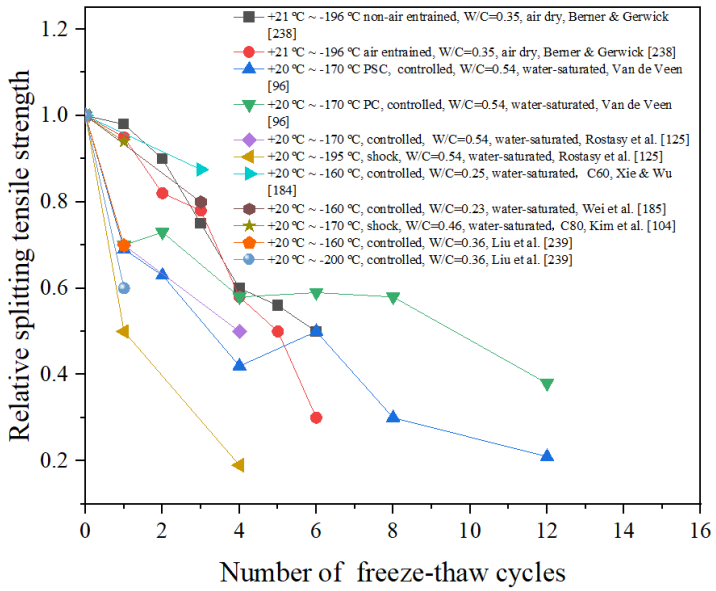

Figure 8. 3 Relative splitting tensile strength versus the number of thermal cycles.

8.2.1.4 Damage parameters

Under low-pressure conditions, concrete or concrete-like materials demonstrate strain softening behaviour, which involves a decrease in strength after initial yielding. This behaviour is simulated using the damage algorithm within the CSCM model. There are five parameters need to be adjusted to capture the damage of concrete after FT cycles, including *B, GFC, D, GFT, GFS.* The parameter *B* specifically relates to the ductile shape

softening behaviour, although limited attention has been paid to compressive softening behaviour despite numerous uniaxial compression tests being conducted. *GFC* represents fracture energy in uniaxial stress, *GFT* is fracture energy in uniaxial tension and *GFS* is fracture energy in pure shear stress. In the current study, the parameter *B* was assigned a default value of 100. In terms of parameter *D*, which governs brittle softening behaviour, a value of 0.001 was established following preliminary simulation attempts. For the parameter *GFS*, the user manual recommends setting it equal to *GFT* which is 100 times less than *GFC* [233]. The fracture parameter at ambient temperature was determined based on the guidelines provided by CEB-FIP [232] as follows,

$$G_f = G_{f0}(\frac{f'_c}{10})^{0.7} \tag{8.1}$$

where G_f represents the fracture energy in N·mm/mm^2, the initial fracture energy, G_{f0}, is influenced by the characteristics of the coarse aggregate used in the concrete, f'_c is the compressive strength of the concrete cylinder in MPa. When the maximum aggregate size d_{max} = 8 mm, G_{f0} = 0.025 N·mm/mm^2. When d_{max} = 16 mm, G_{f0} = 0.030 N·mm/mm^2. When d_{max} = 32 mm, G_{f0} = 0.058 N·mm/mm^2.

Owing to limited study on testing the fracture energy on concrete after low-temperature FT cycles, this article predicts the fracture energy of concrete after FT cycles based on experiments conducted by Xie *et al.* [138]. The empirical formula is $Relative\ G_f = 0.69 + 0.31 \times \exp(-0.19 \times \mathrm{N})$, where N represents the number of FT cycles. The fracture energy calculations of NSC after 10, 20, and 30 FT cycles are summarised in Tables 8.1, 8.2, and 8.3, respectively.

8.2.2 Single element test analysis

Adhering to the outlined procedure, the current study formulated the CSCM material model for NSC under various FT cycles. Single element tests were performed prior to the impact tests.

In the present study, a specific type of concrete material was employed with a uniaxial compressive strength of 53.8 MPa and a w/c ratio of 0.44. This material was utilised to investigate the effects of FT cycles on concrete properties, drawing from Zhou's previous study [130]. The investigation from Zhou *et al.* included various tests on this concrete material, such as uniaxial and triaxial compression tests. The outcomes of these single element tests were compared to experimental data (strain-stress curve). According to Zhou *et al.* [130], the concrete specimen's temperature was subjected to controlled fluctuations, ranging from room temperature down to -165 °C, with a controlled temperature change rate of 2-3 °C per minute and a total of 10, 20, and 30 FT cycles. The axial deformation loading rate for both uniaxial and triaxial compression tests was set at 0.02 mm/min. In the triaxial compression tests, a confining pressure of 20 MPa was applied. The experimental results of concrete for uniaxial compressive strength were 45.3, 42.3 and 40.1 MPa after 10, 20 and 30 FT cycles, respectively. The experimental results of concrete for triaxial compressive strength were 103.1, 90.2, 84.4 and 80.4 MPa after 0, 10, 20 and 30 FT cycles, respectively.

The shear modulus $G = \frac{E}{2(1+v)}$ and the bulk modulus $K = \frac{E}{3(1-2v)}$ where E represents Young's modulus, and v is Poisson's ratio. In the current study, the Poisson's ratio is 0.2, and the Young's modulus after 10, 20 and 30 FT cycles can be obtained based on the strain-stress curve from Zhou *et al.* [130] experimental results in Figure 8.6.

The tensile strength of concrete was calculated by equation $0.6\sqrt{f'_c}$ = 4.4 MPa at room temperature (where f'_c is the uniaxial compressive strength at 20 °C) in the current study

from AS3600:2018 [240]. To enhance the accuracy of predicting the reduction in tensile strength following various FT cycles, an empirical equation has been formulated based on the data presented in Figure 8.3 as follows,

$$\boldsymbol{Relative\ tensile\ strength} = 0.70 + -2.36 \times 10^{-2} \times \mathrm{N} + -0.33 \times \left(\frac{\mathrm{w}}{\mathrm{c}}\right) + -1.58 \times 10^{-3} \times (\mathrm{MC}) + 2.79 \times 10^{-2} \times \mathrm{N} \times \left(\frac{\mathrm{w}}{\mathrm{c}}\right) + 1.18 \times 10^{-3} \times \mathrm{N} \times (\mathrm{MC}) + 8.24 \times 10^{-4} \times \left(\frac{\mathrm{w}}{\mathrm{c}}\right) \times (\mathrm{MC}) + -2.57 \times 10^{-3} \times \mathrm{N} \times \left(\frac{\mathrm{w}}{\mathrm{c}}\right) \times (\mathrm{MC}) \quad (8.2)$$

where N represents to number of cycles, w/c is the ratio between water and cement and MC means moisture content of the concrete.

This equation represents the changes in tensile strength under controlled conditions. Figure 8.4 below shows the comparison of the results between predicted formula and experimental data after cryogenic FT cycles. The coefficient of determination (R^2) for equation (8.2) is 0.85, indicating a good level of accuracy in predicting the tensile strength loss. Therefore, the predicted relative tensile strength formula can be utilised to investigate the tensile strength of concrete after various number of FT cycles. Based on Equation (8.2), it can be obtained that the relative tensile strength after 10, 20 and 30 FT cycles was 0.37, 0.30 and 0.24, respectively. According to the CSCM user's manual [233], the tensile strength f'_t is equal to $\frac{\alpha-\lambda}{\sqrt{3}}$.

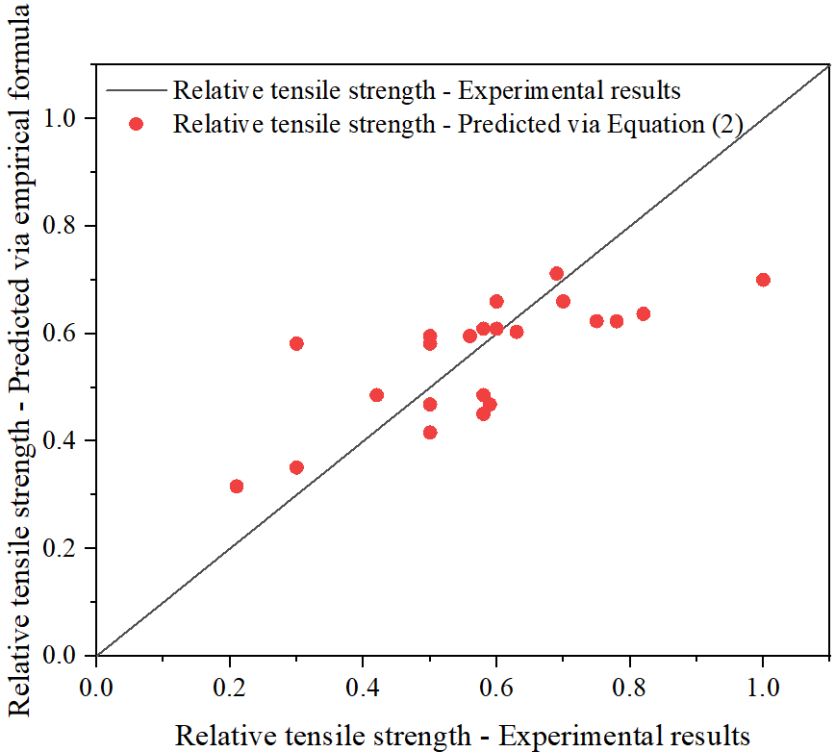

Figure 8. 4 Comparison of predicted relative tensile strength to experimental results.

In terms of the damage parameters, the value of *B* and *D* were 100 and 0.001, respectively, as mentioned previously. In the current study, the maximum aggregate size set as a default value 19 mm. Normally, the fracture energy parameter *GFC*, *GFT* and *GFS* can be automatically generated by inputting unconfined compressive strength in CSCM_CONCRETE model. When the unconfined compressive strength 45.3, 42.3 and 40.1 MPa after 10, 20 and 30 FT cycles were inputted, the value for *GFT* can be generated which is 93.7, 88.1 and 85.2, respectively. The relative fracture energy after 10, 20 and 30 times of FT cycles is 0.74, 0.70 and 0.69, respectively, based on the empirical formula created in Section 8.2.1.4. Therefore, the value *GFT* can be updated by multiplying the relative fracture energy, which is 69.3, 61.6 and 58.8, respectively, after 10, 20 and 30 times of FT cycles. As mentioned in Section 8.2.1.4, the value of *GFS* is equal to *GFT* and the value of *GFC* is 100 times greater than *GFT*. Tables 8.1, 8.2 and 8.3 summarise the modified data for concrete after 10, 20 and 30 FT cycles.

In the single element tests, displacement control in unconfined uniaxial compression testing was achieved using the *PRESCRIBED_MOTION keyword, enabling precise control of the applied displacement (as depicted in Figure 8.5(a)).

Confining pressure was exerted to four surfaces of the NSC model to simulate constraints during the triaxial compression test, while compressive load was applied by pushing down on the top surface. This configuration allowed for the simulation of triaxial compression conditions experienced by the NSC material (as illustrated in Figure 8.5(b)).

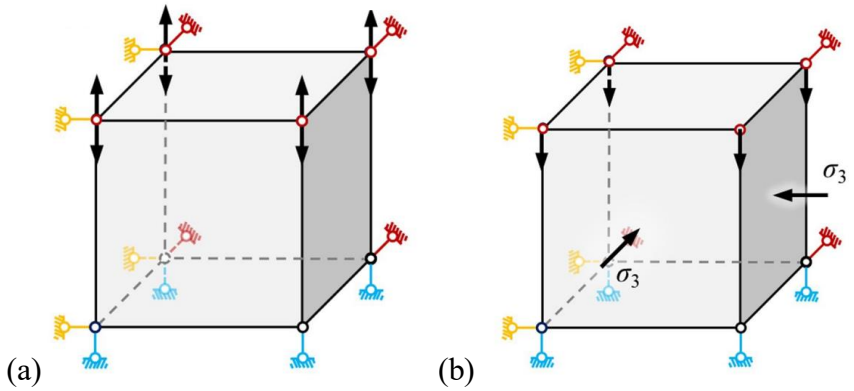

Figure 8. 5 Illustration of single element test: (a) unconfined uniaxial compression test, (b) triaxial compression test [241].

Figure 8.6 illustrates the stress-strain relationship of NSC under uniaxial compression after undergoing 10, 20, and 30 cycles of FT cycles. It can be clearly seen that the simulation result is in good agreement with the experimental data from Zhou *et al.* [130]. Tables 8.1, 8.2, and 8.3 provide a comprehensive summary of the CSCM parameters for NSC across varying numbers of FT cycles, derived from the experimental outcomes. Figure 8.7 illustrates the stress–strain curve of NSC under triaxial compression after 10, 20 and 30 times of FT cycles. The error of ultimate strength was 10.47 %. 11.75 % and 11.92% compared with the experimental results after 10, 20 and 30 times of FT cycles, respectively. In the realm of numerical analysis concerning cementitious materials, forecasted errors below 20% are generally regarded as being within an acceptable range. However, it should be noted that the adjusted parameters within the CSCM model have a

tendency to slightly underestimate material strength under elevated confining pressures [241]. Although the CSCM model exhibits satisfactory approximation to test data in cases without confinement, when it comes to high confinement scenarios, the numerical response becomes unstable to match even the peak strength observed in the experimental data [242].

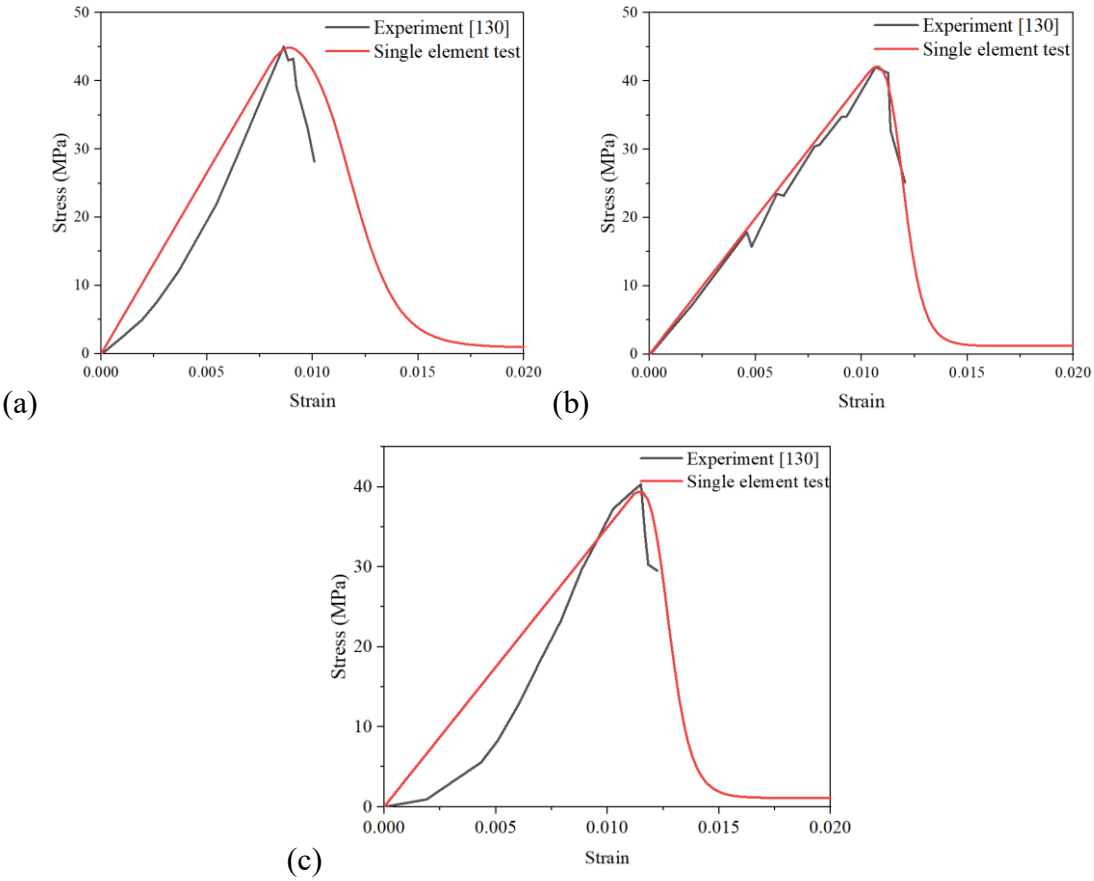

Figure 8. 6 Single model under uniaxial compression against different number of FT cycles (a) 10 times, (b) 20 times, (c) 30 times.

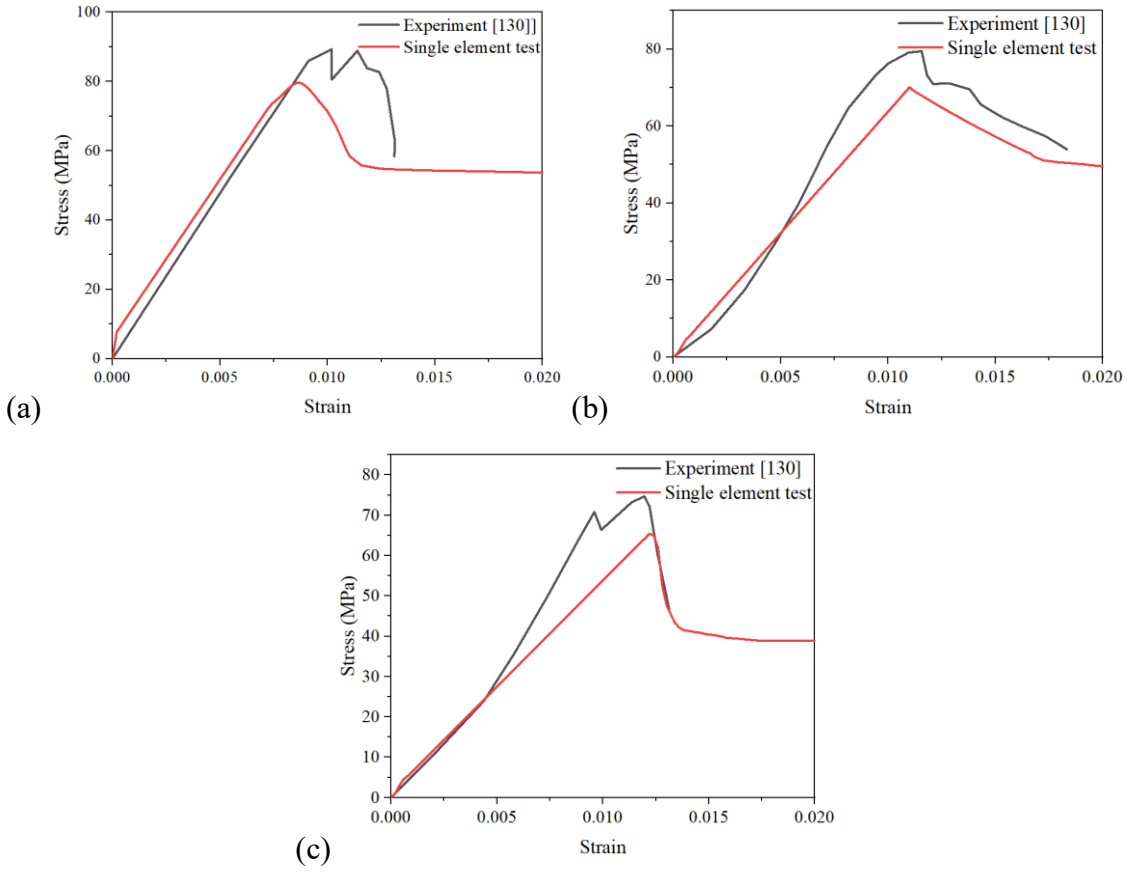

Figure 8. 7 Single model under triaxial compression against different number of FT cycles (a) 10 times, (b) 20 times, (c) 30 times.

Table 8. 1 Material parameters for NSC under 10 times of FT cycles.

Parameter	Value	Parameter	Value	Parameter	Value	Parameter	Value
R_o (kg/m^3)	2400	*NPLOT*	1	*INCRE*	0	*IRATE*	1
ERODE	0	*RECOV*	0	*ITRETRC*	0	*PRED*	0
G (Pa)	2.25E10	*K* (Pa)	2.76E10	N_H	1	C_H	0
α (Pa)	1.33E7	θ (Pa^{-1})	0.35	λ (Pa)	1.051E7	β (Pa^{-1})	1.939E-8
α_1 (Pa)	0.7473	θ_1 (Pa^{-1})	5.96E-10	λ_1 (Pa)	0.17	β_1 (Pa^{-1})	4.828E-8
α_2 (Pa)	0.66	θ_2 (Pa^{-1})	7.17E-10	λ_2 (Pa)	0.16	β_2 (Pa^{-1})	4.828E-8
R	5	X_D (Pa)	1E8	*W*	0.05		
D_1 (Pa^{-1})	2.5E-10	D_2 (Pa^{-2})	3.5E-19				
B	100	*GFC* (Pa*m)	6934	*D*	0.001	*GFT* (Pa*m)	69.34
GFS (Pa*m)	69.34	*PWRC*	5	*PWRT*	1	*PWOD*	0
η_{oc}	1.90E-4	N_c	0.78	η_{ot}	8.155E-5	*Nt*	0.48
OVERC	3.192E7	*OVERT*	3.192E7	*SRATE*	1	*REPOW*	1

Table 8. 2 Material parameters for NSC under 20 times of FT cycles.

Parameter	Value	Parameter	Value	Parameter	Value	Parameter	Value
R_o (kg/m^3)	2400	*NPLOT*	1	*INCRE*	0	*IRATE*	1
ERODE	0	*RECOV*	0	*ITRETRC*	0	*PRED*	0
G (Pa)	1.69E10	*K* (Pa)	2.08E10	N_H	1	C_H	0
α (Pa)	1.27E7	θ (Pa^{-1})	0.34	λ (Pa)	1.051E7	β (Pa^{-1})	1.929E-8
α_1 (Pa)	0.7473	θ_1 (Pa^{-1})	7.47E-10	λ_1 (Pa)	0.17	β_1 (Pa^{-1})	5.456E-8
α_2 (Pa)	0.66	θ_2 (Pa^{-1})	9.0E-10	λ_2 (Pa)	0.16	β_2 (Pa^{-1})	5.456E-8
R	5	X_D (Pa)	1E8	*W*	0.05		
D_1 (Pa^{-1})	2.5E-10	D_2 (Pa^{-2})	3.5E-19				
B	100	*GFC* (Pa*m)	6164	*D*	0.001	*GFT* (Pa*m)	61.64
GFS (Pa*m)	61.64	*PWRC*	5	*PWRT*	1	*PWOD*	0
η_{oc}	1.552E-4	N_c	0.78	η_{ot}	7.6E-5	*Nt*	0.48
OVERC	2.877E7	*OVERT*	2.877E7	*SRATE*	1	*REPOW*	1

Table 8. 3 Material parameters for NSC under 30 times of FT cycles.

Parameter	Value	Parameter	Value	Parameter	Value	Parameter	Value
R_o (kg/m^3)	2400	*NPLOT*	1	*INCRE*	0	*IRATE*	1
ERODE	0	*RECOV*	0	*ITRETRC*	0	*PRED*	0
G (Pa)	1.483E10	*K* (Pa)	1.82E10	N_H	1	C_H	0
α (Pa)	1.23E7	θ (Pa^{-1})	0.33	λ (Pa)	1.051E7	β (Pa^{-1})	1.929E-8
α_1 (Pa)	0.7473	θ_1 (Pa^{-1})	8.176E-10	λ_1 (Pa)	0.17	β_1 (Pa^{-1})	5.746E-8
α_2 (Pa)	0.66	θ_2 (Pa^{-1})	9.862E-10	λ_2 (Pa)	0.16	β_2 (Pa^{-1})	5.746E-8
R	5	X_D (Pa)	1E8	*W*	0.05		
D_1 (Pa^{-1})	2.5E-10	D_2 (Pa^{-2})	3.5E-19				
B	100	*GFC* (Pa*m)	5876	*D*	0.001	*GFT* (Pa*m)	58.76
GFS (Pa*m)	58.76	*PWRC*	5	*PWRT*	1	*PWOD*	0
η_{oc}	1.408E-4	N_c	0.78	η_{ot}	7.344E-5	*Nt*	0.48
OVERC	2.736E7	*OVERT*	2.736E7	*SRATE*	1	*REPOW*	1

8.2.3 Steel reinforcements model

Steel bars possess different thermal properties as compared to the concrete matrix. They exhibit minimal dimensional changes under cryogenic conditions. This difference in thermal expansion and contraction properties between the reinforcement and the concrete matrix can provide some level of protection to the reinforcement. Yan and Xie [243] and Xie [244] conducted research on steel bars at low temperatures, and the results showed

that the elastic modulus, tensile strength, and ultimate strength of the steel bars increased with the decrease of temperature. However, Jung et al. [245] stated that the fatigue failure of steel occurred after 10^4 times load cycles under low temperature. The mechanical characteristics of steel reinforcements exhibit relatively consistent behaviour throughout the FT cycle exposures. The properties of steel bars after low-temperature FT cycling remained unchanged as compared to those at room temperature, a conservative assumption made to guide the numerical simulation results in this study.

8.3 Validation of reinforced concrete panel under impact loadings

As mentioned previously, the safety and performance of many different structures at extremely low temperatures pose challenges, especially for liquefied natural gas storage tanks. This study aims to validate the impact resistance of the reinforced concrete/steel liner composite panels at ambient temperature, inspired by the design of the dome in LNG storage tanks, using the experimental data conducted by Zou *et al.* [246]. The composite target consisted of four parts, including concrete, reinforcements, studs and steel liner. As shown Figure 8.8, the diameter of the panel was 2000 mm. There were two layers of reinforcements with 20 mm @ 200 mm. In addition, eight studs were contained in the target panel where four were arranged along 300 mm radius of the panel and the other were arranged along 700 mm, and the diameter of these studs was 12 mm. The 3 mm thick steel liner was welded at the bottom of the concrete panel. More details on the dimensions of target panel can be found in Zou et al. [246]. To access the impact resistance of concrete panel, a full numerical model was established using LS-DYNA. The numerical model of impactor and target panel is presented in Figure 8.9. The impactor consisted of two parts: mass block and impactor head (100 kg). The radius of smooth spherical head for impactor head was 75 mm, and the height of cylindrical body was 375 mm.

In this study, two specimens were evaluated in comparison with the experimental outcomes. The first specimen was tested with 500 kg impactor at dropping height 35 m, and the impact velocity was 26.19 m/s. The second specimen was tested with 800 kg impactor and the falling height was 25 m (impact velocity was 22.13 m/s). The INITIAL_VELOCITY_GENERATION function in LS-DYNA was employed to achieve the desired impact velocity during the experiments. Three groups of mesh convergence tests have been done, including 5 mm, 10 mm and 20 mm mesh size for concrete, reinforcements, studs, steel liner and impactor. To balance the computational effort and accuracy, the mesh size of concrete, reinforcements, studs, steel liner and impactor was 10 mm (see Figure 8.10).

MAT_CSCM_CONCRETE was utilised for concrete with density 2400 kg/m^3, 43.2 MPa compressive strength and 19 mm aggregate.

MAT_PIECEWISE_LINEAR_PLASTICITY was adopted for studs and reinforcements in the model. MAT_PLASTIC_KINEMATIC was utilised for the steel liner material. The material model for both impactor head and the mass block was MAT_RIGID. Table 8.4 summarises the input parameters for each material.

AUTOMACITC_NODES_TO_SURFACE was utilised to model the contact between reinforcements and impactor, while keyword ERODING_SURFACE_TO_SURFACE was set for concrete and impactor. Besides, AUTOMATIC_SINGLE_SURFACE was adopted between concrete and steel liner. The consideration of reinforcement slippage was not included in the CONSTRAINED_BEAM_IN_SOLID keyword.

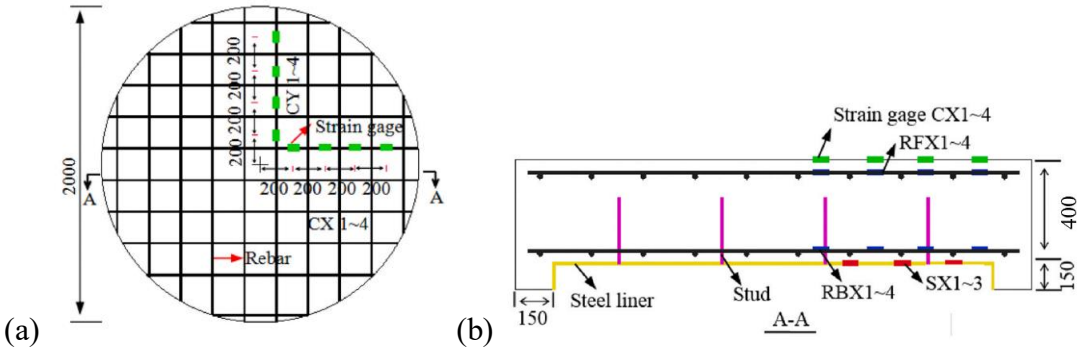

Figure 8. 8 Dimension of composite panel. (a) Front view (b) Side view (unit: mm) [246]

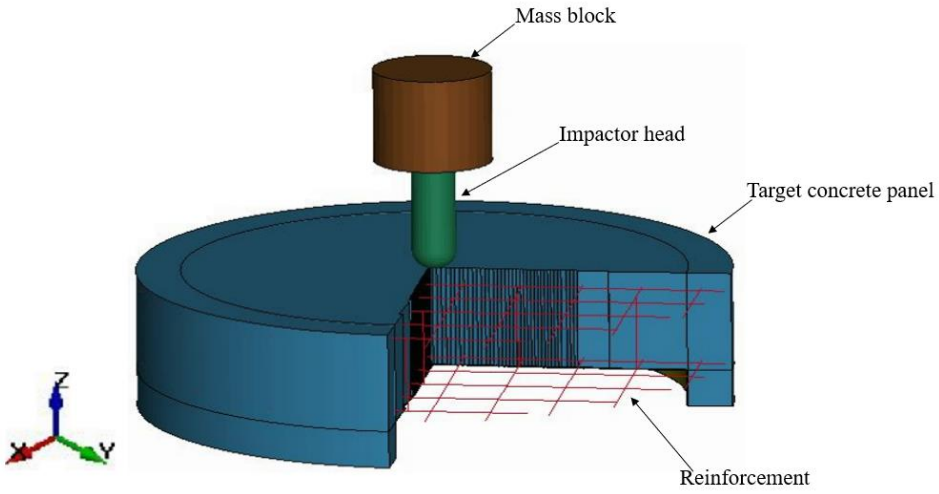

Figure 8. 9 Schematic view of impactor-panel system.

Table 8. 4 Parameters of impactor-panel system.

Material	LS-DYNA Model	Input Parameters	Magnitude
Concrete	MAT_CSCM_CONCRETE	Mass Density NPLOT Compression strength Maximum aggregate	2400 kg/m^3 1 43.2 MPa 19 mm
Steel reinforcement/Stud	MAT_PIECEWISE_ LINEAR_PLASTICITY	Mass density Yield strength Poisson's ratio Young's modulus	7850 kg/m^3 455 MPa 0.3 210 GPa
Steel liner	MAT_PLASTIC_KINEMATIC	Mass density Yield strength Poisson's ratio Young's modulus	7850 kg/m^3 460 MPa 0.3 210 GPa
Impact head	MAT_RIGID	Mass density Poisson's ratio Young's modulus	7850 kg/m^3 0.22 117 GPa
Mass block	MAT_RIGID	Mass density Poisson's ratio Young's modulus	7850 kg/m^3 0.3 210 GPa

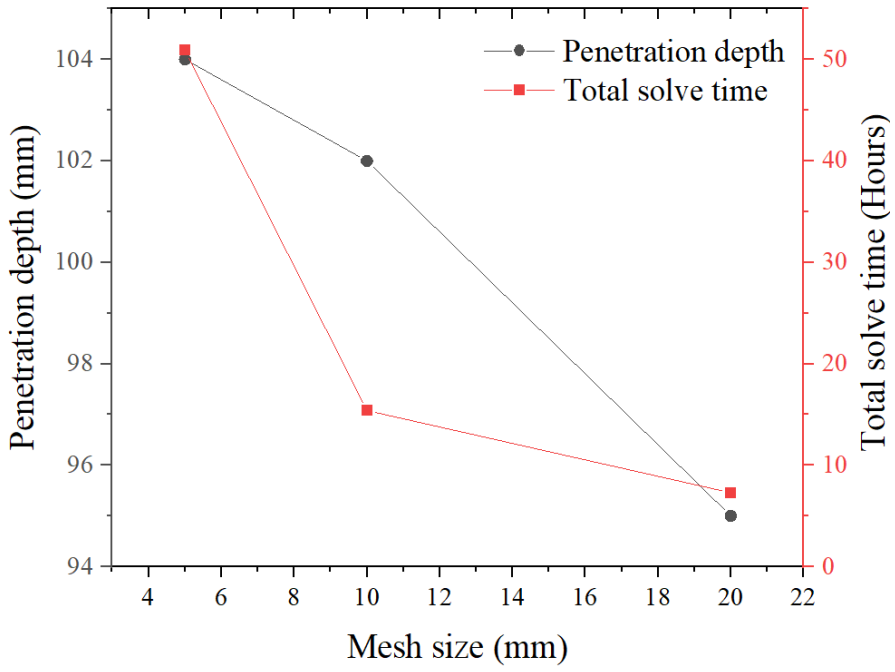

Figure 8. 10 Mesh convergence results of penetration depth

The failure patterns observed in the first specimen closely matched the experimental findings, which is evident from Figure 8.11. D_1 and D_2 represented the maximum and minimum of the crater. The diameter of equivalent circle of the crater (D_{eq}) could be calculated as $\sqrt{D_1 D_2}$. Table 8.5 shows that the numerical prediction of D_{eq} was 322.2 mm, while the experimental result measured 356 mm, resulting in an approximate difference of 9.5%. Furthermore, the penetration depth measured 65 mm in the numerical prediction, whereas the experimental result showed 57 mm, indicating an approximately 14.0% difference. Concerning specimen 2, the numerical prediction for D_{eq} was 333.5 mm, while the experimental measurement recorded 357 mm, exhibiting an approximate difference of 6.6%. The penetration depth was predicted to be 102 mm in the numerical analysis, whereas the experimental data indicated 103 mm, resulting in an approximate difference of 0.97% (see Figure 8.12). The results demonstrated a clear alignment between the numerical predictions and experimental measurements. As a result, employing this numerical model allows for precise simulation of the impact behaviour observed in reinforced concrete panels subjected to FT cycles in subsequent studies.

(a)

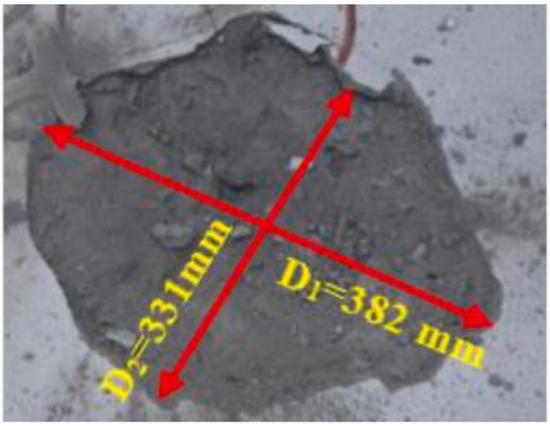

(b)

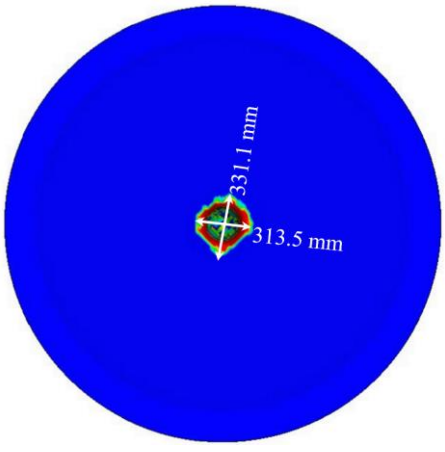

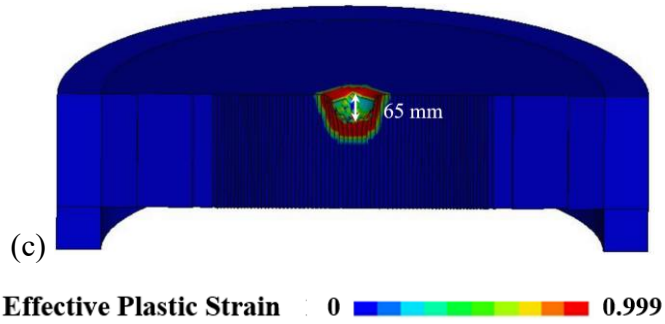

Figure 8. 11 Failure patterns of reinforced concrete panel for specimen 1. (a) Front crater from experiment (b) Front crater from numerical simulation (c) Penetration depth of concrete panel

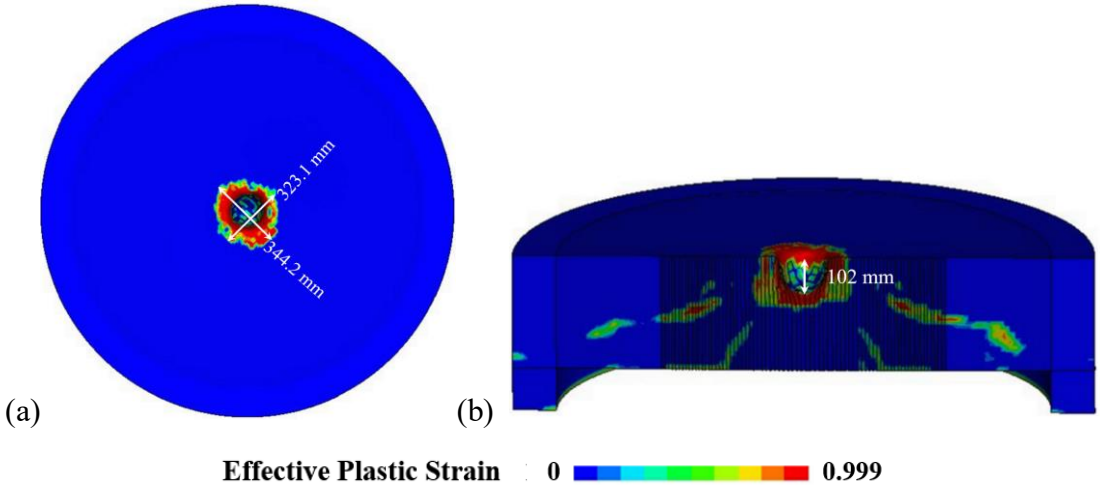

Figure 8. 12 Failure patterns of reinforced concrete panel for specimen 2. (a) Front crater from numerical simulation (b) Penetration depth of concrete panel

Table 8.5 Comparative analysis of numerical and experimental findings for concrete panels.

Numerical Test Trial	Numerical results (mm)		Experimental results (mm)		Error (%)	
	Penetration depth	Equivalent diameter of crater	Penetration depth	Equivalent diameter of crater	Penetration depth	Equivalent diameter of crater
1	65	322.2	57	356	-14	9
2	102	333.5	103	357	1	7

8.4 Impact resistance of reinforced concrete panel after cryogenic FT cycles

In the preceding section, the material and numerical model validation demonstrated its capability to accurately forecast the impact resistance of the designated reinforced concrete panel under normal room temperature conditions. Nevertheless, when it comes to LNG storage tanks, the structural integrity faces an additional obstacle due to the effects of FT cycles. To analyse the influence of FT cycle in relation to reinforced concrete panel after cryogenic FT cycles, four different groups were tested, including 0 time, 10 times, 20 times and 30 times of FT cycles. The temperature ranged from 20 °C ~ -165 °C with cooling rate 2~3 °C/min. A 500 kg impactor was free dropping at 35 m falling height (its impact velocity was 26.19 m/s). The dimension of the reinforced concrete panel was discussed in Section 3.2. In this section, the concrete compressive strength was set as 53.8 MPa. The MAT_CSCM_CONCRETE material model was utilised for analysing concrete without any exposure to FT cycles. Conversely, the MAT_CSCM model was employed to study the varying properties of NSC under various numbers of FT cycles, and the input parameters are summarised in Tables 8.1, 8.2 and 8.3. Other materials such as reinforcements, steel liner and impactor etc. were the same as those indicated in Section 8.3.

The failure patterns of target reinforced concrete panel are presented in Figure 8.13. With an increase in the number of FT cycles, the dimensions of the crater on the upper surface of the target panel also expanded. D_{eq} on the upper surface of the target panel for 0 time, 10 times, 20 times and 30 times of FT cycles was 268.0 mm, 336.7 mm, 351.9 mm and 383.7 mm, respectively. After 10 times, 20 times, as well as 30 times of FT cycles, the equivalent diameter of the crater was 1.25, 1.31 and 1.43 times greater than the specimen that had not undergone any FT cycles. This demonstrated a progressive enlargement of the front crater with each additional FT cycle. With the escalation in the number of FT

cycles, there was a corresponding increase in the penetration depth of the target panel (see Figure 8.14). Specifically, the penetration depth measurements for 0 time, 10 times, 20 times, and 30 times of FT cycles were 61 mm, 82 mm, 90 mm, and 93 mm, respectively. Additionally, after undergoing 10 times, 20 times, and 30 times of FT cycles, the penetration depth increased by 1.34 times and 1.48 times as well as 1.52 times, respectively, as compared to the specimen that without any FT cycles. This indicated a clear and progressive amplification in the penetration depth as the number of FT cycles was augmented. In conclusion, the impact resistance of concrete structures could be influenced by FT cycles.

The repeated exposure to freezing and thawing conditions could lead to an increase in both the size of craters on the surface and the penetration depth (see Figure 8.15). As the number of FT cycles rises, these effects become more pronounced, indicating that concrete structures, especially those subjected to harsh environmental conditions, may experience reduced impact resistance over time. From Section 8.2, it was evident that this phenomenon was related to the decrease in concrete performance such as compressive strength, splitting tensile strength, fracture energy etc. after cryogenic FT cycles. This degradation in impact resistance is a critical consideration for the long-term durability and performance of such structures, warranting careful assessment and appropriate mitigation strategies in design and maintenance practices.

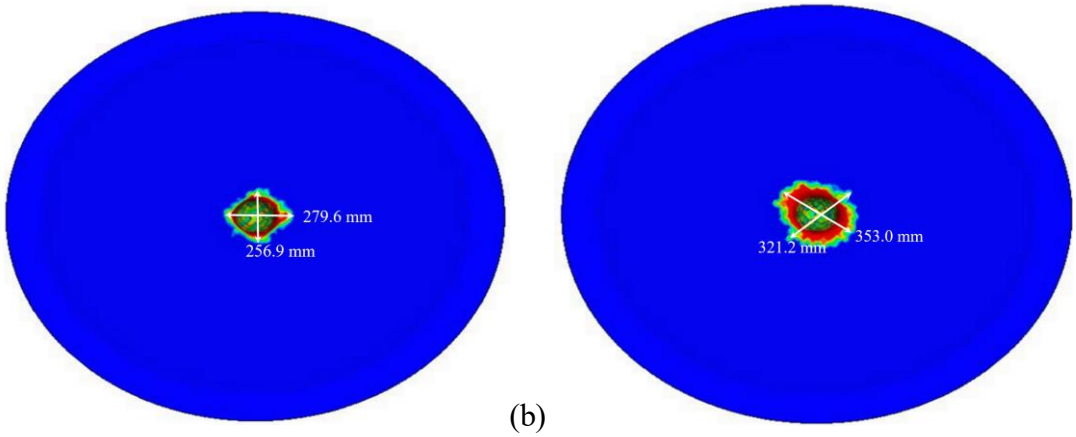

(a) (b)

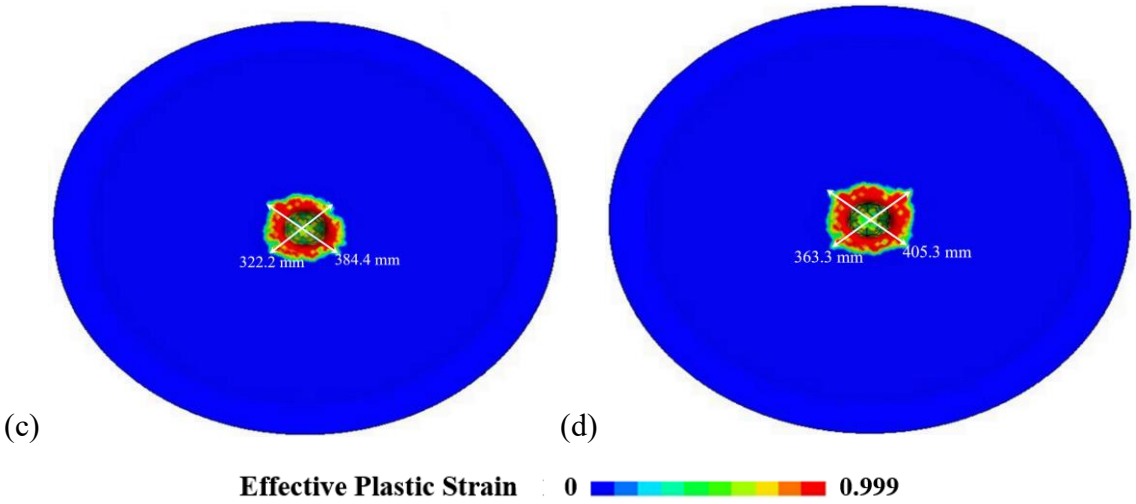

Figure 8. 13 Failure patterns of reinforced concrete panels. (a) 0 time FT cycle (b) 10 times FT cycles (c) 20 times FT cycles (d) 30 times FT cycles

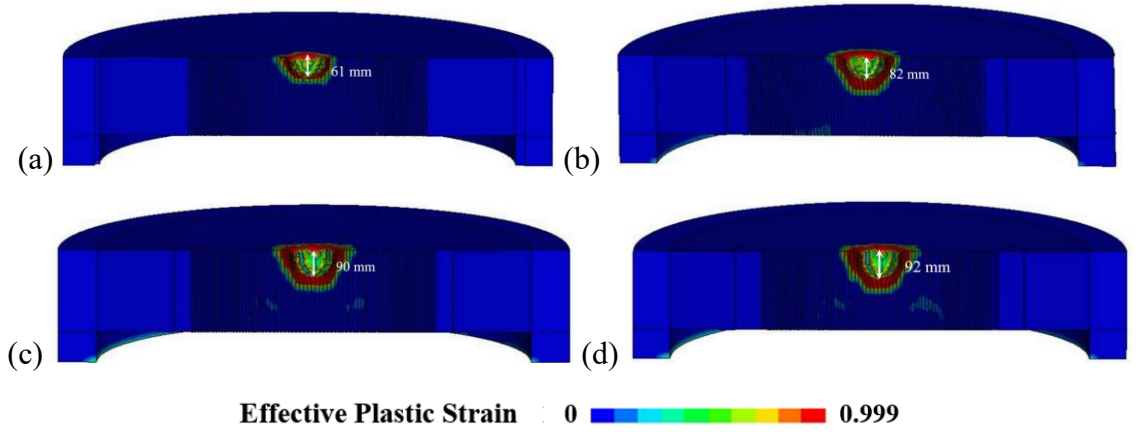

Figure 8. 14 Penetration depth of reinforced concrete panels. (a) 0 time FT cycle (b) 10 times FT cycles (c) 20 times FT cycles (d) 30 times FT cycles

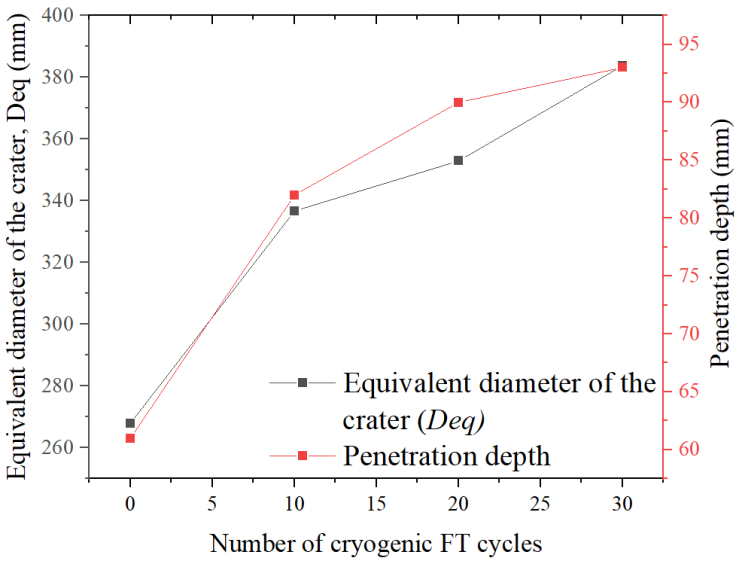

Figure 8. 15 Number of cryogenic FT cycles versus D_{eq} *and penetration depth.*

8.5 Parametric study

Utilising the aforementioned model, a parametric study was conducted to examine the impact behaviour of target concrete panels under both ambient temperature conditions and after undergoing FT cycles. This study aimed to investigate the effects of various parameters on the panel's response. The mesh size and material model were identical to those in Section 8.4. In this section, it would explore the influence of impact velocity and impact mass at ambient temperature and after 10 times of cryogenic FT cycles.

8.5.1 Effect of impact velocity

To assess the impact of varying impact velocities on reinforced concrete panels after undergoing FT cycles, four distinct impact velocity groups were examined. These groups included impact velocities of 19.70 m/s (corresponding to a falling height of 20 m), 22.13 m/s (dropping height of 25 m), and 24.24 m/s (dropping height of 30 m), as well as 26.19 m/s (dropping height of 35 m). A 500 kg weight was used as the impactor during the tests. Figure 8.16 shows the failure patterns of reinforced concrete panels at ambient temperature under different impact velocities. The diameter of the equivalent circle of the crater with falling height 20 m, 25 m and 30 m was 191.1 mm, 221.3 mm and 257.4 mm and the penetration depth was 51 mm, 55 mm and 60 mm, respectively. In other words, the damage area on the top side was larger with the increase in impact mass. Figure 8.17 displays the final damage patterns of the target panels under various impact velocities after 10 FT cycles, revealing that higher impact velocities led to more severe damage to the panels. The diameters of the equivalent circle of the crater at impact velocities of 19.70, 22.13 and 24.24 m/s were measured at 267.2 mm, 278.0 mm, and 304.6 mm, respectively. Comparatively, these values were 0.79 times, 0.83 times, and 0.9 times smaller than the diameter observed at 26.19 m/s impact velocity. That means the diameter

of the crater increased as the impact velocity escalated. It was clear that the target panels at ambient temperature are more resistant than the ones after 10 FT cycles.

Moreover, as the impact velocity increased, it led to a greater penetration depth of the panel, as demonstrated in Figure 8.18. At impact velocities of 19.70, 22.13 and 24.24 m/s, the penetration depths were measured as 54 mm, 70 mm, and 74 mm, respectively. This indicates that higher impact velocities are associated with deeper penetration into the panel. With an equivalent impact weight, it was evident that the impact resistance of concrete panels following 10 FT cycles was inferior as compared to their performance at room temperature.

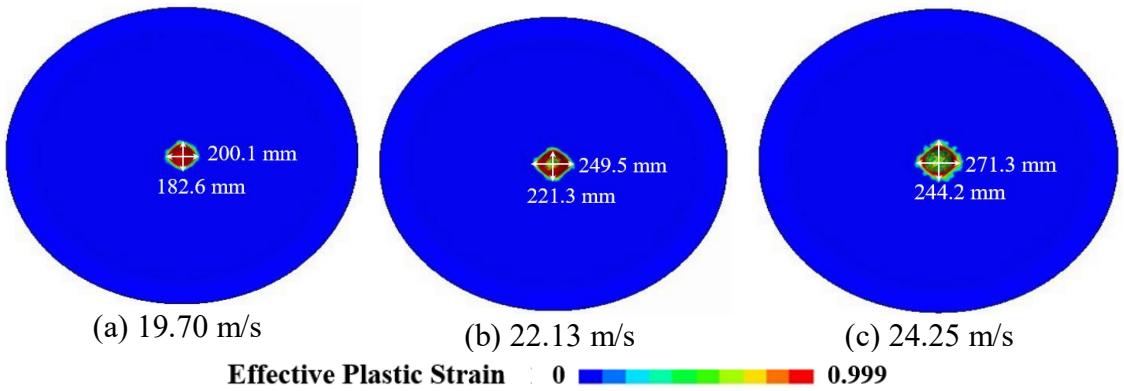

Figure 8. 16 Final damage patterns of target panels at different impact velocities at ambient temperature.

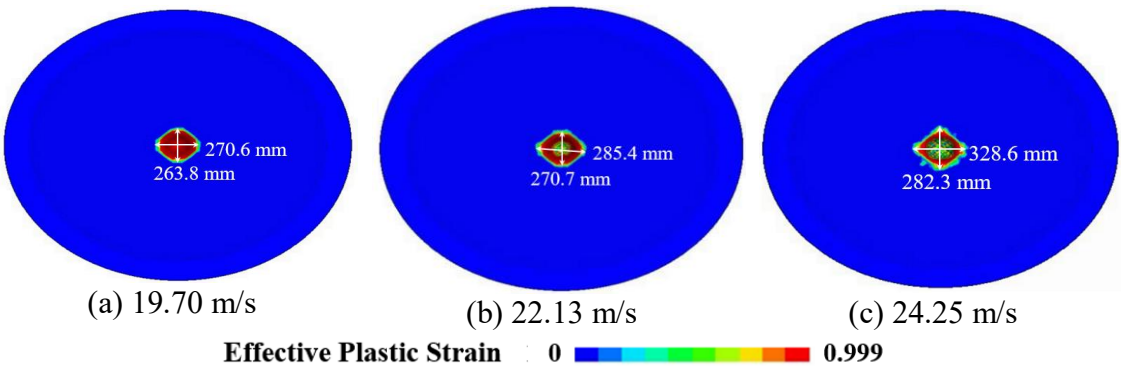

Figure 8. 17 Final damage patterns of target panels at different impact velocities after 10 FT cycles.

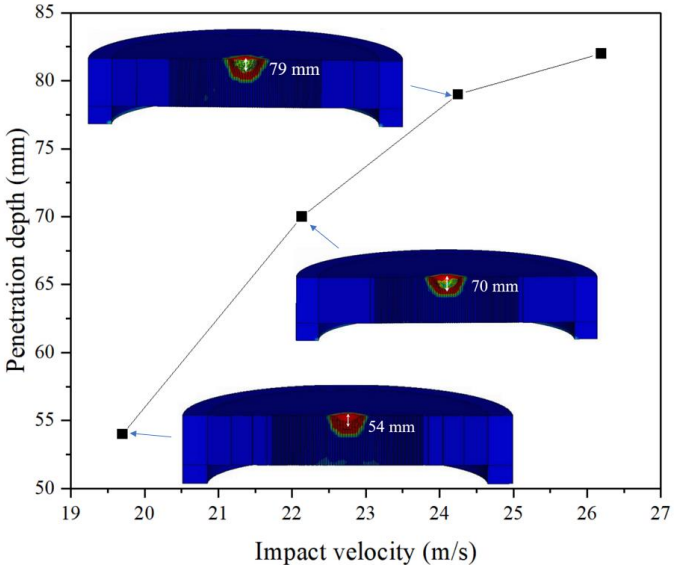

Figure 8. 18 Penetration depth of target panels in different impact velocities.

8.5.2 Effect of impactor weight

The effect of impactor weight was examined by altering the weight of the punch utilised in the tests to 200, 500, and 800 as well as 1100 kg. The falling height was kept constant at 35 m, resulting in an impact velocity of 26.19 m/s during the experiments. Figure 8.19 displays the failure patterns of reinforced concrete panels at ambient temperature under different impactor mass. The diameter of the equivalent circle of the crater with impactor mass 200, 800 and 1100 kg was 231.1 mm, 330.6 mm and 431.1 mm and the penetration depth was 42 mm, 273 mm and 400 mm, respectively. Based on the damage level from Zou *et al.* [246], damage level I refers to the formation of a localised crater solely on the front surface of the reinforced concrete panel upon impact; Damage level II involves not only the presence of a front impact crater but also the emergence and propagation of both radial and circumferential cracks; Damage level III is characterised by the complete perforation of the RC panel, signifying a severe level of structural damage where the panel has been entirely penetrated. Compared with 200 and 800 kg, circumferential and radial cracks were developed in the target concrete panel with 1100 kg, which referred to damage level II. Furthermore, the punching shear failure area increase dramatically with

the increase in impact mass. Figure 8.20 presents the final damage patterns of the target panels under different impact masses subjected to 10 cycles of FT, indicating that higher impact masses resulted in more severe damage to the panels. Notably, when the impact weight reached 1100 kg, the hammer penetrated the entire concrete panel. The diameter of the equivalent circle of the crater at impact masses of 200, 800, and 1100 kg was measured as 260.2 mm, 454.6 mm, and 573.5 mm, respectively. From Figure 8.20(c), it could be observed that the entire target plate was punctured by a high-speed punch, resulting in circumferential and radial cracks. This was the most severe specimen among all tests, which was damage level III. It was significant to highlight that, in Figure 8.18 and Figure 8.19, the diameter of the equivalent circle of the crater on the panel after 10 cycles of FT, demonstrated increments of 1.1 times, 1.3 times, 1.4 times, and 1.3 times in comparison with the panels subjected to ambient temperature conditions, respectively. Additionally, as illustrated in Figure 8.21, an increase in impact mass led to a greater penetration depth of the panel. Specifically, the penetration depth for impact masses of 200, 800, and 1100 kg was measured as 45 mm, 293 mm, and 400 mm, respectively. The penetration depth for 500, 800 and 1100 kg impactor was 1.82 times, 6.5 times, and 8.89 times greater than the 200 kg one. It was noted that the impact resistance of concrete panels exhibited a decline following 10 FT cycles, in contrast to its performance under room temperature conditions at the same impact velocity.

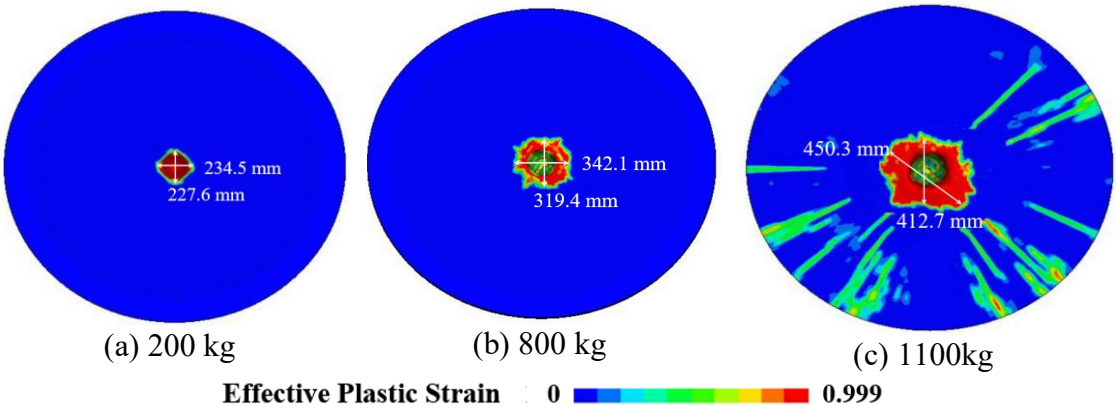

(a) 200 kg (b) 800 kg (c) 1100kg

Figure 8. 19 Final damage patterns of target panels in different impact weights at ambient temperature.

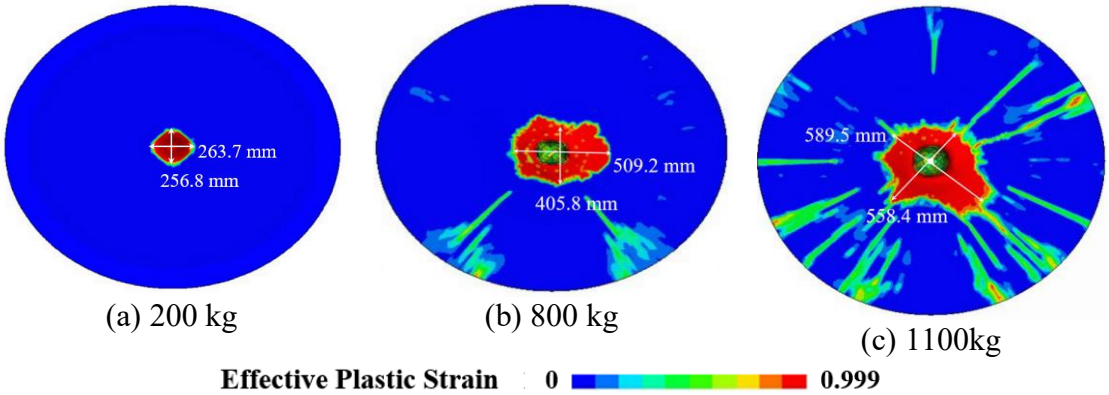

Figure 8. 20 Final damage patterns of target panels in different impact weights after 10 FT cycle.

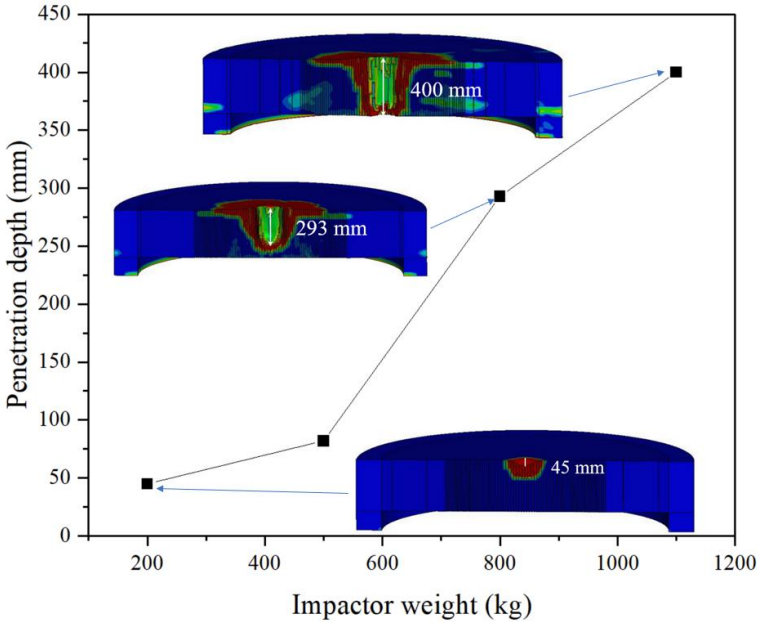

Figure 8. 21 Penetration depth of target panels in different impact mass.

8.6 Limitations

The application scope of the model is specifically targeted at assessing the impact resistance of reinforced concrete structures, particularly in scenarios involving cryogenic FT cycles. This model finds relevance in critical energy infrastructure applications, such as ACLNG storage tanks.

Notwithstanding its contributions, this study does have certain limitations. The findings and conclusions for this study are specific to a typical concrete material with uniaxial

compressive strength of 53.8 MPa and a w/c ratio of 0.44. Variations in material properties, such as compressive strength and w/c ratio, could yield different outcomes, and therefore, the generalisation of the findings to a broader range of concrete compositions may require further experimental investigation and validation.

8.7 Summary

The impact resistance of reinforced NSC panels after FT cycles was investigated using a refined finite element model. The CSCM model was adopted and modified to incorporate various parameters such as shear modulus (G), bulk modulus (K), uniaxial and triaxial compression surface, as well as damage parameters. The subsequent conclusions can be drawn:

- After FT cycles, the elastic modulus, splitting tensile, and compressive strength as well as fracture energy of concrete decreased. As the number of FT cycles increased, the performance of concrete also continuously decreased.
- The modified CSCM model effectively captured the impact behaviour of reinforced concrete panels after FT cycles, considering various mechanical parameters.
- The predictive capability of the numerical model was validated through experimental verification, demonstrating its reliability in assessing the impact resistance of reinforced concrete structures.
- FT cycles were observed to adversely affect the impact resistance of the concrete structures. As the number of FT cycles increased, there was an observable escalation in the dimensions of craters formed on the surface as well as an increase in the penetration depth of the panels. These trends collectively suggested a decline in the impact resistance of the panels with the progression of FT cycles.

Chapter 9. BEHAVIOUR OF ACLNG STORAGE TANK UNDER BLAST LOADING CONSIDERING CRYOGENIC TEMPERATURE EFFECT

9.1 Introduction

This study explores the dynamic performance of ACLNG storage tanks under combined blast loading and cryogenic temperature conditions, which are critical for ensuring their safety and structural integrity. To accurately capture the mechanical behaviour of concrete for both NSC and UHPC at low and cryogenic temperatures, a modified Karagozian & Case Concrete (KCC) model was developed, incorporating temperature-dependent adjustments for material brittleness and strength. The model was validated against experimental data, confirming its effectiveness in predicting the material response under extreme environmental and loading scenarios. A full-scale numerical model of an ACLNG storage tank was established using LS-DYNA, simulating the effects of blast loads at cryogenic temperatures. Results indicate that cryogenic conditions amplify the brittleness of concrete and influence the damage patterns of inner tank under blast loading, emphasising the importance of temperature-sensitive design considerations. The findings of this research contribute to the advancement of ACLNG storage tank design, offering practical guidance for optimising safety and resilience in demanding operational environments.

9.2 Constitutive models and material properties

9.2.1 KCC Concrete model

Many concrete constitutive models such as Karagozian & Case Concrete model (KCC) [247], Riedel-Hiermaier-Thoma (RHT) model [248] and the CSCM are available in

commercial software LS-DYNA [242] and are extensively used on NSC structural modelling against blast loads. As for NSC, the KCC model parameters can be derived automatically using uniaxial compressive strength. This feature renders KCC a very popular concrete constitutive model especially when material characterising results are not available. However, to better simulate the behaviour of CUHPC, it is required to adjust the parameters of the KCC model due to the varied mechanical properties, particularly the tensile capability of UHPC [249]. The strength/stiffness change owing to the cryogenic attack, rate sensitivity change, and damage also needs to be considered for both NSC and CUHPC prior to performing the multi-hazard (cryogenic attack and blast loadings) analysis in the KCC model.

9.2.1.1 Strength surface parameters

The initial yield strength surface $\Delta\sigma_y$, maximum strength surface $\Delta\sigma_m$, and residual strength surface $\Delta\sigma_r$ are the three independent strength surfaces defined by the KCC model [247]. The following definitions apply to these three shear strength surfaces,

$$\Delta\sigma_m = a_0 + \frac{p}{a_1+a_2 p} \quad \text{(maximum strength surface)} \tag{9.1}$$

$$\Delta\sigma_r = \frac{p}{a_{1f}+a_{2f} p} \quad \text{(residual strength surface)} \tag{9.2}$$

$$\Delta\sigma_y = a_{0y} + \frac{p}{a_{1y}+a_{2y} p} \quad \text{(yield strength surface)} \tag{9.3}$$

where

$$p = -\frac{\sigma_1+\sigma_2+\sigma_3}{3} \tag{9.4}$$

is the hydrostatic pressure with σ_1, σ_2 and σ_3 being the principal stresses. Seven material strength surface parameters are $a_0, a_1, a_2, a_{1f}, a_{2f}, a_{1y}, a_{2y}$. Joy and Moxley [250] demonstrated that the initial yield strength for NSC is 0.45 times of its maximum strength

under triaxial compression. The equivalent yield surface point (p', σ_y) can be empirically estimated using Equation (9.5) according to the maximal strength surface point (p, σ_m). The maximum and residual strength can be determined by using the triaxial stress-strain curve. It is worth noting that because the residual strength is zero under unconfined compression test, the residual strength will be zero when the pressure is equal to zero.

$$\begin{cases} \Delta\sigma_y = 0.45\ \Delta\sigma_m \\ p' = p - \dfrac{0.55}{3}\Delta\sigma_m \end{cases} \tag{9.5}$$

Using linear interpolation method, the current failure surface of concrete under different states can be determined with the consideration of the accumulated damage as follows,

$$\Delta\sigma = \sqrt{3J_2} = \begin{cases} \Delta\sigma_y + \eta(\Delta\sigma_m - \Delta\sigma_y), & \lambda \le \lambda_m \quad \text{Strain hardening} \\ \Delta\sigma_r + \eta(\Delta\sigma_m - \Delta\sigma_r), & \lambda > \lambda_m \quad \text{Strain softening} \end{cases} \tag{9.6}$$

where $J_2 = \frac{(\sigma_1-\sigma_2)^2+(\sigma_2-\sigma_3)^2+(\sigma_1-\sigma_3)^2}{6}$ is the second deviatoric stress invariant, η presents the scale factor which is related to the modified effective plastic strain λ. $\eta(\lambda)$ value varies from 0 to 1. The value of η is determined by the damage variable λ. It indicated stain hardening phase where λ increases from 0 to λ_m, and η increases from 0 to 1. It represents for strain softening when η decreases from 1 to 0.

Triaxial compression tests with various confinement levels and unconfined compression tests can also yield data on the strength meridian. Using the unconfined compressive strength of concrete, the KCC model is automatically produced. The following scaling law can be used to create the compressive strength surface characteristics for an updated concrete model in which unconfined compressive strength is given.

$$a_{0n} = a_0 r,\ a_{1n} = a_1,\ a_{2n} = a_2 r \tag{9.7}$$

where $r = \frac{f_{c,new}}{f_{c,old}}$, the unconfined compressive strength of a previously modelled concrete is represented by $f_{c,old}$. The following Equations (9.8)-(9.10) are used to determine the strength surface parameters of normal concrete [251].

$$a_0=0.2956 f_c;\ a_1=0.4463;\ a_2=0.0808/f_c \tag{9.8}$$

$$a_{0y}=0.2232 f_c;\ a_{1y}=0.625;\ a_{2y}=0.2575/f_c \tag{9.9}$$

$$a_{0f}=0;\ a_{1f}=0.4417;\ a_{2f}=0.1183/f_c \tag{9.10}$$

In the present study, uniaxial compressive strength with 41.2 MPa for NSC at room temperature and the compressive strength with 55.7 MPa at -160 ℃ were adopted, based on the experimental results from Yan and Xie [252]. The uniaxial compressive strength with 161.2 MPa for CUHPC is used as examples at room temperature and 211.6 MPa at -160 ℃ from the previous study [219]. The corresponding strength surface parameters are displayed in Table 9.1 and Table 9.2.

Table 9. 1 NSC strength surfaces parameters after modification.

	a_0	a_1	a_2	a_{1f}	a_{2f}	a_{0y}	a_{1y}	a_{2y}
NSC 41.2 MPa KCC default	1.22E+7	0.446	2.0E-9	0.442	2.87E-9	9.20E+6	0.625	6.25E-9
NSC at -160 ºC	1.65E+7	0.479	1.45E-9	0.442	2.12E-9	1.24E+7	0.625	4.62E-9

Table 9. 2 UHPC strength surfaces parameters after modification.

	a_0	a_1	a_2	a_{1f}	a_{2f}	a_{0y}	a_{1y}	a_{2y}
CUHPC at 20 ºC [253]	5.48E+7	0.446	1.15E-9	0.442	1.08E-9	3.5E+7	0.625	3.37E-9
CUHPC at -160 ºC	7.27E+7	0.446	8.73E-10	0.442	8.21E-10	4.7E+7	0.625	2.57E-9

In the KCC model, tensile strength of concrete at cryogenic temperature is another critical parameter to be considered, which can evaluate the residual tensile strength of concrete structures at cryogenic temperature. In terms of NSC, Shi et al. [254] suggested that the

relationship between tensile strength (f'_t) and temperature T from 20 ℃ to −196 ℃ is as follows,

$$f_t = 0.429 f'^{0.509}_c \quad -196℃ \leq T \leq 20℃ \tag{9.11}$$

where f'_c is compressive strength at -160 ºC. Therefore, f'_t=2.85 MPa for NSC at ambient temperature, and f'_t=3.32 MPa for NSC at -160 ℃.

In the current study, the tensile strength regarding CUHPC was used 7.20 MPa at room temperature and 11.25 MPa at -160 °C, respectively [219].

9.2.1.2 Relationship between λ and η

To characterise the hardening and softening of strength for NSC in compressive and tensile meridian, a default relationship between the modified effective plastic strain λ and the strength scale factor η is employed [255]. Additionally, a new modified λ-η relationship is created to satisfy the present UHPC. Table 9.3 presents both the NSC and current CUHPC λ-η relationships.

Table 9. 3 NSC and CUHPC relationships between λ and η in the KCC model.

NSC λ-η relationship		CUHPC λ-η relationship [256]	
λ	η	λ	η
0.0	0.0	0.0	0.0
8E-06	0.85	8E-06	0.85
2.4E-05	0.97	2.4E-05	0.97
4E-05	0.99	4E-05	0.99
5.6E-05	1	5.6E-05	1
7.2E-05	0.99	7.2E-05	0.99
8.8E-05	0.97	8.8E-05	0.97
3.2E-04	0.5	2.5E-04	0.8
5.2E-04	0.1	6.2E-04	0.5
5.7E-04	0.0	1.1E-03	0.3
1.0	0.0	2E-03	0.1
10	0	5E-03	0.0
1E+10	0	1E+10	0.0

9.2.1.3 Damage accumulation parameters

As mentioned earlier, the modified effective plastic strain λ is to account for damage accumulation under both compression and tension. The formula can be defined as follows,

$$\lambda = \begin{cases} \int_0^{\overline{\varepsilon^p}} \frac{d\overline{\varepsilon^p}}{r_f(1+p/r_f f_t)^{b_1}} & \text{for } p \geq 0 \\ \int_0^{\overline{\varepsilon^p}} \frac{d\overline{\varepsilon^p}}{r_f(1+p/r_f f_t)^{b_2}} & \text{for } p < 0 \end{cases} \tag{9.12}$$

where r_f is the rate enhancement factor (DIFs), $d\bar{\varepsilon}^p$ is the effective plastic strain increment, b_1 controls the damage and softening behaviour of stress-strain curve in uniaxial compression and b_2 governs the damage and softening behaviour of stress-strain curve in tension.

Wu and Crawford [255] also demonstrated that the data from the uniaxial compression test is fitted to obtain b_1 regularisation, while b_2 can be generated by fitting numerical fracture energy which can be obtained from tensile test. In this study, b_1 is equal to 0.25 and 0.1 for the target temperature of 20 and -160 ºC for the current CUHPC, whereas b_1 =1.65 and 1.0 at 20 and -160 ºC for NSC. b_2 is assumed to be 1.35 for both NSC and CUHPC at cryogenic temperature.

There is another damage evolution parameter in the KCC model ω which is an associativity parameter that controls volume expansion in shear dilatancy modelling. The element size and discretisation do have an impact on ω selection, albeit the effect is not entirely deterministic. The recommended value for well-confined and NSC concrete components is 0.80 or 0.90, for concrete components with poorly confined and without coarse aggregate is 0.5 or 0.75, whereas high-strength or CUHPC concretes with fine aggregate is less than 0.5 [255]. Hence, ω=0.8 for NSC in the following model validation and ω is taken as 0.5 for CUHPC.

9.2.1.4 Strain rate sensitivity

Strain rate can affect the dynamic behaviour of materials. DIF can be determined as the ratio between the dynamic strength and the static strength, which is utilised to describe the strength enhancement of materials under high strain rate.

The NSC rate sensitivity is adopted from the dynamic compressive and splitting tensile test data [199], as shown in Table 9.4.

Table 9. 4 DIF of NSC at various temperatures [199].

20 ºC		-160 ºC		20 ºC		-160 ºC	
Strain rate	CDIF	Strain rate	CDIF	Strain rate	TDIF	Strain rate	TDIF
0	1	0	1	0	1	0	1
24.61	1.18	39.10	1.12	6.73	2.57	24.32	4.23
37.87	1.39	45.26	1.12	18.92	3.42	25.99	4.26
39.18	1.47	79.38	1.16	22.03	3.41	41.26	4.82
38.63	1.47	83.13	1.20	24.09	3.43	44.26	5.10
76.60	1.54	108.99	1.26	36.77	4.13	58.06	5.29
81.45	1.54	118.88	1.31	41.08	4.01	71.97	5.43
81.81	1.55	155.16	1.36	41.15	3.83	78.79	5.63
87.65	1.55	158.19	1.37	43.76	3.90	-	-
119.30	1.73	-	-	57.2	3.99	-	-
121.30	1.79	-	-	59.38	4.16	-	-
124.01	1.75	-	-	60.64	4.24	-	-
127.00	1.79	-	-	78.05	4.44	-	-
159.97	1.82	-	-	80.90	4.46	-	-
164.28	1.89	-	-	81.14	4.50	-	-
166.63	1.93	-	-	-	-	-	-
207.85	1.94	-	-	-	-	-	-

For UHPC, Chi et al. [219] obtained the DIFs values of CUHPC at 20 and -160 ºC by curve fitting the experimental data, as shown in Table 9.5. The data listed below is adopted to predict the blast resistance of CUHPC at cryogenic temperature attack in the following simulation.

Table 9. 5 DIFs of CUHPC at various temperatures [219].

20 ºC		-160 ºC		20 ºC		-160 ºC	
Strain rate	CDIF	Strain rate	CDIF	Strain rate	TDIF	Strain rate	TDIF
0	1	0	1	0	1	0	1
38.50	1.19	45.22	1.02	20.99	2.00	23.29	2.71
40.72	1.16	50.04	1.07	21.39	2.00	42.33	2.85
41.01	1.18	82.32	1.13	24.79	2.06	46.58	2.90
77.20	1.27	88.86	1.15	25.24	2.31	64.34	3.16
71.70	1.25	119.21	1.27	39.89	2.27	80.48	3.58
81.38	1.32	122.82	1.24	40.63	2.31	-	-
103.15	1.37	161.49	1.30	42.71	2.59	-	-
119.09	1.46	-	-	42.82	2.57	-	-
118.90	1.47	-	-	60.02	2.62	-	-
120.09	1.47	-	-	60.84	2.42	-	-
158.23	1.52	-	-	61.68	2.49	-	-
162.60	1.45	-	-	63.22	2.54	-	-
165.81	1.56	-	-	76.20	2.59	-	-
-	-	-	-	77.38	2.44	-	-
-	-	-	-	81.32	2.77	-	-

9.2.1.5 Equation of state (EOS)

EOS_TABULATED_COMPACTION is used to explain the relationship between pressure and volumetric strain in the KCC model. The pressure is defined as Equation (9.14) following below. Normally, the uniaxial compressive strength can be utilised to automatically generate the EOS of NSC, which is listed in Table 9.6.

$$p = C(\mu) + \gamma_0 \theta(\mu) E_0 \tag{9.14}$$

where γ_0 is the ratio of specific heat, and E_0 is presented as the internal energy per initial volume. $C(\mu)$ is the input pressure from EOS assessed along a 0 K isotherm and $\theta(\mu)$ is thermal coefficient with respect to volumetric strain function, respectively.

In the present model for UHPC, a piecewise EOS is described as follows,

$$\begin{cases} p = K\mu & p < p_{crush} \\ p = p_{crush} + K_{lock}(\mu - \mu_{crush}) & p_{crush} < p < p_{lock} \\ p = K_1\overline{\mu} + K_2\overline{\mu}^2 + K_3\overline{\mu}^3 & p > p_{lock} \end{cases} \tag{9.15}$$

where p_{crush} is the pressure at the first EOS slope change point, whereas p_{lock} is the second slope change point. The elastic bulk modulus $K = p_{crush}/\mu_{crush} = \frac{E}{3(1-2v)}$, where v is presented as the Poisson's ratio and E is the modulus of elasticity. $K_{lock} = (p_{lock} - p_{crush})/(\mu_{plock} - \mu_{crush})$ whereμ_{plock} is the volumetric strain for p_{lock} and $\overline{\mu} = (\mu - \mu_{lock})/(1 + \mu_{lock})$, where $\mu_{lock} = \frac{\rho_{grain}}{\rho_o} - 1$ (ρ_{grain} is the density after compaction and ρ_o is the original density).

Tables 9.6 and 9.7 illustrate the full definitions of the updated EOSs for various temperatures in relation to NSC and CUHPC, respectively.

Table 9. 6 EOS for NSC at various temperatures.

20 ºC (Default)	μ	0	-0.0015	-0.0043	-0.01	-0.0305	-0.0513	-0.0726	-0.0943	-0.174	-0.208
	C (MPa)	0	21.70	47.31	75.96	144.32	217.68	308.83	472.47	2758	4219
	K (GPa)	14.47	14.47	14.67	15.41	18.33	21.27	24.19	26.40	59.41	72.34
-160 ºC	μ	0	-0.0015	-0.0043	-0.01	-0.0305	-0.0513	-0.0726	-0.0943	-0.174	-0.208
	C (MPa)	0	25.23	55.01	88.31	167.81	253.10	359.03	549.35	3207	4906
	K (GPa)	16.82	16.82	17.05	18.15	21.58	25.35	28.92	31.56	71.02	86.49

Table 9. 7 EOS for CUHPC at various temperatures.

20 ºC	μ	0	-0.0016	-0.0043	-0.01	-0.0305	-0.0513	-0.0726	-0.0943	-0.174	-0.2
	C (MPa)	0	29.18	83.66	194.6	503.2	801.5	1107	1418.2	3016.4	4930
	K (GPa)	22.71	22.71	23.39	24.07	30.66	33.38	37.93	41.56	93.57	114
-160 ºC	μ	0	-0.0016	-0.0043	-0.01	-0.0305	-0.0513	-0.0726	-0.0943	-0.174	-0.2
	C (MPa)	0	49.18	107.2	172.1	327.1	493.3	699.8	1070.7	6251	9561
	K (GPa)	27.15	27.15	27.96	28.78	36.65	39.91	45.35	49.69	112	136

9.2.2 Steel reinforcements model

9.2.2.1 Temperature degradation effect

The mechanical properties of steel bars exposed to low temperatures can also change. Chanda [257] has studied the performance of steel in the Arctic region. It found out the yield strength of X80 steel was increased by 4.8% and 11.7% at temperature -30 ℃ and -90 ℃, respectively, in comparison with 25 ℃. Dahmani *et al.* [2] stated the properties

of reinforcing steel and prestressing steel at cryogenic temperature. The study indicated an approximately 77.0% increase in yield strength at -196 ℃ in comparison with 20 ℃ for reinforced steel. It also reported an approximate 17.9% rise in yield strength at -165 ℃ when compared to 20 ℃ for prestressing steel. Yan & Xie [243] investigated the elastic modulus, yield strength, ultimate strength etc. of reinforcing steel HRB335, HRB400 and special low temperature steels (SLTS), ranging from 20~-165 ℃. It showed the elastic modulus, yield strength and ultimate strength for HRB335 were increased by 9.5%, 16.6% and 22.8% at -165 ℃ as compared to 20 ℃. With a temperature decline from 20°C to -165°C, the ductility of HRB335 steel experienced a reduction of 30%. Xie [244] evaluated three types of mild steel (Q235, Q355 and Q460) at cryogenic temperature ranging from 20~-165 ℃. The values of yield strength and ultimate strength for the mild steels notably increased under the influence of low temperatures. The yield and ultimate strength of Q235 increased by 61.1% and 29.0% at -165 ℃ as compared to 20 ℃.

Steel bars possess different thermal properties as compared to the concrete matrix. They exhibit minimal dimensional changes under cryogenic conditions. This difference in thermal expansion and contraction properties between the reinforcement and the concrete matrix can provide some level of protection to the reinforcement. Yan & Xie [243] and Xie [244] conducted research on steel bars at low temperatures, and the results showed that the elastic modulus, tensile strength, and ultimate strength of the steel bars increased with the decrease of temperature. The observed transition point from a ductile to a brittle failure mode for the tested HRB335 and HRB400 type of reinforcing steels was recorded at a threshold temperature of -80 ℃. Figures 9.1 (a) and (b), respectively, show the experimental results of the relative elastic modulus and tensile strength of steel bars based on Yan & Xie and Xie.

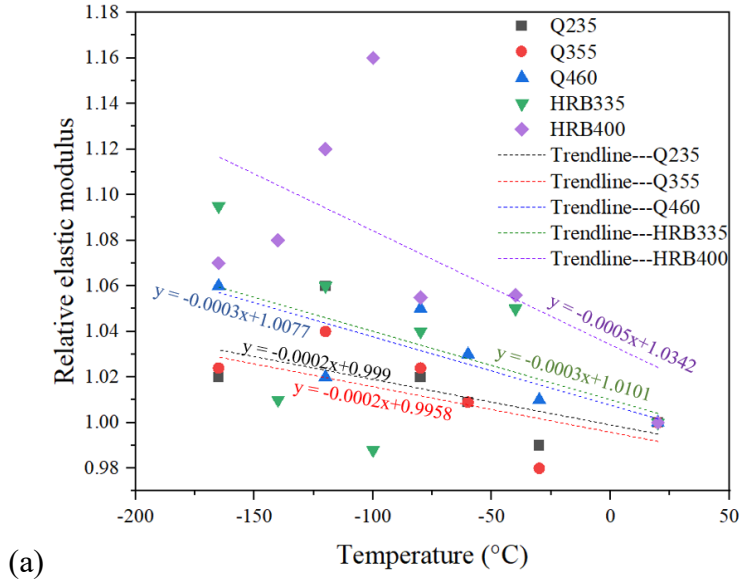

(a)

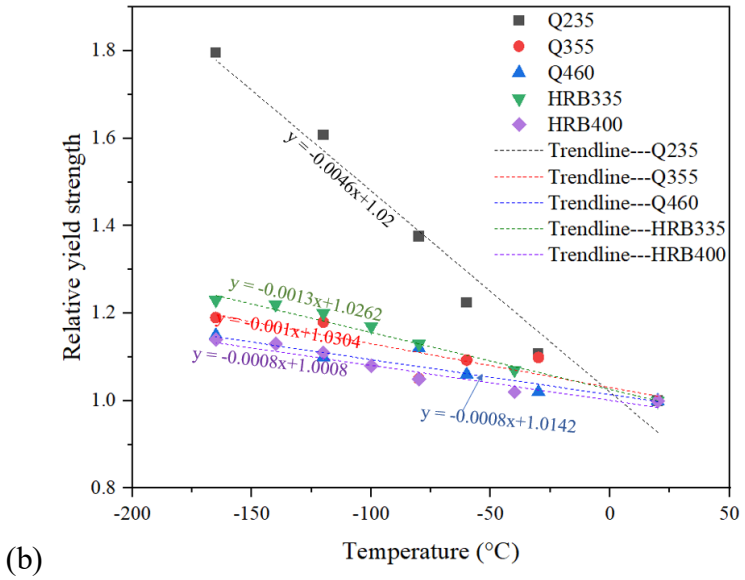

(b)

Figure 9. 1 Effect of the temperature with different steel types. (a) Relative elastic modulus (b) Relative yield strength

In addition, the trendlines were created based on the results. In this study, the properties of steel reinforcement including relative elastic modulus and yield strength will be based on the trendline in HRB335 as the following empirical formulas,

$$I_E = \frac{E_T}{E_a} = -0.0003T + 1.006 \quad -165℃ \leq T \leq 20℃ \tag{9.16}$$

$$I_y = \frac{f_T}{f_a} = -0.0013T + 1.026 \quad -165℃ \leq T \leq 20℃ \tag{9.17}$$

where I_E and I_y represent the relative elastic modulus and yield strength of the steel reinforcements, respectively. E_T and f_T are the elastic modulus and yield strength of the

steel reinforcements at low temperature, while E_a and f_a are the elastic modulus and yield strength of the steel reinforcements at room temperature.

9.2.2.2 Strain rate effect

The yield and ultimate tensile DIFs that suggested by CEB [258] are provided as follows,

$$\text{YDIF} = \frac{f_y}{f_{y0}} = 1.0 + \left(\frac{6.0}{f_{y0}}\right)\ln\left(\frac{\dot{\varepsilon_s}}{\dot{\varepsilon_{s0}}}\right) \tag{9.18}$$

$$\text{UDIF} = \frac{f_u}{f_{u0}} = 1.0 + \left(\frac{7.0}{f_{u0}}\right)\ln\left(\frac{\dot{\varepsilon_s}}{\dot{\varepsilon_{s0}}}\right) \tag{9.19}$$

where f_y is the dynamic yield strength and f_u is presented as ultimate tensile strength; f_{y0} and f_{u0} are static yield strength and ultimate tensile strength in MPa; $\dot{\varepsilon_s}$ is strain rate and $\dot{\varepsilon_{s0}}$ is strain rate at quasi-static state, which is equal to $50 \times 10^{-5}\ s^{-1}$.

9.3 Validation of reinforced concrete beam under static load at cryogenic temperature

To verify the accuracy of the reinforced concrete model at cryogenic temperature, the quasi-static test from Liu et al. [113] was adopted. The dimensions of reinforced concrete beam were 40 mm × 40 mm × 300 mm in width × height × length. The diameter (ϕ) of primary and secondary reinforcement was 4 mm, and the diameter (ϕ) for stirrup was 1.6 mm (see Figure 9.2). More details on the dimensions of reinforced concrete beams can be found in Liu et al. [113]. A full numerical reinforced concrete model was established to verify the quasi-static test and used the implicit solver in LSDYNA for Finite Element analysis. From Figure 9.3, it could be seen that the numerical model was mainly divided into three parts, including reinforced concrete beam, loading platen as well as the support. The mesh size of concrete, reinforcement, loading platen and support was 10 mm, 5 mm,

10 mm and 10 mm, respectively. MAT_CONCRETE_DAMAGE_REL3 was utilised as concrete model. In the model, the MAT_PIECEWISE_LINEAR_PLASTICITY material model was applied to represent the behaviour of steel rebars, and MAT_RIGID was adopted for loading platen and the support. The material properties employed in this numerical simulation are summarised in Table 9.8. The loading was placed at the upper surface of the reinforced concrete beam, and the distance between the two loading platens was 80 mm. Displacement loading was added to loading platen. In the current study, the results will be compared with the experimental data at room temperature and -160 ℃ .

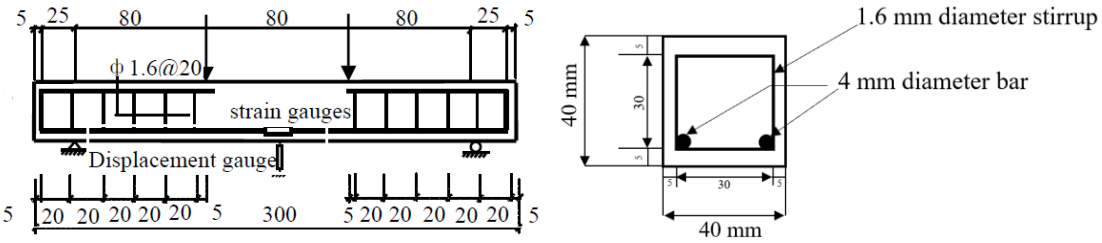

Figure 9. 2 Dimensions of reinforced concrete beam [113].

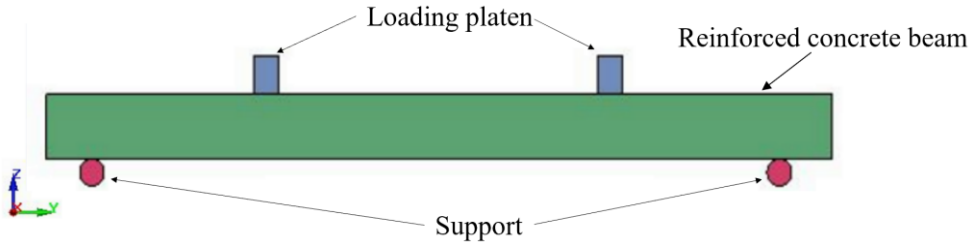

Figure 9. 3 Schematic view of reinforced concrete beam.

Table 9. 8 Parameters of concrete and steel reinforcement in quasi-static test.

Material	LS-DYNA Model	Input Parameters	20 ℃	-160 ℃
Concrete	MAT_CONCRETE_DAMAGE_REL3 MAT_ADD_EROSION	Mass Density	2400 kg/m^3	2400 kg/m^3
		Strength parameters	Follow Table 9.1	Follow Table 9.1
		λ-η relationship	Follow Table 9.3	Follow Table 9.3
		EOS	Follow Table 9.6	Follow Table 9.6
		Maximum principal strain	0.9	0.9
Steel reinforcement	MAT_PIECEWISE_LINEAR_PLASTICITY	Mass density	7800 kg/m^3	7800 kg/m^3
		Yield strength	329 MPa	368 MPa
		Poisson's ratio	0.3	0.3
		Young's modulus	198 GPa	204 GPa
Loading platen & support	MAT_RIGID	Mass density	7800 kg/m^3	7800 kg/m^3
		Poisson's ratio	0.3	0.3
		Young's modulus	210 GPa	210 GPa

The final failure pattern of reinforced concrete beams under displacement loading is shown in Figure 9.4, revealing distinct bending of the reinforced concrete beam. The experimental data from the quasi-static four-point bending test conducted by Liu et al. [113] was used to validate the performance of model. As shown in Figure 9.5, the simulation results at 20 °C are in good agreement with the experimental load-deflection curve obtained from Liu et al.'s study. To enhance the precision of the numerical simulation, a comparison was made between the displacement curve derived from the numerical model and the corresponding experimental data, yielding an error of approximately 11.43%. When considering the cryogenic temperature of -160 °C, the simulation results also aligned well with the experimental data from Liu et al. [113]. The model was able to capture the changes in the material behaviour and structural response due to the low-temperature environment. The load-deflection curve at -160 °C exhibited a higher initial stiffness and ultimate load-bearing capacity as compared to the 20 °C case, which was consistent with the expected behaviour of reinforced concrete beam under cryogenic conditions. This difference corresponded to an error of approximately 12.51% between the numerical model and the experimental data at -160 °C with respective to the maximum deflection. This validation provided confidence in the reliability and applicability of model for further investigations of reinforced concrete structures in cryogenic environments, such as the ACLNG storage tanks will discuss in the following sections.

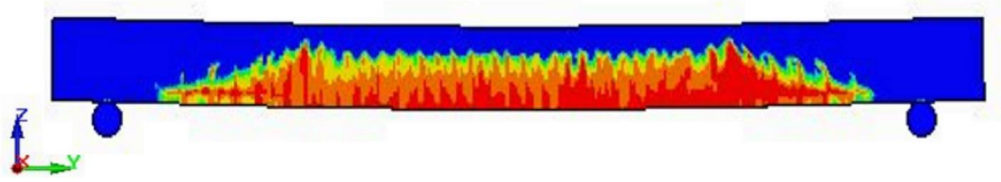

(a)

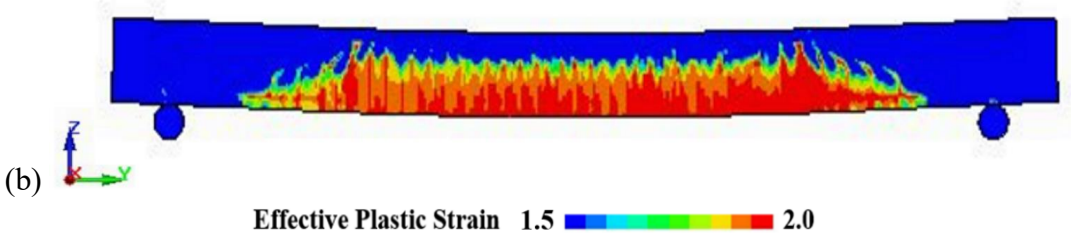

Figure 9. 4 Failure patterns of reinforced concrete beam. (a) at 20 °C (b) at -160°C.

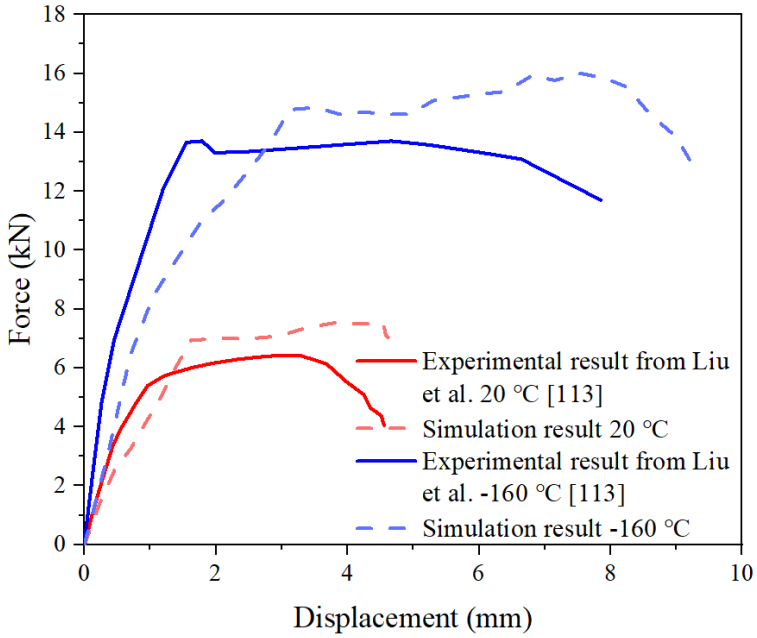

Figure 9. 5 Experiment and simulation results with respect to load-deflection curve.

9.4 Validation of Prestressed concrete slab under blast loading

9.4.1 Material model and properties

In LS-DYNA, the pressure of air is typically represented by the following equation when simulating the air model using MAT_NULL and Equation of State (EOS) LINEAR_POLYNOMIAL [141], is expressed as Equation (3.1). Air is modelled by an idea gas, which can be achieved by setting C_0=C_1=C_2=C_3=C_6=0, and C_4=C_5=γ-1. The pressure of idea gas is given by Equation (3.2). In the simulation, γ=1.4, ρ_0=1.225 kg/m^3 and E is 2.5× 10^5 J/m^3.

The pressure of TNT generated by a chemical explosion is described by MAT_HIGH_EXPLOSIVE_BURN using Jones-Wilkins-Lee (JWL) EOS, which can be

calculated by Equation (3.3). The material characteristics and EOS parameters for ANFO are listed in Table 9.9.

Table 9. 9 Material characteristics and EOS for explosives.

Parameter	ANFO [259]
ρ_0 (kg/m^3)	830
v_0 (m/s)	3879
P_{CJ} (GPa)	3.25
A (GPa)	231.8
B (GPa)	3.414
R_1	6.76
R_2	1.07
ω	0.36
E_0 (J/m^3)	1.58×10^9

The strain between the concrete beam and prestressing tendon can be expressed as follows [260],

$$\varepsilon_T = \varepsilon_C + \varepsilon_{Te} \tag{9.20}$$

where ε_C is the strain of concrete shrinkage, ε_{Te} denotes the tensile strain of prestressing tendon due to contact force, and the ε_T represents the shortening of the prestressing tendon when the temperature drops without contact force.

The prestressing forces were applied to the tendons via the temperature-induced rebar shrinkage. Based on the strain compatibility equation of concrete and prestressing tendon, the temperature change (ΔT) can be obtained:

$$\Delta T \times \alpha = \frac{f}{A_C E_C} + \frac{f}{A_s E_s} \tag{9.21a}$$

$$\Delta \mathrm{T} = \frac{f}{\alpha} \times \left(\frac{1}{A_C E_C} + \frac{1}{A_s E_s}\right) \tag{9.21b}$$

f is the pre-stressing force in kN, $A_s$and E_s are cross section area and elastic modulus of tendon, respectively; A_C and E_C stand for the corresponding measures of concrete; ΔT is

the change of temperature; α is the thermal expansion coefficient of tendons, which was 0.0001 [260] in this study.

The prestressed steel reinforcement included 7-strand steel wires with a diameter of 15.2 mm, a nominal diameter of 15.7 mm^2, an ultimate strength of 1860 MPa. The tendon specimens were subjected to a prestressing force of approximately 510 kN.

The MAT_ELASTIC_PLASTIC_THERMAL material model was adopted for the prestressed tendons. Applying prestressing forces to the tendons was managed using the control card CONTROL_DYNAMIC_RELAXATION in LS-DYNA.

9.4.2 Finite element model

The finite element model of the prestressed concrete slab was validated against experimental results reported by Choi et al. [261]. The dimensions of the slab were 1 m × 1.4 m × 0.3 m in width, length and height (see Figure 9.6). The model consisted of an explosive charge, air, and a prestressed concrete slab, as shown in Figure 9.7. The mesh size for all elements was 10 mm, and the standoff distance between the explosive and the slab was 1 m. The air and explosive were modelled using the ALE multi-material group approach. The concrete slab was meshed with solid elements, and the CONSTRAINED_LAGRANGE_IN_SOLID approach was used to couple the ALE multi-material group and the concrete slab interaction. No rebar slippage was considered for this model in the CONSTRAINED_BEAM_IN_SOLID.

The spherical explosive with a charge weight of 25 kg was modelled using the INITIAL_VOLUME_FRACTION_GEOMETRY approach. The concrete material was represented using the MAT_CONCRETE_DAMAGE_REL3 model at 20 °C for NSC.

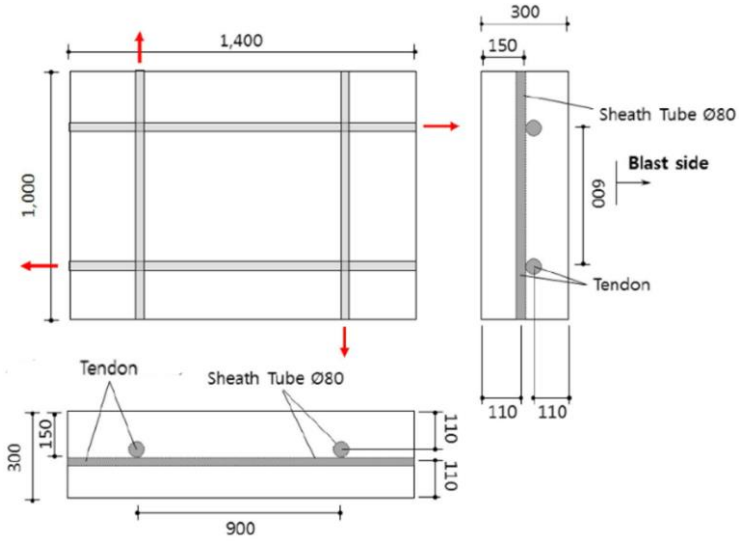

Figure 9. 6 Dimension and reinforcement of prestressed concrete slab in explosion test [261] (unit: mm).

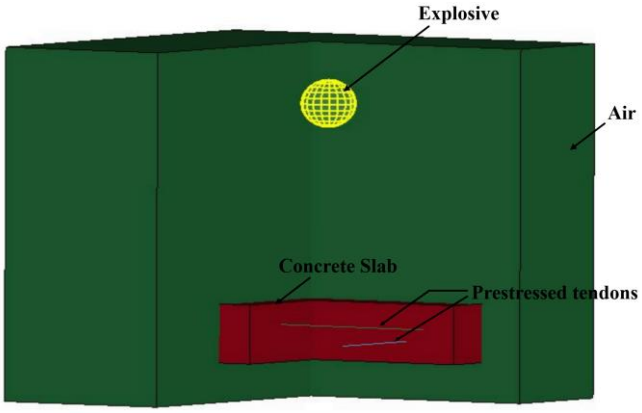

Figure 9. 7 Finite element model of prestressed concrete slab.

9.4.3 Model validation

The time history curves of the midspan response, comparing the experimental data and the numerical simulation results, are shown in Figure 9.8. The maximum deflection behaviour was measured using an LVDT installed at the centre of the bottom surface of the concrete specimen. The experimental and numerical results showed good agreement in terms of the overall deflection behaviour. The numerical simulation was closely matching the experimental data. The peak deflection values from the two approaches were also in close proximity with approximately 12.5% differences, indicating that the finite element model was able to accurately capture the maximum response of the prestressed concrete slab under the blast loading conditions.

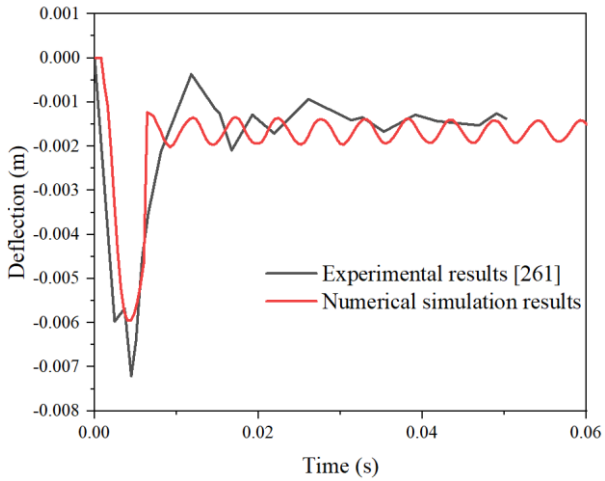

Figure 9. 8 Time history curves of midspan response.

9.5 Blast resistance of ACLNG storage tank at cryogenic temperature

The ACLNG storage tank considering cryogenic temperatures effect subjected to blast loading was investigated, focusing on a tank with a storage capacity of 80,000 m^3. Figure 9.9 illustrates the structural components and overall configuration of the ACLNG storage tank. The tank's structural specifications included an outer diameter of 59.7 m and an inner diameter of 55.5 m, assuming with the LNG liquid level at 35 m. The thickness of the outer wall, inner tank wall and tank base slab was 0.6 m. The detail dimensions of ACLNG storage are presented in Table 9.10. Both outer and inner tanks were constructed using a cast-in-place prestressed reinforced concrete structure. Figure 9.10 shows the cross-section of ACLNG storage tank wall. The outer tank with a reinforced concrete dome was to robust performance under extreme loads. The prestressed steel reinforcement included 7-strand steel wires with a diameter of 15.2 mm, a nominal diameter of 15.7 mm^2, having a yield strength of 1600 MPa and ultimate strength of 1860 MPa, offering high strength and durability. The spacing for both vertical and circumferential tendon was 250 mm. The reinforcement consisted of two layers with Φ 20 mm @ 200 mm for outer & inner wall as well as the base slab.

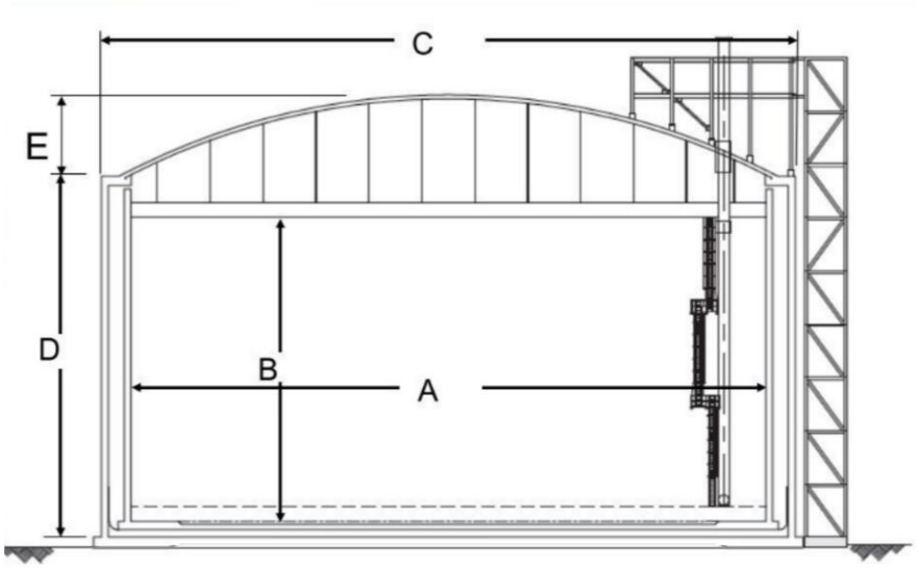

Figure 9. 9 Schematic diagram of ACLNG storage tank.

Table 9. 10 Dimension of ACLNG storage tank (in unit: m) [262].

A	B	C	D	E	Tank wall thickness	Tank base slab
55.5	35	60.9	55.5	8	0.6	0.6

To simulate the dynamic response of the tank under explosive loading, a full scale ACLNG storage tank model was established in LS-DYNA with dimensions of 70 m × 70 m × 65 m in X, Y, Z directions for air zone (see Figure 9.10).

The MAT_NULL was employed for LNG, the same as the air, and the GRUNEISEN EOS was utilised for LNG, which can define the pressure of the material under compression as:

$$P = \frac{\rho_0 C^2 \mu[1+\left(1-\frac{\gamma_0}{2}\right)\mu-\frac{a}{2}u^2}{[1-(S_1-1)\mu-S_2\frac{\mu^2}{\mu+1}-S_3\frac{\mu^2}{(\mu+1)^2}]^2} + (\gamma_0 + a\mu)E \qquad (9.22)$$

and for the pressure when the material expands as:

$$P = \rho_0 C^2 \mu + (\gamma_0 + \alpha\mu)E \qquad (9.23)$$

where C is the intercept of the curve (u_s-u_p) regarding shock velocity; S_1, S_2, S_3 are the coefficients of (u_s-u_p) curve slope; γ_0 is the constant; E is internal energy and μ is

volume change rate which is equal to $\frac{\rho}{\rho_0} - 1$ (ρ and ρ_0 are material density and initial material density, respectively). The GRUNEISEN equation of state parameters: C=2200 m/s, S_1=0, S_2=0, S_3=0, γ_0=0, ρ = 480 kg/m^3 [263].

The air, explosive and LNG were modelled using the Arbitrary Lagrangian-Eulerian (ALE) multi-material group, while the concrete tank was represented using a Lagrangian mesh. The interaction between the ALE multi-material group and the ACLNG storage tank structure was facilitated using the CONSTRAINED_LAGRANGE_IN_SOLID, ensuring accurate coupling of the materials. The parameter of ACLNG storage tank is listed in Table 9.11 in details.

According to AS 3961: 2017 [264], the safety standards required a fully surrounding fence to be placed at least 1.5 m away from the ACLNG storage tank. Therefore, the distance between the explosive and the outer tank in this analysis was 1.5 m. The INITIAL_VOLUME_FRACTION_GEOMETRY function was applied to model a rectangular explosive equivalent to a small delivery truck carrying a charge weight of 1.8 t TNT [162].

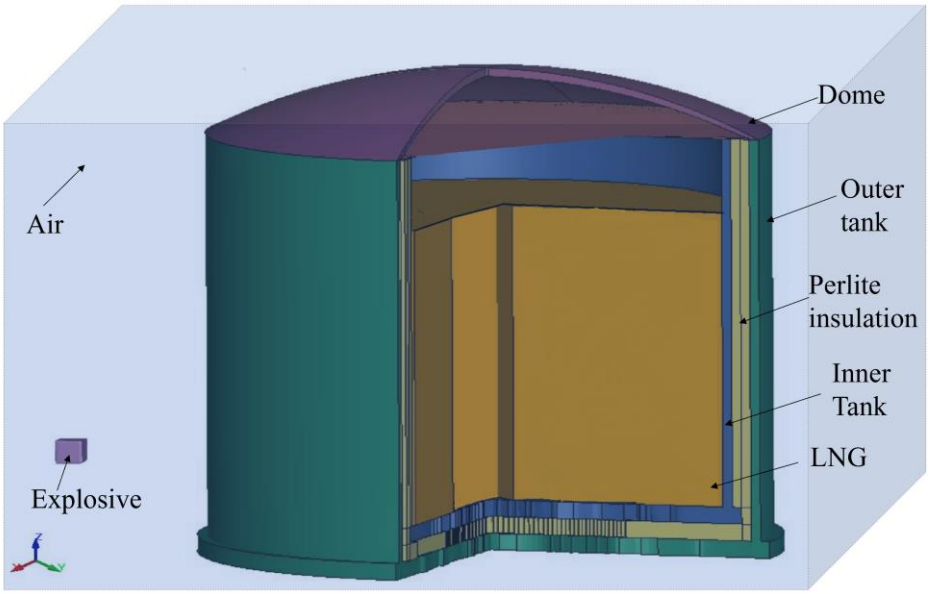

Figure 9. 10 Finite element model of ACLNG storage tank.

Table 9. 11 Parameters of ACLNG storage tank.

Material	LS-DYNA Model	Input Parameters	NSC	UHPC
Concrete (including outer & inner wall, dome and base slab)	MAT_CONCRETE_ DAMAGE_REL3	Mass Density	2400 kg/m^3	2400 kg/m^3
		Strength parameters	Follow Table 9.1	Follow Table9. 2
		λ-η relationship	Follow Table 9.3	Follow Table 9.3
		DIF	Follow Table 9.4	Follow Table 9.5
		EOS	Follow Table 9.6	Follow Table 9.7
	MAT_ADD_ EROSION	Maximum principal strain	0.8	0.8
Steel reinforcement	MAT_PIECEWISE_ LINEAR_ PLASTICITY	Mass density	7800 kg/m^3	7800 kg/m^3
		Yield strength	Follow Eq. (9.19)	Follow Eq. (9.19)
		Poisson's ratio	0.3	0.3
		Young's modulus	Follow Eq. (9.18)	Follow Eq. (9. 18)
		Strain rate	Follow Eq. (9.20) & (9.21)	Follow Eq. (9.20) & (9.21)
Prestressed tendon	MAT_ELASTIC_PLA STIC_THERMAL	Mass density	7850 kg/m^3	7850 kg/m^3
		Yield strength	1600	1600
		Poisson's ratio	0.3	0.3
		Young's modulus	195	195
Perlite insulation [72]	MAT_PLASTIC_ KINEMATIC	Mass density	66 kg/m^3	66 kg/m^3
		Yield strength	0.5 MPa	0.5 MPa
		Poisson's ratio	0.4	0.4
		Young's modulus	13.3 GPa	13.3 GPa

The structural response of the ACLNG storage tank under blast loading is significantly influenced by the cryogenic temperature environment. As shown in Figure 9.11, the outer and inner tanks exhibited distinct deformation patterns, likely exacerbated by the low operating temperature of -160 °C. The outer tank (Figure 9.11(a)) experienced a more uniform distribution of effective plastic strain, indicating a global bending response. However, the inner tank (Figure 9.12(b)) displayed a more localised concentration of strain. This suggested that the inner tank was more vulnerable to localised damage and potential failure under the combined effects of blast loading and cryogenic temperatures. The low operating temperature can embrittle the concrete and alter the material properties, leading to reduced ductility and increased susceptibility to cracking and spalling. The time history curves in Figure 9.12 further demonstrated the dynamic response of the outer tank, revealing an initial rapid deformation followed by gradual stabilisation. However, the cryogenic conditions may accelerate the rate of deformation and increase the peak

displacement, posing a greater challenge for the tank's structural integrity. These results highlighted the importance of considering the coupled effects of the outer and inner tank configurations, as well as the dynamic nature of the blast loading and the cryogenic temperature environment, in assessing the overall structural performance of the ACLNG storage system.

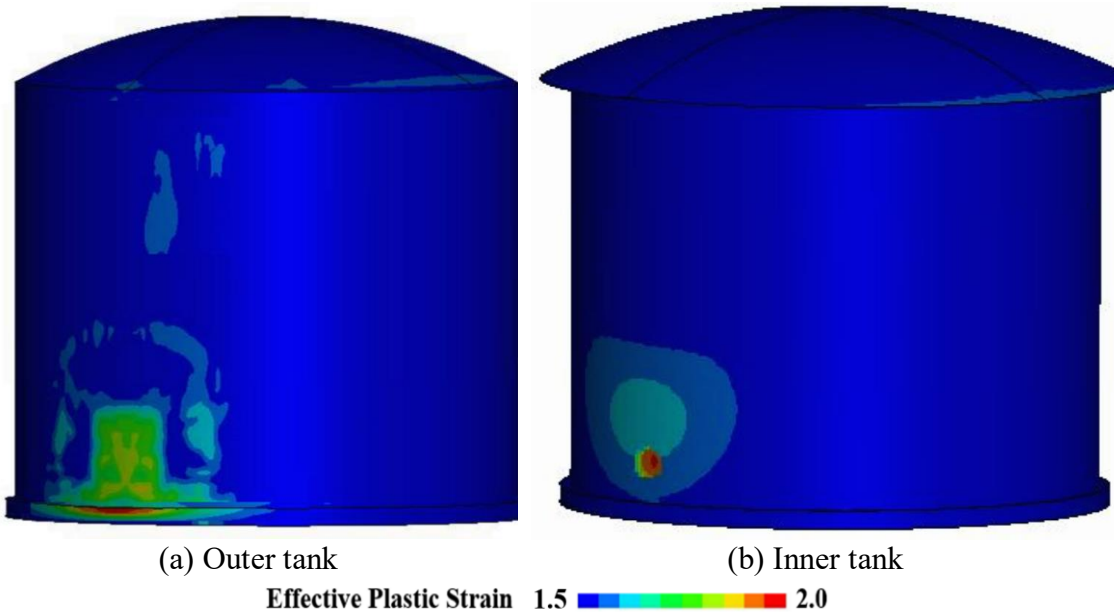

Figure 9. 11 The outer and inner ACLNG storage tank response.

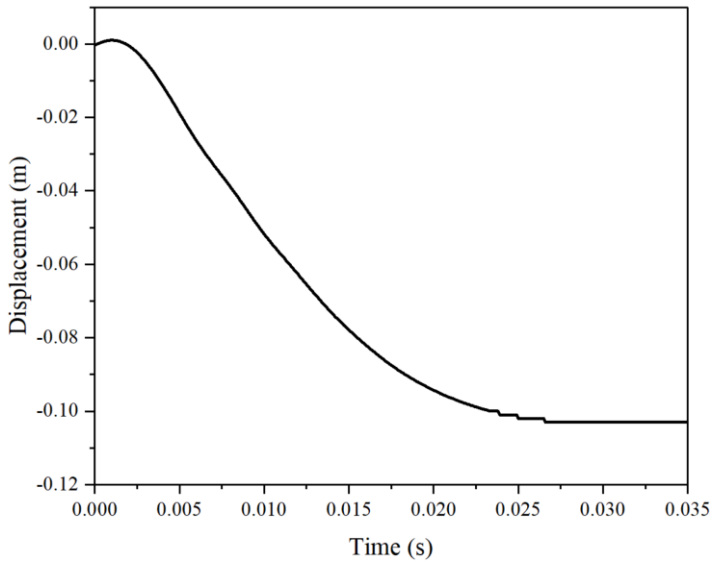

Figure 9. 12 Time history curves of outer tank response.

9.6 Parametric Study

9.6.1 Influence of concrete material

The damage patterns of the inner tank response were investigated for two different inner tank materials: NSC and CUHPC. The outer tank material was NSC for both cases in Figure 9.11 and Figure 9.13 subjected to 1.8 tons TNT charge weight. In the case of the inner tank with NSC (Figure 9.11 (b)), the damage pattern exhibited a larger affected area as compared to the inner tank with UHPC (Figure 9.13). The NSC inner tank showed more extensive spall damage, indicating a higher degree of deformation and potential loss of structural integrity. This can be attributed to the lower compressive strength and ductility of NSC as compared to CUHPC. The cryogenic temperatures experienced by the inner tank likely exacerbated the damage response. The lower temperature could have reduced the ductility and impact resistance of NSC, leading to more extensive spalling and deformation under the explosive loading. The combination of the cryogenic environment and the blast loading proved challenging for the NSC inner tank, resulting in a larger affected area and more severe spall damage. On the other hand, the inner tank with CUHPC (Figure 9.13) displayed a smaller affected area and less severe spall damage. The higher strength and improved ductility of CUHPC allowed the inner tank to better resist the deformation and spalling, leading to a more localised and controlled damage response. Moreover, the CUHPC inner tank exhibited a superior performance in the cryogenic environment. The high performance of CUHPC allowed the inner tank to better resist the combined effects of the low temperatures and the blast loading. The comparison between the two inner tank materials highlighted the advantages of using CUHPC over NSC for the inner tank in ACLNG storage tanks. The CUHPC inner tank exhibited a more advantageous damage pattern, with reduced spall damage and a smaller affected area,

suggesting enhanced structural performance and integrity under the given loading conditions.

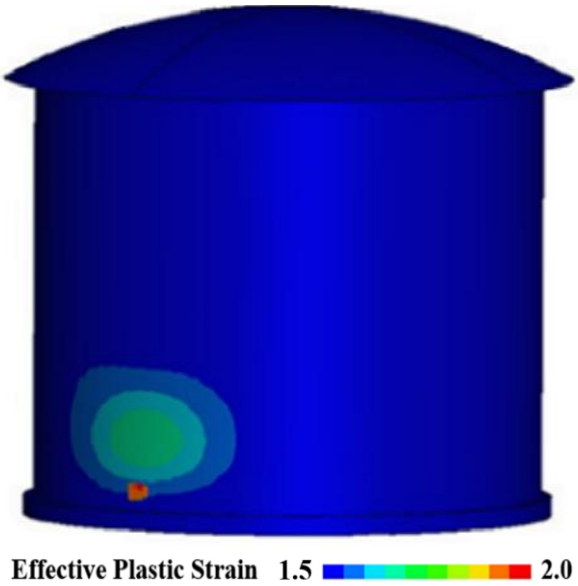

Figure 9. 13 Damage patterns of inner tank response with CUHPC.

The decision to investigate the ACLNG storage tank configuration with UHPC for both the outer and inner tanks was driven by the need to explore advanced material solutions that could provide enhanced protection and performance under the demanding operating conditions.

In the CUHPC configuration (Figure 9.14), both the outer and inner tanks exhibited improved damage resistance in comparison with the NSC case (Figure 9.11). The outer tank with CUHPC showed a more localised damage pattern, with a smaller affected area. Similarly, the inner tank with UHPC displayed a higher degree of damage containment, with a smaller affected zone. It is important to note that the concrete material used for both the outer and inner tanks was NSC in Section 9.5, which may exhibit reduced ductility and increased susceptibility to cracking and spalling under the combined effects of cryogenic temperatures and blast loading.

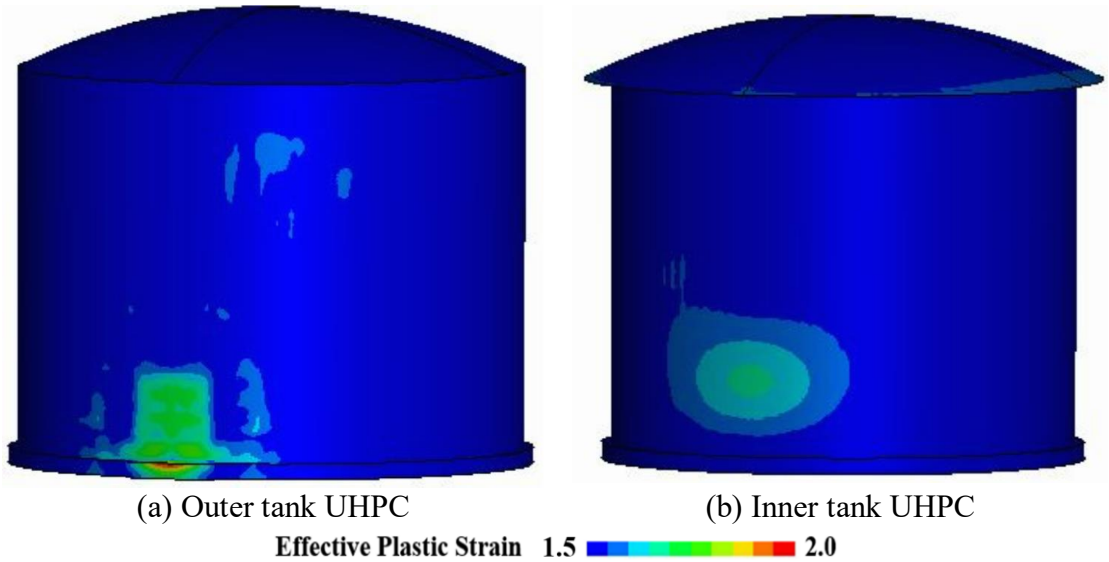

(a) Outer tank UHPC (b) Inner tank UHPC

Figure 9. 14 Damage patterns of ACLNG storage tank response with UHPC.

9.6.2 Influence of liquid level

The influence of liquid level on the damage patterns of the inner tank in the ACLNG storage system is a critical consideration. Figure 9.15 presents the damage profiles of the inner tank under various liquid level conditions subjected to a 1.8 tons TNT explosive load with NSC for inner tank. When the liquid level was higher, as shown in Figure 9.15(a) with 75% filling, the presence of the cryogenic LNG exerted a greater internal pressure on the inner tank walls. This increased pressure helped to confine the deformation of inner tank. As the liquid level decreased to 50% in Figure 9.15(b), the internal pressure reduced, allowing the inner tank walls to deform. It showed the damage area for 50% filling was larger in comparison with the cases with 100% and 75% liquid level. When the tank was completely empty, as depicted in Figure 9.16(c), the lack of internal pressure from the LNG, it was obvious that the damage area for inner tank was the largest of all the four groups. This indicated that higher liquid levels actually enhance the blast resistance of the ACLNG storage tank.

These observations suggest that the liquid level plays a significant role in the inner tank's response to blast loading. Maintaining higher liquid levels in the ACLNG storage tank

was beneficial for improving the blast resistance and containment capabilities of the system. The confining effect of the cryogenic liquid helped to mitigate the potential for catastrophic, large-scale failures under extreme loading conditions.

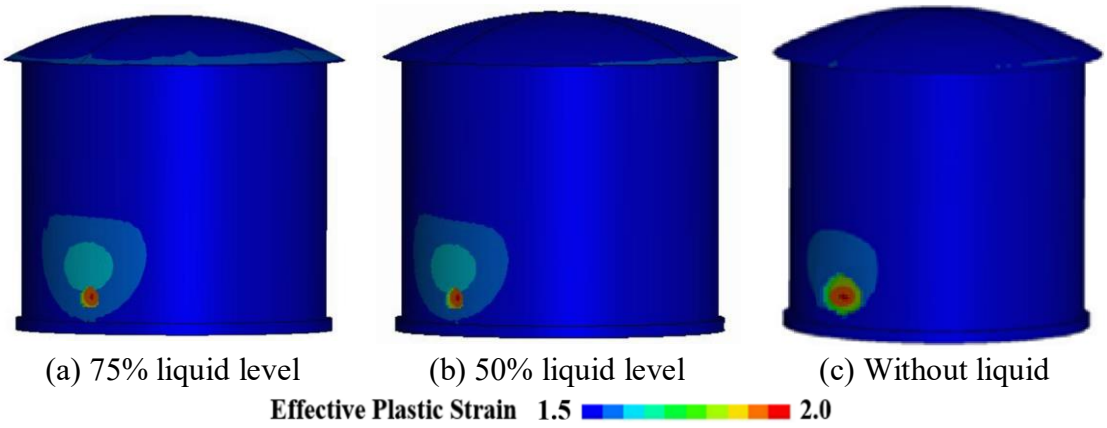

Figure 9. 15 Damage patterns of inner tank response with various liquid level.

9.6.3 Influence of charge weight

The magnitude of the TNT charge weight has a significant impact on the damage patterns observed in the ACLNG storage tank under blast loading conditions, as evident from the results presented in Figures 9.17 and 9.18 for outer tank and inner tank, respectively. Four different charge weights were tested, including 454 kg, 1.8 tons, 4.5 tons and 27 tons. The magnitude of charge weight that investigated was based on equivalent TNT of SUV/Van, water truck as well as semitrailer [162]. Figure 9.16 depicts the damage profiles of the outer tank in response to varying TNT charge weights, including 454 kg, 4.5 tons, and 27 tons. As the charge weight increased, the effective plastic strain distribution within the outer tank structure became more intense and widespread. For the smaller 454 kg TNT charge (Figure 9.16(a)), the strain concentrated in localised regions, particularly at the base and along the upper portion of the tank walls. However, as the charge weight increased to 4.5 tons (Figure 9.16(b) and Figure 9.17(b)) and further to 27 tons (Figure 9.16(c) and Figure 9.17(c)), the damage zone expanded, covering a larger area of the outer tank. The intense blast loading caused the concrete to go through severe damage. It

suggested that the concrete has reached its ultimate capacity and experienced complete fracture or spalling, creating a significant opening or hole in the tank.

The increased TNT charge weight directly correlated with the magnitude of the blast-induced loading on the ACLNG storage tank. Higher charge weights generated more intense pressure waves and higher impulsive loads, leading to more severe and extensive deformations in both the outer and inner tank structures.

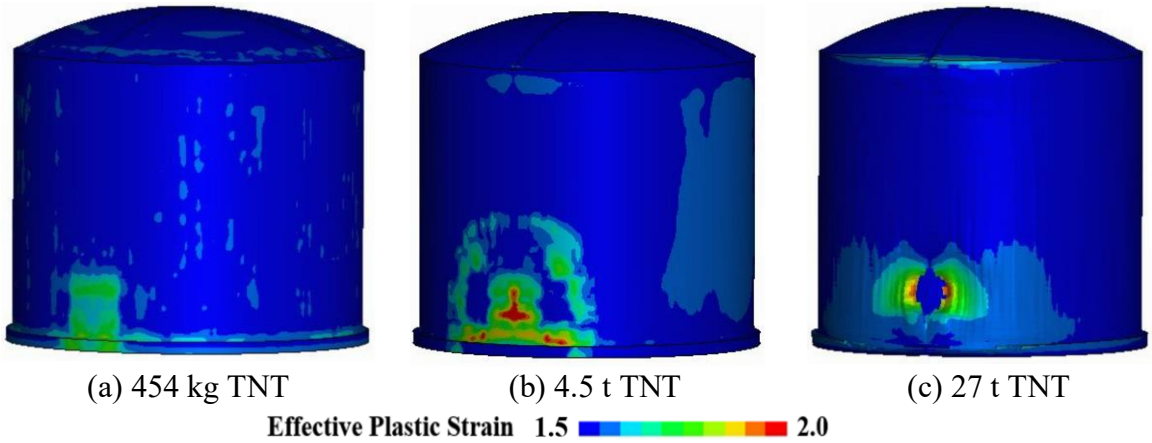

Figure 9. 16 Damage patterns of outer tank response with various TNT charge weight.

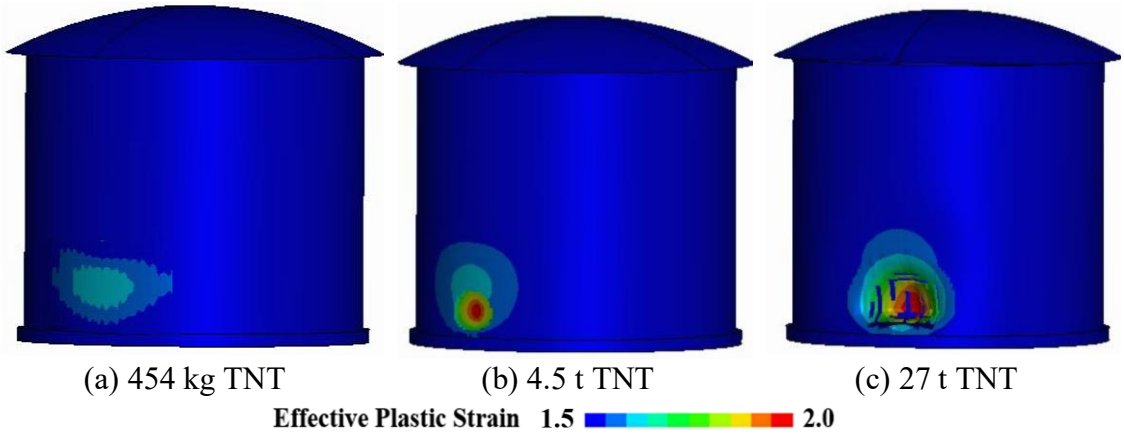

Figure 9. 17 Damage patterns of inner tank response with various TNT charge weight.

9.7 Summary

The study comprehensively investigates the structural response of ACLNG storage tanks under combined blast loading and cryogenic temperatures.

- The modified Karagozian & Case Concrete (KCC) model effectively captures the temperature-dependent material response, providing a robust numerical simulation framework.
- CUHPC demonstrated superior performance as compared to NSC under blast loading and cryogenic temperatures, with better damage resistance and reduced spalling, indicating enhanced structural integrity.
- Cryogenic temperatures significantly impact concrete material properties, increasing brittleness and reducing ductility.
- Higher liquid levels in the storage tank improve blast resistance by providing internal pressure that helps confine deformation. Completely empty tanks show the most extensive damage, suggesting that maintaining adequate liquid levels is crucial for structural resilience.
- Increasing TNT charge weights directly correlate with more severe and widespread damage, leading to more extensive deformations to both outer and inner tank structures.

Chapter 10. CONCLUSIONS AND OUTLOOK

10.1 Conclusions

The research investigated the response of buried gas pipelines subjected to blast loading. Additionally, the primary aim of this study was to comprehensively examine and characterise the dynamic mechanical properties of concrete materials at cryogenic temperatures and after FT cycles, with the ultimate goal of enhancing the blast and impact resistance of ACLNG storage tanks.

Based on the analysis and discussions presented in the previous chapters, the primary findings can be summarised as follows:

- The behaviour of buried steel gas pipelines subjected to ground surface explosions was investigated, the influence of factors such as charge weight, pipe diameter, wall thickness, burial depth, and soil type on pipeline damage was analysed. The research found that increasing TNT magnitude and pipe diameter increases damage potential, while increasing stand-off distance, pipe wall thickness, and burial depth reduces damage. Different steel grades and soil properties significantly influence pipeline response, with API X80 showing better blast resistance as compared to other grades. An empirical formula to predict pipeline cross-sectional flattening, was developed which is crucial for assessing pipeline safety and serviceability in urban energy distribution systems.
- While dynamic strengths generally increased with higher strain rates, the sensitivity to strain rate decreased significantly at cryogenic temperatures for compression, as evidenced by decreasing CDIFs for both NSM and CUHPC. In contrast, the DIFs for both compression and tension of GUHPC were found to be

higher at lower temperatures, indicating that GUHPC became more sensitive to strain rate effects in cryogenic conditions.

- The increased number of cryogenic FT cycles resulted in a notable increment in the strain rate sensitivity of concrete and decrease its ability to withstand dynamic loading. When compared to NSC, the increase ratio of DIF for UHPC after FT cycles was much lower, which was likely contributed to the steel fibres. These fibres could enhance energy absorption and delay crack propagation, especially at high strain rates.

- Cryogenic temperatures significantly impact concrete material properties, increasing brittleness and reducing ductility. UHPC demonstrated superior performance as compared to NSC under blast loading and cryogenic temperatures, with better damage resistance and reduced spalling, indicating enhanced structural integrity of ACLNG storage tank.

10.2 Outlook

The research conducted within this thesis has contributed to advancing the understanding of the dynamic behaviour of concrete materials and reinforced structures subjected to cryogenic temperature conditions or after cryogenic FT cycles subjected to extreme loadings. It has also provided new information to the performance of buried steel pipelines and full-scale ACLNG storage tanks under complex loading scenarios. Despite these advancements, several areas warrant further exploration to broaden the application and enhance the practical implications of the findings.

- Further research focuses on the development and evaluation of protective methods for buried gas pipelines subjected to blast/impact loadings, incorporating UHPC as a protective structural material.
- While the current research examined concrete performance under specific temperature conditions, the long-term effects of repeated FT cycles require additional exploration. Future studies should extend the experimental framework to more number of FT cycles to better simulate the service conditions of structures in regions with extreme temperature fluctuations
- The current study utilised steel fibres only for CUHPC and GUHPC. Future investigations should systematically evaluate how various fibre types (e.g., PVA, PP, basalt), geometries (e.g., hooked-end, twisted, corrugated), and hybrid combinations affect the mechanical properties and failure mechanisms of UHPC at cryogenic temperatures or after FT cycles. Particular attention should be given to how different fibres influence the strain rate sensitivity and crack propagation patterns under dynamic loading. This research direction could lead to optimised fibre-reinforcement systems specifically designed for cryogenic or FT cycles applications, potentially enhancing both strength and ductility characteristics.
- This thesis primarily explores the macroscopic analysis of the dynamic mechanical performance of concrete. While some analyses were conducted using SEM and CT scanning to examine the microstructure of different types of concrete at low/cryogenic temperatures or after FT cycles, these analyses were relatively preliminary and lacked systematic and detailed investigation into the material changes under such conditions. For example, a comprehensive understanding of the microstructural evolution, including pore structure, crack propagation, and phase transformations, remains unexplored. In future work, a more in-depth and

systematic microstructural analysis will be carried out to investigate the changes in concrete materials under low/cryogenic temperatures and after FT cycles. This will involve advanced imaging techniques and quantitative methods to provide a clearer understanding of the material behaviour at the microscopic level.

- Additionally, studies will concentrate on the dynamic performance of reinforced concrete structures under low/cryogenic temperatures and after FT cycles, particularly their blast and impact resistance. Experimental investigations will include testing various reinforcement configurations, concrete compositions, and boundary conditions to replicate real-world scenarios.

Ultimately, the findings from these studies aim to bridge the gap between material-level understanding and structural-level applications, contributing to the design and optimisation of concrete structures in extreme environments, including their implementation in critical infrastructure such as pipelines, ACLNG storage tanks, and other cryogenic facilities.

Appendix A Relevant Regulations and Standards

Here are some main Regulatory and Statutory in Australia, which specify the natural gas distribution and transmission system, different pipelines design and protection etc.

- AS/NZA 2566.2: 2002 Buried flexible pipelines Part 2: installation
- AS/NZS 2885 : 2018 Pipeline—Gas and liquid petroleum
- AS/NZS 3725:2007 Design for installation of buried concrete pipes
- AS 3814:2018 – Industrial and Commercial Gas-Fired Appliances
- AS 3961:2017 The storage and handling of liquefied natural gas
- AS/NZS 4058:2007 Precast concrete pipes (pressure and non-pressure)
- AS/NZS 4645.2:2018 Gas distribution networks Part 2: Steel Pipe systems
- AS 4564-2011 Specification for natural gas
- AS/NZS 5601.1:2013 gas installation

Appendix B. Minimum depth of cover [5, 12, 265].

Loading condition		**Minimum cover H (mm)**
Not subject to vehicle loading		300
Land for agricultural use		600
Subject to vehicular way:		
(1) no carriageway		450
(2) sealed carriageways		600
(3) unsealed carriageways		750
Pipelines in embankment or other construction equipment loads		750
Location		
Roadways		450
Private property		300
Rock (High density community area)	MAOP ≤ 210 kPa	450
	MAOP ≤ 500 kPa; DN ≤ 150 mm Steel	450
	MAOP> 500kPa or DN > 150 mm Steel	600
Sandy/clay areas (High density community area)	MAOP ≤ 210 kPa	600
	MAOP ≤ 500 kPa; DN ≤ 150 mm Steel	750
	MAOP> 500kPa or DN > 150 mm Steel	750

Appendix C. TNT equivalent mass of different type of vehicles [149].

Type of vehicles	Explosives TNT Equivalent mass (kg)
Sedan	227
SUV/van	454
Small delivery truck	1814
Container/water truck	4536
Semitrailer	27216

Appendix D. Physical characteristics of Dampier to Bunbury natural gas pipeline system.

Section	Pipe diameter (mm)	Pipe wall thickness (mm)	Steel grade
Alcoa Wagerup	350	9.5	APL X42
Dampier to Kwinana junction	660	8.70	APL X65
	660	12.7	APL X65
Downstream of MLV 7	660	8.74	APL X70
Kwinana junction to main line valve 141	550	7.64	APL X65
Main line valve 141 to main line valve 150	500	5.56	APL X65
Pinjar	350	7.1	APL X52
South west cogeneration lateral	450	6.35	APL X60

Appendix E. Validation of empirical formula for pipeline safety.

W (kg)	S (mm)	D_{bd} (mm)	ϕ (mm)	δ (mm)	σ (MPa)	ρ (kg/m^3)	G (MPa)	K_u (MPa)	Empirical results	Numerical results
10	0	760	660	5.56	360	1400	1.74	5.52	0.099	0.102
15	0	760	660	5.56	360	1400	1.74	5.52	0.119	0
20	0	760	660	5.56	360	1400	1.74	5.52	0.139	0.135
20	25	550	660	5.56	360	1400	1.74	5.52	0.210	0.32
25	50	720	660	5.56	360	1400	1.74	5.52	0.150	0.161
30	75	770	660	5.56	360	1400	1.74	5.52	0.138	0.156
23	0	760	660	5.2	290	1255	24	5.52	0.187	0.302
23	0	760	660	6.1	500	1255	13.7	5.52	0.160	0.168
23	0	760	660	7	560	1255	6.9	5.52	0.133	0.175
23	0	760	660	5.56	400	1255	1.724	15	0.189	0.24
23	0	760	660	5.56	400	1255	1.724	30	0.207	0.353
23	0	760	660	5.56	400	1255	13.7	5.52	0.177	0.187
50	15	660	350	12.1	360	1400	1.74	5.52	0.004	0.0032
42	20	770	450	10.4	360	1400	1.74	5.52	0.006	0.0044
35	0	700	550	8.5	360	1400	1.74	5.52	0.102	0.111
70	0	1200	580	6.2	360	1400	1.74	5.52	0.123	0.195
50	0	1500	600	5.7	580	1600	1.74	420	0.405	0.352
23	0	800	620	5.56	360	1800	1.74	5.52	0.050	0.07
23	0	350	860	5.56	360	1400	1.74	5.52	0.368	0.52
200	0	700	700	5.56	580	1600	2.524	30	0.882	0.99
80	0	550	800	5.56	360	1300	20	200	0.749	0.974
150	0	430	650	11.2	360	1500	2.5	250	0.885	0.72
60	0	800	660	9.8	360	1620	6.6	25	0.133	0.101
70	0	500	730	6.7	360	1780	10	56	0.414	0.32
55	0	700	700	8.5	360	1300	24	78	0.326	0.26

Appendix F. Test results of NSM in compression SHPB test at 20, -70 and 160 ℃.

Temperature (T)	Strain rate (s^{-1})	Dynamic compressive strength ($f'_{c,d}$)	CDIF
20 ℃	24.61	41.68	1.18
	37.87	48.97	1.39
	39.18	51.85	1.47
	38.63	51.77	1.47
	76.60	54.25	1.54
	81.45	54.27	1.54
	81.81	54.5	1.55
	87.65	54.82	1.55
	119.30	61.10	1.73
	121.30	63.10	1.79
	124.01	61.60	1.75
	127.00	63.03	1.79
	159.97	64.15	1.82
	164.28	66.77	1.89
	166.63	68.19	1.93
	207.85	68.30	1.94
-70 ℃	37.28	52.51	1.22
	42.51	53.56	1.24
	72.60	55.24	1.28
	76.13	59.20	1.37
	84.25	59.25	1.37
	118.21	62.11	1.44
	121.11	66.59	1.54
	160.22	68.88	1.59
-160 ℃	39.10	57.78	1.12
	45.26	58.03	1.12
	79.38	60.15	1.16
	83.13	61.91	1.20
	108.99	65.14	1.26
	118.88	68.05	1.31
	155.16	70.44	1.36
	158.19	70.82	1.37

Appendix G. Test results of NSM in splitting tensile SHPB test at 20, -70 and 160 ℃.

Temperature (T)	Strain rate (s^{-1})	Dynamic splitting tensile strength ($f'_{t,d}$)	TDIF
20 ℃	6.73	6.48	2.57
	18.92	8.63	3.42
	22.03	8.59	3.41
	24.09	8.65	3.43
	36.77	10.40	4.13
	41.08	10.10	4.01
	41.15	9.66	3.83
	43.76	9.84	3.90
	57.2	10.05	3.99
	59.38	10.48	4.16
	60.64	10.69	4.24
	78.05	11.18	4.44
	80.90	11.24	4.46
	81.14	11.36	4.50
-70 ℃	21.39	10.45	3.73
	26.86	12.75	4.55
	37.95	13.10	4.68
	45.91	14.07	5.03
	51.49	14.35	5.13
	60.86	15.16	5.41
	78.02	15.84	5.66
	82.64	15.94	5.69
-160 ℃	24.32	12.98	4.23
	25.99	13.07	4.26
	41.26	14.81	4.82
	44.26	15.66	5.10
	58.06	16.24	5.29
	71.97	16.68	5.43
	78.79	17.28	5.63

Appendix H. Test results of NSM in compressive SHPB test after cryogenic FT cycles.

Temperature range	NO. FT	Strain rate	Dynamic compressive strength ($f'_{c,d}$)	DIF
-160~20 ℃	2	82.76	51.53	1.55
		85.62	55.74	1.68
		128.47	54.22	1.63
		131.36	56.06	1.69
		181.25	68.43	2.06
		185.44	66.80	2.01
	4	83.21	55.35	1.84
		79.29	52.55	1.75
		127.77	53.79	1.79
		125.87	54.62	1.81
		175.17	62.72	2.08
		174.22	61.51	2.04
	8	81.22	50.52	1.97
		82.96	52.61	2.05
		128.56	54.19	2.11
		134.16	49.81	1.94
		160.65	55.35	2.16
		180.29	58.46	2.28

Appendix I. Test results of CUHPC SHPB test in compressive at 20, -70 and 160 ℃.

Temperature (T)	Strain rate (s^{-1})	Dynamic compressive strength ($f'_{c,d}$)	CDIF
20 ℃	38.50	191.18	1.19
	40.72	187.66	1.16
	41.01	189.86	1.18
	77.20	204.88	1.27
	71.70	202.05	1.25
	81.38	212.75	1.32
	103.15	221.32	1.37
	119.09	236.13	1.46
	118.90	236.52	1.47
	120.09	237.40	1.47
	158.23	245.12	1.52
	162.60	233.20	1.45
	165.81	250.86	1.56
-70 ℃	39.06	203.57	1.05
	52.07	218.03	1.13
	81.57	237.81	1.23
	78.24	237.50	1.23
	75.03	243.05	1.26
	83.30	250.36	1.29
	121.25	260.66	1.35
	119.66	265.46	1.37
	114.72	260.48	1.35
	161.10	261.91	1.35
	162.55	266.51	1.38
-160 ℃	45.22	215.09	1.02
	50.04	225.70	1.07
	82.32	239.35	1.13
	88.86	244.11	1.15
	119.21	268.09	1.27
	122.82	262.51	1.24
	161.49	274.53	1.30

Appendix J. Test results of CUHPC SHPB test in splitting tensile at 20, -70 and 160 ℃.

Temperature (T)	Strain rate (s^{-1})	Dynamic splitting tensile strength ($f't,d$)	TDIF
20 ℃	20.99	15.02	2.00
	21.39	15.01	2.00
	24.79	15.43	2.06
	25.24	17.34	2.31
	39.89	17.06	2.27
	40.63	17.36	2.31
	42.71	19.39	2.59
	42.82	19.29	2.57
	60.02	19.63	2.62
	60.84	18.14	2.42
	61.68	18.65	2.49
	63.22	19.05	2.54
	76.20	19.42	2.59
	77.38	18.28	2.44
	81.32	20.74	2.77
-70 ℃	19.89	22.52	2.22
	24.51	24.71	2.44
	40.11	25.98	2.57
	41.98	21.85	2.16
	59.99	30.86	3.05
	60.40	26.42	2.61
	77.61	29.15	2.88
	81.38	32.91	3.25
-160 ℃	23.29	30.51	2.71
	42.33	32.02	2.85
	46.58	32.63	2.90
	64.34	35.52	3.16
	80.48	40.22	3.58

Appendix K. Compressive SHPB test results of CUHPC after cryogenic FT cycles.

Temperature range	NO. FT	Static strength (MPa)	Strain rate (s^{-1})	Dynamic compressive strength (MPa)	DIF
-160~20 ℃	0	161.46	78.86	212.41	1.32
			80.84	215.95	1.34
			134.13	250.03	1.55
			177.67	252.32	1.56
	2	159.6	81.90	210.69	1.32
			85.22	213.44	1.34
			131.14	241.87	1.52
			132.78	243.55	1.53
			179.26	256.84	1.61
			181.72	262.31	1.64
	4	155.72	86.76	223.40	1.43
			97.20	235.87	1.51
			125.66	232.33	1.49
			131.72	233.48	1.50
			171.48	248.37	1.60
			180.81	260.04	1.67
	8	151.51	82.99	215.97	1.43
			80.95	221.37	1.46
			130.31	229.46	1.51
			155.50	243.52	1.61
			163.17	258.33	1.71
			193.61	273.45	1.80

Appendix L. Dynamic compressive SHPB test results of GUHPC at 20, -70 and -160 ℃.

Temperature (℃)	Static strength (MPa)	Strain rate (s^{-1})	Dynamic compressive strength (MPa)	CDIF
20	139.08	38.74	160.99	1.16
		42.57	160.18	1.15
		43.59	162.19	1.17
		43.78	158.62	1.14
		76.02	167.18	1.20
		77.50	172.99	1.24
		80.73	172.60	1.24
		86.44	174.19	1.25
		91.46	180.69	1.30
		97.37	183.00	1.32
		100.60	187.08	1.35
		118.60	185.15	1.33
		120.14	187.87	1.35
		138.77	185.87	1.34
		141.53	189.52	1.36
		156.57	185.86	1.34
		160.41	192.67	1.39
		166.49	194.04	1.40
-70	143.12	40.04	177.80	1.24
		45.22	190.05	1.33
		79.15	192.88	1.35
		80.26	205.61	1.44
		82.70	201.67	1.41
		109.65	202.95	1.42
		115.75	196.00	1.37
		122.66	209.85	1.47
		124.50	212.52	1.48
		139.48	215.65	1.51
		161.20	221.49	1.55
		167.60	226.49	1.58
-160	145.84	38.05	201.22	1.38
		44.67	204.34	1.40
		81.87	211.22	1.45
		83.77	214.07	1.47
		116.80	226.87	1.56
		121.65	232.90	1.60
		150.02	231.43	1.59
		160.30	245.91	1.69

Appendix M. Dynamic tension SHPB test results of GUHPC at 20, -70 and -160 ℃.

Temperature (℃)	Static strength (MPa)	Strain rate (s^{-1})	Dynamic splitting tensile strength (MPa)	TDIF
20	12.40	20.11	21.69	1.75
		20.75	20.31	1.64
		23.19	24.11	1.94
		24.83	23.24	1.87
		38.08	25.72	2.07
		39.21	24.45	1.97
		42.60	24.32	1.96
		51.16	26.38	2.13
		51.28	26.00	2.10
		59.24	28.83	2.33
		60.36	24.47	1.97
		60.66	27.60	2.23
		75.71	27.36	2.21
		78.12	31.58	2.55
		82.47	28.91	2.33
		82.66	30.41	2.45
		85.73	32.33	2.61
-70	14.74	21.18	28.26	2.28
		22.29	28.92	2.33
		43.42	32.81	2.65
		45.78	30.23	2.44
		63.52	33.15	2.67
		64.07	31.71	2.56
		71.27	36.86	2.97
		73.94	33.84	2.73
		78.37	37.02	2.99
		81.28	36.27	2.93
-160	18.60	19.14	34.38	2.77
		36.17	35.61	2.87
		41.83	36.00	2.90
		56.84	38.24	3.08
		63.14	36.59	2.95
		66.87	38.24	3.08
		79.12	40.20	3.24
		81.97	42.50	3.43

Appendix N. Alterations in concrete characteristics subsequent to FT cycles in comparison to no FT

	References	Temperature range	W/C	Moisture Content (%)	Thermal Cycles															
					0	1	2	3	4	5	6	8	10	12	14	15	16	20	25	30
Compressive strength	Van de Veen [96]	20 ºC ~ -170 ºC	0.54	water saturated	1	0.75	0.79	\	0.63	\	0.65	0.58	\	0.5	\	\	\	\	\	\
		20 ºC ~ -170 ºC	0.54	water saturated	1	0.81	0.82	\	0.7	\	0.65	0.59	\	0.51	\	\	\	\	\	\
	Lee *et al.* [97]	8 °C ~ -52 °C	0.48	\	1	0.98	\	\	\	\	\	\	0.95	\	\	\	\	\	\	0.95
	Rostásy & Punch [124]	20 °C ~ -85 °C	0.5	7.2	1	0.92	\	0.99	\	\	\	\	0.97	\	\	\	\	\	\	\
			0.5	11.1	1	0.89	\	0.86	\	\	\	\	0.61	\	\	\	\	\	\	\
			0.49	7.3	1	1	\	1.1	\	\	\	\	0.96	\	\	\	\	\	\	\
			0.52	13.4	1	0.95	\	0.86	\	\	\	\	0.62	\	\	\	\	\	\	\
	Rostásy *et al.* [125]	20 °C ~ -170 °C	0.54	water saturated	1	0.85	\	\	0.65	\	\	\	\	\	\	\	\	\	\	\
	Kim *et al.* [104]	15 °C ~ -190 °C	0.47	\	1	0.96	\	\	\	\	\	\	\	\	\	\	\	\	\	\
	Shi *et al.* [126]	15 °C ~ -120 °C	0.57	\	1	\	\	\	\	\	\	\	\	\	\	\	0.75	\	\	0.7
		15 °C ~ -190 °C	0.57	\	1	\	\	\	\	\	\	\	\	\	\	\	0.7	\	\	0.8
	Zhou *et al.* [130]	20 °C ~ -165 °C	0.44	\	1	\	\	\	\	\	\	\	0.842	\	\	\	\	0.786	\	0.75
	Xie &Wu [184]	20 ºC ~ -160 ºC	0.4	\	1	\	\	0.9	\	\	\	\	\	\	\	\	\	\	\	\
		20 ºC ~ -160 ºC	0.25	\	1	\	\	0.92	\	\	\	\	\	\	\	\	\	\	\	\
	Wei *et al.* [185]	20 ºC ~ -160 ºC	0.23	\	1	\	\	0.9	\	\	\	\	\	\	\	\	\	\	\	\

Splitting tensile strength	Van de Veen [96]	20 ºC ~ -170 ºC	0.54	water saturated	1	0.69	0.63	\	0.42	\	0.5	0.3	\	0.21	\	\	\	\	\	\
		20 ºC ~ -170 ºC	0.54	water saturated	1	0.7	0.73	\	0.58	\	0.59	0.58	\	0.58	\	\	\	\	\	\
	Rostásy & Punch [124]	20 °C ~ -85 °C	0.5	7.2	1	1.17	\	1.1	\	\	\	\	1.01	\	\	\	\	\	\	\
			0.5	11.1	1	0.89	\	0.9	\	\	\	\	0.54	\	\	\	\	\	\	\
			0.49	7.3	1	0.9	\	0.81	\	\	\	\	0.805	\	\	\	\	\	\	\
			0.52	13.4	1	0.8	\	0.6	\	\	\	\	0.43	\	\	\	\	\	\	\
	Rostásy *et al.* [125]	20 °C ~ -170 °C	0.54	water saturated	1	0.7	\	\	0.5	\	\	\	\	\	\	\	\	\	\	\
	Kim *et al.* [104]	20 °C ~ -170 °C	0.47	\	1	0.91	\	\	\	\	\	\	\	\	\	\	\	\	\	\
	Xie &Wu [184]	20 ºC ~ -160 ºC	0.25	water saturated	1	\	\	0.88	\	\	\	\	\	\	\	\	\	\	\	\
		20 ºC ~ -160 ºC	0.23	water saturated	1	\	\	0.8	\	\	\	\	\	\	\	\	\	\	\	\
	Liu *et al*. [239]	20 °C ~ -160 °C	0.36	\	1	0.7	\	\	\	\	\	\	\	\	\	\	\	\	\	\
		20 °C ~ -200 °C	0.36	\	1	0.6	\	\	\	\	\	\	\	\	\	\	\	\	\	\
	Berner & Gerwick [238]	21 ºC ~ -196 ºC	0.35	air dry (non-air entrained)	1	0.98	0.9	0.75	0.6	0.56	0.5	\	\	\	\	\	\	\	\	\
		21 ºC ~ -196 ºC	0.35	air dry (air entrained)	1	0.95	0.82	0.78	0.58	0.5	0.3	\	\	\	\	\	\	\	\	\

Modulus of Elasticity	Lee *et al.* [97]	8 °C ~ -52 °C	0.48	\	1	1	\	\	\	\		\	0.948	\	\	\	\	\	\	0.91
	Shi *et al.* [127]	-30 °C ~ -120 °C	0.5	4.62	1	1.11	0.85	\	0.83	\	0.96	0.79	0.79	\	\	\	\	\	\	\
		20 °C ~ -120 °C	0.5	4.62	1	0.98	1.03	\	0.97	\	\	0.87	0.73	0.77	0.87	\	0.8	\	\	\
	Shi *et al.* [128]	10 °C ~ -40 °C	0.51	\	1	0.94	\	1.05	\	\	0.91	\	0.81	\	\	0.89	\	\	\	\
		10 °C ~ -160 °C	0.49	\	1	\	\	\	\	\	\	\	1.18	\	\	1.01	\	0.98	0.86	0.73
	Goto & Miura [234]	20 °C ~ -196 °C	0.26	water saturated	1	0.98	0.96	0.95	0.96	0.81	0.79	0.6	0.5	\	\	\	\	\	\	\
			0.36	water saturated	1	0.97	0.9	0.87	0.9	0.82	0.57	\	\	\	\	\	\	\	\	\
			0.46	water saturated	1	0.9	0.7	0.61	0.58	\	\	\	\	\	\	\	\	\	\	\
			0.36	4.96	1		0.9	\	0.87	\	0.65	0.59	\	\	\	\	\	\	\	\
			0.36	4.57	1	\	0.93	\	0.94	\	0.93	0.932	0.932	0.926	0.924	\	0.926	0.92	\	0.79
			0.36	4.33	1	\	0.93	\	0.94	\	0.93	0.933	0.933	0.927	0.926	\	0.928	0.928	\	0.82
			0.36	3.71	1	\	0.93	\	0.95	\	0.93	0.935	0.915	0.936	0.933	\	0.938	0.928	\	0.87
	Yamane *et al.* [235]	20 °C ~ -196 °C	0.5	water saturated	1	0.5	\	0.18	\	\	\	\	\	\	\	\	\	\	\	\
			0.61	water saturated	1	0.29	\	0.09	\	\	\	\	\	\	\	\	\	\	\	\
	Rostasy and Wiedemann [236]	20 °C ~ -170 °C	0.5	water saturated	1	\	\	\	\	\	\	0.35	\	\	\	\	\	\	\	\
			0.55	water saturated	1	\	\	\	\	\	\	0.22	\	\	\	\	\	\	\	\
			0.6	water saturated	1	\	\	\	\	\	\	0.16	\	\	\	\	\	\	\	\
			0.65	water saturated	1	\	\	\	\	\	\	0.13	\	\	\	\	\	\	\	\
			0.7	water saturated	1	\	\	\	\	\	\	0.11	\	\	\	\	\	\	\	\
Fracture energy	Xie *et al.* [138]	20 °C ~ -80 °C	0.82	\	1	\	\	\	\	0.81	\	\	0.71	\	\	\	\	\	\	\
		20 °C ~ -80 °C	0.5	\	1	\	\	\	\	0.86	\	\	0.81	\	\	\	\	\	\	\
		20 °C ~ -80 °C	0.36	\	1	\	\	\	\	0.77	\	\	0.7	\	\	\	\	\	\	\
Bond strength	Lee *et al.* [97]	20 °C ~ -70 °C	0.48	\	1	0.99	\	\	\	\	\	\	0.975	\	\	\	\	\	\	0.92
	Xie *et al.* [137]	20 °C ~ -40 °C	0.36	\	1	\	\	0.94	\	\	\	\	\	\	\	\	\	\	\	\
		20 °C ~ -75 °C	0.36	\	1	\	\	0.87	\	0.86	\	\	\	\	\	\	\	\	\	\
		20 °C ~ -120 °C	0.36	\	1	\	\	0.86	\	0.81	\	\	\	\	\	\	\	\	\	\

References

1. APGA, *Australia's gas transmission pipeline system*. 2021: Australian Pipelines and Gas Association
2. Dahmani, L., A. Khenane, and S. Kaci, *Behavior of the reinforced concrete at cryogenic temperatures.* Cryogenics, 2007. **47**(9-10): p. 517-525.
3. PHMSA, *Pipeline Incident 20 Year Trends*. 2021, Pipeline and Hazard Material Safety Administration
4. Government, A., *Australian energy regulator "Network & Pipelines"*.
5. standard, A.N.Z., *'AS/NZS 5601.1:2013 gas installation'*. 2013, SAI Global.
6. Standard, A.N.Z., *AS/NZS 4058:2007 Precast concrete pipes (pressure and non-pressure)*. 2007, SAI Global.
7. Standard, A.N.Z., *AS/NZS 3725:2007 Design for installation of buried concrete pipes*. 2007, SAI Global.
8. Smith, N., N. BYRNE, M. COATES, V. LINTON, and K. VAN ALPHEN, *Identifying the commercial, technical and regulatory issues for injecting renewable gas in Australian distribution gas networks*. 2017, Research Report.
9. Specification, A., *5L (2012) Specification for line pipe*. 2018, American Petroleum Institute (API). Washington DC.
10. Bott, I.D.S., L.F. De Souza, J.C. Teixeira, and P.R. Rios, *High-strength steel development for pipelines: a Brazilian perspective.* Metallurgical and Materials Transactions A, 2005. **36**(2): p. 443-454.
11. Biezma, M., M. Andrés, D. Agudo, and E. Briz, *Most fatal oil & gas pipeline accidents through history: A lessons learned approach.* Engineering failure analysis, 2020. **110**: p. 104446.
12. standard, A.N.Z., *AS/NZS 4645.2:2018 Gas distribution networks Part 2: Steel Pipe systems*. 2018, SAI Global.
13. ATCO, *ADDITIONAL INFORMATION FOR WORKING AROUND GAS INFRASTRUCTURE*. 2018, GAS DIVISION.
14. Jackson, G. and J. Powell, *A novel concept for offshore LNG storage based on primary containment in concrete.* Arup Energy, London, 2004.
15. Kogbara, R.B., S.R. Iyengar, Z.C. Grasley, E.A. Masad, and D.G. Zollinger, *A review of concrete properties at cryogenic temperatures: Towards direct LNG containment.* Construction and Building Materials, 2013. **47**: p. 760-770.
16. Jackson, G., J. Powell, K. Vucinic, and D. Harwood. *Delivering LNG tanks more quickly using unlined concrete for primary containment*. in *14th International Conference and Exhibition on Liquefied Natural Gas*. 2004.
17. Rezazadeh, A., L. Talarico, G. Reniers, V. Cozzani, and L. Zhang, *Applying game theory for securing oil and gas pipelines against terrorism.* Reliability Engineering & System Safety, 2019. **191**: p. 106140.

18. GTD, *Global Terrorism Database*. 2021, University of Maryland National Consortium for the Study of Terrorism and Responses to Terrorism An Emeritus Center of Excellence of the U.S. Department of Homeland Security

19. Corporation, R., *RAND database of worldwide terrorism incidents.* 2014.

20. Reuters, *Syria says pipeline blast was terrorist attack, U.S. suspects IS*. 2020.

21. ANZCTC, *Improvised explosive device (IED) guideline for crowded places*, A.-N.Z.C.-T. Committee, Editor. 2017, Commonwealth of Australia.

22. EGIG, *EGIG 10th report of the European gas pipeline incident data Group (period 1970 – 2016)*. 2018.

23. Zhu, B., N. Jiang, C. Zhou, X. Luo, Y. Yao, and T. Wu, *Dynamic failure behavior of buried cast iron gas pipeline with local external corrosion subjected to blasting vibration.* Journal of Natural Gas Science and Engineering, 2021. **88**: p. 103803.

24. Ramírez-Camacho, J.G., E. Pastor, R. Amaya-Gómez, C. Mata, F. Muñoz, and J. Casal, *Analysis of crater formation in buried NG pipelines: A survey based on past accidents and evaluation of domino effect.* Journal of Loss Prevention in the Process Industries, 2019. **58**: p. 124-140.

25. Authority, N.O.P.S., *Final Report of the Findings of the investigation into the Pipe Rupture and Fire Incident on 3 June 2008 at the Facilities Operated by Apache Energy Ltd on Varanus Island, October 2008.* 2009.

26. Australia, C.o., *Matters relating to the gas explosion at Varanus Island, Western Australia*, S.C.o. Economics, Editor. 2008, The Senate.

27. ABC, N., *WA gas shortage to last 6 months*, in *ABC NEWS*. 2008.

28. *Enbridge Inc. Natural Gas Pipeline Rupture and Fire*, in *Nation Transportation Safety Board*. 2019.

29. NEWS, A., *Kentucky pipeline blast leaves 1 dead, 5 injured*. 2019.

30. ATSDR, *Kentucky Gas Pipeline Explosion ACE investigation*. 2019, Agency for Toxic Substances and Disease Registry

31. Atkinson, G., *Blast damage to storage tanks and steel clad buildings.* Process Safety and Environmental Protection, 2011. **89**(6): p. 382-390.

32. Zhang, R., J. Jia, H. Wang, and Y. Guan, *Shock response analysis of a large LNG storage tank under blast loads.* KSCE Journal of Civil Engineering, 2018. **22**: p. 3419-3429.

33. Glasstone, S. and P.J. Dolan, *The effects of nuclear weapons*. 1977: US Department of Defense.

34. Pape, R., K.R. Mniszewski, and A. Longinow, *Explosion phenomena and effects of explosions on structures. I: Phenomena and effects.* Practice Periodical on Structural Design and Construction, 2010. **15**(2): p. 135-140.

35. Kinney, G.F. and K.J. Graham, *Explosive shocks in air*. 2013: Springer Science & Business Media.

36. Rao, B., L. Chen, Q. Fang, J. Hong, Z.-x. Liu, and H.-b. Xiang, *Dynamic responses of reinforced concrete beams under double-end-initiated close-in explosion.* Defence Technology, 2018. **14**(5): p. 527-539.

37. Gel'fand, B., I. Voskoboinikov, and S. Khomik, *Recording the Position of a Blast‐Wave Front in Air.* Combustion, Explosion and Shock Waves, 2004. **40**(6): p. 734-736.

38. Engineers, A.S.o.C. *Blast protection of buildings*. 2011. American Society of Civil Engineers.

39. 3-340-02, U., *Structures to resist the effects of accidental explosions.* US Department of the Army, Navy and Air Force Technical Manual, 2008.

40. Song, K., Y. Long, C. Ji, F. Gao, and H. Chen, *Experimental and numerical studies on the deformation and tearing of X70 pipelines subjected to localized blast loading.* Thin-Walled Structures, 2016. **107**: p. 156-168.

41. Stevens, D.J., J.M. Puryear, N. Smith, and M.H. Gomez. *Effects of close-in charges on pipeline components*. in *Structures Congress 2012*. 2012.

42. Wu, J., C. Ji, Y. Long, K. Song, and Q. Liu, *Dynamic responses and damage of cylindrical shells under the combined effects of fragments and shock waves.* Thin-Walled Structures, 2017. **113**: p. 94-103.

43. Maáachowski, J., *Effect of blast wave on chosen structure–numerical and experimental study.* International Journal of Mathematics and Computers in Simulation, 2008. **2**: p. 238-245.

44. De, A., *Centrifuge modeling of explosion craters formed over underground structures*, in *GeoCongress 2008: Geosustainability and Geohazard Mitigation*. 2008. p. 311-318.

45. Jiang, N., B. Zhu, C. Zhou, H. Li, B. Wu, Y. Yao, and T. Wu, *Blasting vibration effect on the buried pipeline: A brief overview.* Engineering failure analysis, 2021. **129**: p. 105709.

46. Yang, Y., X. Xie, and R. Wang, *Numerical simulation of dynamic response of operating metro tunnel induced by ground explosion.* Journal of rock mechanics and geotechnical engineering, 2010. **2**(4): p. 373-384.

47. Abedi, A.S., N. Hataf, and A. Ghahramani, *Analytical solution of the dynamic response of buried pipelines under blast wave.* International Journal of Rock Mechanics and Mining Sciences, 2016. **88**: p. 301-306.

48. Wang, Z. and Y. Lu, *Numerical analysis on dynamic deformation mechanism of soils under blast loading.* Soil Dynamics and Earthquake Engineering, 2003. **23**(8): p. 705-714.

49. Wang, Z., Y. Lu, and H. Hao, *Numerical investigation of effects of water saturation on blast wave propagation in soil mass.* Journal of Engineering Mechanics, 2004. **130**(5): p. 551-561.

50. Prochazka, P., A. Kravtsov, and S. Peskova, *Blast impact on structures of underground parking.* Undergr Spaces Des Eng Environ Asp, 2008. **102**: p. 11-19.

51. Ambrosini, D. and B. Luccioni, *Effects of underground explosions on soil and structures.* Underground Space, 2020. **5**(4): p. 324-338.

52. TM5-855-1, *Fundamentals of protective design for conventional weapons*. 1986, US: US Army Engineers Waterways Experimental Station.

53. Qian, H., Z. Zong, C. Wu, J. Li, and L. Gan, *Numerical study on the behavior of utility tunnel subjected to ground surface explosion.* Thin-Walled Structures, 2021. **161**: p. 107422.

54. Kausel, E., *Early history of soil–structure interaction.* Soil Dynamics and Earthquake Engineering, 2010. **30**(9): p. 822-832.

55. Lu, Y., Z. Wang, and K. Chong, *A comparative study of buried structure in soil subjected to blast load using 2D and 3D numerical simulations.* Soil Dynamics and Earthquake Engineering, 2005. **25**(4): p. 275-288.

56. Robert, D., A. Britto, and S. Setunge, *Efficient approach to simulate soil–pipeline interaction.* Journal of Pipeline Systems Engineering and Practice, 2020. **11**(1): p. 04019046.

57. Ambrosini, R.D. and B.M. Luccioni, *Craters produced by explosions on the soil surface.* 2006.

58. Cooper Jr, H.F., *Estimates of crater dimensions for near-surface explosions of nuclear and high-explosive sources*. 1976, R and D Associates, Marina del Rey, CA (USA).

59. Peekema, R.M., *Causes of natural gas pipeline explosive ruptures.* Journal of Pipeline Systems Engineering and Practice, 2013. **4**(1): p. 74-80.

60. Ambrosini, R.D., B.M. Luccioni, R.F. Danesi, J.D. Riera, and M.M. Rocha, *Size of craters produced by explosive charges on or above the ground surface.* Shock Waves, 2002. **12**(1): p. 69-78.

61. Lee, S.W., S.J. Choi, and J.-H.J. Kim, *Analytical study of failure damage to 270,000-kL LNG storage tank under blast loading.* Computers and Concrete, 2016. **17**(2): p. 201-214.

62. Sun, Y., C. Wang, W. Wang, T. Li, and T. Yang, *Dynamic response analysis of a small-scaled ACLNG storage tank under penetration and explosion loadings.* Acta Mechanica Sinica, 2023. **39**(10): p. 123110.

63. Beidoou, *How to improve The Excavator Bucket Teeth Service Life*. 2021.

64. Brooker, D.C., *Numerical modelling of pipeline puncture under excavator loading. Part I. Development and validation of a finite element material failure model for puncture simulation.* International journal of pressure vessels and piping, 2003. **80**(10): p. 715-725.

65. Brooker, D.C., *Numerical modelling of pipeline puncture under excavator loading. Part II: parametric study.* International journal of pressure vessels and piping, 2003. **80**(10): p. 727-735.

66. Brooker, D.C., *Experimental puncture loads for external interference of pipelines by excavator equipment.* International journal of pressure vessels and piping, 2005. **82**(11): p. 825-832.

67. Liu, X., H. Zhang, M. Xia, K. Wu, Y. Chen, Q. Zheng, and J. Li, *Mechanical response of buried polyethylene pipelines under excavation load during pavement construction.* Engineering Failure Analysis, 2018. **90**: p. 355-370.

68. Xu, T., A. Yao, H. Jiang, Y. Li, and X. Zeng, *Dynamic response of buried gas pipeline under excavator loading: Experimental/numerical study.* Engineering Failure Analysis, 2018. **89**: p. 57-73.

69. Jiang, F., S. Dong, Y. Zhao, Z. Xie, and C.G. Soares, *Investigation on the deformation response of submarine pipelines subjected to impact loads by dropped objects.* Ocean Engineering, 2019. **194**: p. 106638.

70. Wu, K., H. Zhang, X. Liu, D. Bolati, G. Liu, P. Chen, and Y. Zhao, *Stress and strain analysis of buried PE pipelines subjected to mechanical excavation.* Engineering Failure Analysis, 2019. **106**: p. 104171.

71. Zhai, X., X. Zhao, and Y. Wang, *Numerical modeling and dynamic response of 160,000-m 3 liquefied natural gas outer tank under aircraft impact.* Journal of Performance of Constructed Facilities, 2019. **33**(4): p. 04019039.

72. Peng, Q., H. Wu, D. Wang, Y. He, and H. Chen, *Numerical simulation of aircraft crash on large-scale LNG storage tank.* Engineering Failure Analysis, 2019. **96**: p. 60-79.

73. Gay, L.F. and S.K. Sinha, *Resilience of civil infrastructure systems: literature review for improved asset management.* International Journal of Critical Infrastructures, 2013. **9**(4): p. 330-350.

74. Akiyama, M., D.M. Frangopol, and H. Ishibashi, *Toward life-cycle reliability-, risk-and resilience-based design and assessment of bridges and bridge networks under independent and interacting hazards: emphasis on earthquake, tsunami and corrosion.* Structure and Infrastructure Engineering, 2020. **16**(1): p. 26-50.

75. Cimellaro, G.P., A.M. Reinhorn, and M. Bruneau, *Framework for analytical quantification of disaster resilience.* Engineering structures, 2010. **32**(11): p. 3639-3649.

76. Bocchini, P., D.M. Frangopol, T. Ummenhofer, and T. Zinke, *Resilience and sustainability of civil infrastructure: Toward a unified approach.* Journal of Infrastructure Systems, 2014. **20**(2): p. 04014004.

77. Bruneau, M., et al., *A framework to quantitatively assess and enhance the seismic resilience of communities.* Earthquake spectra, 2003. **19**(4): p. 733-752.

78. Quiel, S.E., S.M. Marjanishvili, and B.P. Katz, *Performance-based framework for quantifying structural resilience to blast-induced damage.* Journal of Structural Engineering, 2016. **142**(8): p. C4015004.

79. Shafieifar, M., M. Farzad, and A. Azizinamini, *Experimental and numerical study on mechanical properties of Ultra High Performance Concrete (UHPC).* Construction and Building Materials, 2017. **156**: p. 402-411.

80. Su, Y., J. Li, C. Wu, P. Wu, and Z.-X. Li, *Influences of nano-particles on dynamic strength of ultra-high performance concrete.* Composites Part B: Engineering, 2016. **91**: p. 595-609.

81. Su, Q., H. Wu, H. Sun, and Q. Fang, *Experimental and numerical studies on dynamic behavior of reinforced UHPC panel under medium-range explosions.* International Journal of Impact Engineering, 2021. **148**: p. 103761.

82. Muthukrishnan, S., S. Ramakrishnan, and J. Sanjayan, *Effect of alkali reactions on the rheology of one-part 3D printable geopolymer concrete.* Cement and Concrete Composites, 2021. **116**: p. 103899.

83. Mahmood, A.H., S.J. Foster, and A. Castel, *High-density geopolymer concrete for Port Kembla breakwater upgrade.* Construction and Building Materials, 2020. **262**: p. 120920.

84. Collins, F. and J.G. Sanjayan, *Effect of pore size distribution on drying shrinking of alkali-activated slag concrete.* Cement and Concrete Research, 2000. **30**(9): p. 1401-1406.

85. Benhelal, E., G. Zahedi, E. Shamsaei, and A. Bahadori, *Global strategies and potentials to curb CO2 emissions in cement industry.* Journal of cleaner production, 2013. **51**: p. 142-161.

86. Atiş, C., E. Görür, O. Karahan, C. Bilim, S. İlkentapar, and E. Luga, *Very high strength (120 MPa) class F fly ash geopolymer mortar activated at different NaOH amount, heat curing temperature and heat curing duration.* Construction and building materials, 2015. **96**: p. 673-678.

87. García-Lodeiro, I., A. Palomo, A. Fernández-Jiménez, and D. Macphee, *Compatibility studies between NASH and CASH gels. Study in the ternary diagram Na2O–CaO–Al2O3–SiO2–H2O.* Cement and Concrete Research, 2011. **41**(9): p. 923-931.

88. Thokchom, S., P. Ghosh, and S. Ghosh, *Acid resistance of fly ash based geopolymer mortars.* International Journal of Recent Trends in Engineering, 2009. **1**(6): p. 36.

89. Pan, Z. and J.G. Sanjayan, *Stress–strain behaviour and abrupt loss of stiffness of geopolymer at elevated temperatures.* Cement and Concrete Composites, 2010. **32**(9): p. 657-664.

90. Hosan, A., S. Haque, and F. Shaikh, *Compressive behaviour of sodium and potassium activators synthetized fly ash geopolymer at elevated temperatures: A comparative study.* Journal of Building Engineering, 2016. **8**: p. 123-130.

91. Monfore, G. and A. Lentz, *Physical properties of concrete at very low temperatures*. 1962.

92. Goto, Y. and T. Miura. *Mechanical properties of concrete at very low temperatures*. in *Proceedings of 21st Japan Congress on Materials Research*. 1978.

93. MITSUI, K., T. YONEZAWA, and I. TAKAYUKI, *Mechanical Properties of High Strength Concreteunder Cryogenic At-mosphere.* Proceedings of the Japan Concrete Institute (in Janpanese), 1997. **19**(1): p. 175-180.

94. Lin, H., Y. Han, S. Liang, F. Gong, S. Han, C. Shi, and P. Feng, *Effects of low temperatures and cryogenic freeze-thaw cycles on concrete mechanical properties: A literature review.* Construction and Building Materials, 2022. **345**: p. 128287.

95. Huo, Y., H. Sun, D. Lu, Z. Chen, and Y. Yang, *Mechanical properties of concrete at low and ultra-low temperatures-a review.* Journal of Infrastructure Preservation and Resilience, 2022. **3**(1): p. 1-15.

96. Van de Veen, V., *Properties of concrete at very low temperatures: A survey of the literature.* Report Stevin Laboratory, Concrete Structures 25-87-2, 1987.

97. Lee, G., T. Shih, and K.-C. Chang, *Mechanical properties of concrete at low temperature.* Journal of Cold Regions Engineering, 1988. **2**(1): p. 13-24.

98. Wiedemann, G., *Zum Einfuss Tiefer Temperaturen auf Festigkeitund Verformung von Beton* in *Institute for Building Materials, Solid Construction, and Fire Protection*. 1982, Technical University of Braunschweig.

99. Gong, F., Y. Wang, T. Ueda, and D. Zhang, *Modeling and mesoscale simulation of ice-strengthened mechanical properties of concrete at low temperatures.* Journal of Engineering Mechanics, 2017. **143**(6): p. 04017022.

100. Gong, F., T. Ueda, and D. Zhang, *Two‐dimensional rigid body spring method based micro‐mesoscale study of mechanical strengthening/damaging effects to concrete by frost action.* Structural Concrete, 2018. **19**(4): p. 1131-1145.

101. Zhengwu, J., D. Zilong, Z. Xinping, and L. Wenting, *Increased strength and related mechanisms for mortars at cryogenic temperatures.* Cryogenics, 2018. **94**: p. 5-13.

102. Amran, M., S.-S. Huang, A.M. Onaizi, N. Makul, H.S. Abdelgader, and T. Ozbakkaloglu, *Recent trends in ultra-high performance concrete (UHPC): Current status, challenges, and future prospects.* Construction and Building Materials, 2022. **352**: p. 129029.

103. Kim, M.-J., D.-Y. Yoo, S. Kim, M. Shin, and N. Banthia, *Effects of fiber geometry and cryogenic condition on mechanical properties of ultra-high-performance fiber-reinforced concrete.* Cement and Concrete Research, 2018. **107**: p. 30-40.

104. Kim, M.-J., S. Kim, S.-K. Lee, J.-H. Kim, K. Lee, and D.-Y. Yoo, *Mechanical properties of ultra-high-performance fiber-reinforced concrete at cryogenic temperatures.* Construction and Building Materials, 2017. **157**: p. 498-508.

105. Yoo, D.-Y., S.-T. Kang, J.-H. Lee, and Y.-S. Yoon, *Effect of shrinkage reducing admixture on tensile and flexural behaviors of UHPFRC considering fiber distribution characteristics.* Cement and Concrete Research, 2013. **54**: p. 180-190.

106. Jin, L., C. Xie, W. Yu, and X. Du, *Effect of steel fiber content on failure strength and toughness of UHPC-CA at low temperature: an experimental investigation.* Journal of Building Engineering, 2024: p. 109976.

107. Vandewalle, L., *Bond between a reinforcement bar and concrete at normal and cryogenic temperatures.* Journal of materials science letters, 1989. **8**(2): p. 147-149.

108. Jin, L., K. Liu, R. Zhang, W. Yu, and X. Du, *Bond behavior between steel bar and concrete considering cryogenic temperatures and confinement.* Case Studies in Construction Materials, 2023. **18**: p. e01856.

109. Zhang, R., K. Liu, L. Jin, W. Yu, and X. Du, *Bond-Slip Behavior between Deformed Rebar and Concrete at Cryogenic Temperatures.* Journal of Materials in Civil Engineering, 2023. **35**(10): p. 04023356.

110. Ohlsson, U., P.A. Daerga, and L. Elfgren, *Fracture energy and fatigue strength of unreinforced concrete beams at normal and low temperatures.* Engineering Fracture Mechanics, 1990. **35**(1-3): p. 195-203.

111. Maturana, P., J. Planas, and M. Elices, *Evolution of fracture behaviour of saturated concrete in the low temperature range.* Engineering Fracture Mechanics, 1990. **35**(4-5): p. 827-834.

112. Rocco, C., J. Planas, G. Guinea, and M. Elices, *Fracture properties of concrete under cryogenic conditions.* Borst et al.(eds) pp, 2001: p. 1-8.

113. Liu, S., X. Gu, Q. Huang, and W. Zhang, *Experimental study on the bending behavior of reinforced concrete beams under super-low temperature*, in *Earth and Space 2010: Engineering, Science, Construction, and Operations in Challenging Environments*. 2010. p. 3537-3544.

114. Yan, J. and J. Xie, *Behaviours of reinforced concrete beams under low temperatures.* Construction and Building Materials, 2017. **141**: p. 410-425.

115. Liu, Y., J. Xie, and J.-B. Yan, *Flexural and fracture performance of UHPC exposed to low-temperature environment.* Construction and Building Materials, 2023. **373**: p. 130865.

116. Xie, J., Y. Liu, M.-L. Yan, and J.-B. Yan, *Mode Ⅰ fracture behaviors of concrete at low temperatures.* Construction and Building Materials, 2022. **323**: p. 126612.

117. Zhang, H., B. He, X. Zhu, Q. Wang, and Z. Jiang, *The use of AE technique for identifying ductility degradation against cryogenic on flexural performance of UHPC at various temperature conditions.* Cement and Concrete Composites, 2023. **137**: p. 104904.

118. Krstulovic-Opara, N., *Liquefied natural gas storage: Material behavior of concrete at cryogenic temperatures.* ACI materials journal, 2007. **104**(3): p. 297.

119. MacLean, T.J. and A. Lloyd, *High strain rate and low temperature effects on the compressive behaviour of concrete.* International Journal of Protective Structures, 2021. **12**(1): p. 73-94.

120. Su, H., Z. Zhu, T. Li, and H. Xiang, *Experimental studies and numerical analysis of the dynamic mechanical properties of concrete at low temperatures.* Construction and Building Materials, 2023. **404**: p. 133221.

121. Qiao, Y., H. Wang, L. Cai, W. Zhang, and B. Yang, *Influence of low temperature on dynamic behavior of concrete.* Construction and Building Materials, 2016. **115**: p. 214-220.

122. Jin, L., K. Liu, R. Zhang, W. Yu, X. Du, and X. Deng, *Combined effects of cryogenic temperature and strain rates on compressive behavior of concrete.* International Journal of Damage Mechanics, 2022. **31**(9): p. 1396-1419.

123. Li, Y., Y.-G. Zhang, W. Liu, Z.-H. Yan, and Z.-C. Gu. *Effect of ultra-low temperature freeze-thaw cycle on the flexural performance of hybrid fiber RC beams subjected to monotonic and repeated loading*. in *Structures*. 2024. Elsevier.

124. Rostásy, F. and U. Pusch, *Strength and deformation of lightweight concrete of variable moisture content at very low temperatures.* International Journal of Cement Composites and Lightweight Concrete, 1987. **9**(1): p. 3-17.

125. Rostasy, F., U. Schneider, and G. Wiedemann, *Behaviour of mortar and concrete at extremely low temperatures.* Cement and Concrete Research, 1979. **9**(3): p. 365-376.

126. Shi, X., W. Wang, L. Qian, and J.L.Li, *Experimental study on compressive strength of concrete with different water content experiencing cryogenic freeze-thaw cycles from room temperature to-190 ℃.* Cryogenics (in Chinese), 2017. **2**: p. 17-22.

127. Shi, X., J. Li, W. Wang, L. Qian, and C. Ma, *Experimental study on stress-strain relationships of concrete undergoing cryogenic freeze-thaw cycles from room temperature or -30 ℃ to -120 ℃.* Concrete (in Chinese), 2017. **12**: p. 1-5.

128. Shi, X., Y. LI, L. QIAN, J. LI, and W. WANG, *Experimental Study on elastic modulus of concrete undergoing freeze-thaw cycle action with different ultralow temperature ranges.* Engineering Mechanics (in Chinese), 2019. **36**(8): p. 106-113,140.

129. Shi, X., W. Wang, and J. Tian, *Experimental study on the compressive strength of concrete of different strength grades experiencing ultralow temperature freeze-thaw cycle action.* Engineering Mechanics (in Chinese), 2020. **37**(2): p. 211-220,240.

130. Zhou, D., J. Liu, P. Duan, L. Cheng, and B. Lou, *Damage evolution law an mechanism of concrete under cryogenic freeze-thaw cycles.* J. Build. Mater., 2021: p. 1-13.

131. Sun, M., D. Xin, and C. Zou, *Damage evolution and plasticity development of concrete materials subjected to freeze-thaw during the load process.* Mechanics of Materials, 2019. **139**: p. 103192.

132. He, B., X. Zhu, Q. Ren, and Z. Jiang, *Effects of fibers on flexural strength of ultra-high-performance concrete subjected to cryogenic attack.* Construction and Building Materials, 2020. **265**: p. 120323.

133. He, B., X. Zhu, H. Zhang, Q. Zheng, H. Zhao, O. Onuaguluchi, N. Banthia, and Z. Jiang, *Flexural failure of ultra-high performance concrete subjected to the alternating cryogenic and elevated temperature via acoustic emission characterization.* Cement and Concrete Composites, 2024. **151**: p. 105583.

134. He, B., O. Onuaguluchi, N. Banthia, H. Zhang, Q. Ren, Y. Zhang, and Z. Jiang, *Failure mechanism of steel fiber pullout in UHPC affected by alternating cryogenic and elevated variation.* Cement and Concrete Composites, 2024. **149**: p. 105518.

135. He, B., M. Xie, Z. Jiang, C. Zhang, and X. Zhu, *Temperature field distribution and microstructure of cement-based materials under cryogenic freeze-thaw cycles.* Construction and Building Materials, 2020. **243**: p. 118256.

136. Liu, J., D. Zhou, L. Cheng, R. Wu, Y. Xi, and M. Zou, *A review on evolution laws and mechanism of concrete performance under cryogenic circumstance from multi-scale perspectives.* Journal of Building Engineering, 2023. **64**: p. 105666.

137. Xie, J., Q. Wei, and H. LI, *Bonding properties between reinforcement and concrete after freeze-thaw cycles at extra-low temperatures.* Journal of Tianjing University (Science and Technology), 2013. **46**: p. 1012-1018.

138. Xie, J., M. YAN, and Y. LIU, *Effect of freezing and thawing on fracture performance of concrete at polar low temperature.* Engineering Mechanics (in Chinese), 2021. **39**: p. 1-11.

139. Li, N., Z. Jin, K. Shen, G. Long, Y. Yu, Q. Fu, C. Xiong, B. Pang, and X. Zhang, *Strategies to improve the impact resistance of self-compacting concrete (SCC) after freeze-thaw cycles.* Journal of Building Engineering, 2023. **66**: p. 105854.

140. Gan, L., Y. Liu, Z. Zhang, J. Liu, H. Jin, and Y. Sun, *Dynamic mechanical properties of concrete with freeze-thaw damage under different low-temperature conditions.* Journal of Building Engineering, 2023. **80**: p. 107986.

141. Hallquist, J.O., *LS-DYNA® keyword user's manual Volume II material models.* Livermore, California, USA, 2013.

142. Dobratz, B.M., *LLNL explosives handbook: properties of chemical explosives and explosives and explosive simulants*. 1981, Lawrence Livermore National Lab., CA (USA).

143. Krieg, R.D., *A simple constitutive description for cellular concrete*. 1986: Sandia National Laboratories.

144. Mandal, J., A. Agarwal, and M. Goel, *Numerical modeling of shallow buried tunnel subject to surface blast loading.* Journal of Performance of Constructed Facilities, 2020. **34**(6): p. 04020106.

145. Esmaeili, M. and B. Tavakoli, *Finite element method simulation of explosive compaction in saturated loose sandy soils.* Soil Dynamics and Earthquake Engineering, 2019. **116**: p. 446-459.

146. ETA, T.P., B.H. ETA, and C. Chou, *Rollover Simulations for Vehicles using Deformable Road Surfaces.* 2012.

147. Abedini, M., C. Zhang, J. Mehrmashhadi, and E. Akhlaghi. *Comparison of ALE, LBE and pressure time history methods to evaluate extreme loading effects in RC column*. in *Structures*. 2020. Elsevier.

148. Mussa, M.H., A.A. Mutalib, R. Hamid, S.R. Naidu, N.A.M. Radzi, and M. Abedini, *Assessment of damage to an underground box tunnel by a surface explosion.* Tunnelling and underground space technology, 2017. **66**: p. 64-76.

149. Koneshwaran, S., *Blast response and sensitivity analysis of segmental tunnel*. 2014, Queensland University of Technology.

150. Johnson, G.R. and W.H. Cook, *Fracture characteristics of three metals subjected to various strains, strain rates, temperatures and pressures.* Engineering fracture mechanics, 1985. **21**(1): p. 31-48.

151. Kim, N.-H., C.-S. Oh, Y.-J. Kim, K.-B. Yoon, and Y.-H. Ma, *Comparison of fracture strain based ductile failure simulation with experimental results.* International Journal of Pressure Vessels and Piping, 2011. **88**(10): p. 434-447.

152. Chong, J., L. Yuan, T. Xianshu, G. Zhenru, and L. Yuchun, *Local damage effects of X70 steel pipe subjected to contact explosion loading.* Chinese Journal of High Pressure Physics, 2013. **27**: p. 567-574.

153. He, Y., Z. Liu, Y. Ma, P. Cai, and Z. Zuo, *Numerical simulation study on the effect of large explosive contact pipeline explosion on pipeline damage.* Thin-Walled Structures, 2022. **174**: p. 109146.

154. Kulak, R.F. and C. Bojanowski. *Modeling of cone penetration test using SPH and MM-ALE approaches*. in *8th European LS-DYNA users conference*. 2011.

155. Xu, T., A. Yao, X. Zeng, and Y. Li, *Study on the security conditions of parallel laying gas transmission pipelines under blast loading*, in *ICPTT 2011: Sustainable Solutions For Water, Sewer, Gas, And Oil Pipelines*. 2011. p. 1401-1411.

156. Busch, C.L. and R.A. Tarefder, *Evaluation of appropriate material models in LS-DYNA for MM-ALE finite element simulations of small-scale explosive airblast tests on clay soils.* Indian Geotechnical Journal, 2017. **47**(2): p. 173-186.

157. El-Danaf, E., M. Baig, A. Almajid, W. Alshalfan, M. Al-Mojil, and S. Al-Shahrani, *Mechanical, microstructure and texture characterization of API X65 steel.* Materials & Design, 2013. **47**: p. 529-538.

158. Cao, Y., Y. Zhen, M. Song, H. Yi, F. Li, and X. Li, *Determination of Johnson–Cook parameters and evaluation of Charpy impact test performance for X80 pipeline steel.* International Journal of Mechanical Sciences, 2020. **179**: p. 105627.

159. DBP, *DAMPIER TO BUNBURY NATURAL GAS PIPELINE SYSTEM: DESCRIPTION OF THE GAS TRANSMISSION SYSTEM*. 2011.

160. Association, C.S., *CSA Z662-03—Oil and Gas Pipeline Systems.* Canadian Standards Association, Mississauga, ON, 2003.

161. Gresnigt, A., *Plastic design of buried steel pipelines in settlement areas.* Heron (Delft), 1986. **31**(4): p. 1-113.

162. Chipley, M., W. Lyon, R. Smilowitz, P. Williams, C. Arnold, W. Blewett, L. Hazen, and F. Krimgold, *Primer to Design Safe School Projects in Case of Terrorist Attacks and School Shootings. Buildings and Infrastructure Protection Series. FEMA-428/BIPS-07/January 2012. Edition 2.* US Department of Homeland Security, 2012.

163. Australia, S., *AS/NZS 2885 : 2018 Pipeline－Gas and liquid petroleum*, in *fourth edition*. 2018, SAI Global.

164. Shi, X., L. Qian, C. Ma, J. LI, and W. Wang, *Experimental study on the temperature field of concrete during cooling from room temperature to-196℃ and then returning to room temperature.* Engineering Mechanics (in chinese), 2018. **35**(5): p. 162-169.

165. Hedayati, R. and M. Sadighi, *Bird strike: an experimental, theoretical and numerical investigation*. 2015: Woodhead Publishing.

166. Follansbee, P. and C. Frantz, *Wave propagation in the split Hopkinson pressure bar.* Journal of Engineering Materials and Technology, 1983. **105**.

167. Kolsky, H., *An investigation of the mechanical properties of materials at very high rates of loading.* Proceedings of the Physical Society. Section B, 1949. **62**(11): p. 676.

168. Lindholm, U., *Some experiments with the split hopkinson pressure bar∗.* Journal of the Mechanics and Physics of Solids, 1964. **12**(5): p. 317-335.

169. Zhang, D., J. Niu, P. Chen, P. Ranjith, and W. Nie, *Mechanical properties of concrete under different water content and low temperature conditions.* Materials and Structures, 2023. **56**(4): p. 71.

170. Jiang, Z., B. He, X. Zhu, Q. Ren, and Y. Zhang, *State-of-the-art review on properties evolution and deterioration mechanism of concrete at cryogenic temperature.* Construction and Building Materials, 2020. **257**: p. 119456.

171. Marechal, J., *Variations in the modulus of elasticity and Poisson's ratio with temperature.* Special Publication, 1972. **34**: p. 495-504.

172. CEB-FIP, *Model Code 1990 for Concrete Structures, Comit e Euro-International du B eton and F ed eration Internationale de la Pr econtrainte*. 1993, Thomas Telford, London.

173. Malvar, L.J. and J.E. Crawford, *Dynamic increase factors for concrete.* DTIC document, 1998. **1**(1.4): p. 1.6.

174. Malvar, L.J., *Review of static and dynamic properties of steel reinforcing bars.* Materials Journal, 1998. **95**(5): p. 609-616.

175. Bischoff, P. and S. Perry, *Compressive behaviour of concrete at high strain rates.* Materials and structures, 1991. **24**: p. 425-450.

176. Grote, D., S. Park, and M. Zhou, *Dynamic behavior of concrete at high strain rates and pressures: I. experimental characterization.* International journal of impact engineering, 2001. **25**(9): p. 869-886.

177. Zhang, M., H. Wu, Q. Li, and F. Huang, *Further investigation on the dynamic compressive strength enhancement of concrete-like materials based on split Hopkinson pressure bar tests. Part I: Experiments.* International journal of impact engineering, 2009. **36**(12): p. 1327-1334.

178. Chen, X., S. Wu, and J. Zhou, *Experimental and modeling study of dynamic mechanical properties of cement paste, mortar and concrete.* Construction and Building Materials, 2013. **47**: p. 419-430.

179. Hao, Y., H. Hao, G. Jiang, and Y. Zhou, *Experimental confirmation of some factors influencing dynamic concrete compressive strengths in high-speed impact tests.* Cement and concrete research, 2013. **52**: p. 63-70.

180. Petrovic, J., *Review mechanical properties of ice and snow.* Journal of Materials Science, 2003. **38**: p. 1-6.

181. Wu, X. and V. Prakash, *Dynamic compressive behavior of ice at cryogenic temperatures.* Cold Regions Science and Technology, 2015. **118**: p. 1-13.

182. Liu, P., X. Zhou, Q. Qian, F. Berto, and L. Zhou, *Dynamic splitting tensile properties of concrete and cement mortar.* Fatigue & Fracture of Engineering Materials & Structures, 2020. **43**(4): p. 757-770.

183. Chen, X., Y. Shao, L. Xu, and C. Chen, *Experimental study on tensile behavior of cement paste, mortar and concrete under high strain rates.* Journal of Wuhan University of Technology-Mater. Sci. Ed., 2015. **30**(6): p. 1268-1273.

184. Xie, J. and H. Wu, *Experimental research on concrete strength under freeze–thaw recycle action with ultra-low temperature.* Journal of Civil, Architectural & Environmental Engineering, 2012. **34**: p. 165-168.

185. Wei, Q., J. Xie, and H. Wu, *Experimental analysis on properties of concrete after freeze-thaw cycles under extra-low temperatures.* Engineering Mechanics (in Chinese), 2013. **30**(Special issue): p. 125-131.

186. Chi, K., J. Li, R. Shao, L. Chen, S. Xu, and C. Wu, *Experimental study on impact behaviour of normal strength mortar at cryogenic temperatures and after freeze-thaw cycles.* Construction and Building Materials, 2024. **440**(0950-0618): p. 137497.

187. Shi, C., Z. Wu, J. Xiao, D. Wang, Z. Huang, and Z. Fang, *A review on ultra high performance concrete: Part I. Raw materials and mixture design.* Construction and Building Materials, 2015. **101**: p. 741-751.

188. Wu, Z., C. Shi, K.H. Khayat, and L. Xie, *Effect of SCM and nano-particles on static and dynamic mechanical properties of UHPC.* Construction and Building Materials, 2018. **182**: p. 118-125.

189. Mousavi, S.M., M.M. Ranjbar, and R. Madandoust, *Combined effects of steel fibers and water to cementitious materials ratio on the fracture behavior and brittleness of high strength concrete.* Engineering Fracture Mechanics, 2019. **216**: p. 106517.

190. He, B., H. Zhang, X. Zhu, Q. Zheng, O. Onuaguluchi, N. Banthia, and Z. Jiang, *Thermal-dependent brittleness effect of ultra-high performance concrete exposed to cryogenic flexural loads by acoustic emission evaluation.* Cement and Concrete Composites, 2023. **139**: p. 105056.

191. Kim, M.-J. and D.-Y. Yoo, *Cryogenic pullout behavior of steel fibers from ultra-high-performance concrete under impact loading.* Construction and Building Materials, 2020. **239**: p. 117852.

192. Khan, M. and M. Iqbal. *Strain rate and size effects on dynamic tensile behaviour of standard and high-strength concrete: An experimental study*. in *Structures*. 2024. Elsevier.

193. Hobbs, D. *The tensile strength of rocks*. in *International Journal of Rock Mechanics and Mining Sciences & Geomechanics Abstracts*. 1964. Elsevier.

194. Guo, Y., G. Gao, L. Jing, and V. Shim, *Response of high-strength concrete to dynamic compressive loading.* International Journal of Impact Engineering, 2017. **108**: p. 114-135.

195. Ngo, T., P. Mendis, and A. Whittaker, *A rate dependent stress-strain relationship model for normal, high and ultra-high strength concrete.* International Journal of Protective Structures, 2013. **4**(3): p. 451-466.

196. Huang, D., Y. Feng, Q. Xia, J. Tian, and X. Li, *Research on mechanical properties and durability of early frozen concrete: A review.* Construction and Building Materials, 2024. **425**: p. 135988.

197. Park, S.H., D.J. Kim, and S.W. Kim, *Investigating the impact resistance of ultra-high-performance fiber-reinforced concrete using an improved strain energy impact test machine.* Construction and Building Materials, 2016. **125**: p. 145-159.

198. Yang, L., X. Lin, and R.J. Gravina, *Evaluation of dynamic increase factor models for steel fibre reinforced concrete.* Construction and building materials, 2018. **190**: p. 632-644.

199. Chi, K., J. Li, R. Shao, L. Chen, S. Xu, and C. Wu, *Experimental study on impact behaviour of normal strength mortar at cryogenic temperatures and after freeze-thaw cycles.* Construction and Building Materials, 2024. **440**: p. 137497.

200. Monteiro, P.J., A.I. Rashed, J. Bastacky, and T.L. Hayes, *Ice in cement paste as analyzed in the low-temperature scanning electron microscope.* Cement and Concrete Research, 1989. **19**(2): p. 306-314.

201. Wang, L. and L. Yang, *Progress in impact dynamics.* Wang LL, Yu TX, Li YC, eds, 1992: p. 88-116.

202. Gao, G., E. Tang, G. Yang, Y. Han, M. Chang, K. Guo, and L. He, *Parameter determination and verification of ZWT viscoelastic dynamic constitutive model of Al/Ep/W material considering strain rate effect.* International Journal of Impact Engineering, 2024. **184**: p. 104816.

203. Fu, T., Z. Zhu, D. Zhang, Z. Liu, and Q. Xie, *Research on damage viscoelastic dynamic constitutive model of frozen soil.* Cold Regions Science and Technology, 2019. **160**: p. 209-221.

204. Li, B., Z. Zhu, J. Ning, T. Li, and Z. Zhou, *Viscoelastic–plastic constitutive model with damage of frozen soil under impact loading and freeze–thaw loading.* International Journal of Mechanical Sciences, 2022. **214**: p. 106890.

205. Chen, J. and L. Wang, *Rate-dependent constitutive equation of cement mortar.* J. Ningbo Univ.(NSEE), 2000. **2**: p. 1-5.

206. Wu, X., S. Wang, J. Yang, J. Zhao, and X. Chang, *Damage characteristics and constitutive model of lightweight shale ceramsite concrete under static-dynamic loading.* Engineering Fracture Mechanics, 2022. **259**: p. 108137.

207. Rabotnov, Y.N. *Paper 68: On the equation of state of creep*. in *Proceedings of the Institution of Mechanical Engineers, Conference Proceedings*. 1963. SAGE Publications Sage UK: London, England.

208. Wang, L., Z. Jiang, and J. Chen. *Studies on Rheological Relation of Materials by Taking into Account the Rate-dependent Evolution of Internal Defects at High Strain Rates*. in *IUTAM Symposium on Rheology of Bodies with Defects: Proceedings of the IUTAM Symposium held in Beijing, China, 2–5 September 1997*. 1999. Springer.

209. Wang, L., X. Dong, and Z. Sun, *Dynamic constitutive behavior of materials at high strain rate taking account of damage evolution.* Explosion and Shock Waves, 2006. **26**(3): p. 193.

210. Taerwe, L.R., *Influence of steel fibers on strain-softening of high-strength concrete.* Materials Journal, 1993. **89**(1): p. 54-60.

211. Li, W. and J. Xu, *Mechanical properties of basalt fiber reinforced geopolymeric concrete under impact loading.* Materials Science and Engineering: A, 2009. **505**(1-2): p. 178-186.

212. Fu, Q., Y. Xie, G. Long, D. Niu, H. Song, and X. Liu, *Impact characterization and modelling of cement and asphalt mortar based on SHPB experiments.* International Journal of Impact Engineering, 2017. **106**: p. 44-52.

213. Yu, Q., W. Zhuang, and C. Shi, *Research progress on the dynamic compressive properties of ultra-high performance concrete under high strain rates.* Cement and Concrete Composites, 2021. **124**: p. 104258.

214. Alhozaimy, A., P. Soroushian, and F. Mirza, *Mechanical properties of polypropylene fiber reinforced concrete and the effects of pozzolanic materials.* Cement and Concrete Composites, 1996. **18**(2): p. 85-92.

215. Liu, J., D. Zhou, L. Cheng, S. An, L. Guo, H. Xue, and R. Wu, *Analysis of damage and fracture characteristics for concrete subjected to cryogenic freeze-thaw cycles: An acoustic emission and digital image correlation study.* Journal of Building Engineering, 2024: p. 109841.

216. Hassan, M. and K. Wille, *Comparative experimental investigations on the compressive impact behavior of fiber-reinforced ultra high-performance concretes using split Hopkinson pressure bar.* Construction and Building Materials, 2018. **191**: p. 398-410.

217. Ren, G., H. Wu, Q. Fang, and J. Liu, *Effects of steel fiber content and type on dynamic compressive mechanical properties of UHPCC.* Construction and building materials, 2018. **164**: p. 29-43.

218. Hou, X., S. Cao, W. Zheng, Q. Rong, and G. Li, *Experimental study on dynamic compressive properties of fiber-reinforced reactive powder concrete at high strain rates.* Engineering Structures, 2018. **169**: p. 119-130.

219. Chi, K., J. Li, R. Shao, J. Liu, Z. Liu, and C. Wu, *Experimental exploration on impact characteristics of ultra-high performance concrete at low and cryogenic temperature.* Submitted to Journal of Building Engineering, 2024.

220. Chi, K., J. Li, and C. Wu, *Behaviour of reinforced concrete panels under impact loading after cryogenic freeze-thaw cycles.* Construction and Building Materials, 2024. **414**: p. 135058.

221. Qi, J., Z. Wu, Z.J. Ma, and J. Wang, *Pullout behavior of straight and hooked-end steel fibers in UHPC matrix with various embedded angles.* Construction and Building Materials, 2018. **191**: p. 764-774.

222. Nath, P. and P.K. Sarker, *Use of OPC to improve setting and early strength properties of low calcium fly ash geopolymer concrete cured at room temperature.* Cement and Concrete Composites, 2015. **55**: p. 205-214.

223. Lu, S., J.-Y. Xu, E.-L. Bai, and X. Luo, *Effect of particles with different mechanical properties on the energy dissipation properties of concrete.* Construction and Building Materials, 2017. **144**: p. 502-515.

224. Liu, K., J. Liu, J. Li, M. Tao, and C. Wu. *Experimental investigation of heating–cooling effects on the mechanical properties of geopolymer-based high*

performance concrete heated to elevated temperatures. in *Structures*. 2023. Elsevier.

225. Khan, M.Z.N., Y. Hao, H. Hao, and F.U.A. Shaikh, *Experimental evaluation of quasi-static and dynamic compressive properties of ambient-cured high-strength plain and fiber reinforced geopolymer composites.* Construction and Building Materials, 2018. **166**: p. 482-499.

226. Bahmani, H. and D. Mostofinejad, *Microstructure of ultra-high-performance concrete (UHPC)–a review study.* Journal of Building Engineering, 2022. **50**: p. 104118.

227. Negahban, E., A. Bagheri, and J. Sanjayan, *Pore gradation effect on Portland cement and geopolymer concretes.* Cement and Concrete Composites, 2021. **122**: p. 104141.

228. Tedesco, J.W. and C.A. Ross, *Experimental and numerical analysis of high strain rate splitting-tensile tests.* Materials Journal, 1993. **90**(2): p. 162-169.

229. Sandison, G.A., M.P. Loye, J.C. Rewcastle, L.J. Hahn, J.C. Saliken, J.G. McKinnon, and B.J. Donnelly, *X-ray CT monitoring of iceball growth and thermal distribution during cryosurgery.* Physics in Medicine & Biology, 1998. **43**(11): p. 3309.

230. Zhu, X., L. Brochard, Z. Jiang, and M. Vandamme, *Molecular simulations of premelted films between CSH and ice: Implication for cryo-suction in cement-based materials.* Cement and Concrete Research, 2023. **174**: p. 107341.

231. Wiedemann, G., *Zum Einflubtiefer Temperaturen auf Festingkeit und Ferformung von Beton.* Dissertation Technische Universitat Braunschweig, 1982. **149**.

232. Béton, C.E.-I.d., *CEB-FIP model code 1990: Design code*. 1993: Thomas Telford Publishing.

233. Murray, Y.D., *Users manual for LS-DYNA concrete material model 159*. 2007, United States. Federal Highway Administration. Office of Research ….

234. Goto, Y. and T. Miura, *Deterioration of concrete subjected to repetitions of very low temperatures.* Transactions of the Japan Concrete Institute, 1979: p. 183-190.

235. Yamane, S., H. Kasami, and T. Okuno, *Properties of concrete at very low temperatures.* Special Publication, 1978. **55**: p. 207-222.

236. Rostasy, F.S. and G. Wiedemann, *Strength and deformability of concrete after low temperature cycles.* Proceedings, Second International Conference on Cryogenic Concrete, , Amsterdam 1983. **8 pp.**

237. Hallgeir Kornen and J.H. Andersen, *Properties of cryogenic concrete.* The Nordic Concrete Federation, Oslo, 1983: p. 149-165.

238. Berner, D.E. and B. Gerwick. *Static and cyclic behavior of structural lightweight concrete at cryogenic temperatures*. in *Ocean Space Utilization'85: Proceedings of the International Symposium Nihon University, Tokyo, Japan, June 1985 Volume 2*. 1985. Springer.

239. Liu, j., H. Liang, M. Han, X. Shi, and Y. Cui, *Experimental study on tensile strength of concrete subjected to differenet ultra low temperatures and returning to room temperature.* Special Structures, 2021. **38 (6)**: p. 8-14.

240. Australia, S., *AS 3600:2018- Australian Standard for Concrete Structures*, in *BD-002: Concrete Structures, Sydney*. 2018.

241. Yin, X., Q. Li, X. Xu, B. Chen, K. Guo, and S. Xu, *Investigation of continuous surface cap model (CSCM) for numerical simulation of strain-hardening fibre-reinforced cementitious composites against low-velocity impacts.* Composite Structures, 2023. **304**: p. 116424.

242. Wu, Y., J.E. Crawford, and J.M. Magallanes. *Performance of LS-DYNA concrete constitutive models*. in *12th International LS-DYNA users conference*. 2012.

243. Yan, J.-B. and J. Xie, *Experimental studies on mechanical properties of steel reinforcements under cryogenic temperatures.* Construction and Building Materials, 2017. **151**: p. 661-672.

244. Xie, J., R. Xi, C. Tong, and J.-B. Yan, *Mechanical properties of Q235 ~ Q460 mild steels at low temperatures.* Construction and Building Materials, 2023. **363**: p. 129850.

245. Jung, D.-H., J.-K. Kwon, N.-S. Woo, Y.-J. Kim, M. Goto, and S. Kim, *S–N fatigue and fatigue crack propagation behaviors of X80 steel at room and low temperatures.* Metallurgical and Materials Transactions A, 2014. **45**: p. 654-662.

246. Zou, D., J. Sun, H. Wu, Y. Hao, Z. Wang, and L. Cui, *Experimental and numerical studies on the impact resistance of large-scale liquefied natural gas (LNG) storage outer tank against the accidental missile.* Thin-Walled Structures, 2021. **158**: p. 107189.

247. Malvar, L.J., J.E. Crawford, J.W. Wesevich, and D. Simons, *A plasticity concrete material model for DYNA3D.* International journal of impact engineering, 1997. **19**(9-10): p. 847-873.

248. Borrvall, T. and W. Riedel. *The RHT concrete model in LS-DYNA*. in *Proceedings of The 8th European LS-DYNA user conference*. 2011.

249. Lin, X., *Numerical simulation of blast responses of ultra-high performance fibre reinforced concrete panels with strain-rate effect.* Construction and Building Materials, 2018. **176**: p. 371-382.

250. Joy, S. and R. Moxley, *Material characterization, WSMR-5 3/4-inch concrete.* Report to the Defense Special Weapons Agency, 1993.

251. Malvar, L.J., J.E. Crawford, and K.B. Morrill, *K&C concrete material model release III-automated generation of material model input.* Karagozian and Case Structural Engineers, 2000. **Technical Report 650 TR-99-24.3**.

252. Hammoud, R., A. Yahia, and R. Boukhili, *Triaxial compressive strength of concrete subjected to high temperatures.* Journal of materials in civil engineering, 2014. **26**(4): p. 705-712.

253. Liu, J., J. Li, J. Fang, K. Liu, Y. Su, and C. Wu, *Investigation of ultra-high performance concrete slabs under contact explosions with a calibrated K&C model.* Engineering Structures, 2022. **255**: p. 113958.

254. Shi, X., Y. Ju, C. Ma, J. Zheng, and T. Zhang, *Experimental study on tensile strength of concrete exposed to cryogenic temperature.* Chinese.] Build. Struct, 2016. **46**(13): p. 86-89.

255. Wu, Y. and J.E. Crawford, *Numerical modeling of concrete using a partially associative plasticity model.* Journal of Engineering Mechanics, 2015. **141**(12): p. 04015051.

256. Xu, Z., J. Li, H. Qian, and C. Wu, *Blast resistance of hybrid steel and polypropylene fibre reinforced ultra-high performance concrete after exposure to elevated temperatures.* Composite Structures, 2022: p. 115771.

257. Chanda, S., *Temperature effects on dynamic fracture of pipeline steel.* 2015.

258. Béton, C.E.-I.d., *Concrete structures under impact and impulsive loading: Synthesis report*. 1988: Comite euro-international du beton.

259. Sanchidrian, J.A., R. Castedo, L.M. Lopez, P. Segarra, and A.P. Santos, *Determination of the JWL constants for ANFO and emulsion explosives from cylinder test data.* Central European journal of energetic materials, 2015. **12**(2): p. 177--194.

260. Do, T.V., T.M. Pham, and H. Hao, *Numerical investigation of the behavior of precast concrete segmental columns subjected to vehicle collision.* Engineering Structures, 2018. **156**: p. 375-393.

261. Choi, J.-H., S.-J. Choi, J.-H.J. Kim, and K.-N. Hong, *Evaluation of blast resistance and failure behavior of prestressed concrete under blast loading.* Construction and Building Materials, 2018. **173**: p. 550-572.

262. Arup, E., *All-Concrete LNG Tank for Small Scale LNG*. Arup Energy.

263. Zou, D., Y. Hao, H. Wu, J. Sun, L. Xu, and J. Li, *Safety assessment of large-scale all steel LNG storage tanks under wind-borne missile impact.* Thin-Walled Structures, 2022. **174**: p. 109078.

264. Standard, A., *AS 3961:2017 The storage and handling of liquefied natural gas*. 2017, Standards Australia: Australia.

265. standard, A.N.Z., *AS/NZA 2566.2: 2002 Buried flexible pipelines Part 2: installation*. 2002, SAI Global.